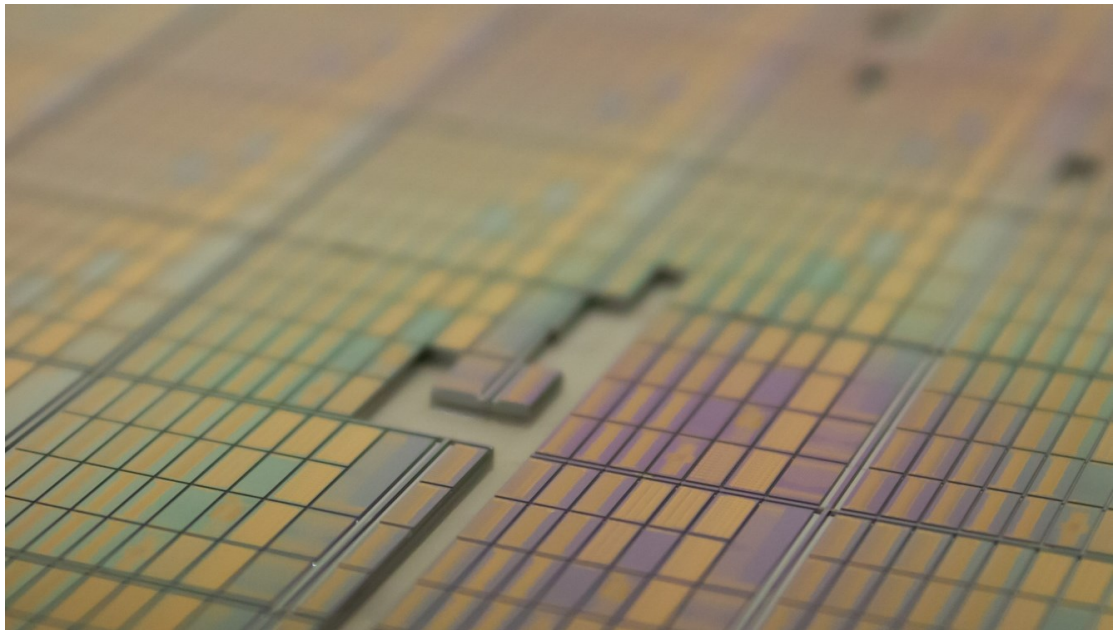


UNIVERSITÀ DEGLI STUDI DI PAVIA
DOTTORATO DI RICERCA IN FISICA – XXXIII CICLO

Silicon Photonic Integrated Circuits for Quantum Applications

Federico Andrea Sabattoli



Tesi per il conseguimento del titolo



Università degli Studi di Pavia
Dipartimento di Fisica

DOTTORATO DI RICERCA IN FISICA – XXXIII CICLO

Silicon Photonic Integrated Circuits for Quantum Applications

Federico Andrea Sabattoli

Submitted to the Graduate School of Physics in partial
fulfillment of the requirements for the degree of

DOTTORE DI RICERCA IN FISICA
DOCTOR OF PHILOSOPHY IN PHYSICS

at the
University of Pavia

Supervisor: Prof. Matteo Galli

*To my love, Greta
and to my special daughter, Chloe*

Contents

1	Introduction	3
1.1	Quantum computing	3
1.2	Quantum communication	6
1.3	Integrated quantum photonics	7
1.4	Organization of the manuscript	8
2	Building Blocks of Silicon Photonic Integrated Circuits	11
2.1	Integrated optical waveguides	11
2.1.1	Linear optical parameters	13
2.1.2	Nonlinear optical parameters	16
2.1.3	Losses in integrated waveguides	22
2.2	Fundamental building blocks	24
2.2.1	Edge couplers	24
2.2.2	Directional couplers	26
2.2.3	Mach-Zehnder Interferometers	31
2.2.4	Thermal phase shifters	33
2.3	Microring resonators	35
2.3.1	Linear behavior	36
2.3.2	Figures of merit	39
2.3.3	Simulation of coupling parameter	42
2.3.4	FWM in microring resonators	44
3	Devices for Integrated Quantum Photonics	49
3.1	Microring resonators as sources of nonclassical states of light	50
3.2	Efficient generation of entangled frequency bins	55
3.3	Resonators in series: the superradiance	59
3.4	Linearly coupled resonators	59
3.4.1	W states	62
3.4.2	Frequency conversion	65
3.5	Linearly uncoupled resonators	71
3.5.1	Directional coupler isolation	73

3.5.2	Mach-Zehnder interferometer isolation	77
3.5.3	Pump recycling	81
3.6	Integrated bragg filters	82
3.7	Additional test structures	88
3.7.1	Microring resonators	88
3.7.2	Edge Couplers	88
4	Fabrication of Silicon Photonic Integrated Circuits	91
4.1	Silicon Optical Waveguides	91
4.1.1	Optical Lithography	93
4.1.2	Etching	101
4.1.3	H ₂ Annealing	104
4.1.4	Line Edge Roughness analysis	104
4.1.5	Encapsulation	105
4.2	Electrical circuits	107
4.2.1	Heaters	110
4.2.2	Pads	113
4.2.3	Electrical characterization	118
4.3	Deep Etch and Dicing	118
5	High Quality Factor Ring Resonators	129
5.1	Characterization methods	129
5.2	Characterization of ring resonators	133
6	Nonlinear Coupling of Linearly Uncoupled Resonators	145
6.1	Directional coupler isolation	145
6.1.1	Linear characterization	146
6.1.2	Suppression of parasitic processes in d-SFWM	150
6.2	Mach-Zehnder interferometer isolation	161
6.2.1	Linear characterization	164
6.2.2	Nonlinear characterization	166
7	Conclusions and Perspectives	171
	List of Publications and Conferences	175
	Acknowledgments	179
	Bibliography	181

Chapter 1

Introduction

Quantum technologies are today emerging as a new class of devices capable of harnessing quantum mechanics to improve the performance of the classical counterparts, or to bring new functionalities. The possibility of processing, storing and transmitting the information encoded in quantum mechanical systems promises to bring exceptional advances in different scientific and technological areas, such as computation [1], communication [2], metrology [3], sensing [4], and even lithography [5]. Today, quantum technologies are considered a key element for the scientifically and technological development: governments launched large research programs focused on quantum technologies [6], a relevant number of start-up companies offering quantum solutions to specific markets arose, and also large global companies such as Google, IBM, Intel, Microsoft and Toshiba are heavily investing in quantum technologies [7].

1.1 Quantum computing

One of the most exciting and popular application of quantum information science is quantum computing. The basic idea is to replace the use of the classical bit, whose logical states are either 0 or 1, with the quantum information basic building block: the qubit, which is defined, in general, as a superposition of two orthogonal states,

$$|\Psi\rangle = \alpha |0\rangle + \beta |1\rangle \quad (1.1)$$

Thus, the qubit can be described by two complex values, α and β , whose squared modulus are the probabilities to measure the qubit in the states, respectively, $|0\rangle$ and $|1\rangle$. The potentiality of the use of qubits is clear when dealing with states composed by many of them. The state that describe a system with two qubits is given, in general, by the superposition of four orthogonal states

$$|\Psi\rangle = \alpha_{00} |00\rangle + \alpha_{01} |01\rangle + \alpha_{10} |10\rangle + \alpha_{11} |11\rangle \quad (1.2)$$

and, hence, it is specified by four complex values. Similarly a system with n qubits is described by the superposition of 2^n orthogonal states and, therefore, 2^n complex values are needed to define it. This means that if one would be able to build a state with $n = 300$ qubits, then it would be impossible to store all the needed complex quantities on a classical computer, since their number would be higher than the estimated number of atoms in the Universe [1].

Therefore, it is clear that the development of a feasible technological platform on which it is possible to implement the processing of quantum information has the potential to efficiently solve hard computational tasks. However, it is important to underline that the development of quantum computing has not the goal to replace classical computation in all the fields. We can compare the development of quantum computers with the evolution of another class of devices based on quantum mechanics: the lasers. These devices allowed people to use light in a different way, exploiting its coherence, but they did not replace light bulbs for many applications. Similarly, one can expect that quantum computers won't be an improved version of ordinary computers, but they will be used to solve specific classes of problems that classical calculators cannot tackle [8], such as the implementation of Shor's quantum algorithm for factorizing large numbers [1], or the efficient simulation of quantum systems¹ [9].

Relevant improvements have been realized in the last two decades on the development of superconducting quantum computers based on the fabrication of Josephson junctions, which are used to design anharmonic oscillators whose two lowest-energy level allows one to encode the qubits [10, 11]. This approach meets quite well the five criteria pointed out by DiVincenzo [12] to realize a feasible quantum computer: in fact, superconductive qubits are scalable, since they are fabricated on chip, their initialization and addressing is viable, the implementation of a universal set of quantum gates is possible and, even if their decoherence time is not exceptionally long, thousands of gate operations have been demonstrated [11]. Several companies (such as Google [13], IBM [14], and Rigetti [15]) and research institutes (such as IMEC [16]) are investing a considerable amount of resources working on this technology, developing architectures with several tens of qubits. Recently, these efforts led to the demonstration of the supremacy of quantum computing over classical computation [17].

The main drawbacks of this approach are the challenging connectivity among superconductive qubits when the system is scaled up [18], and the complexity of the instrumentation used to cool down the system (the operating temperature is within 10 and 100 mK) and to set and measure the qubits' state. Obviously, these points have an important impact on the cost of superconductive devices, which is estimated to be around 10 000 \$ per qubit [19].

¹It's famous the Richard Feynman's quote "Nature isn't classical, dammit, and if you want to make a simulation of nature, you'd better make it quantum mechanical, and by golly it's a wonderful problem, because it doesn't look so easy"

Alternative solutions have been proposed so far, such as trapped ions [20, 21], nuclear spins [22, 23], or quantum dots [24, 25] (more details can be found in the review [8]). In addition, also photons have been investigated for the realization of a quantum hardware [26]: in particular, the encoding of the qubit by using orthogonal polarization states seemed appealing due to the low impact of decoherence. An universal set of quantum gates with which photonic qubits can be manipulated requires simple linear optical components, such as phase-shifters and waveplates, but also a strong nonlinear interaction of the photons, which is a demanding task. However, the discovery of the KLM scheme in 2001 [27] opened the way towards the implementation of a universal set of quantum gates by using just linear components. This led to the experimental proof-of-principle demonstrations of photonic quantum gates with two [28, 29] or three [30] qubits, as well as small-scale quantum algorithms [31, 32]. Even if in 2008 the first integrated photonic quantum logic gate was demonstrated [33], promising to improve the scalability of the photonic approach as described in Section 1.3, some problems limit the development of qubit-based quantum optical computing. First, the KLM scheme is based on the realization of a *probabilistic* gate, which is of little use since the probability of success of the computation decreases exponentially with the number of gates [26]. In parallel, photon losses and limited detection efficiency lead to a relevant increase of the sources needed to perform a computational task [34].

Other approaches have been proposed to improve the feasibility of optical quantum computing; among them, the continuous variable approach gained a significant interest in the last few years. The basic idea is to replace the use of discrete systems with continuous variables (CV) [35, 36] and encode the computational tasks by using a set of operators acting on the observables of a quantum state. In particular, it can be shown that universal quantum computation can be realized by implementing some gates involving linear effects (such as phase and amplitude modulation, phase shift, and interference), second-order nonlinear effect (optical squeezing) and third-order nonlinear effect (cubic phase shift) [37]. The implementation of the cubic phase shift gate is still a demanding task. However, a subclass of CV quantum computing, the Gaussian Boson Sampling [38, 39], found many applications, ranging from the identification of dense subgraph [40] to the simulation of vibronic spectra of molecules [41]. In particular, the implementation of this technique allows one to avoid the use of cubic phase gates. Recently, the advantage of quantum computation using Gaussian Boson Sampling has been demonstrated [42]: a photonic quantum computer with 50 indistinguishable single-mode squeezed states was used to perform a computational task that state-of-the-art simulation strategies and supercomputers would realize in around 1 billion years, proving the relevant impact that photonics can have on quantum computing.

1.2 Quantum communication

Another very active field in which quantum technologies can provide important benefits is the communication. “Quantum communication is the art of transferring a quantum state from one place to another” [2], and the processing of quantum information allows tasks that classical methods could achieve far less efficiently. The most promising application of quantum communication is quantum key distribution (QKD), which consists in the sharing of encrypted keys between the transmitter and the receiver such that the security is not accessible by classical communications [43, 44]. The first protocol based on quantum cryptography is the famous BB84, which was proposed in 1984 by Bennet and Brassard [45]. Without entering into details, I will provide a brief description of BB84 to get the flavor of the topic. The idea is to encode the information sent by the transmitter (usually called Alice) by using two sets of bases of the Hilbert space $|0\rangle, |1\rangle$ and $|A\rangle, |B\rangle$ such that

$$\begin{aligned} |A\rangle &= \frac{1}{\sqrt{2}} (|0\rangle + |1\rangle) \\ |B\rangle &= \frac{1}{\sqrt{2}} (|0\rangle - |1\rangle) \end{aligned} \tag{1.3}$$

Half of the sent bits are encoded using eigenstates the first basis (thus the qubits will be in state $|0\rangle$ or $|1\rangle$), and the eigenstates of the second basis are used for the remaining part ($|A\rangle$ or $|B\rangle$). Then, the receiver (Bob) has to choose the basis with which he measures the qubits: if it corresponds to the basis used by Alice, he gets the same value encoded by her. Once the transmission is performed, they publicly state the used basis for each photon and they discard the data related to the ones with which they used different bases. Now, the most important passage: they can compare publicly Bob’s measures and Alice’s input states for a portion of the kept data. If they find some inconsistencies, this means that an eavesdropper intercepted some of the qubits: this leads to the discard of the message and to the repetition of the procedure. In fact, the idea is based on a fundamental theorem of quantum information, the non cloning theorem, which demonstrates the impossibility of copying an unknown quantum state. Thus, eavesdropping would cause the disruption of the original qubit and the impossibility of emitting an identical photon. More complex and sophisticated protocols have been proposed later. For instance, Ekert described in 1991 a variation of BB84 in which entangled states could enhance the security of communication [46].

If it is true that in principle one could use several systems to encode the quantum information to be communicated, it is clear that photons are the natural candidates for this task [47]. First, modern communication technologies are based on the use of infrared light propagating in optical fibers: thus, the implementation of QKD protocols using infrared photons would automatically benefits from the use of already developed communication platforms and instrumentation. In addition,

photons offers many possibility of encoding. Polarization has been widely used as its manipulation is relatively simple by using waveplates and polarizers [34]. However, standard single-mode optical fibers lead to relatively short decoherence times of polarization-encoded qubits, and this choice is not suitable for long-range communication. Thus, other forms of encoding can be exploited, such as phase, time and frequency.

Quantum communication, and in particular QKD, is already a feasible technology: fiber-based QKD was proven to work over 300 km of optical fiber [48], satellite-based QKD was used, in combination with metropolitan fiber networks, to encrypt a full videoconference between Beijing and Vienna [49], and several medium-sized enterprises (such as IDQuantique, Quintessence Labs, or MagiQ Technologies) are already selling their devices to banks, governments, and other customers with highest security requirements [7].

1.3 Integrated quantum photonics

Integrated photonics consists in the realization of thousands of optical devices on millimetric chips that allows one to generate, manipulate and detect light, leading to the realization of very complex circuits. Thus, it can offer many resources to implement quantum technologies, with the possibility of integrate on chip sources of single and entangled photons [50–55], squeezed light [56, 57], and coherent radiation [58, 59], as well as electro-optic phase modulators [60–62], optical filters [63–65] and even single-photon detectors [66–68]. Different platforms can be adopted, such as silicon-on-insulator (SOI) [51, 52, 69], silicon nitride [55–57], silicon oxynitride (SiON or hydrex) [70, 71], lithium niobate (LN) [72], indium phosphide (InP) [73, 74], gallium arsenide (GaAs) [75], silica-on-silicon [33, 76], and laser-writing on silica [77, 78]. All the platforms have pros and cons, which make them more suitable for the realization of one component or another. In addition, since the transmitter and the receiver are not on the same chip, one can think about hybrid systems, as it has been reported in 2017 where the first fully integrated chip-to-chip QKD system was implemented with an InP transmitter chip and a SiON receiver chip [73]. Among all the possible technologies, however, Silicon Photonics seems the most appealing for industrial and commercial applications [44]. The continuous growing of internet traffic [79] pushed and pushes the development of more efficient and cost effective solutions to manipulate high data rates. Silicon Photonics is recognized as a key technology in this field since it can exploit complementary metal-oxide semiconductor (CMOS) fabrication processes, which are nowadays very well developed and they allows for the commercialization of incredibly complex devices at reasonable costs [80]. In addition, it naturally guarantees the integration with CMOS circuits, with the possibility of building complex photonic circuits driven by on-chip electronics [80, 81]. Finally, many efforts have been made to integrate other photonic platforms, such as SiN [82, 83], and III-V semiconductors [58, 84, 85],

demonstrating that the platform can be enriched by other materials still keeping the advantages about scalability and feasibility of the fabrication.

The development of integrated quantum photonics brought already interesting and exciting results: starting from the first realization of the Hong-Ou-Mandel [86] experiment on chip in 2012 [87], state-of-the-art devices arrived to include more than 650 optical components for the generation, manipulation and measurement of multidimensional entangled states [88]. In addition, a photonic quantum computer based on continuous variable, whose core is composed of integrated squeezers, has been made available on the cloud by the Canadian company Xanadu², proving the relevance of integrated optics even in the computation field.

However, there are still some challenges that research institutes and industries have to face up with. The main problem is the reduction of the losses in the system. In fact, by simply analyzing the BB84 protocol briefly explained above, it is clear that losing a photon means the disruption of the only carrier of the quantum information. Hence, the losses in the system should be reduced to obtain higher fidelity of the quantum state.

Another very relevant issue is represented by the full integration of all the components. In fact, up to now fully integrated quantum chips with sources, circuits and detectors have never been realized [44]. This is due to some technical issues, such as the feasibility of integrated filters with which suppress the bright light used to pump the photon sources, as well as the integration of single-photon detectors (working at cryogenic temperatures) with active components such as switches, phase shifters and lasers. Finally, fabrication errors and imperfection of the components (imperfect cross-section or waveguide non-uniformity) affect the performance of quantum operations based on interference and measurement. However, the continue improvement of the quality of the fabrication and the possibility to realize programmable photonic circuits [81, 89] to enable the feedback control of the quantum device [90] push towards the feasibility of complex integrated quantum photonic circuits.

1.4 Organization of the manuscript

The work presented in this manuscript focused on the development of silicon photonic integrated circuits (PICs) with different goals. First, I tried to tackle the problem of the reduction of optical losses in integrated circuits. As discussed above, this is very important for the manipulation of the nonclassical states, but it is also fundamental to realize efficient and bright sources of entangled photon pairs or heralded single photons by using high-quality-factor microring resonators. Then, I realized several innovative photonic integrated PIC based on the use of ring resonators: (i) linearly coupled resonators for the generation of W states and the frequency conversion; (ii) nonlinearly coupled resonators to experimentally prove

²<https://www.xanadu.ai/>

the suppression of parasitic processes that affect the generation of squeezed light in integrated circuits; (iii) devices for the efficient generation of frequency-encoded entangled states; (iv) circuits to prove the efficacy of placing several sources in series to improve their efficiency (in analogy with Dicke superradiance); (v) integrated filters based on Bragg scattering to attenuate the pump that allows one to generate nonclassical state exploiting spontaneous four wave mixing.

In Chapter 2 the basic building blocks used for the realization of the circuits are presented, as well as the calculations and finite element simulations performed to define their geometrical parameters. The third chapter collects the description of the structures I designed, focusing on their goals and the details of the circuits. Chapter 4 resumes my activities at the CEA-Leti research center in Grenoble (France), where I worked to follow the fabrication of the integrated circuits in a 200-mm CMOS pilot foundry. In particular, I describe in detail the process flow developed to realize low-losses silicon waveguides with high mode confinement, which is based on the thermal annealing of them. Since the huge number of the proposed experiments, not all of them have been realized during my PhD course. The optical measures I performed are presented in Chapters 5 and 6. The linear characterization of the microring resonators is reported in Chapter 5: several devices are analyzed, showing the impact of the annealing procedure on the devices. In addition, the limits of the treatments are described. Finally, in Chapter 6 I describe the results related to the use of nonlinear coupled resonators, which allowed me to demonstrate a strategy to suppress parasitic noise in dual-pump spontaneous four-wave mixing that can be extremely relevant for the realization of sources of squeezed light.

Chapter 2

Building Blocks of Silicon Photonic Integrated Circuits

The starting point in the realization of a photonic integrated circuit (PIC) is the design and the simulation of its optical and electric components. In this chapter the basic optical elements, such as optical waveguides, directional couplers, edge couplers, and Bragg filters, are described, with a specific focus on their optical behavior (both linear and nonlinear). Their geometrical parameters are obtained with finite elements simulations, which are briefly detailed. In addition, the use of thermal phase shifters to modify the spectral response of the optical elements is illustrated. The described building blocks are then assembled to design different devices, which are presented in Chapter 3.

2.1 Integrated optical waveguides

Photonic integrated circuits are based on the manipulation of light which propagates within optical waveguides. The confinement of the electromagnetic radiation is usually obtained by exploiting the phenomenon of total internal reflection (TIR) at the interface of two dielectric materials with different refractive indexes ($n_1 < n_0$), which constrains the light in the medium with higher refractive index [91].

A very simple configuration one can study is the symmetric *slab* waveguide, composed of a dielectric layer with refractive index surrounded by another dielectric material having a lower refractive index (see Figure 2.1). However, the building of PICs requires the use of some *optical wires*, which can be obtained by exploiting TIR also in the lateral dimension. The most straightforward structure one can imagine is the *strip* (or rectangular) waveguide [92, 93], which is composed of a strip of a material with higher refractive index (the core) embedded into a matrix made of a

material with a lower refractive index (the *cladding*). Another solution that can be adopted is the *rib* waveguide [94, 95], composed of a strip of higher index material placed on top of a slab and surrounded by the cladding, as shown in Figure 2.1. Other solutions can be exploited, such as slot waveguides [96, 97] or photonic crystal waveguides [98, 99], which are adopted for specific applications and materials (see [100] for more details).

This work is focused on the use of simple strip waveguides composed of silicon embedded in a silicon dioxide matrix. One can obtain this kind of waveguides starting from a silicon-on-insulator (SOI) wafer composed of a silicon substrate, a buried oxide layer (BOX) made of silica and an upper layer of silicon, which is patterned by a lithographic and etching processes to create the wires with rectangular cross-section. Then, a further layer of SiO_2 is deposited to create the strip waveguides (more details about the fabrication are given in Chapter 4). This technology is the basis of Silicon Photonics [101, 102], which is a very promising platform for integrated photonics, since it allows to realize on-chip a huge range of devices, from sources of coherent light to detectors. In addition, as already mentioned, the nonlinear dielectric response of silicon can be exploited to generate photon pairs and, thus, entangled or single-photon states of light through spontaneous four-wave mixing [50, 103]. Therefore, the adoption of encapsulated SOI strip waveguides in this work, which has the goal to realize sources of nonclassical states of light, is motivated by the following points.

1. Nonlinear optics takes great advantage of the spatial confinement attainable in integrated waveguides [104, 105]. In fact, the smaller is the effective area of the nonlinear interaction, the more intense is its strength. As one can expect, the effective area in integrated waveguides is much smaller with respect to bulk solutions involving crystals, allowing one to operate even with modest pump power.
2. Silicon is a good material for nonlinear optics, since the high value of its third order nonlinear susceptibility [106?] which further increase the intensity of the nonlinear processes.
3. The optical devices based on CMOS materials (such as silicon or silicon nitride) can be realized in CMOS foundries with advanced processes and equipment [107] which allows one to have high-quality chips at reasonable costs [80, 108]. This makes the platform already mature from a commercial point of view, as it is confirmed by the fact that several Silicon Photonics products are already on the market [109].
4. The presence of the oxide cladding on top of the waveguides protects the devices from the environment and allows one to add additional layers, such as metals for thermal tuning of the effective index.

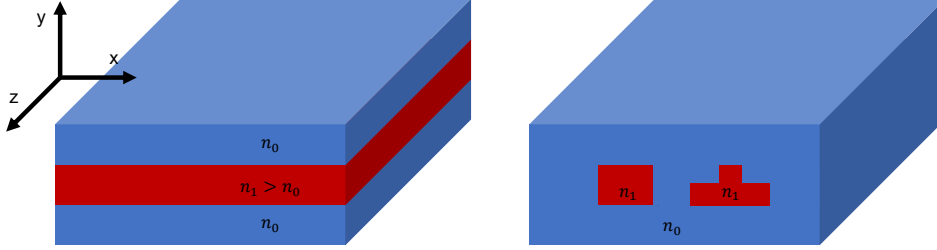


Figure 2.1: Scheme of common optical waveguides. On the left a slab waveguide is presented, where the light is confined in the xz plane. On the right, the ridge and the rib waveguides are shown, which are typically used to guide the light in PICs.

In the following sections the optical characteristics of the used waveguides are analyzed to detail these points.

2.1.1 Linear optical parameters

The study of optical modes in dielectric materials leads to the search of solutions of Maxwell equations. If we assume that the medium does not absorb and that no sources are present, they can be written in the form [91]:

$$\nabla \times \mathbf{H} = i\omega\epsilon_0 n^2 \mathbf{E}, \quad \nabla \times \mathbf{E} = -i\omega\mu \mathbf{H} \quad (2.1)$$

where n is the refractive index of the material, ω is the angular frequency, $\epsilon_0 = 8.854 \cdot 10^{-12} \text{ F/m}$ is the vacuum dielectric permittivity, and μ is the magnetic permeability of the material. Maxwell equations have well known analytical solutions for slab waveguides, which correspond to optical modes that can be classified as TE (transverse electric) or TM (transverse magnetic). In TE modes, only the components E_y , H_x , and H_z are different than zero, and the electric field is perpendicular to the dielectric layers (xz plane in Figure 2.1). On the other hand, TM modes have only H_y , E_x , and E_z different than zero. If we assume $\hat{\mathbf{z}}$ to be the direction of propagation, the electric field in the TE modes (and a similar expression is associated to the magnetic field for TM modes) turns out to be:

$$\mathbf{E} = E_y \hat{\mathbf{y}} = E_m(x, y) e^{i(\omega t - \beta_m z)} \hat{\mathbf{y}} \quad (2.2)$$

where ω is the angular frequency and $E_m(x, y)$ describe the mode distribution. The propagation constant β_m depends on the frequency, and it gives the information about the dispersion of the optical modes. It can be expanded in a Taylor series around a central frequency ω_0 as:

$$\beta(\omega) \doteq n_{eff}(\omega) \frac{\omega}{c} = \beta_0 + \beta_1(\omega - \omega_0) + \frac{1}{2} \beta_2(\omega - \omega_0)^2 \quad (2.3)$$

where β_0 is the wavevector at ω_0 , while β_1 and β_2 are related to the effective index n_{eff} and its derivatives. β_1 is the inverse of the group velocity

$$\beta_1 = \frac{\partial \beta}{\partial \omega} = \frac{1}{v_g} = \frac{n_g}{c} = \frac{1}{c} \left(n_{eff} + \omega \frac{\partial n_{eff}}{\partial \omega} \right) \quad (2.4)$$

while β_2 is the group velocity dispersion (GVD). The dispersion of the group velocity is sometimes defined through the dispersion parameter D

$$D = \frac{\partial \beta_1}{\partial \lambda} = -\frac{2\pi c}{\lambda^2} \cdot \text{GVD} \quad (2.5)$$

which is usually given in units of $[\frac{\text{ps}}{\text{nm} \cdot \text{km}}]$. The use of these units comes from the fiber optics community, since D gives the group delay difference (typically in the order of ps) of two optical pulses propagating for 1 km and having their central wavelengths separated by 1 nm [110].

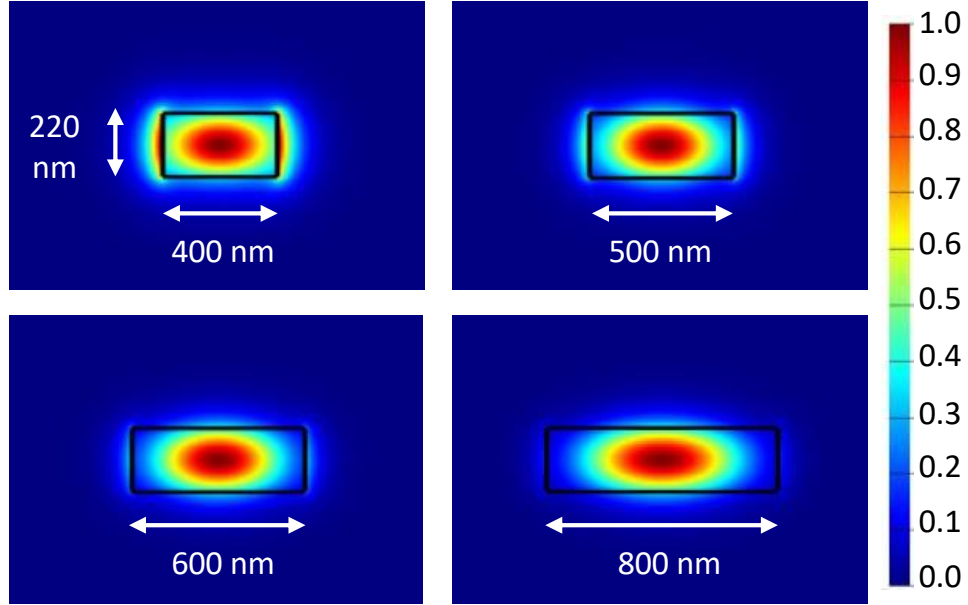


Figure 2.2: Profiles of the modes for silicon waveguides with height = 220 nm and width equal to 400 nm, 500 nm, 600 nm, and 800 nm. The plot shows the normalized intensity of the electric field.

Unfortunately, in the case of strip and rib waveguides is not possible to find analytic solutions of the Maxwell equations. However, one can build an effective slab waveguide that approximate the desired geometry (as in the *effective index*

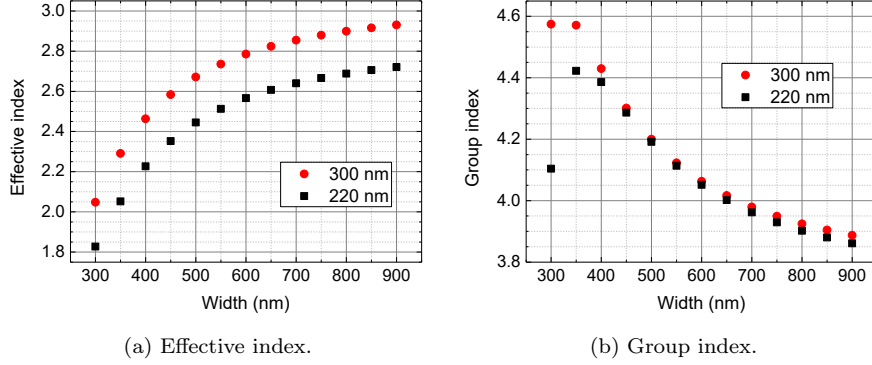


Figure 2.3: Effective and group index at $\lambda = 1550$ nm of strip waveguides having different widths. The red circles show the properties of 300-nm thick waveguides, while the black squares are associated with the 220-nm silicon layer.

method [91]) or it is possible to use numerical methods, such as the Finite Difference Eigenmode (FDE) method [111]. The adoption of numerical analysis increases the complexity of the calculation, but it gives more accurate results.

The optical characteristics of the silicon strip waveguides used in this work are calculated with the FDE solver available with the commercial software LumericalTM MODE. The simulation region ($4 \times 3 \mu\text{m}^2$) is divided into square cells having 10-nm sides. First, the effective index and the group index of the waveguides have been calculated by varying the width of the waveguides, while the height, given by the Si layer, has been fixed equal to 220 nm or 300 nm (which are the thicknesses used during the fabrication). The results are shown in Figure 2.3: as one can see, the effective index is between the refractive index of silicon ($n_{Si} \approx 3.4757$ [112, 113] at $\lambda = 1.55$ nm) and SiO_2 ($n_{SiO_2} \approx 1.4440$ [113, 114] at $\lambda = 1.55$ nm), as one can expect. In addition, the effective index of the 300-nm waveguides is higher with respect to the 220-nm ones, since the higher confinement of the optical mode in the silicon region. The same trend can be observed by increasing the width (and thus reducing the field intensity in the oxide region, as shown in Figure 2.2).

Before starting the design, it's needed to choose the width of the waveguides to realize the lithographic mask (while the thickness can be changed by using different wafers). In this work the width of the waveguide is chosen to be equal to 600 nm, with an higher confinement in the silicon region with respect to the standard single-mode waveguides (with sections around $440 \times 220 \text{ nm}^2$ and $285 \times 300 \text{ nm}^2$ [115]). In fact, this allows to reduce the optical intensity at the interface, which leads to lower losses due to the roughness [116]. In addition, as it is shown in the next section 2.1.2, this choice allows one to maximize the strength of the nonlinear interaction.

The dispersion of the silicon strip waveguides used in this work (cross-section $600 \times 220 \text{ nm}^2$ and $600 \times 300 \text{ nm}^2$) has been calculated: in Figure 2.4 the estimated values of the effective index n_{eff} , the group index n_g , and the dispersion parameter D are shown. The values agree with other simulations that can be found in literature [117, 118]. The refractive indexes of silicon and silica are taken from the fit of some measures from [113] in the spectral range from 1150 nm to 2000 nm; however, more accurate results can be obtained using the real values of the wafers, which can be determined through ellipsometric measures.

2.1.2 Nonlinear optical parameters

A material is defined *nonlinear* when its dielectric response to an external electric field, i.e. the induced electric polarization, is not linearly proportional to the external field. Thus, if the field is sufficiently small, the polarization can be approximated as

$$P_i = \varepsilon_0 \left[\chi_{ij}^{(1)} E_j + \chi_{ijk}^{(2)} E_j E_k + \chi_{ijkl}^{(3)} E_j E_k E_l + \dots \right], \quad (2.6)$$

where $\chi_{ij}^{(1)}$, $\chi_{ijk}^{(2)}$, and $\chi_{ijkl}^{(3)}$ are, respectively, the first-order, second-order, and third-order electric susceptibilities. In (2.6), the subscripts refer to the spatial components of fields: $\chi^{(1)}$ is a second-rank tensor, $\chi^{(2)}$ is a third-rank tensor, and so on. Crystalline silicon has a diamond cubic crystal structure: this implies that the second-order optical nonlinearity is negligible ($\chi_{ijk}^{(2)} \approx 0$) [?]. However, its third order element is 100 times larger than that of silica glass in the telecommunication band [106, 119–121], permitting the observation of nonlinear interaction even at low power levels in silicon waveguides [122]. This stimulated the investigation of several nonlinear phenomena remarkable for their application in telecommunication technologies, such as cross phase modulation (XPM) [123, 124], self phase modulation (SPM) [125, 126], third harmonic generation (THG) [127, 128], and four-wave mixing (FWM) [129–131].

The third-order susceptibility is, in general, a complex tensor. If we consider only the interaction between electrical field having the same polarization, we can write the element of the tensor $\chi_{iii}^{(3)}$ as [121, 132]:

$$\chi_{iii}^{(3)} = \frac{4\varepsilon_0 c^2 n^2}{3\omega} \left[\frac{\omega}{c} n_2 + \frac{i}{2} \beta_T \right]. \quad (2.7)$$

n_2 is the Kerr coefficient, which describes the variation of the effective index with an external electric field having an intensity I due to the nonlinear response (*Kerr effect* [91?]):

$$\Delta n = n_2 I \quad (2.8)$$

while β is the coefficient related to the two-photon absorption (TPA). In fact, silicon is a transparent material in the near infrared, since the energy of the electronic band

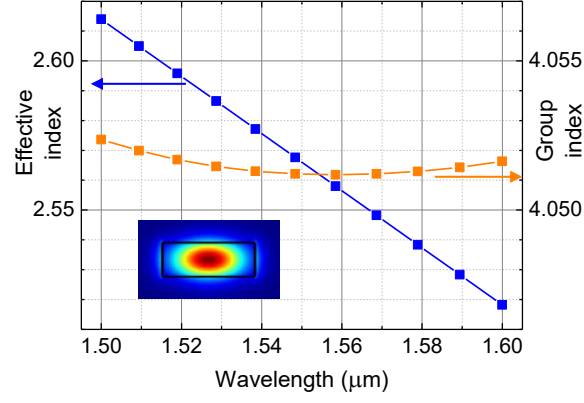
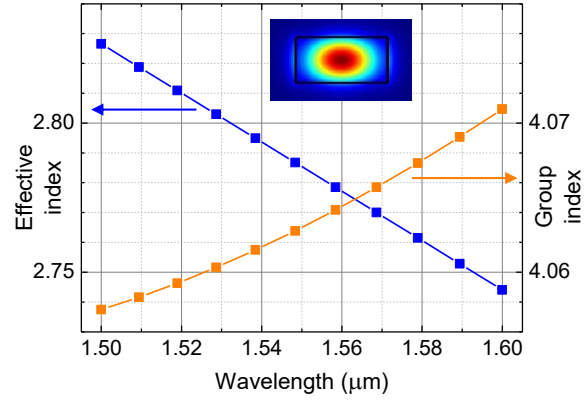
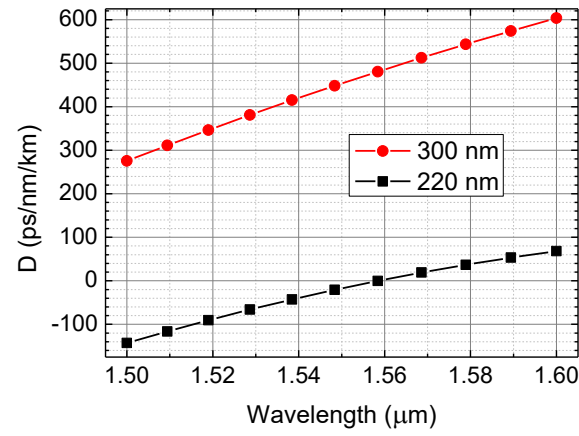
(a) $600 \times 220 \text{ nm}^2$.(b) $600 \times 300 \text{ nm}^2$.(c) Dispersion parameter D .

Figure 2.4: Effective index n_{eff} , group index n_g , and dispersion parameter D of silicon waveguides with $600 \times 220 \text{ nm}^2$ and $600 \times 300 \text{ nm}^2$ cross-section with respect to the wavelength.

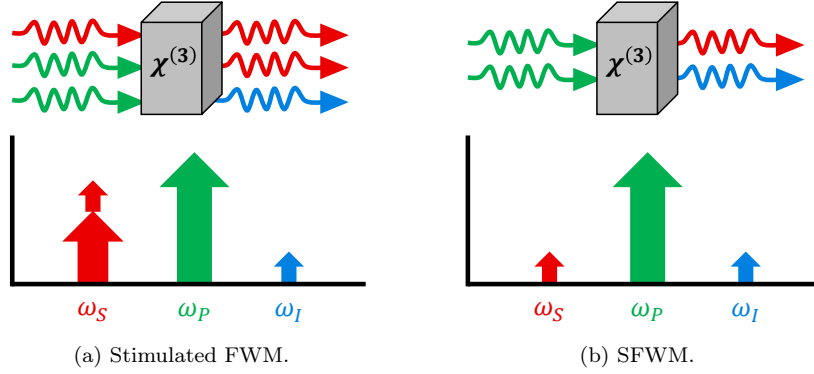


Figure 2.5: Schematics of FWM with a single pump at $\omega_P = \omega_1 = \omega_2$, which leads to the generation of photons at ω_S and ω_I .

gap (1.1 eV) is higher than the energy of the photons (around 0.8 eV). However, the simultaneous absorption of two photons, assisted by phonons because of the indirect band gap [133, 134], can bring to a modification of the power attenuation coefficient (defined in section 2.1.3) which results to be dependent on the intensity of the optical mode. The presence of TPA is one of the most important disadvantage in the use of silicon for nonlinear applications: in fact, it limits the optical power one can couple to the waveguides. Thus, other materials with lower n_2 but negligible β_T such as SiO_2 [135, 136], Si_3N_4 [137–139], Hidex [140], and MgF_2 [141] are used for applications where high optical power is needed, such as generation of combs [54, 142–145] or squeezed light [56, 57].

Among the nonlinear processes one can observe in SOI waveguides, FWM is the most interesting for quantum applications. In fact, it allows the generation of nonclassical states of light, such as entangled photons [51–53, 63, 70] or heralded single photons [146, 147]. FWM consists in the conversion of two input photons at frequencies ω_1 and ω_2 into two photons at frequencies ω_S and ω_I (called signal and idler), such that energy and momentum are conserved:

$$\begin{aligned}\omega_1 + \omega_2 &= \omega_S + \omega_I \\ \hbar k_1 + \hbar k_2 &= \hbar k_S + \hbar k_I,\end{aligned}\tag{2.9}$$

This process occurs spontaneously when two lasers at ω_1 and ω_2 interact with a $\chi^{(3)}$ material, and in this case it is called Spontaneous Four Wave Mixing (SFWM). Alternatively, it can be stimulated by coupling an additional laser at ω_S or ω_I . In the following paragraphs stimulated FWM and SFWM are described, assuming the conservation of energy and momentum (2.9), and the continuous wave (CW) operation of the used lasers.

Stimulated four-wave mixing The stimulated version of FWM can be described through a *classical* approach [91, 121], which allows one to obtain the coupled differential equation that describe the evolution of the field amplitudes in a $\chi^{(3)}$ material. Considering the degenerate case of FWM with a single pump field at $\omega_P = \omega_1 = \omega_2$ (as depicted in Figure 2.5), the evolution of the fields along the direction of propagation $\hat{\mathbf{z}}$ is given by:

$$\begin{aligned}\frac{\partial E_P}{\partial z} &= \left(i\beta_P - \frac{\alpha_P}{2}\right) E_P \\ \frac{\partial E_S}{\partial z} &= \left(i\beta_S - \frac{\alpha_S}{2}\right) E_S + \gamma E_P^2 E_I^* \\ \frac{\partial E_I}{\partial z} &= \left(i\beta_I - \frac{\alpha_I}{2}\right) E_I + \gamma E_P^2 E_S^*\end{aligned}\quad (2.10)$$

where E_P , E_S , and E_I are, respectively, the amplitudes of the pump, signal, and idler fields ($|E_P| \gg |E_S|, |E_I|$ is assumed). In equation (2.10) β_P , β_S , and β_I are the propagation constants of the fields, α_P , α_S , and α_I the power attenuation coefficients (which will be described in section 2.1.3), and γ is the nonlinear coefficient [148]:

$$\gamma = \frac{3\chi^{(3)}\omega}{n^2\varepsilon_0 c^2 A_{eff}} = \frac{n_2\omega}{c A_{eff}}. \quad (2.11)$$

where A_{eff} is the effective area of the nonlinear interaction. If we assume the presence of a pump laser at ω_P and a seed laser at ω_S , the power of the generated idler beam turns out to be

$$P_I = (\gamma L)^2 P_P^2 P_S \quad (2.12)$$

where L is the length of the waveguide in which the fields propagate, while P_P and P_S are the optical power of, respectively, the pump and the signal. Stimulated FWM can be enhanced by using resonators, as it will be shown in section 2.3.4.

Spontaneous four-wave mixing (SFWM) The spontaneous version of FWM can be observed by coupling just one laser at ω_P . Equations (2.12) cannot be used, since they suggest that the absence of the field at ω_S inhibits the process. However, in this case it is possible to exploit the vacuum fluctuations of the electromagnetic field to initiate the process, and the produced photon flux can be derived only in the framework of the quantum theory of light.

The starting point is the Hamiltonian [149]:

$$\hat{H} = \hat{H}_L + \hat{H}_{NL} \quad (2.13)$$

where \hat{H}_L is the linear part which is given by

$$\hat{H}_L = \int dk \hbar \omega \hat{a}_k^\dagger \hat{a}_k \quad (2.14)$$

and \hat{H}_{NL} is the nonlinear Hamiltonian that can be written as:

$$\hat{H}_{NL} = - \int dk_1 dk_2 dk_3 dk_4 S(k_1, k_2, k_3, k_4) \hat{a}_{k_1}^\dagger \hat{a}_{k_2}^\dagger \hat{a}_{k_3} \hat{a}_{k_4} + H.c. \quad (2.15)$$

$S(k_1, k_2, k_3, k_4)$ is the nonlinear coupling term, which includes the effect of the nonlinear parameter γ defined in equation (2.11), while \hat{a}_i are the ladder operators associated with the interacting fields. By following the backward Heisenberg picture approach [150], it is possible to derive the average power of generated idler and signal photons:

$$P_{I,S} = \frac{\hbar\omega_P}{\mathcal{T}} (\gamma P_P L)^2, \quad (2.16)$$

where L is the length of the waveguide, \mathcal{T} is the generation bandwidth time which takes into account the phase-matching conditions (2.9), and γ is the nonlinear parameter of the waveguide. The calculation that leads to the equation (2.16) are extensively described in [149]: it is not the purpose of this manuscript going into detail of the mathematical derivation.

Dual-pump SFWM (d-SFWM) Another version of FWM can be realized if two pump lasers are coupled to the nonlinear waveguide [151]. In this case, two photons at ω_{P_1} and ω_{P_2} can be converted into two photons at ω_T such that $2\omega_T = \omega_{P_1} + \omega_{P_2}$. The average power turns out to be

$$P_T = 4 \frac{\hbar\omega_T}{\mathcal{T}} (\gamma L)^2 P_{P_1} P_{P_2}, \quad (2.17)$$

where the factor 4 comes from the nonlinear Hamiltonian (2.15): in fact, with single-pump SFMW the nonlinear coupling term S is non-zero for $k_3 = k_4 = k_P$, while with d-SFWM we have to take into account both $(k_3 = k_{P_1}, k_4 = k_{P_2})$ and $(k_3 = k_{P_2}, k_4 = k_{P_1})$. Thus, the integral in (2.15) is doubled, and the generated power is quadrupled. It is worth to note that the process is only apparently more efficient from an energetic point of view: in fact, if we suppose $P_{P_1} + P_{P_2} = P_P$, the product $P_{P_1} P_{P_2}$ is maximum when $P_{P_1} = P_{P_2} = P_P/2$, and (2.17) turns out to give the same generated power as (2.16).

Nonlinear parameter Finally, we focus on the estimation of the nonlinear parameter of the waveguide and, in particular, on the effective area of the nonlinear interaction, which appears in equation (2.11). A_{eff} is defined as [149]¹:

$$|A_{eff}| = \left[\int dx dy \frac{n^4 \chi^{(3)}(x, y) |d(x, y)|^4}{\chi^{(3)} \varepsilon_0^2 n^8(x, y)} \right]^{-1} \quad (2.18)$$

¹See equation (A2) in the appendix A.

where n is the refractive index of the nonlinear material and it is assumed, for simplicity, constant with respect to the frequency, while $d(x, y)$ is the profile of the mode, which is given in $\left[\sqrt{\frac{F}{m^3}} = \sqrt{\frac{C}{V \cdot m^3}}\right]$ since it follows the normalization condition [150]²:

$$\int dxdy \frac{|d(x, y)|^2}{\varepsilon_0 n^2(x, y)} \frac{v_p(x, y)}{v_g(x, y)} = 1 \quad (2.19)$$

Sometimes another definition of A_{eff} is used [138, 152, 153], which has been proposed by Agrawal [148] to describe 3rd-order nonlinear effects in optical fibers:

$$A_{eff} = \frac{\left(\int |E(x, y)|^2 dxdy\right)^2}{\int |E(x, y)|^4 dxdy}. \quad (2.20)$$

However, equation (2.20) assumes that the field is entirely confined in the nonlinear material. This approximation works properly in optical fibers: in fact, both the core and the cladding are made of silica, and their nonlinear response is very similar. However, this is not the case for silicon integrated waveguides, where the nonlinear response of the cladding is neglected (with $\chi_{clad}^{(3)} \ll \chi_{core}^{(3)}$). Thus, (2.20) is not accurate, since the fraction of the optical mode in the cladding material is not negligible [154], and it can lead to an overestimation of the efficiency of the nonlinear process. However, equation (2.20) can be corrected by limiting the integral in the denominator only to the area of the core material [155, 156]:

$$A_{eff} = \frac{\left(\int |E(x, y)|^2 dxdy\right)^2}{\int_{core} |E(x, y)|^4 dxdy}. \quad (2.21)$$

Figure 2.6a shows the comparison between the results of the calculation of the effective area by using equations (2.20) and (2.21) for a waveguide whose thickness is fixed (220 nm) and the width varies between 400 nm and 900 nm. As can be seen, the values for the smallest waveguides are quite different: this is due to the lower confinement in the core (as it can be seen in Figure 2.2), which makes the denominator in (2.20) significantly greater than in (2.21). Then, the underestimation of the effective area leads to an overestimation of the nonlinear parameter, as it is shown in Figure 2.6b. When the width is increased, the field is almost entirely confined in the core of the waveguide, and the two results are closer.

Finally, Figure 2.7 shows the effective area and the nonlinear parameters with respect different values of the width of the waveguide for two values of the thickness (220 nm and 300 nm). As one can expect, the maximum value of the nonlinear parameter is a trade-off between having a small modal area (i.e. high intensity of the electromagnetic radiation) and keeping a good confinement in the core (which is

²See equation (8).

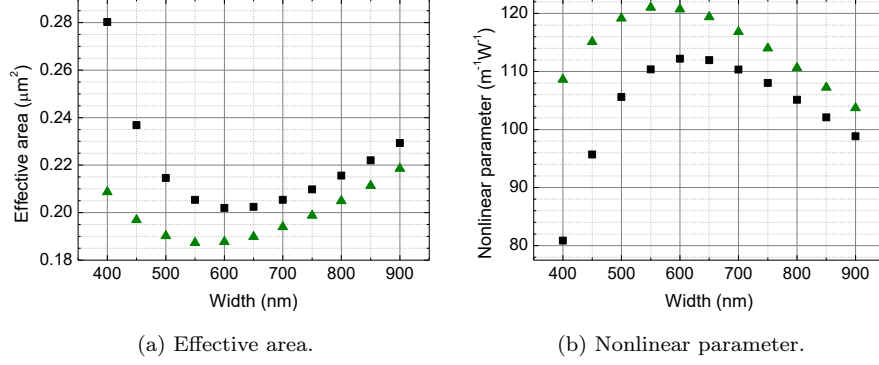


Figure 2.6: Effective area and nonlinear parameter at $\lambda = 1550$ nm with the thickness of the silicon layer equal to 220 nm. The green triangles show the results calculated with equation (2.20), while the black squares show the results obtained with equation (2.21).

the region with the highest nonlinear response). The maximum effective strength of the interaction is in waveguides having 550-600 nm of width, with $\gamma \approx 110 \text{ W}^{-1}\text{m}^{-1}$.

2.1.3 Losses in integrated waveguides

A key aspect that allows the use of integrated waveguides in practical applications is the reduction of propagation losses. Optical losses can be divided into two classes: the linear losses, which are independent on the optical power, and the nonlinear losses, which increases with the mounting of the optical intensity.

In principle, one could expect that the linear losses in silicon waveguides are negligible, since silicon is transparent in the near infrared. However, in practice there are two main sources of linear losses in silicon waveguides: the scattering caused by the roughness of their sidewalls and the absorption due to impurities that can deposit on them.

Scattering of light can be reduced by adopting proper strategies. For example, it is possible to use larger waveguides to reduce the fraction of the mode around the edges; however this approach is not a great solution for nonlinear applications, since the enlargement of the waveguide implies the reduction of the effective area, as can be seen in Figure 2.7. In addition, the increase of the cross-section could make the waveguide multimode, which is detrimental for several devices in which single-mode operation is fundamental, such as modulators, filters, and couplers. Another possibility is described in [116], where a H_2 -annealing treatment is used after the etching to smoothen the sidewalls of the waveguides. This technique, applied in this

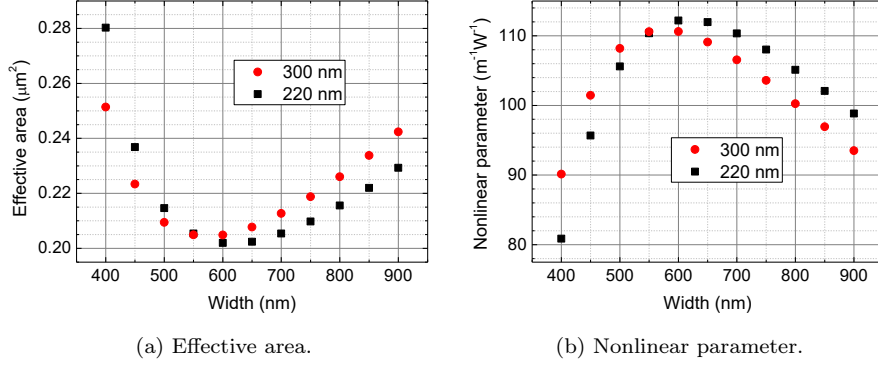


Figure 2.7: Effective area and nonlinear parameter at $\lambda = 1550$ nm. The results are obtained with equation (2.21).

work and described in Chapter 4, effectively reduce the roughness, and allows one to obtain state-of-the-art propagation losses [82].

The presence of impurities where the field is confined provides intra-gap energy levels, which leads to linear absorption even if the bandgap of silicon is larger than the energy of the photons in the near infrared. In general, this effect is more severe with silicon structures not embedded in a silica matrix, since external particles can deposit on the sidewalls [157], while it is possible to mitigate this problem with encapsulated device by properly monitoring the contamination of the machines used during the fabrication. Naturally, this effect can be useful sometimes, as one can realize silicon-based photodetectors via selective ion implantation [158, 159]. Another source of absorption is due to the generation of surface states between the silicon and the silica, as it is detailed in [160]. This effect is hard to eliminate, and it can be exploited as well to realize detectors based on the generation of current [161, 162] or on the variation of the local capacitance of the sample [160].

If we neglect the nonlinear losses, the optical power at the end of a waveguide with length L is given by [91]:

$$P(L) = P(0)e^{-\alpha L} \quad (2.22)$$

where α is the *power attenuation coefficient* which quantifies the losses per unit of length [m^{-1}]. However, α is typically expressed in [dB/cm], and the conversion factor can be derived by considering that the transmission, expressed in decibel, is given by:

$$10 \cdot \log\left(\frac{P(L)}{P(0)}\right) = -\alpha_{dB/m} \cdot L \quad (2.23)$$

Thus, by using equation (2.22) we obtain:

$$10 \cdot (-\alpha_{1/m} L) \cdot \log(e) = -\alpha_{dB/m} \cdot L \quad (2.24)$$

and we finally get the conversion factor

$$\alpha_{1/m} = \frac{1}{10 \cdot \log(e)} \alpha_{dB/m} \approx 0.23 \cdot \alpha_{dB/m} = 23 \cdot \alpha_{dB/cm} \quad (2.25)$$

The state of the art for single-mode rectangular waveguides is α lower than 0.5 dB/cm [82, 115].

The nonlinear losses depend on the optical power circulates in the waveguide. Thus, they can be neglected at low power, but they can be extremely significant for higher intensity of the electromagnetic field. The main process that is involved in silicon waveguides is TPA, which simultaneously promotes two electrons from the valence to the conduction band, as we discussed in the previous section. In addition, another process is very effective: the free-carrier absorption (FCA). It consists in the absorption of photons by electrons in the conduction band: in fact, they are not linked to specific energetic levels, and they can easily increase their energy [121]. Normally, the average number of photons in the silicon conduction band is negligible; however, linear absorption and TPA can populate it [163], inducing FCA. As can be seen in [157], the role of FCA is extremely severe in silicon structures with high optical power, causing a degrading of the optical response of the devices (especially the optical resonators).

2.2 Fundamental building blocks

In this section, the basic building blocks used in the mask are detailed. They are exploited to realize more complex devices, and the comprehension of their optical behavior is fundamental to understand the structures described in the following sections.

2.2.1 Edge couplers

Integrated photonic platforms offer the possibility to place on-chip a huge range of devices, from lasers to detectors. However, typically one needs to couple the light from an external system to the chip or vice versa. This task turns out to be quite demanding. In fact, the principal problem is related to the big mismatch between the modal area of an integrated silicon waveguide, which is around $0.1 \mu\text{m}^2$, and of the telecom single-mode fibers, which have a mode field diameter around $10 \mu\text{m}$.

The capability of efficiently coupling light in and out of silicon PICs is a key issue of Silicon Photonics. In fact, the costs of packaging dominate the overall cost of products based on integrated photonic circuits [80], and many different solutions are

investigated to develop fast, reliable, high-yield, and low-cost packaging techniques [164]. For quantum applications in particular, keeping the coupling losses as low as possible is crucial, since they degrade the purity of the generated nonclassical state. Moreover, their effect is detrimental if the state is composed of two or more photons and the measures involve coincidence counts between two or more detectors.

A very practical approach to tackle the problem of coupling is the use of grating couplers. They are periodic structures that diffract light from the waveguide to free-space, enabling the alignment of a fiber on top of the chip. Obviously, they are assisted by a direct taper, which enlarges the waveguide before reaching the grating region, as can be seen in Figure 2.8a. The main advantage of this solution is represented by the possibility to couple to waveguides placed anywhere on the chip, enabling wafer-scale automated testing [117]. However, it is difficult to reach extremely low values of the coupling losses over a large spectral band: most devices exhibit around 3 dB of coupling loss and few tens of nanometers of bandwidth [165, 166]. In addition, simple designs are typically polarization sensitive. Several approaches have been proposed to overcome these limits, which require more complex design strategies or fabrication processes, such as multi-etch grating with bottom reflectors [167–169], the use of photonic crystal structures [170], or subwavelength grating tapers [171, 172].

An alternative solution is the *edge* (or *butt*) coupling, which consists in placing a fiber close to the side of the chip and to enlarge the optical mode in the waveguide. Typically, an inverse taper can be used to gently reduce the dimension of the waveguide and let the mode to expand [173]. This kind of structures typically exhibits less than 1 dB of coupling loss with a 3-dB bandwidth of hundreds of nanometers and an almost polarization insensitive behavior [174]. Even in this case, more complex structures can be adopted to increase the coupling efficiency, such as suspended tapers [175], multilayer patterned overlay structures [176] or subwavelength gratings [171]. As one can understand, the main drawback in the use of edge couplers is that all the input and output waveguides must be connected to the edges of the sample. In addition, it is mandatory to properly cleave the wafer to test the optical structures, making this approach unpractical for wafer-level testing. More details about the different strategies adopted by academic and industrial groups are provided in [164].

The approach adopted for the realization of the mask is the edge coupling through simple inverse tapers. In fact, a recent work [174] shows that 100- μm long tapers which bring single-mode waveguides to $250 \times 160 \text{ nm}^2$ wide tips (see Figure 2.8b) exhibit low coupling losses ($\approx 0.7 \text{ dB}$) over a large band. Instead of defining the facet of the chip at the end point of the taper, an oxide gap is added and this allows one to reduce the roughness of the interface and, thus, the coupling losses. In addition, a tilted facet is designed to reduce back-reflections, and 1 μm of oxide gap is left between the tip and the facet (enough to compensate eventual misalignment of the lithographic mask). The length of the taper is fixed equal to

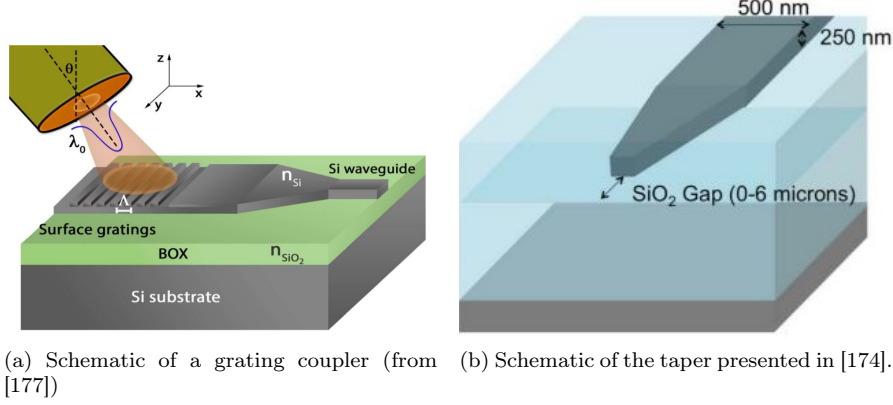


Figure 2.8

100 μm to obtain an adiabatic transition.

2.2.2 Directional couplers

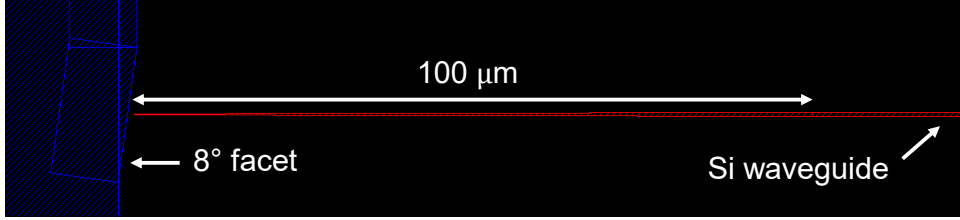
The directional coupler (DC) is a very common component to split and combine light [117], which is used in integrated optical circuits, as well as in fiber components [178]. The basic idea is to use two parallel waveguides close enough to let the optical power to be coupled from one waveguide to the other. DCs can be modelled by using the Eignemode Expansion Method (EME) which decompose the local field into multiple modes (called *supermodes*) [117]. The local field is given by the sum of the supermodes, which are propagated by simply taking into account their propagation constants. In a DC composed of single-modes waveguides, two supermodes can be found, with a small difference in the effective index $\Delta n = n_1 - n_2$: one mode is symmetric and the other is asymmetric (as shown in Figure 2.12). If we consider that at $z = 0$ the field is confined in one waveguide of the directional coupler (labeled “A” in Figure 2.11), we can find a distance (cross-over length, L_z) at which a π phase shift difference between the modes leads to the confinement of the local field in the other waveguide (B), as depicted in Figure 2.11. This occurs with [117]:

$$\beta_1 L_z - \beta_2 L_z = \frac{2\pi}{\lambda} (n_1 - n_2) L_z = \pi, \quad (2.26)$$

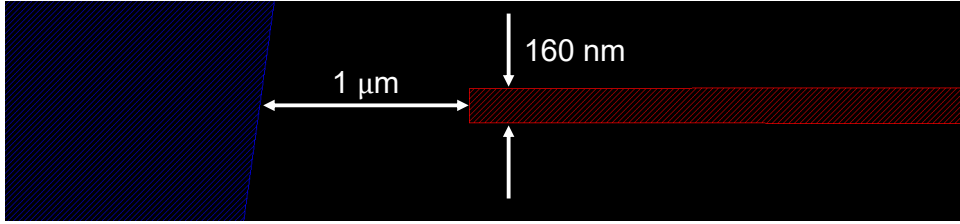
and L_z turns out to be

$$L_z = \frac{\lambda}{2\Delta n} \quad (2.27)$$

Form this picture it is possible to find that in the device shown in Figure 2.10 the fraction of power coupled from the port IN_1 (IN_2) to the port OUT_2 (OUT_1) is



(a) Image of the inverse taper on the design.



(b) Zoom of the tip near the facet.

Figure 2.9

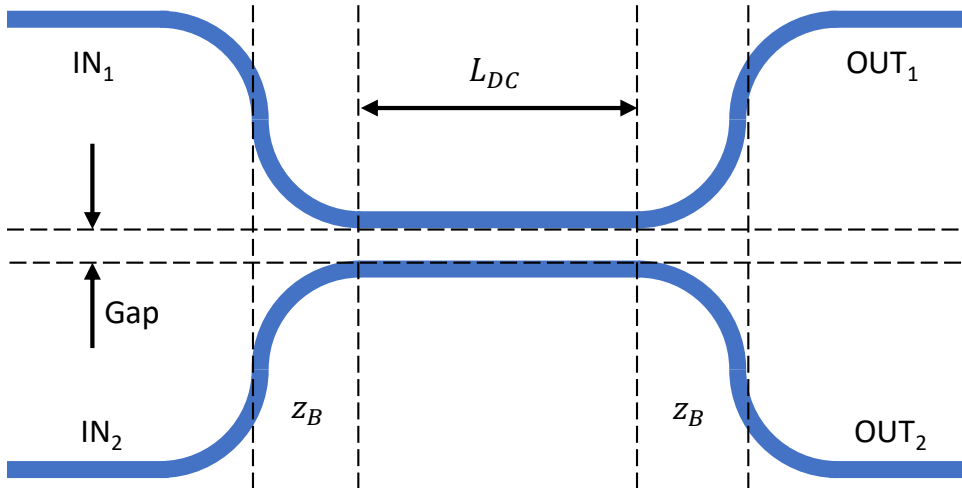


Figure 2.10: Scheme of the directional coupler.

given by

$$K^2 = \frac{P_{OUT_2}}{P_{IN_1}} = \frac{P_{OUT_1}}{P_{IN_2}} = \sin^2(\kappa \cdot L_{DC}) \quad (2.28)$$

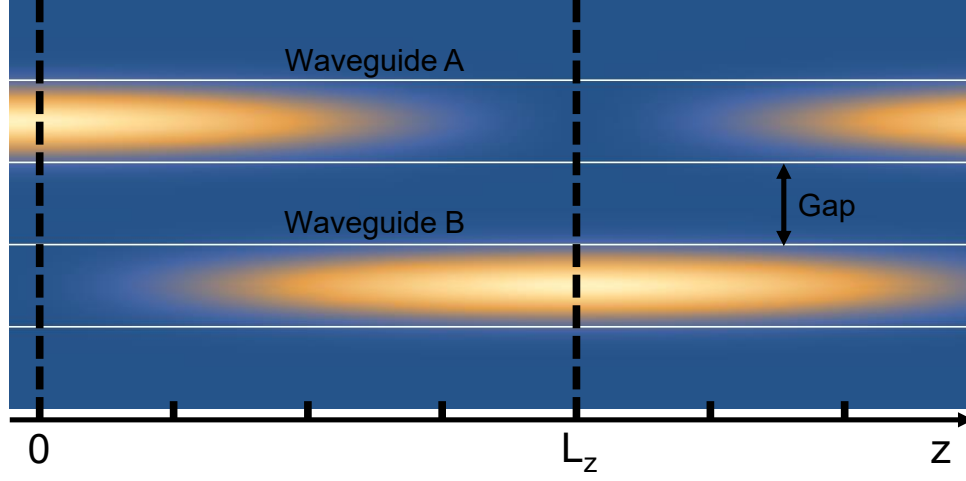


Figure 2.11: Sketch of the propagation of the electromagnetic field in a directional coupler.

where L_{DC} is the length of the directional coupler, and κ is the coupling coefficient defined as

$$\kappa = \frac{\pi \Delta n}{\lambda} = \frac{\pi}{2L_z} \quad (2.29)$$

Similar results can be found by using the Coupled Mode Theory (CMT) [91, 179], in which the coupling of the waveguides is considered as a perturbation of the effective index. However, EME gives more accurate results in case of strong coupling and for high index contrast waveguides [117].

In equation (2.28) the contribution of the bends is neglected, since the coupling is assumed equal to zero with $L_{DC} = 0$. To take into account also the small coupling in the bending area, we can introduce an effective length z_b , and equation (2.28) becomes

$$K^2 = \sin^2(\kappa \cdot (L_{DC} + z_b)) \quad (2.30)$$

Finally, if the two waveguides have a different effective index ($\Delta n_0 = n_A - n_B \neq 0$), equation (2.30) should be corrected into

$$K^2 = \frac{\kappa^2}{\kappa^2 + s^2} \sin^2\left([\kappa^2 + s^2]^{0.5} \cdot (L_{DC} + z_b)\right) \quad (2.31)$$

where $s = 2\pi\Delta n_0/\lambda$ is the phase mismatch term [180].

As can be seen from equation (2.29), the value of κ can be found by the estimation of the effective indexes of the supermodes. Then, some simulations using the FDE mode solver by Lumerical have been run, and the results are shown in Figure 2.13.

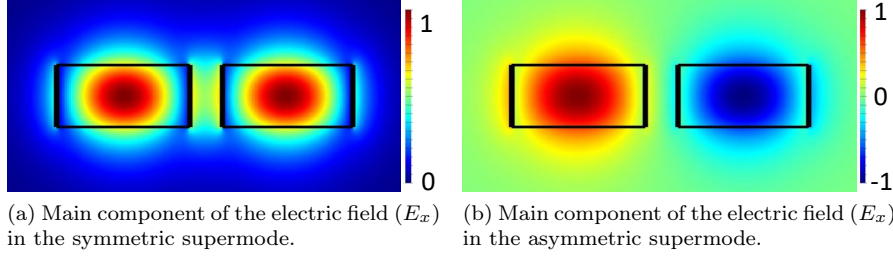


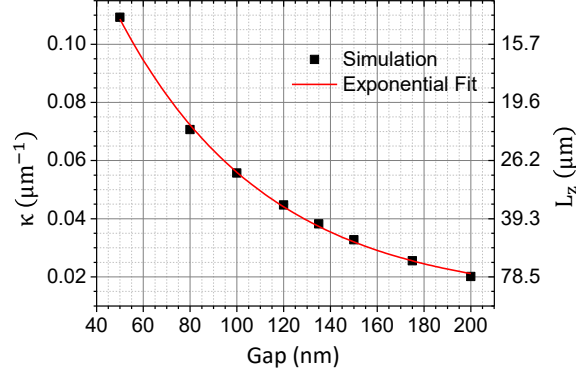
Figure 2.12: Mode distribution of the supermodes in the directional coupler. The cross-section of the waveguide is $600 \times 220 \text{ nm}^2$, and the gap is equal to 150 nm .

The coupling parameter κ turns out to have an exponential dependence on the gap between the two waveguides (see Figure 2.13a): this is reasonable, since it is related to the overlap between the single-waveguide optical modes, which have spatial profiles that decay exponentially out of the core.

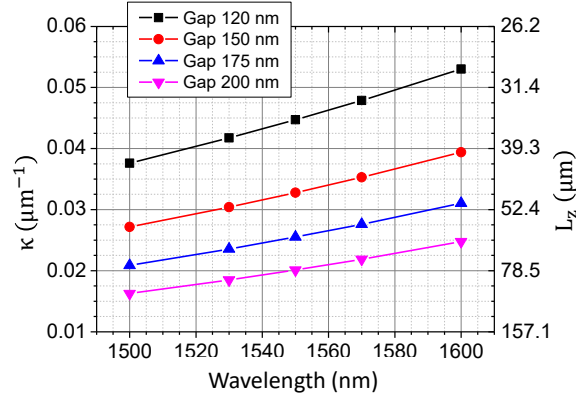
Frequency dependence A very important aspect in the use of the directional couplers is the dependence of the coupling parameter on the frequency, as shown in Figure 2.13b. From equation 2.29 one could expect that the coupling is inversely proportional to the wavelength. However, even Δn is frequency dependent: in fact, the mode is less confined with higher values of the wavelength, and this leads to an increase of the coupling.

This behavior has, naturally, a relevant impact on the optical response of the device, and it is not desirable for applications where broadband components are requested. In Figure 2.14 is shown the power coupled to the second waveguide K^2 with a gap equal to 150 nm calculated from equation 2.31 by assuming $s = 0$ and by neglecting the contribution of the bent waveguides ($z_b = 0$). The length of the three curves are chosen to obtain a coupling equal to 0% ($\kappa L = \pi$), 50% , and 10% . As can be seen, the greater is L_{DC} , the more relevant is the dependence on the frequency. A simple solution to this problem is to use a Mach-Zehnder interferometer [181], which has, however, a larger footprint. Alternatively, other approaches have been proposed to design compact and broadband devices, such as the use of plasmonic DCs [182], asymmetric DCs with phase control [183], or DCs composed of bent waveguides [184].

Bent contribution Finally, the value of z_b can be estimated by running Finite Difference Time Domain (FDTD) simulations of a DC with $L_{DC} = 0$, similarly to what is done to estimate the coupling of the ring resonators with adjacent waveguides (see section 2.3). However, the simulation of such a device is much more demanding than the microring's point coupler, since the simulation area is bigger.



(a) Coupling parameter as a function of the gap between the waveguides.



(b) Coupling parameter as a function of the wavelength.

Figure 2.13: Estimation of the coupling parameter κ in equation (2.31) at $\lambda = 1550$ nm. The simulated directional coupler is composed of two ridge silicon waveguides with 600×220 nm² cross-section.

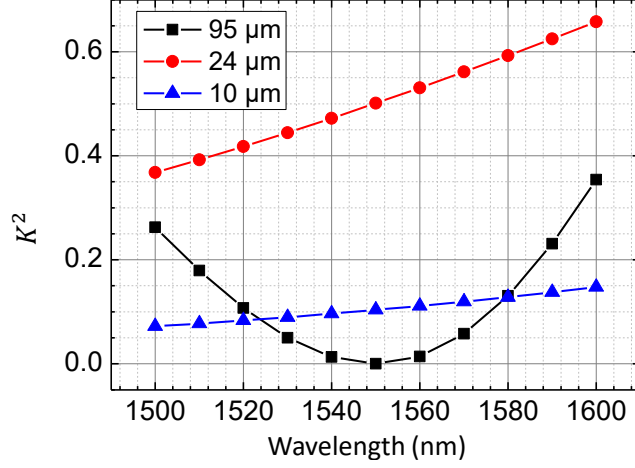


Figure 2.14: Coupled power of DCs with $600 \times 220 \text{ nm}^2$ cross-section waveguides with 150 nm of gap. The black, red, and blue points shows the coupling at different wavelength of DC with L_{DC} equal to, respectively, 95 μm , 24 μm , and 10 μm , which makes the coupling equal to 0%, 10%, and 50% at 1550 nm.

In fact, the FDTD solver by Lumerical does not allow to place monitors of the field perpendicular to bent waveguides. Thus, we can use as a first approximation the results shown in Figure 2.24 and apply the following formula:

$$z_b = \frac{\sin^{-1}(\sqrt{K_0^2})}{\kappa} \approx \frac{\sin^{-1}(\sqrt{K_{pc}^2})}{\kappa} \quad (2.32)$$

where K_0^2 is the coupling of a directional coupler with $L_{DC} = 0$ and K_{pc}^2 is the coupling of a bent waveguide and a straight one (larger than K_0^2). In Figure 2.15 it is possible to observe that z_b is almost constant ($3.9 \pm 0.3 \mu\text{m}$) with respect to the gap, where the point coupler is calculated with a radius of curvature equal to 30 μm . This is not surprising: with bigger gaps, K_{pc}^2 is reduced, and the same effect occurs with κ . In the directional couplers used in the design, it has been assumed $z_b = 3 \pm 1 \mu\text{m}$, which is smaller with respect to the estimation presented in Figure 2.15: in fact, in a directional coupler there are two approaching bent waveguides, while the simulation of the point coupler in a ring resonator includes a straight waveguide close to a bent one, leading to an overestimation of z_b .

2.2.3 Mach-Zehnder Interferometers

Mach-Zehnder interferometers (MZIs) are widely adopted in silicon photonics, especially for filtering [181, 185, 186], multiplexing [187–189], and the realization of

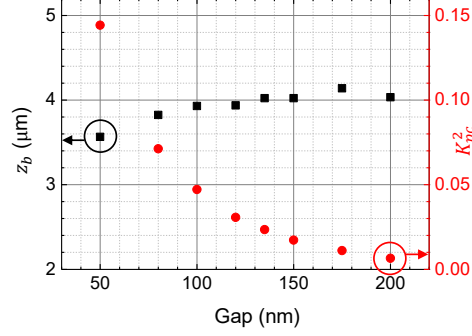


Figure 2.15: Estimation of z_b from equation (2.32). The value of the coupling due to the point coupler (K_{pc}^2) are calculated by FDTD simulations. The radius of curvature taken into account is $30 \mu\text{m}$.

modulators [61, 62, 190]. The basic mechanism is the following: the input power is divided into two different waveguides and then recombined; thus, the output depends on the interference between the fields in the two paths. In addition, phase shifters can be placed on the two arms to manipulate the optical response.

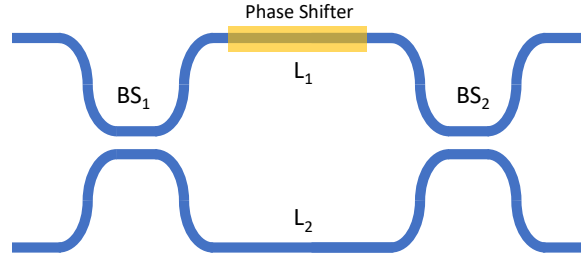


Figure 2.16: Scheme of a MZI where two directional couplers are used as beam splitters (BS).

A simple realization of a MZI in silicon PICs is shown in Figure 2.16, where two DCs are used as beam splitters: this configuration is very common, since it is straightforward to design and realize. The optical response of the device can be obtained by building its transfer matrix, and applying it to the electric fields at the input:

$$\begin{aligned}
\begin{pmatrix} E_1^{out} \\ E_2^{out} \end{pmatrix} &= U_{MZI} \begin{pmatrix} E_1^{in} \\ E_2^{in} \end{pmatrix} = U_{BS_2} U_L U_{BS_1} \begin{pmatrix} E_1^{in} \\ E_2^{in} \end{pmatrix} \\
&= \begin{pmatrix} t_2 & i\sigma_2 \\ i\sigma_2 & t_2 \end{pmatrix} \begin{pmatrix} e^{ik_1 L_1} & 0 \\ 0 & e^{ik_2 L_2} \end{pmatrix} \begin{pmatrix} t_1 & i\sigma_1 \\ i\sigma_1 & t_1 \end{pmatrix} \begin{pmatrix} E_1^{in} \\ E_2^{in} \end{pmatrix}
\end{aligned} \tag{2.33}$$

where t and σ are the coefficients expressing the transmission and coupling of the electric field in the directional couplers, which are related to K^2 in equation (2.31) through the relations

$$\sigma = \sqrt{K^2} \quad t = \sqrt{1 - \sigma^2} = \sqrt{1 - K^2} \tag{2.34}$$

while L_i and k_i are, respectively, the length of the two waveguides and the wavevectors which take into account their different effective indexes.

2.2.4 Thermal phase shifters

The spectral response of the optical structures is related to the effective index of the waveguides, which is dependent on their geometrical dimensions, as can be seen in Figure 2.3a, and on other physical quantities, such as the effective optical characteristics of the materials and the temperature. Thus, if the device involves many resonant structures, the adoption of strategies that can control independently their optical response is fundamental. The simplest method is to locally change the temperature of the chip through a thermal phase shifter (TPS): this can be realized with a piece of metal which is placed on top of the waveguide and acts as a resistor: if an external voltage is applied, the metal dissipates thermal power following the Ohm's law $P_{th} = V \cdot i$, and this allows the tuning of the optical properties of the waveguide.

A very important parameter for the design of the TPS is the thickness (h_c in Figure 2.18) of the oxide layer used to encapsulate the silicon waveguides. In fact, if the layer is too thick, the heating is not efficient, and the spectral tuning would be possible only with high electrical powers, which lead to the unwanted heating of adjacent structures (thermal cross-talk). On the other hand, if the metallic strip is too close to the waveguide, the mode can experience additional losses due to the absorption of the metal. Thus, the FDE mode solver is used to study the effect of the TPS: in Figure 2.17 one can observe that if the thickness is higher than 700 nm, the impact on the optical mode is negligible (the estimated propagation losses are lower than 0.1 dB/cm). Hence, the target thickness for the SiO₂ layer is set equal to 800 nm.

Among the uses of TPSs, it is worth to mention the possibility of tuning the coupling of the directional couplers [180]. In fact, if a TPS is placed asymmetrically with respect to the waveguides of the directional coupler (see Figure 2.18), an asymmetric variation of the effective indexes of the two waveguides is induced [i.e.

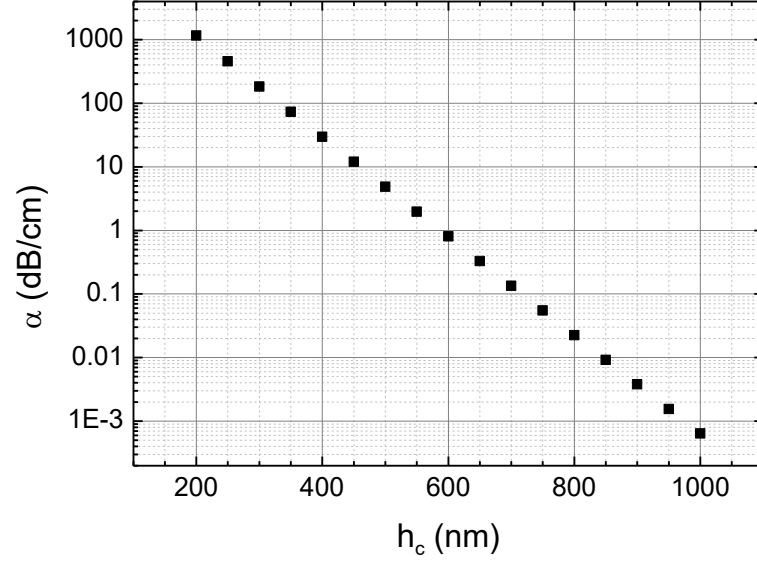


Figure 2.17: Results of the FDE simulation of a $600 \times 220 \text{ nm}^2$ silicon waveguide with a $800 \times 110 \text{ nm}^2$ titanium heater on top and an oxide interleaving layer with thickness h_c (as shown in Figure 2.18).

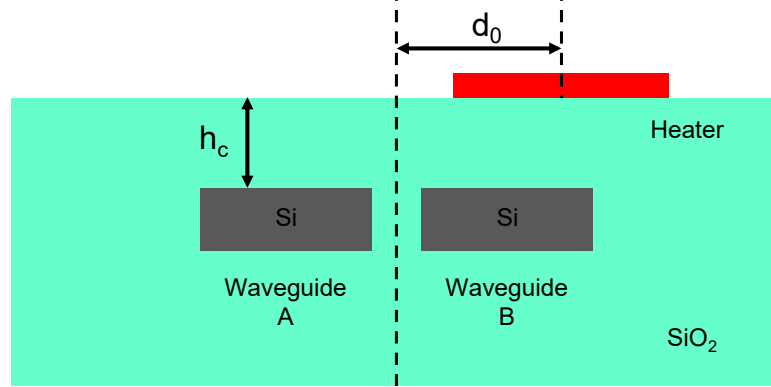


Figure 2.18: Schematic to show the positioning of the heater to tune the directional coupler.

$s \neq 0$ in equation (2.31)].

An optimal position of the heater can be found, as pointed out in [180]. In fact, if

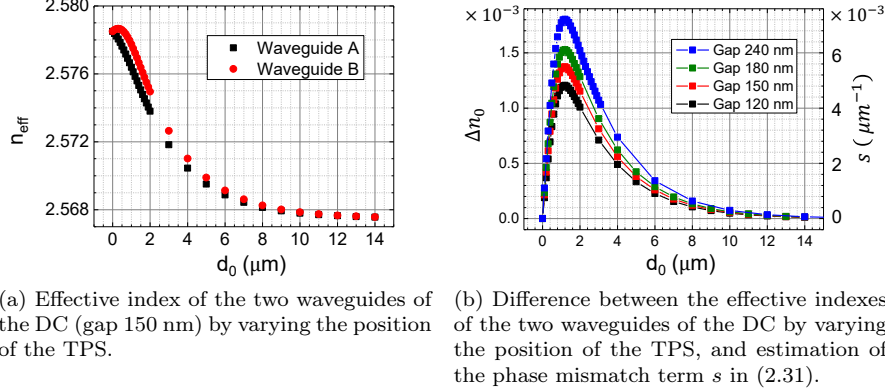


Figure 2.19: Results of FDE simulation to estimate the impact of the heating of a phase shifter placed asymmetrically with respect to a directional coupler.

the TPS is too close to the center of the DC, it would heat both the waveguides, and this would lead to $s \neq 0$. On the other hand, if it is too far from the center, its effect would be negligible. Thus, the Lumerical's heat transport solver (HEAT) is used to calculate the temperature profile of the cross-section when the TPS is switched on. Then, the heat map is imported in MODE: the indexes of the two modes are calculated and the phase mismatch s is estimated for different values of the position of the heater.

The values of Δn_0 are strictly dependent on the thermal power dissipated by the heater: a more accurate simulation is needed to properly model the material used for the phase shifter. However, it is possible to estimate the optimal value for d_0 , which is $1.2 \mu\text{m}$, and this value does not change with small variation of the gap between the two waveguides, as can be observed in Figure 2.19b. Furthermore, it is possible to observe that the bigger is the gap, the greater is s : in fact, a larger separation of the waveguides leads to a greater difference of their effective indexes.

2.3 Microring resonators

Microring resonators are simple structures composed of a bent waveguide closed to itself: in this way it is possible to create an optical cavity which forces the light to circulate in a closed path. They have been widely investigated in the last three decades [191], since they are suitable for a variety of applications, ranging from optical filters [64, 192] and multiplexers [193, 194], to modulators [60, 190, 195], passing through delay lines [196, 197]. In addition, the capability to confine the light enhances the interaction of the radiation with matter: this can be very

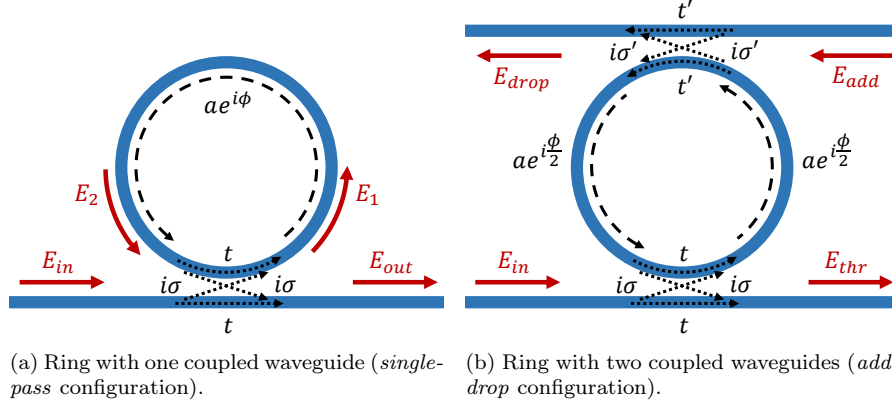


Figure 2.20

useful, for example, for the realization of optical sensors [198–200]. In addition, the nonlinear interaction of light with matter can be enhanced as well [201, 202]. This can be exploited for many applications, such as wavelength conversion [202–204], generation of non-classical states of light for quantum communication such as heralded single-photons [71, 205–208], and entangled photons [51–53, 208, 209]), generation of squeezed light for optical quantum computation [56, 57], and soliton comb formation for metrology and telecommunications [142, 144, 210–212], but also to access to novel nonlinear phenomena and dynamics [213].

2.3.1 Linear behavior

The electromagnetic radiation is resonant only if the optical length of the ring is a multiple of the wavelength. In fact, if this happens, after a round-trip the light interferes constructively. The resonant condition is, thus,

$$\begin{aligned}
 kL &= \frac{2\pi}{\lambda_0} n_{eff} \cdot 2\pi R = 2\pi m \\
 L &= 2\pi R = \frac{\lambda_0}{n_{eff}} m
 \end{aligned}
 \tag{2.35}$$

where $L = 2\pi R$ is the length of the circular ring resonator, λ_0 is the vacuum wavelength, n_{eff} is the effective index of the waveguide, and m is an integer number.

The simplest way to couple the light to a microring is to place a waveguide close to the resonator, as shown in the sketch in Figure 2.20. To calculate the transmission of the device, which is related to the ratio between the electric field E_{in} at the *input* port and the electric field E_{out} at the *through* port, we can assume that the point

coupler is lossless and can be described through the unitary matrix [86, 91]:

$$U_{pc} = \begin{pmatrix} t & i\sigma \\ i\sigma & t \end{pmatrix} \quad (2.36)$$

where t is the transmission coefficient, σ is given by the coupling and they are linked through the equation $t^2 + \sigma^2 = 1$. Hence, the electric fields shown in Figure 2.20 are given by:

$$\begin{aligned} E_{out} &= tE_{in} + i\sigma E_2 \\ E_1 &= tE_2 + i\sigma E_{in} \\ E_2 &= ae^{i\phi} E_1 \end{aligned} \quad (2.37)$$

where a express the reduction of the amplitude of the electric field due to the losses and ϕ is the phase collected through the round-trip ($\phi = k \cdot L$). Then, it is easy to obtain the ratio between E_{out} and E_{in} :

$$\frac{E_{out}}{E_{in}} = \frac{t - ae^{i\phi}}{1 - ta e^{i\phi}} \quad (2.38)$$

and the power transmission is given by

$$T = \left| \frac{E_{out}}{E_{in}} \right|^2 = \frac{t^2 + a^2 - 2at \cos \phi}{1 + a^2 t^2 - 2at \cos \phi} \xrightarrow{(2.35)} \frac{(a - t)^2}{(1 - at)^2} \quad (2.39)$$

where the last passage is valid if equation (2.35) is satisfied (i.e. if the radiation is on resonance). Equation (2.39) can be written as a function of the propagation losses coefficient [α in equation (2.22)] and the coupling between the waveguide and the ring K^2 . In fact,

$$\begin{aligned} a &= \sqrt{\frac{P(2\pi R)}{P(0)}} = \sqrt{e^{-\alpha 2\pi R}} = e^{-\alpha \pi R} \approx 1 - \alpha \pi R = 1 - \frac{\alpha L}{2} \\ t &= \sqrt{1 - K^2} \approx 1 - \frac{K^2}{2} \end{aligned} \quad (2.40)$$

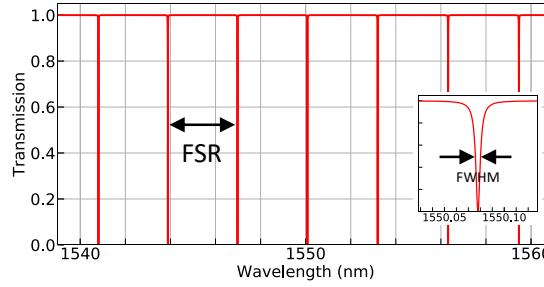
where we assume αL and K^2 to be much lower than 1. Thus (2.39) becomes

$$T \xrightarrow{(2.35)} \frac{(a - t)^2}{(1 - at)^2} \approx \left| \frac{K^2 - \alpha L}{K^2 + \alpha L} \right|^2 \quad (2.41)$$

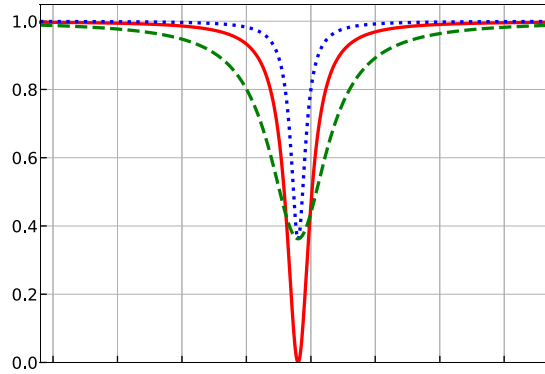
The minimum of the transmission corresponds with the resonant condition. It can be equal to zero if the losses in the ring are equal to the coupling: this condition is called *critical* coupling, and it gives the maximum intensity of the field in the microring, as is proved below. If the losses are lower than the coupling (i.e. $a > t$), then the resonator is *overcoupled*: in fact, at each turn is injected more power with

respect to what is lost due to the losses. On the other hand, if the coupling is weak (i.e. $a < t$), the system is in the *undercoupling* condition. Finally, the maximum of the transmission occurs when $\phi = (2m + 1)\pi$, and (2.39) becomes

$$T(\phi = \pi) = \frac{(a + t)^2}{(1 + at)^2} \approx 1 \quad (2.42)$$



(a) Full spectrum over 20-nm spectral band.



(b) Variation of the spectrum with respect to the coupling condition. The red line shows the resonance in the critical coupling condition ($K^2 = \alpha L$), while the blue dotted and the dashed green lines represent the spectrum of the same ring with, respectively, $K^2 = \alpha L/2$ (undercoupling), and $K^2 = 2\alpha L$ (overcoupling).

Figure 2.21: Calculated spectrum of a silicon ring resonator with radius equal to 30 μm .

Microring resonators can be used with more than one coupled waveguides. This is the case of the *add-drop* configuration, which is shown in Figure 2.20b. The main

difference is that it's possible to collect the light on resonance from the drop port. In fact, when the transmission is zero ($E_{thr} = 0$), the light is confined in the resonator and it can leave it from the second waveguide coupled to the ring.

Regarding the condition of the coupling, the mechanism is similar to what we described in the previous case. The system is critically coupled if the coupling is equal to the losses, which are given by the sum of the round-trip losses αL and the coupling to the second waveguide $|\sigma'|^2$. Typically, the add-drop is symmetric (i.e. $t \approx t'$): thus, the critical coupling condition is obtained if the losses are negligible with respect to the couplings. A more detailed description can be found for example in [191, 214].

2.3.2 Figures of merit

Ring resonators are characterized by some key figures of merit, which are summarized in this section. They can be estimated from the optical spectrum of the device, and they allow to estimate their performances with respect to the applications in which they are used.

Free Spectral Range The spectral distance between two resonant modes of a resonator is the *free spectral range* (FSR). It can be calculated by combining equations (2.3) and (2.35). In fact, we can express the difference between the wavevectors associated with the mode of order m and $m + 1$:

$$(k_{m+1} - k_m) = \frac{2\pi}{L} \approx \frac{n_g}{c} 2\pi (\nu_{m+1} - \nu_m) \quad (2.43)$$

and we obtain

$$FSR_\nu = (\nu_{m+1} - \nu_m) = \frac{c}{n_g L} = \frac{c}{n_g 2\pi R}. \quad (2.44)$$

Finally, we can express the FSR in wavelength by applying the transformation $\Delta\lambda/\lambda = \Delta\nu/\nu$:

$$FSR_\lambda = \frac{\lambda^2}{n_g 2\pi R}. \quad (2.45)$$

Quality factor The quality factor, or Q-factor, is a dimensionless quantity which quantifies the temporal confinement of light in the resonator. In fact, the more the light remains in the resonator, the higher is the value of the quality factor. It is defined as the ratio between the total energy stored in the resonator and the fraction of the energy that is lost in the following optical cycle, multiplied by 2π . Alternatively, the quality factor can be defined as 2π multiplied by the number of oscillations of the field in the resonator before the circulating energy is depleted to 1/e of the initial energy:

$$Q = 2\pi \frac{\tau}{T} = \omega\tau \quad (2.46)$$

where τ is the dwelling time (or the time constant) of the resonator, since the intensity of resonant field decays as $e^{-t/\tau}$. It can be shown that these definitions are equivalent to a third one, which is more useful from a practical point of view. Since the transmission spectra of the ring exhibits a lorentzian shape (Figure 2.21), it is easy to measure the full-width at half maximum (FWHM) of the resonances. Then, it can be shown that the quality factor is given by:

$$Q = \frac{\nu}{\Delta\nu} = \frac{\lambda}{\Delta\lambda} \quad (2.47)$$

where $\Delta\nu$ and $\Delta\lambda$ are, respectively, the FWHM in frequency and wavelength. We can now derive the dependence of the quality factor with respect to the losses associated with the resonator. Let's consider a simple ring without any coupled waveguide. The intensity of the electric field after a single roundtrip will be given by

$$I = I_0 e^{-t_{RT}/\tau} = I_0 e^{-\alpha L} \quad (2.48)$$

where t_{RT} is the round-trip time given by L/v_g . Thus, by using equations (2.46) and (2.48), the Q-factor of a resonator without the effect of coupled waveguides can be expressed as

$$Q_i = \omega \frac{t_{RT}}{\alpha L} = \frac{2\pi n_g}{\alpha \lambda} \quad (2.49)$$

where αL is almost equal to the round-trip losses, since $1 - e^{-\alpha L} \approx \alpha L$. Q_i is the *intrinsic* quality factor, since it quantifies the effect of the losses of the material without taking into account the geometry of the device.

If a waveguide is coupled, we can generalize equation (2.49). In fact, if the coupling is equal to K^2 , the roundtrip losses are given by $\alpha L + K^2$, and equation (2.49) becomes

$$Q_L = \omega \frac{t_{RT}}{(\alpha L + K^2)} = \frac{2\pi n_g L}{(\alpha L + K^2) \lambda} = \left(\frac{1}{Q_i} + \frac{1}{Q_c} \right)^{-1} \quad (2.50)$$

where Q_L is called *loaded* quality factor and Q_c is the quality factor associated to the coupling. As can be seen, if the resonator is in the critical coupling condition, $Q_i = 2Q_L$. If the coupling is higher than the losses ($K^2 > \alpha L$), the light is less confined in the resonator with respect to the critical coupling condition: thus, the quality factor decreases (while the FWHM increases, as it is shown with the green dashed line in Figure 2.21b). On the other hand, a reduction of the coupling increases the dwelling time: hence, the quality factor increases and the resonance is narrower (see the blue dotted line in Figure 2.21b).

Finesse and Intensity Enhancement Another very important parameter related to the ring resonators is the *finesse*, which is a dimensionless quantity defined

as the ratio between the FSR and the FWHM. Thus, it is given by:

$$\mathcal{F} = \frac{FSR_\nu}{\Delta\nu} = \frac{Q \cdot FSR_\nu}{\nu} = \frac{Q \cdot c}{\nu n_g L} = \frac{2\pi}{(\alpha L + K^2)} \quad (2.51)$$

The finesse is obviously very important when the resonator is used as a filter. In fact, it quantifies the ratio between the part of the optical spectrum which is on resonance with respect to the non-resonant part.

In addition, it can be shown that it is related to the intensity enhancement within the cavity. As one can expect, the resonant modes exploit an enhancement of their intensity inside the resonator. This can be calculated from the ratio between E_1 and E_{in} in Figure 2.20a, which gives:

$$IE = \left| \frac{E_1}{E_{in}} \right|^2 = \left| \frac{\sigma}{1 - at e^{i\phi}} \right|^2 \quad (2.52)$$

The maximum intensity enhancement occurs on resonance, and it turns out to be

$$\begin{aligned} IE &= \left| \frac{E_1}{E_{in}} \right|^2 \xrightarrow{(2.35)} \left| \frac{\sigma}{1 - at} \right|^2 \approx \frac{K^2}{(K^2 + \alpha L)^2 / 4} = \\ &= \frac{\mathcal{F}}{2\pi} \frac{4K^2}{K^2 + \alpha L} = \frac{\mathcal{F}}{\pi} \cdot \frac{2}{1 + \alpha L / K^2} = \frac{2\mathcal{F}}{\pi} \left(1 - \frac{Q_L}{Q_i} \right) \stackrel{\text{c.c.}}{=} \frac{\mathcal{F}}{\pi} \end{aligned} \quad (2.53)$$

When the ring is in critical coupling, the intensity enhancement is simply given by the finesse divided by π . Finally, one can observe from (2.53) that the intensity enhancement is proportional to $Q_L (1 - Q_L / Q_i)$. Thus, it assumes the maximum value (with Q_i fixed) for $Q_L = Q_i / 2$, which is the critical coupling condition.

Visibility The simplest way to evaluate the coupling condition of a microring resonator is to determine how deep are its resonances, i.e. their visibility. This quantity is defined from the ratio between the maximum and the minimum of the transmission (2.39):

$$V = 1 - \frac{T(\phi = 2\pi)}{T(\phi = \pi)} \approx 1 - \left| \frac{K^2 - \alpha L}{K^2 + \alpha L} \right|^2 \quad (2.54)$$

where the approximation is obtained by using equations (2.40), (2.41), and (2.42). The relation between the visibility and the quality factor is shown in Figure 2.22. If the resonator is in the critical coupling condition, the visibility is equal to 1. If the visibility is lower, it is impossible to estimate if the coupling is higher or lower than the losses. However, the characterization of another identical microring with a different coupling provides a second point in the plot in Figure 2.22, enabling the recognition of the coupling condition.

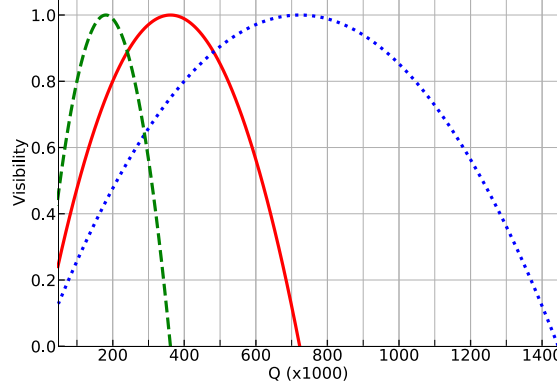


Figure 2.22: Visibility with respect to loaded quality factor of a silicon microring resonator. The green dashed, the continuous red, and the blue dotted lines show the result of the variation of the coupling with α equal to, respectively, 2 dB/cm, 1 dB/cm, and 0.5 dB/cm.

Finally, it is interesting to note that equations (2.49), (2.50), and (2.54) can be used to derive the dependence of the visibility on the loaded and intrinsic quality factors (Q_L , and Q_i):

$$V \approx 1 - \left| \frac{1/Q_c - 1/Q_i}{1/Q_L} \right|^2 = 1 - \left| 1 - \frac{2Q_L}{Q_i} \right|^2 = \frac{4Q_L}{Q_i} \cdot \left(1 - \frac{Q_L}{Q_i} \right) \quad (2.55)$$

This relation can be used, ideally, to derive the intrinsic quality factor (useful to estimate the losses of the waveguides) from two quantities (Q_L and V) that can be directly derived from the optical spectrum. In fact, we get

$$Q_i = \frac{2Q_L}{1 \pm \sqrt{1 - V}} \quad (2.56)$$

where the plus is associated with the undercoupling condition. However, as discussed in [215], the non ideality of the coupling can lead to an overestimation of the losses, since parasitic coupling processes take place.

2.3.3 Simulation of coupling parameter

A fundamental parameter to determine the behavior of the microring resonator is the coupling between the ring and the waveguide. It depends on different geometrical elements, such as the cross-section of the waveguide, since the more the field is confined, the lower is the coupling. In addition, it is exponentially decaying with

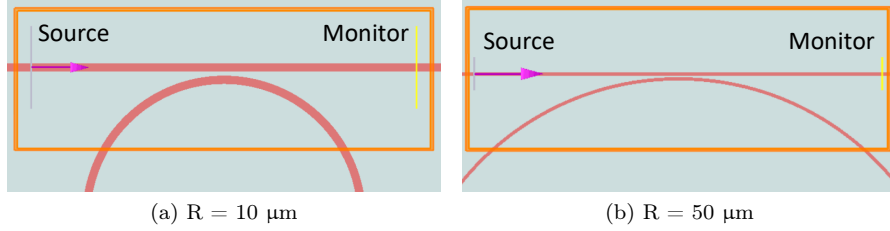


Figure 2.23: The FDTD are (orange) includes the point coupler, the source of the mode, and the monitor of the field.

the gap, which plays the most important role. Finally, also the radius of curvature is significant, since higher radii increase the coupling.

A typical method to estimate the coupling is to run some Finite Difference Time Domain (FDTD) simulations. This method consists in the division of the space into small cells (with sides lower than $\lambda_0/10n$, where n is the refractive index of the material) and to solve the discretized time-dependent Maxwell equations [216, 217]. As it has been already discussed, the main drawback of the method is that the simulations can be quite long and require a lot of memory. Thus, it is worth to mention that the coupling parameter can be estimated also with a generalized version of the coupled mode theory [218] or the super modes method [219], which allow one to obtain faster results with a discrete accuracy.

The FDTD software by LumericalTM has been used to simulate the coupling with three different bent waveguides (with radii of curvature equal to 10 μm , 30 μm , and 50 μm). The basic idea is to place a source of the mode coupled to the straight waveguide far enough from the point coupler to consider negligible the coupling with the ring. Then, a field monitor is positioned on the waveguide after the point coupler at the same distance used for the source (see Figure 2.23): the detected power allows one to estimate the coupled field. The results of the simulations are presented in Figure 2.24. As can be seen, the coupling parameter K_{pc} depends exponentially on the gap, and the decaying constants are similar ($54.8 \pm 0.9 \text{ nm}^{-1}$, $49.2 \pm 1.0 \text{ nm}^{-1}$, and $50.5 \pm 1.7 \text{ nm}^{-1}$ for, respectively, 50 μm , 30 μm , and 10 μm).

Finally, from the results shown in Figure 2.25 we can obtain the information needed to design the ring resonators: the coupling coefficients are divided by the round-trip length of the resonator, and this allows the calculation of a sort of *coupling per length*, which can be directly compared with the propagation losses of the waveguide. The simulations with the different radii give very similar results, and from the exponential fits it is possible to estimate directly the required gap to obtain a resonator in critical coupling. For example, if we suppose that the propagation losses are between 0.5 dB/cm and 1.5 dB/cm, we would design gaps between 200 nm and 260 nm.

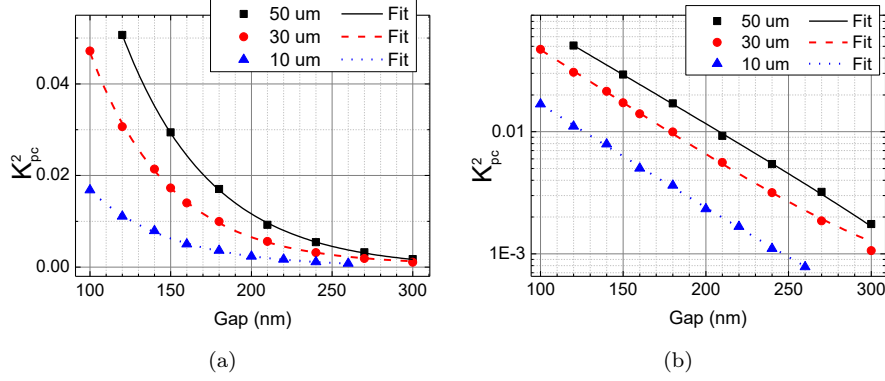


Figure 2.24: Results of FDTD simulations of a point coupler, i.e. a straight waveguide coupled to a bend. Each point corresponds to a different simulation. The black squares shows the results of the simulations with a radius of curvature equal to 50 μm , while the red circles and the blue triangles are associated, respectively, to 30 μm and 10 μm . The sets of point are fit with a decaying exponential function $y_0 + Ae^{-x/\Gamma}$.

2.3.4 FWM in microring resonators

As we saw in the previous section, the electromagnetic field experiences an enhancement in resonant structures. This effect is extremely powerful in the framework of nonlinear optics. In fact, since the nonlinear phenomena involve the interaction of several fields, their enhancement leads to a tremendous amplification of the process. We will focus on the description of FWM in microring resonators, and in particular we will derive the analogous of the equations (2.12), (2.16), and (2.17) to quantify the generated power through, respectively, stFMW, SFWM, and d-SFWM.

Stimulated FWM The observation of the enhancement of stimulated FWM in integrated microring resonators has been realized for the first time by Absil and colleagues in 2000 [202]. As presented in their work, if we suppose to have a pump laser at ω_P and a signal laser at ω_S both resonant with the microring, the generated power within a third resonance at $\omega_I = 2\omega_P - \omega_S$ is given by:

$$P_I = (\gamma L)^2 (IE_P)^2 (IE_S) (IE_I) P_P^2 P_S \approx (\gamma L)^2 (IE_P)^4 P_P^2 P_S \quad (2.57)$$

where L is the length of the resonator, γ is the nonlinear parameter, IE_j and P_i are, respectively, the intensity enhancement and the optical power in the coupled waveguide of the field at ω_j . By comparing the generated power in the resonator (2.57) with the case of a simple waveguide (2.12), we can note that the process is

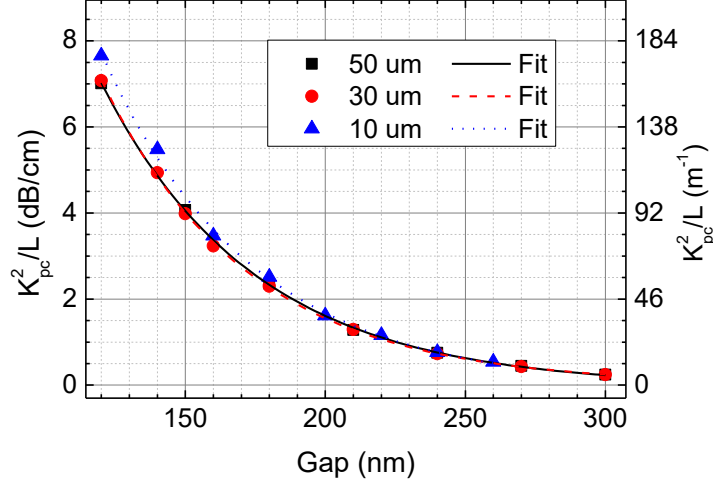


Figure 2.25: Effective coupling per length calculated from the ratio of the coupling coefficients shown in in Figure 2.24 and the length of the correspondent resonators ($L = 2\pi R$).

enhanced by the fourth power of the intensity enhancement. If we consider resonator in critical coupling and we assume that the intensity enhancement of the resonances at ω_I , ω_P , and ω_S is the same, we can write (2.57) as a function of the optical and the geometrical parameters of the structures [131]:

$$P_I = \gamma^2 \left(\frac{Q \cdot c}{\pi \nu n_g} \right)^4 \frac{1}{L^2} P_P^2 P_S \quad (2.58)$$

SFWM Spontaneous four-wave mixing takes advantage, as well, of the field enhancement in the resonator. Again, the theory used for stimulated FWM developed in the framework of classical electromagnetism is not sufficient to describe this process. Therefore, we consider the Hamiltonian of the system composed of the resonator and a waveguide coupled to it [103, 149]:

$$\hat{H} = \hat{H}_{wg} + \hat{H}_R + \hat{H}_c \quad (2.59)$$

$$\begin{aligned} \hat{H}_{wg} = & \sum_{\mu} \hbar \omega_{\mu} \int dz \, \hat{w}_{\mu}^{\dagger}(z) \hat{w}_{\mu}(z) + \\ & + \frac{i}{2} \hbar v_{g\mu} \int dz \, \left(\frac{\partial \hat{w}_{\mu}^{\dagger}(z)}{\partial z} \hat{w}_{\mu}(z) - H.c. \right) \end{aligned} \quad (2.60)$$

$$\hat{H}_R = \sum_{\mu} \hbar\omega_{\mu} \hat{b}_{\mu}^{\dagger} \hat{b}_{\mu} - \sum_{\mu_1, \mu_2, \mu_3, \mu_4} S_{\mu_1, \mu_2, \mu_3, \mu_4} \hat{b}_{\mu_1}^{\dagger} \hat{b}_{\mu_2}^{\dagger} \hat{b}_{\mu_3} \hat{b}_{\mu_4} \quad (2.61)$$

$$\hat{H}_{cp} = \sqrt{2\pi\hbar} \sum_{\mu} \sum_{\mu} \left[c_{\mu} \hat{b}_{\mu}^{\dagger} \hat{w}_{\mu}(0) + H.c. \right] \quad (2.62)$$

where \hat{H}_{wg} , \hat{H}_R , \hat{H}_c are the Hamiltonians that describe, respectively, the waveguide, the ring resonator and their coupling; the indexes μ_i denotes the modes of the microring, \hat{w} is the channel field operator, \hat{b} is the ring field operator, c is the waveguide-resonator coupling constant, and S in the nonlinear operator analogous to what has been used in (2.15). Following the calculation described in detail in [103], we obtain the generated power through SFWM in microring resonators:

$$\begin{aligned} P_I = P_S &= (\gamma L)^2 (\text{IE}_P)^2 \sqrt{\text{IE}_S \cdot \text{IE}_I} \frac{\hbar\omega c}{2n_g L} P_P^2 \approx \\ &\approx (\gamma L)^2 \left(\frac{Q \cdot c}{\pi\nu n_g L} \right)^3 \frac{\hbar\omega c}{2n_g L} P_P^2 \end{aligned} \quad (2.63)$$

where the approximation is valid if the resonator is in the critical coupling condition and all the fields experience the same intensity enhancement. As can be observed, the ratio between the generated power through stimulated FWM and SFWM can be written in the form [131]:

$$\frac{P_{I,sp}}{P_{I,st}} = \frac{1}{4Q} \frac{\hbar\omega^2}{P_S} \quad (2.64)$$

Note that, similarly to equation (2.58), P_j are the optical powers in the coupled waveguide. This is particularly relevant if we want to calculate the generation rate of photons at ω_I and ω_S , or the generation rate of photon pairs. In fact, the rate of signal and idler photons that are coupled to the waveguide can be simply calculated by taking equation (2.63) and dividing by the photon energy $\hbar\omega$, thus getting:

$$R^{\text{wg}} = (\gamma L)^2 (\text{IE}_P)^2 \sqrt{\text{IE}_S \cdot \text{IE}_I} \frac{c}{2n_g L} P_P^2 \quad (2.65)$$

To estimate the internal generation rate, i.e. the rate of generated photons in the resonator, we have to take into account its different output channels. In fact, a photon generated in the ring can be coupled to the waveguide with a probability $K^2/(\alpha L + K^2)$, and it can be lost (due to scattering or absorption) with probability $\alpha L/(\alpha L + K^2)$. Thus, the internal generation rate is given by:

$$R_I^r = R_S^r = R^r = R^{\text{wg}} \cdot \frac{\alpha L + K^2}{K^2} \stackrel{\text{c.c.}}{=} 2 \cdot R^{\text{wg}} \quad (2.66)$$

which is twice the rate in equation (2.65) in the critical coupling condition.

The generation rate of photon pairs in the resonator is obviously equal to R^r , since the process occurs in the microring. However, since the fraction of photons

that are coupled to the waveguide is $K^2/(\alpha L + K^2)$, the rate of photon pairs in the waveguide turns out to be:

$$R_{\text{pairs}}^{\text{wg}} = R^{\text{r}} \left[\frac{K^2}{\alpha L + K^2} \right]^2 \stackrel{\text{c.c.}}{=} \frac{R^{\text{r}}}{4} = \frac{R^{\text{wg}}}{2} \quad (2.67)$$

d-SFWM Naturally, also d-SFWM can be observed in microring resonator [56, 57, 220]. If we consider two lasers at ω_{P_1} and ω_{P_2} resonant with the ring and if there is a third resonance at ω_T such that $2\omega_T = \omega_{P_1} + \omega_{P_2}$, the generated power turns out to be

$$\begin{aligned} P_T &= 4(\gamma L)^2 (\text{IE}_T)^2 \sqrt{\text{IE}_{P_1} \cdot \text{IE}_{P_2}} \frac{\hbar \omega c}{2n_g L} P_{P_1} P_{P_2} \approx \\ &\approx 4(\gamma L)^2 \left(\frac{Q \cdot c}{\pi \nu n_g L} \right)^3 \frac{\hbar \omega c}{2n_g L} P_{P_1} P_{P_2} \end{aligned} \quad (2.68)$$

where P_{P_1} and P_{P_2} are the power of the lasers at ω_{P_1} and ω_{P_2} .

Chapter 3

Devices for Integrated Quantum Photonics

In this chapter I describe the devices realized during the fabrication run I followed. In fact, a significant part of my work consisted in the design of integrated optical structures with different goals in the framework of integrated quantum photonics. In the following sections, the underlying motivation and the theory of the devices is briefly discussed, as well as the choice of their components. In addition, their position on the fabricated $22 \times 22 \text{ mm}^2$ die is highlighted, and additional information about the designed lithographic masks are provided.

The devices are realized by exploiting five different lithographic steps, which correspond to five optical masks and, thus five different design layers. A scheme of the cross-section of the devices is shown in Figure 4.31.

- The first layer (named *waveguide*) is used to define the silicon ridge optical waveguides. The associated mask has a minimum critical dimension (CD min), which is the smallest value that can be patterned of the silicon elements or of the gaps between them, equal to 120 nm. The associated mask is characterized by a very large opening area (i.e. the portion of the total area that is etched after the lithography), which is around 98.7% of the chip.
- The second layer (*heater*) is used to pattern the TiTiN metallic layer exploited to realize the tunable phase shifter. The CD min is bigger (800 nm), which is equal to the width of the TPSs. The opening area is equal to 97 %.
- The third layer (*vias*) is meant to pattern the holes in the silica used to connect the *heater* level with the *pads* level, which is described below. It has a CD min equal to 10 μm , which is equal to the dimension of the holes to etch in the silica, and the smallest opening area of the sets of masks: 0.3%.

Layer	Name	Description	Color	CD min
1	Waveguide	Silicon optical circuits	Red	120 nm
2	Heater	Thermal phase shifter	Yellow	800 nm
3	Vias	Electrical connection of layers 2 and 4	White	10 μm
4	Pads	Pads for external electrical contact	Green	10 μm
5	Deep Etch	Trenches for the edge coupling	Blue	10 μm

Table 3.1: The five layers used for the realization of the devices.

- The fourth layer (*pads*) is used to pattern the upper metallic level, which is used to electrically connect external voltage sources to the TPSs. The contact is realized through multi-contact wedges, which lean on top of metallic pads. The CD min is 10 μm , and the opening area is equal to 23%.
- Finally, the fifth layer (*deep etch*) allows to define the trenches needed to realize the facets of the edge couplers, as discussed in section 2.2.1. CD min is equal to 10 μm and opening area is 16%. This layer divide the chip into 35 subdies, which are labeled as shown in Figure 3.1b.

Within the following sections, several schemes of the devices are displayed. They are taken from the database which collects all the patterns used to define the structures. I will refer to the database with the information of the patterns as “gds”, which is the extension of the database file, typically encoded in the GDSII format¹. These database can be opened (and eventually edited) by using specific software, such as KLayout².

The full gds of my project is shown in Figure 3.1a, where the layers are displayed with different colors, as indicated in Table 3.1. It has been designed by using the open source Nazca designTM framework³, which includes several Python libraries developed to realize gds files with integrated optical circuits.

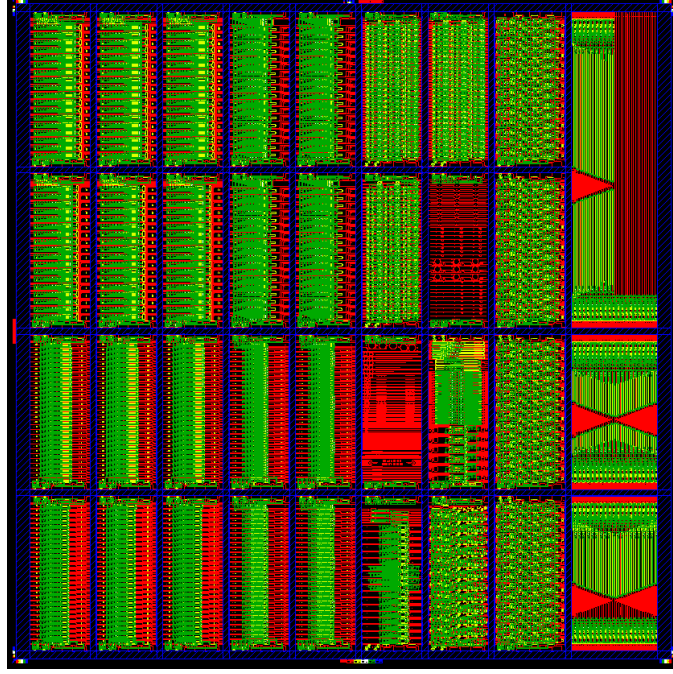
3.1 Microring resonators as sources of nonclassical states of light

The majority of the devices designed and fabricated in this work are based on the use of microring resonators. In fact, among all their uses in the field of integrated photonics, they are widely exploited for the generation of nonclassical states of light through the nonlinear interaction of their modes [50, 221].

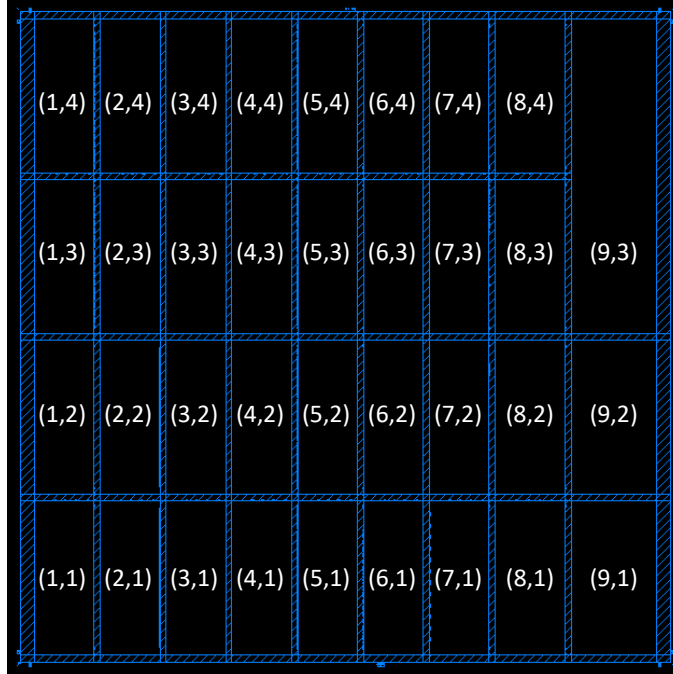
¹It is worth to mention that recently an alternative format has been developed (OASIS format, extension .oas) which allows one to deal with files having smaller sizes.

²<https://www.klayout.de/>

³<https://nazca-design.org/>



(a) Image of the gds with all the layers.



(b) Image of the layer 5, which defines the external trenches. The labels define the subdies and will be used in the text to determine the location of the devices.

Figure 3.1: Images taken from the gds. The chip ($22 \times 22 \text{ mm}^2$) is divided into 35 subdies to increase the number of edge couplers that can be placed.

As discussed in the previous chapter, SFWM occurring in a microring resonator is characterized by the Hamiltonian (2.59). If it is applied on an initial coherent vacuum state, the resulting output state is a two-mode squeezed vacuum state [103, 122]:

$$|\Psi\rangle = e^{\beta C_{II}^\dagger - h.c.} |0\rangle_s |0\rangle_i \quad (3.1)$$

where C_{II}^\dagger is the creation operator of the pair defined as

$$C_{II}^\dagger = \frac{1}{\sqrt{2}} \int d\omega_s d\omega_i \phi(\omega_s, \omega_i) a_{\omega_s}^\dagger a_{\omega_i}^\dagger \quad (3.2)$$

and $\phi(\omega_s, \omega_i)$ is the bi-photon wavefunction, which is assumed to be normalized and it satisfies $|\phi(\omega_s, \omega_i)|^2 = \delta(\omega_s + \omega_i - 2\omega_p)$ in the continuous wave pump case. Typically, $|\beta| \ll 1$, and thus (3.1) becomes

$$|\Psi\rangle \approx |0\rangle_s |0\rangle_i + \beta |1\rangle_s |1\rangle_i + \frac{\beta^2}{2} |2\rangle_s |2\rangle_i \quad (3.3)$$

where $|\beta|^2$ and $|\beta|^4/4$ are the probability of generating two and four photons, respectively. Since the experiments typically are based on the detection of at least one photon and the probability to generate multiple pairs is negligible, the state in (3.3) can be written as

$$|\Psi\rangle \approx \frac{\beta}{\sqrt{2}} \int d\omega_s d\omega_i \phi(\omega_s, \omega_i) a_{\omega_s}^\dagger a_{\omega_i}^\dagger |0\rangle_s |0\rangle_i \quad (3.4)$$

where the dependence on the bi-photon wavefunction is restored.

The bi-photon wavefunction is fundamental to describe the generated state, and it is a fundamental element to understand if the generated photons are *entangled*. Two objects are defined *entangled* when they are characterized by a certain degree of correlation that cannot be explained by deterministic theories. They are described by a single quantum-mechanical state, and the single-object state can't be described independently of the state of the other. This is exactly the case of the state generated through SFWM by using a continuous-wave pump laser at frequency ω_p , where the total energy of the two photons is known to be equal to $2\hbar\omega_p$, but the values of the individual frequencies is undetermined. The generation of time-energy entangled photons has been proposed for the first time by Franson in 1989 [222], as well as an experiment based on two interferometers to quantify the degree of entanglement [223]. This technique is now a routine experiment in the field of quantum optics [51, 55, 208, 224, 225] which allows one to prove the possibility of generating time-energy entangled photons in microring resonators.

An example of the realization of the Franson experiment is presented in a work I took part [209], in which a silicon microring resonator is inserted in a fiber laser cavity enabling the generation of entangled photons without the use of an external

laser. The experimental set-up is shown in Figure 3.2a: a laser cavity is built by using a boosted optical amplifier (BOA) and a microring resonator in the add-drop configuration. Additional band-pass filters are used to make the cavity to lase around one resonance of the microring and to reduce the noise coming from the amplified spontaneous emission of the BOA. Finally, a tunable Fabry-Perot is placed to select one mode of the external cavity, whose FSR is much smaller than the resonance linewidth. An unbalanced MZI is then used to realize the Franson experiment: the unbalance between the arms leads to the presence of three peaks on the coincidence histogram (Figure 3.2b). In particular, the central one depends on the phase ϕ applied to one arm of the interferometer, since the peak is the result of the interference between the manipulated quantum states, and the visibility of the fringes is related to the degree of entanglement.

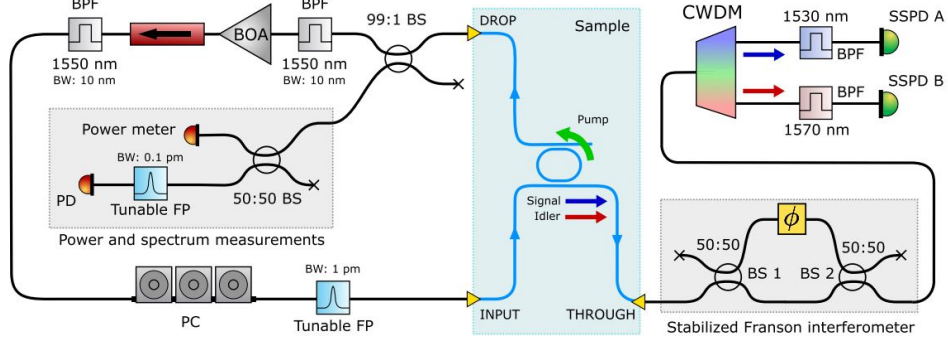
An interesting property of the generated two-photon state is the possibility of changing the degree of entanglement by playing with the coherence of the pump. In fact, as suggested in [103], the use of a pulsed laser leads to the generation of nearly uncorrelated pairs in integrated resonators. In particular, the correlation between the generated photons is minimum when the bandwidth of the pulsed laser is broader than the linewidth of the resonance. This can be understood by noticing that the pump frequency is not precisely defined, due to the bandwidth of the pulses. Thus, the total energy of the generated two photons is not defined anymore, and the frequency of the idler photons is no longer dependent on the frequency of signal ones. This effect has been observed [226] by measuring the square modulus of the bi-photon wavefunction (named *joint spectral density*) of the two-photon states generated by a CW and a pulsed laser, which proves the reduction of the degree of correlation of the pairs generated when using the pulsed laser.

The possibility of generating uncorrelated photons is particularly relevant for the realization of single-photon sources. The generated pairs can be routed on different paths: signal photons on path A and idler photons on path B. Then, the detection of a photon on path A heralds the presence of a photon in the path B, and this allows one to use microring resonators as sources of heralded single photons. The use of pulsed lasers is fundamental for this kind of applications, since it allows one to generate *identical* single photons, i.e. photons having the same state. In fact, if the pairs are uncorrelated, the bi-photon wavefunction turns out to be separable ($\phi(\omega_s, \omega_i) = \phi_s(\omega_s)\phi_i(\omega_i)$), and the state in (3.4) becomes:

$$|\Psi\rangle \approx |\Psi\rangle_s |\Psi\rangle_i = \frac{\beta}{\sqrt{2}} \int d\omega_s \phi_s(\omega_s) a_{\omega_s}^\dagger |0\rangle_s \int d\omega_i \phi_i(\omega_i) a_{\omega_i}^\dagger |0\rangle_i \quad (3.5)$$

and it is clear that any operation of one photon doesn't modify the state of the other.

A significant quantity that can be defined to quantify the degree of entanglement is the Schmidt number, which is derived from the Schmidt decomposition technique [227]. It consists in the decomposition of the bi-photon wavefunction as a superpo-



(a) Experimental set-up used to generate entangled photon-pairs through SFWM in silicon microring resonator in a self-pumping scheme [209].

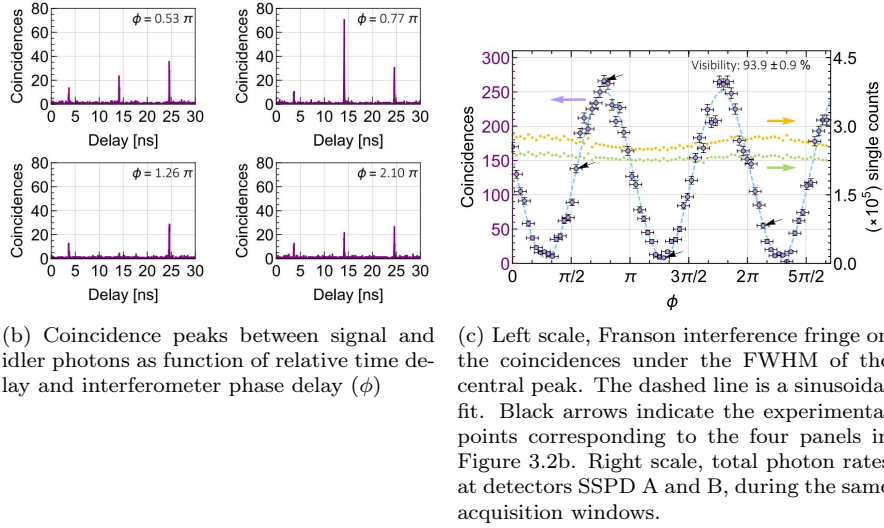


Figure 3.2: Images from [209].

sition of modes forming orthonormal basis of the Hilbert spaces associated to the two photons:

$$\phi(\omega_s, \omega_i) = \sum_{n=0}^{\infty} \lambda_n u_n(\omega_s) v_n(\omega_i) \quad (3.6)$$

Then, the Schmidt number is defined as

$$K = \frac{1}{\sum_n \lambda_n^2} \quad (3.7)$$

If the generated state is separable, then the Schmidt number is equal to 1. On the other hand, a non-separable state correspond to high values of K and, thus, stronger degree of entanglement.

Finally, it is important to mention a relevant aspect about the generation of heralded single-photons with microring resonators. The generated state operating with conventional resonators is not completely separable, and the Schmidt number can't be lower than 1.09 [103, 226]. This is due to the shape of the resonances, which is Lorentzian. However, it has been shown [207, 228] that the use of interferometric couplers allows one to increase the purity of the generated states.

3.2 Efficient generation of entangled frequency bins

Albeit typical systems to process and manipulate quantum information are based on two-level quantum states (qubits), high-dimensional entangled states turn out to be very appealing towards the realization of practical and powerful systems for quantum computation [53]. In fact, increasing the number of entangled photons and/or their dimensionality leads to a simplification the complexity of quantum circuits [27, 229], and to enhance their robustness and immunity to noise [230, 231].

As already pointed out in the manuscript, integrated nonlinear circuits offer the opportunity to mimic the approach adopted in bulk systems in which parametric down conversion allows one to use energy and frequency to encode the information [232, 233]. In fact, the efficient process of SFWM in micrometric resonators can be exploited to generate many photons pairs which are symmetrically distributed with respect to the frequency of the pump [54, 224], with the generated state that can be written as

$$|\Psi\rangle = \sum_m \alpha_m |m\rangle_S |m\rangle_I \quad (3.8)$$

where $|m\rangle_{S(I)}$ is the state associated to the signal (idler) photon generated in the resonance at m ($-m$) FSRs from the resonance of the pump. Then modulators, filters and phase shifters can be used to manipulate and control the generated nonclassical states [53, 70, 234]. In particular, it is fundamental for quantum communication application to test the entanglement of the generated photons. This can be realized by a phase modulator, as it is described in [53]: in fact, a two frequency-bin input state is projected on three different states $|1\rangle, |2\rangle, |S\rangle$, as shown in Figure 3.3a where $|S\rangle$ is given by the superposition of the two other states:

$$|S\rangle = \frac{1}{\sqrt{2}} (|1\rangle + e^{i\phi} |2\rangle), \quad (3.9)$$

being ϕ the relative phase between the input states. If this procedure is applied to both signal and idler photons (Figure 3.3b), then the coincidences between the photons in the superposition states depend on the phase ϕ . This verification scheme

is similar to what is performed using a Franson-like experiment with time-energy entangled photons [51, 209, 222]. In addition, the projection of different output states allows one to perform the tomography of the quantum state, as shown in [53].

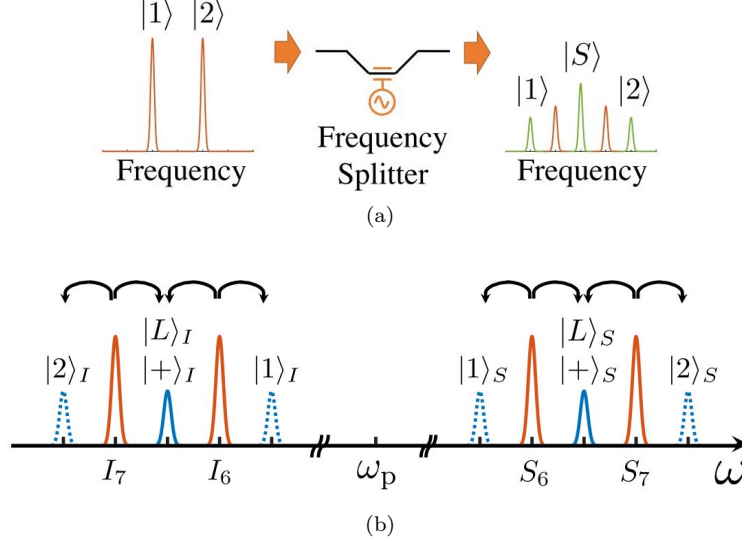


Figure 3.3: Scheme for the validation of the entanglement of a two frequency-bin input state, which is projected on three output different states, including a superposition state $|S\rangle$. The frequency splitter is a phase modulator. Images from [53].

The main drawback in the use of conventional microring resonators for the generation of these frequency bins is the relation between the efficiency of the modulation and the strength of the nonlinear interaction leading to the generation of pairs. In fact, a proper and complete control of the generated states requires the possibility of efficiently modulating at frequencies in the order of the FSR of the resonator (i.e. the frequency separation of the bins). However, commercial electro-optical modulators have their fundamental frequency in the order of few tens of GHz, and this imposes the reduction of the FSR (i.e. the use of large rings), which leads to decrease the finesse (2.51) and the intensity enhancement (2.53) of the resonators.

Recently, Liscidini and Sipe proposed a scheme [235] that enables the generation of frequency-bin encoded qudit states by using small resonators (with high finesse) and allowing the possibility of working with almost arbitrary small modulating frequencies. The device is shown in Figure 3.4: a beam splitter divides the input laser into two waveguides, and two rings with different radii are pumped. Then, if we focus on the photons generated in the m -th resonances, we can write the associated

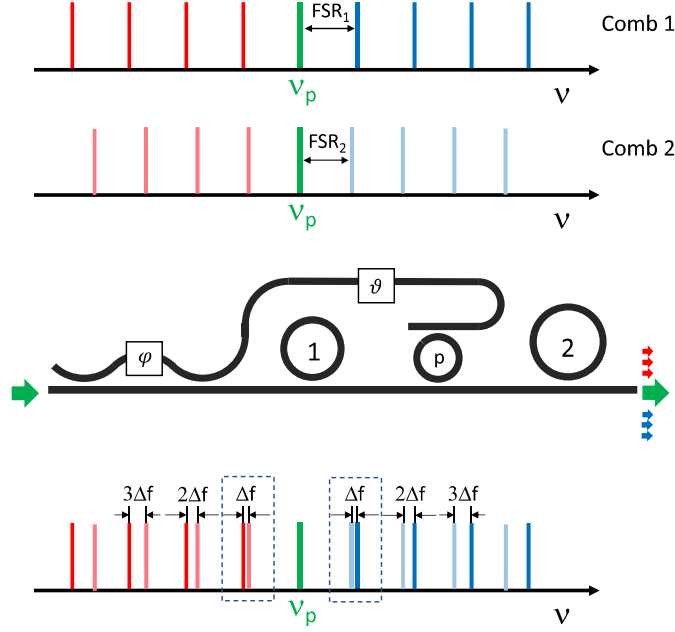


Figure 3.4: Generation of frequency encoded qubits through the coherent pumping of two rings having different FSRs (Figure from [235]).

state as [235]:

$$|\Psi\rangle = \frac{1}{\sqrt{|\beta_1^m|^2 + |\beta_2^m|^2}} [\beta_1^m |1\rangle_I^m |1\rangle_S^m + \beta_2^m e^{i\varphi} |2\rangle_I^m |2\rangle_S^m], \quad (3.10)$$

where β_i^m is the generation efficiency of the i -th resonator at the m -th resonance, and $|1\rangle_{I(S)}^m$ is the idler (signal) photon generated in the i -th resonator. As can be seen, the generation efficiency can be controlled by acting on the MZI (i.e. by changing the ratio of the coupling to the output waveguides), and the phase φ allows one to build different states, as discussed in [235]. The main point is that the frequencies of the bins differs from a multiple of the difference of the rings' FSRs, which can be arbitrary small (being limited only by the linewidth of the resonances), and this choice does not affect the generation efficiency, as detailed in [235].

As one can observed, the state in (3.10) is still a qubit, since only two pairs of resonances are involved. However, the idea can be generalized allowing the generation of a qudit, as shown in Figure 3.5: the input laser is splitted in d paths to

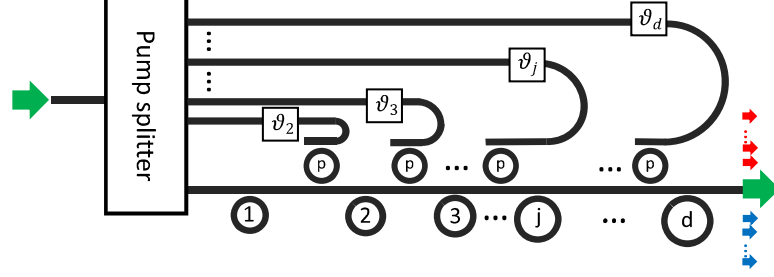


Figure 3.5: Generation of frequency encoded qudits through the coherent pumping of d rings having different FSRs (Figure from [235]).

pump d different rings, whose FSRs are defined as

$$\text{FSR}_n = \text{FSR}_1 + (n - 1)\Delta f \quad n = 1, \dots, d \quad (3.11)$$

and the generated state is the generalized version of (3.10)

$$|\Psi\rangle = \frac{1}{\sqrt{\sum_{n=1}^d |\beta_n^m|^2}} \sum_{n=1}^d \beta_n^m |n\rangle_I^m |n\rangle_S^m. \quad (3.12)$$

Five subdies of the chip are dedicated to the realization of such a circuit. In particular, the goal is the generation of a qudit with $d = 4$ bu using the device shown in Figure 3.6. Three MZIs are used to split the pump in four paths: the length of the directional couplers in the MZIs is $17.5 \mu\text{m}$, while each arm is $275\text{-}\mu\text{m}$ long. The gap in the directional coupler is equal to 120 nm : this value guarantees the 50:50 splitting for the $600 \times 300 \text{ nm}^2$ at 1550 nm , but not for the $600 \times 220 \text{ nm}^2$, as shown in Figure 3.22a. However, a different operating wavelength can be used, and, in addition, the MZI works properly even if the splitting ratio of the DCs is not exactly 50:50.

Then, four additional small rings in the add-drop configuration are used to control the coupling to the main rings. Their radius is $11 \mu\text{m}$ or $22 \mu\text{m}$, while the gaps are equal to 120 nm , 150 nm , or 180 nm . The main rings are bigger: the radius of the first ring in the row is equal to $29.3 \mu\text{m}$, while the others have the radius increased by $0.1 \mu\text{m}$, $0.3 \mu\text{m}$, or $0.5 \mu\text{m}$. The gaps of the main rings are identical within the device, and assume values from 120 nm to 240 nm with 20-nm span. Finally, the subdie (7,1) has devices with the width of the waveguide equal to 500 nm , to overcome eventual problems due to the multimode nature of the 600-nm waveguides.

In the end, as for the devices to perform the frequency conversion, the waveguide layer is too dense to place electric pads for all the devices. Then, two different masks

for the *vias* and for the *pads* level have been used, as detailed in Table 4.3: thus, not all the device are connected on all the subdies. A full list of the devices with their characteristics is available at [236].

3.3 Resonators in series: the superradiance

The collective action of several emitters has been studied by Dicke in 1954 [237]. In this work, he pointed out that spontaneous emission of a gas of atoms can exploit an enhancement due to the coherent nature of their action: the *superradiance*. In fact, the presence of N emitters leads to constructive interference of the emitted radiation, whose intensity results to scale as N^2 .

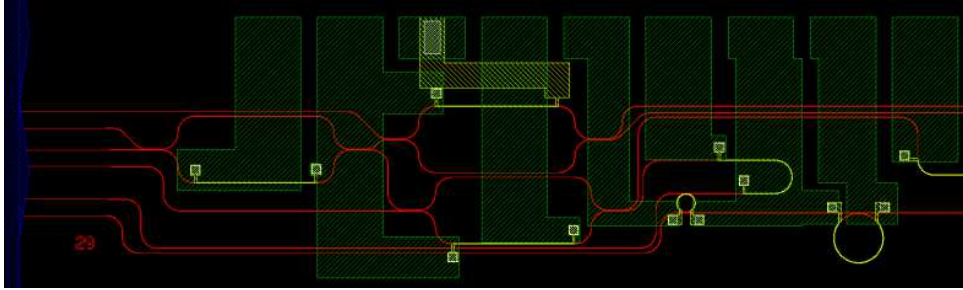
Recently, Onodera and colleagues proposed a scheme involving ring resonators that can exploit the same concept [238]. N identical rings are placed in series (Figure 3.7a), and as long as their distance is lower than the coherence length of the pump, the total generation rate scales with the second power of the number of the resonators.

To prove that, the scheme proposed in [238] (Figure 3.7a) should be modified. In fact, the remaining pump in the coupled waveguide is attenuated by the resonators, which act as filters. However, we can use add-drop resonators, as displayed in Figure 3.7b: five identical rings with radius equal to $29.3\text{ }\mu\text{m}$ are designed in the add-drop configuration, such that the drop port of the i -th ring is connected to the input port of the $i+1$ -th resonator. In addition, several TPS are placed to control the spectral alignment of the rings, and to make the emitted radiation to interfere constructively by controlling the phase between the sources. Six structures are designed, where the only different parameter is the gap between the resonators and the coupled waveguides, which assumes values between 120 nm and 195 nm at 15-nm steps. The structures are placed in the subdie (6,1).

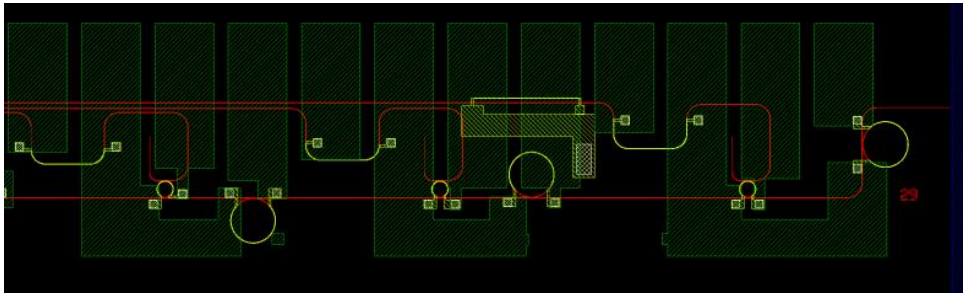
3.4 Linearly coupled resonators

Ring resonators can be used also as a component of a more complex structure. In fact, coupling of microrings allows one to explore innovative configurations useful for different applications, such as spectral filtering and multiplexing [65, 239, 240] and slow light delay lines [241–243]. In addition, it can brings relevant benefits also for the applications involving nonlinear optics, since the possibility to enhance the nonlinear interaction [244, 245], and to engineer the dispersion of the waveguide [246] to suppress unwanted nonlinear phenomena [56, 247] or to individually control the enhancement of the fields involved in the nonlinear interaction [248]. Among all the possible geometries, we focus on the devices depicted in Figure 3.8.

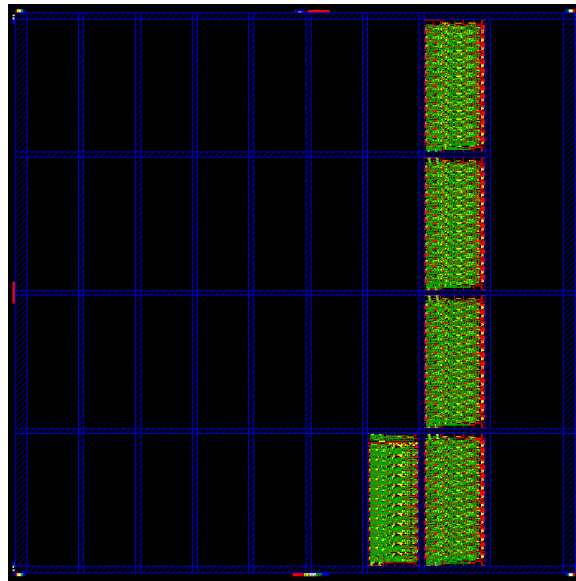
The physical mechanism of the device presented in Figure 3.8a consists in the splitting of the optical modes of the first resonator R_1 when they have the same



(a) Left part of the device #29.



(b) Right part of the device #29.

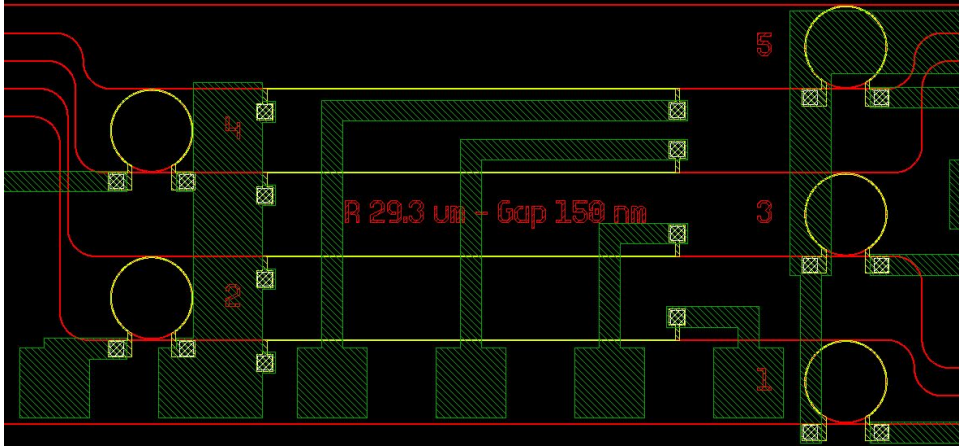


(c) Location of the devices on the chip.

Figure 3.6: Device on the chip for the generation of entangled frequency bins.

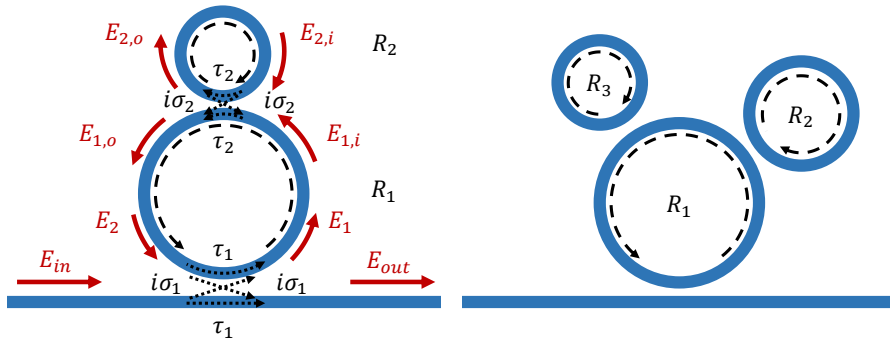


(a) Scheme proposed in [238] to realize the constructive interference of radiation emitted by N identical rings.



(b) Frame from the gds with the designed device, where 5 add-drop filters are used in series.

Figure 3.7: Device for the implementation of Dicke's superradiance by using integrated ring resonators.



(a) One resonator coupled to a main microring.

(b) Two resonators coupled to a main microring.

Figure 3.8: Devices with linearly coupled rings.

energy of the modes of the second resonator R_2 . This effect can be effectively described with two different models, as discussed in [247]: the coupled-mode model (CMM) and the frequency domain model (FDM). These approaches can be applied also to other similar devices, such as the one shown in Figure 3.8b where two rings are coupled to a main bigger resonator.

CMM is a quantum description of the system, which is particularly useful to evaluate its dynamics: the method consists in the construction of the Hamiltonian of the device, which is composed of a linear part (including the coupling between the modes), and a nonlinear part⁴. On the other hand, FDM involves a transfer-matrices approach, which allows one to easily determine the spectral response of the device. In fact, the fields displayed in Figure 3.8a are connected through equations similar to the ones used for the simple ring in (2.37). Thus, the spectrum of the device is given by the equations [247]:

$$\begin{aligned} t_{12} &= \frac{E_{1,o}}{E_{1,i}} = \tau_2 - \frac{\sigma_2^2 e^{i\phi_2 - \alpha L_2}}{1 - \tau_2 e^{i\phi_2 - \alpha L_2}} \\ \left| \frac{E_{out}}{E_{in}} \right|^2 &= \left| \tau_1 - \frac{t_{12} \sigma_1^2 e^{i\phi_1 - \alpha L_1}}{1 - t_{12} \tau_1 e^{i\phi_1 - \alpha L_1}} \right|^2 \end{aligned} \quad (3.13)$$

where the coefficients τ_1 , σ_1 , and τ_2 , σ_2 quantify, respectively, the coupling of R_1 with the waveguide and of the two bent waveguides composing the resonators, as shown in Figure 3.8a; the phase terms $\phi_i = k_i L_i$ are due to the propagation of the light with wavevector k_i in the resonator R_i , whose length is L_i , and α is the propagation losses coefficient.

In Figure 3.9 the spectrum of the device composed of two circular resonators (with radii 30 μm and 10 μm) is displayed, with $\sigma_1 = 0.15$ and $\alpha = 1$ dB/cm. As can be seen, one resonance every three is splitted, since the ratio of the radii is equal to three. In addition, the bigger is the coupling σ_2 between the bent waveguides composing the resonators, the bigger are the coupling and the splitting of the modes. In the following paragraphs, two applications of such structures are detailed.

3.4.1 W states

Entangled state can be composed of more than two system: multipartite entangled states can be realized, with correlations that cannot be interpreted as a generalization of bipartite entanglement. Among them, tripartite entangled states are subject of study, since their interesting characteristics.

Tripartite states are divided into two classes [249]: Greenberger-Horne-Zeilinger (GHZ) states and W states. The former have been exploited for the implementation of quantum communication protocols involving teleportation [250] and super-dense

⁴See section A1 of Appendix A in [247] for further details.

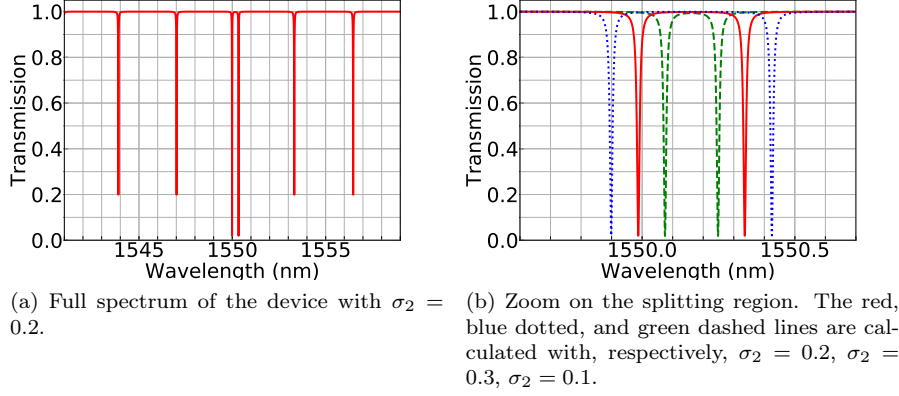


Figure 3.9: Calculated optical response of the device in Figure 3.8a by using equation (3.13). L_1 and L_2 are assumed to be 30 μm and 10 μm , respectively. The optical parameters used are $n_{eff} = 2.566$, $n_g = 4.05$, $\sigma_1 = 0.15$, and $\alpha = 1$ dB/cm, while each curve has a different value for σ_2 .

coding [251, 252], while the latter are promising for the realization of several quantum protocols [253, 254], since they are even more robust with respect to losses [255].

The general form of the W state is the following:

$$|W\rangle = \frac{1}{\sqrt{3}} (|AAB\rangle + |ABA\rangle + |BAA\rangle) \quad (3.14)$$

where $|A\rangle$ and $|B\rangle$ are two orthogonal states representing the system. In principle, one could encode the W state by using a single particle, and the states $|A\rangle$ and $|B\rangle$ can be the ground ($|0\rangle$) and the excited state ($|1\rangle$) of the system. Nevertheless, for many protocols three different particles are needed.

Typically, polarization entanglement is exploited: the W states are encoded through the linear manipulation of photons generated via spontaneous parametric down conversion (SPDC) [253]. However, it has been shown that energy entanglement can be exploited as well to generate W states in an integrated optics platform [256]: this brings several advantages, such as the scalability and efficiency of the generation process, but also a higher robustness for the transmission in long-range optical fibers [54, 257–259].

The scheme proposed in [256] relies on the preparation of the W state in the form

$$|W\rangle = \frac{1}{\sqrt{3}} (|\omega_1\omega_1\omega_2\rangle + |\omega_1\omega_2\omega_1\rangle + |\omega_2\omega_1\omega_1\rangle) \quad (3.15)$$

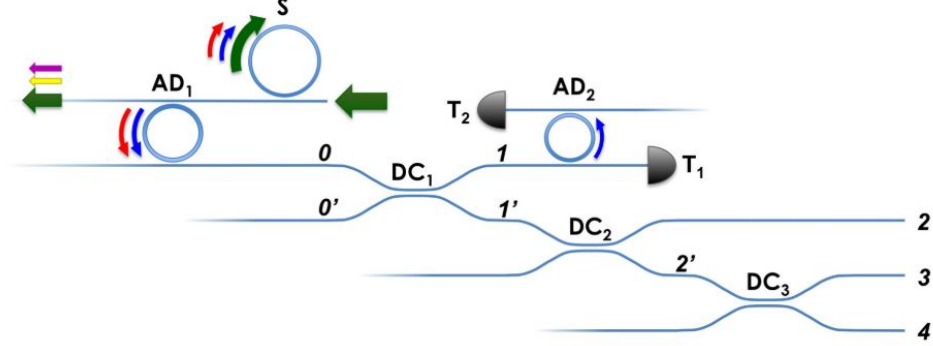


Figure 3.10: Scheme for the generation of W state presented in [256].

where ω_1 and ω_2 represent two different frequencies of the photons, which are generated through SFWM. One can use single-pump SFWM to generate those photons, as described in [256]. In fact, the state produced can be expressed as:

$$|\psi\rangle = \left(1 - \frac{\beta^2}{2}\right) |\text{vac}\rangle + \beta \hat{C}_{II}^\dagger |\text{vac}\rangle + \frac{1}{2} [\beta \hat{C}_{II}^\dagger]^2 |\text{vac}\rangle + \dots \quad (3.16)$$

where β is the generation probability and \hat{C}_{II}^\dagger is the creation operator for a photon pair. As can be seen, it is possible to generate two photon pairs, each composed of an idler and a signal photon. Then, three beam splitters in series can be used to generate the W state (see Figure 3.10): one photon at ω_2 is detected after the output port 1 and it heralds the presence of the other three photons in the port 1'. If the coupling power ratio of the three BSs is properly chosen (25%, 33%, and 50%), it is possible to show [256] that the output state is the desired one.

A simple way to verify the nature of the generated state is to measure the threefold coincidence probabilities on channels 2, 3, and 4, which are defined as [253]

$$p_{jjj} = \frac{c_{jjj}}{\sum_{x,y,z} c_{xyz}} \quad j, x, y, z = \omega_1, \omega_2 \quad (3.17)$$

where c_{xyz} is the number of recorded xyz events. The measure of these probabilities would give $p_{\omega_1\omega_1\omega_2} = p_{\omega_1\omega_2\omega_1} = p_{\omega_2\omega_1\omega_1} = 1/3$ and $p = 0$ for the other cases. However, this result can be obtained also with other nonclassical states [253, 260]. Thus, it is possible to measure the threefold detection probabilities on a different basis:

$$\begin{aligned} |C\rangle &= \frac{1}{\sqrt{2}}(|A\rangle + i|B\rangle) \\ |D\rangle &= \frac{1}{\sqrt{2}}(|A\rangle - i|B\rangle) \end{aligned} \quad (3.18)$$

which allows to exclude the possibility that the generated state is not a W state [253].

For polarization encoded entanglement, the use of half-wave plates enables the measures on different basis (horizontal $|H\rangle$ and vertical $|V\rangle$ or left $|L\rangle$ and right $|R\rangle$ circular polarizations). In the energy entanglement, the same transformations can be obtained by the use of modulators [53, 70] and modulating at $(\omega_1 - \omega_2)/2$:

$$\begin{aligned} |+\rangle &= \frac{1}{\sqrt{2}}(|\omega_1\rangle + i|\omega_2\rangle) \\ |-\rangle &= \frac{1}{\sqrt{2}}(|\omega_1\rangle - i|\omega_2\rangle) \end{aligned} \quad (3.19)$$

where the two states can be obtained by applying a π phase shift to the photon at ω_2 . The main problem with this approach is that commercial modulators have low efficiency when operate at frequencies higher than 50 GHz, forcing to work with very big rings with a small FSR [235]. This limit can be overcome by using a structure composed of two coupled resonators (Figure 3.11): two lasers can be placed on resonance with the main resonator at ω_{P_1} and ω_{P_2} to generate photons through dual-pump spontaneous four-wave mixing (d-SFWM) such that

$$\omega_{P_1} + \omega_{P_2} = \omega_1 + \omega_2 \quad (3.20)$$

where ω_1 and ω_2 are the frequencies of two splitted modes of the structure. Then, their difference in frequency could be in the order of tens of GHz, since it is given by the coupling of the two resonators.

The designed device is presented in Figure 3.12. Three MZIs are used as beam splitters, since they have a broader bandwidth with respect to the directional couplers, and are easier to tune. Then, two coupled-rings structures are placed at each input waveguide of the first MZI: this allows to increase the number of devices that can be placed on the mask to find the perfect coupling (between the rings and with the waveguide). In each device the four structures with the coupled rings are labeled from 1 to 4 (see Figure 3.12c). The radii of the four main rings are $R_1 = 30 \mu\text{m}$, $R_2 = 30.3 \mu\text{m}$, $R_3 = 30.6 \mu\text{m}$, and $R_4 = 30.9 \mu\text{m}$. The coupled rings in the upper part of the subdies have radii $r_i = 2R_i/3$ (i.e. $20 \mu\text{m}$, $20.2 \mu\text{m}$, $20.4 \mu\text{m}$, and $20.6 \mu\text{m}$), while in the lower part $r_i = R_i/3$ (i.e. $10 \mu\text{m}$, $10.1 \mu\text{m}$, $10.2 \mu\text{m}$, and $10.3 \mu\text{m}$). Different gaps are used to investigate the different regimes of coupling to the waveguide and between the rings: additional information about the specific parameters used for each device are available here [236]. Finally, these structures are characterized by four output edge couplers; thus, the optical experiment will require the positioning and alignment of five fibers.

3.4.2 Frequency conversion

The coupled resonators in Figure 3.8a have been proposed by Heuck and colleagues with the aim to perform frequency conversion at single-photon level, which

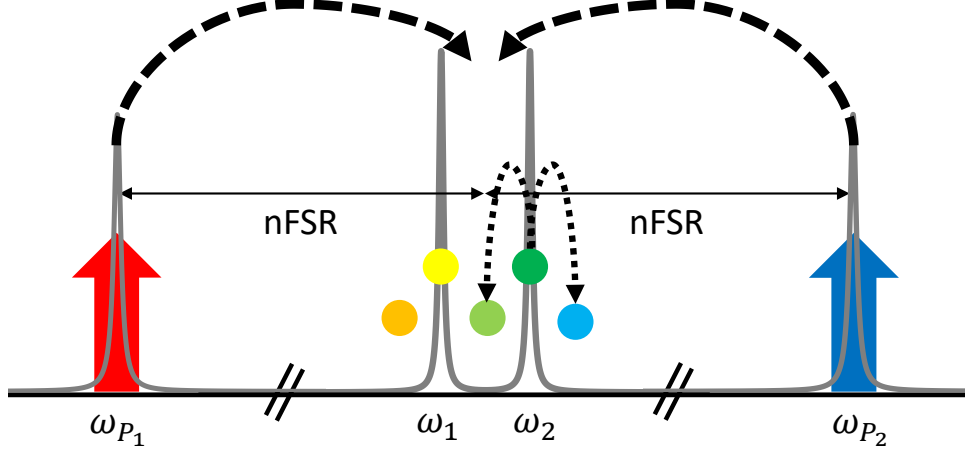
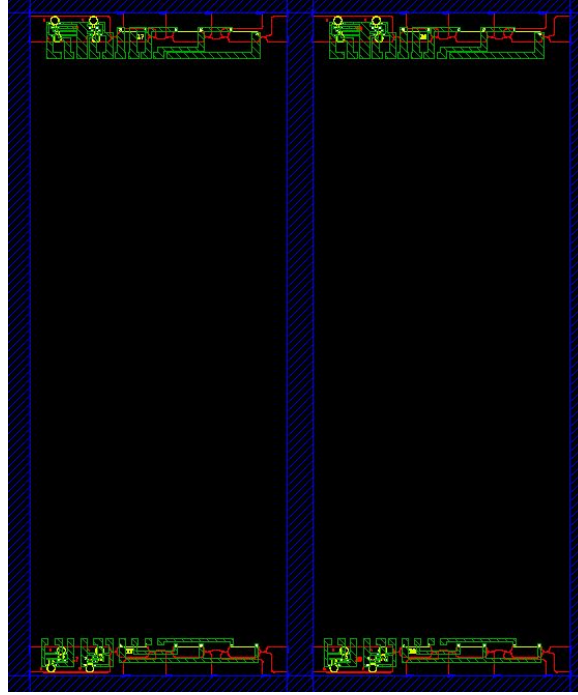


Figure 3.11: Scheme for the generation of W state using coupled resonators.

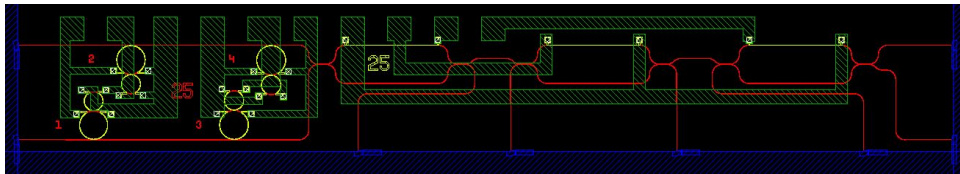
is particularly interesting for quantum applications. In fact, it allows one to match specific spectral channels for multiplexing, as well as to use high-performance detectors in a different spectral region [156]. The idea is to exploit Bragg Scattering FWM (BS-FWM), which involves two laser at frequencies ω_{P_1} and ω_{P_2} and leads to the conversion of one photon at ω_S into an other photon at ω_{I_+} [261, 262]. The phenomenon leads to the suppression of photons at ω_S and ω_{P_1} , and the generation of photons at ω_{I_+} and ω_{P_2} , such that

$$\hbar\omega_S + \hbar\omega_{P_1} = \hbar\omega_{I_+} + \hbar\omega_{P_2} \quad (3.21)$$

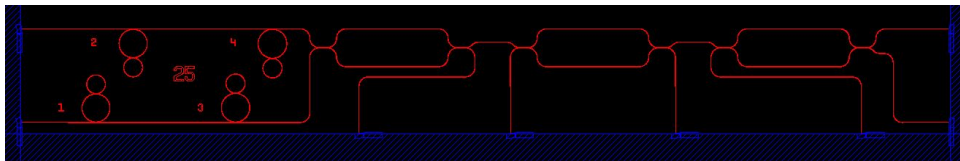
This process has been used to obtain efficient and low-noise frequency conversion at single-photon level in a Si_3N_4 resonator [156], with different kind of conversions: intraband conversion (with $\omega_{I_+}, \omega_S \gg \omega_{P_1}, \omega_{P_2}$), interband downconversion ($\omega_{I_+} \ll \omega_S$) or interband upconversion ($\omega_{I_+} \gg \omega_S$). As one can expect, in the case of intraband conversion (Figure 3.13), single-frequency conversion efficiency is limited by the presence of two possible idler resonances (I_+ and I_-) which satisfy equation (3.21): thus, the maximum efficiency is equal to 50% (while 25% is measured in [156] with 16 mW power per pump). This problem can be tackled by suppressing the conversion at the frequency of one idler resonance, which can be done by properly designing the dispersion of the waveguide such that only one resonance is phase-matched, and this effect is larger if the spectral distance between the two pumps is wider. On the other hand, the solution proposed by Heuck and colleagues [247] involves the adoption of an additional resonator which can split one of the two output resonances, enabling an increase of the efficiency of the process (Figure [247]). The splitting of the resonance at ω_{I_-} inhibits the competing BS-FWM process which



(a) Position in the subdies of the devices for the generation of W states.



(b) Device for the generation of W states.



(c) Device for the generation of W states. Detail of the layer 1 with the silicon waveguides. In each device the four structures with the coupled rings are labeled from 1 to 4.

Figure 3.12: Images of the gds with the devices for the generation of W states.

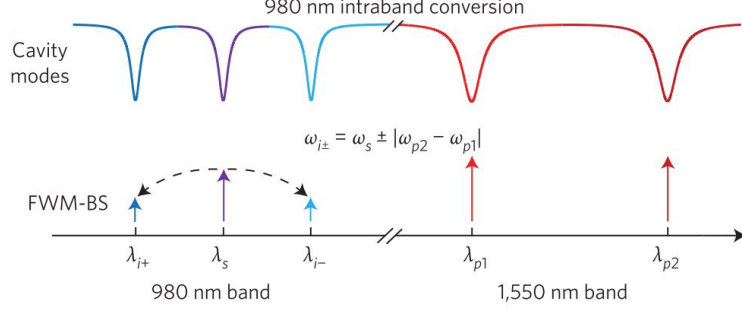


Figure 3.13: Scheme of the intraband conversion efficiency (from [156]).

involves the suppression of photons at ω_{P_2} and at ω_S and the creation of photons at ω_{P_1} and at ω_{I_-} .

However, there are other nonlinear processes that can occur in such a system and could generate photons at ω_{I_+} : in fact, the two lasers at ω_{P_1} and ω_{P_2} could pump SFWM-processes following the energy conservation equations:

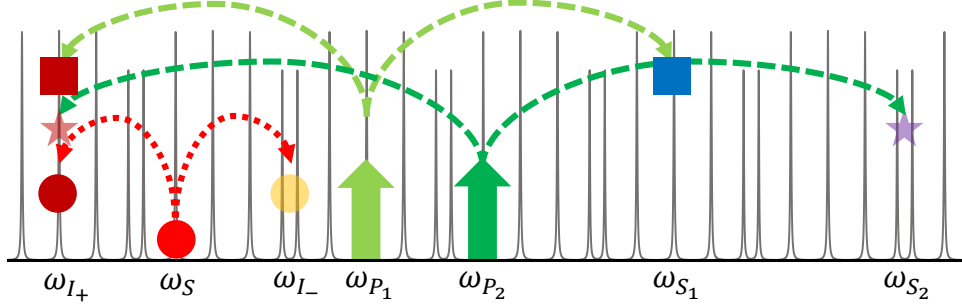
$$\begin{aligned} \hbar\omega_{P_1} + \hbar\omega_{P_1} &\rightarrow \hbar\omega_{I_+} + \hbar\omega_{S_1} \\ \hbar\omega_{P_2} + \hbar\omega_{P_2} &\rightarrow \hbar\omega_{I_+} + \hbar\omega_{S_2} \end{aligned} \quad (3.22)$$

These processes do not reduce the efficiency of the frequency conversion, but can generate photons with the same frequency of the converted ones, increasing the noise of the output state. As can be shown, the process pumped by the laser at ω_{P_2} is automatically suppressed due to the splitting of the resonance at ω_{S_2} given by the second resonator. However, no splitting occurs at ω_{S_1} .

Both the works described above [156, 247] rely on the fact that the BS-FWM pumps are far in frequency from ω_{I_+} . For example, in [156] $\lambda_{P_1} \approx \lambda_{P_2} \approx 1550$ nm, while $\lambda_I \approx \lambda_S \approx 980$ nm. Therefore, it is extremely hard to satisfy the energy-conservation condition for a SFWM process pumped by a 1550-nm laser and generating photons at 980 nm (and at 3700 nm). However, if all the photons are within the same spectral band, one has to carefully control the dispersion of the waveguide not to generate photons at ω_{I_+} due to SFWM.

A possible solution is to exploit the device shown in Figure 3.8b. In fact, the presence of a third resonator allows the splitting of additional resonances. In Figures 3.14b and 3.14c are displayed the schemes for the device with three coupled resonators: as can be observed, the splitting of the resonance at ω_{S_2} allows the suppression of all the SFWM processes pumped by the lasers at ω_{P_1} and ω_{P_2} .

Regarding the efficiency, we can consider BS-FWM process as a sort of st-FWM, where the pumps are the laser at ω_{P_1} and the input photon at ω_S , while the second laser at ω_{P_2} acts as the seed. Thus, we can use an equation similar to (2.57) to



(a) Scheme proposed in [247], with all the photons in the same spectral region.

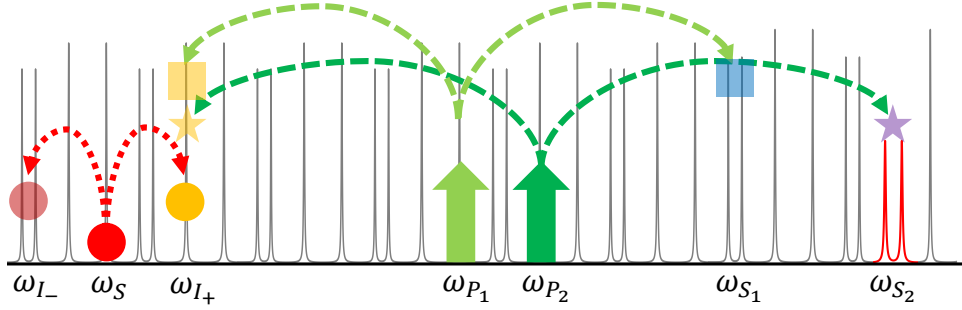
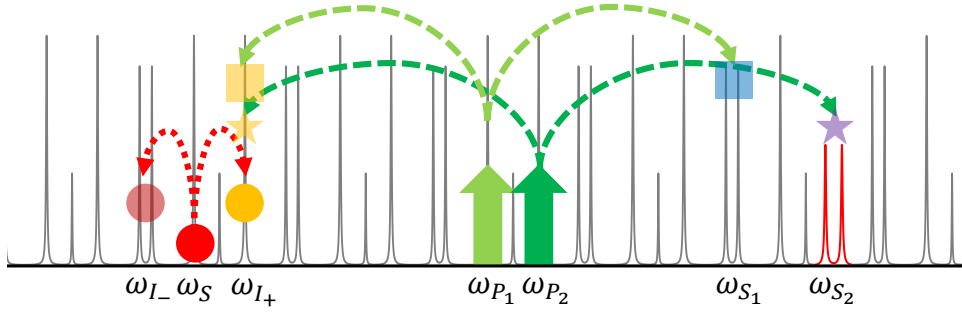
(b) Scheme proposed in this thesis with three coupled rings having radii R_1 , $R_2 = R_1/3$ and R_3 , where R_1 and R_3 are incommensurable. The splitting due to the third resonator is highlighted in red.(c) Scheme proposed in this thesis with three coupled rings having radii R_1 , $R_2 = 2/3 R_1$ and R_3 , where R_1 and R_3 are incommensurable. The splitting due to the third resonator is highlighted in red.

Figure 3.14: Schemes of the processes leading to frequency conversion by using linearly coupled resonators. The dotted lines shows the frequency conversion processes through BS-FWM, while the dashed lines highlight SFWM processes.

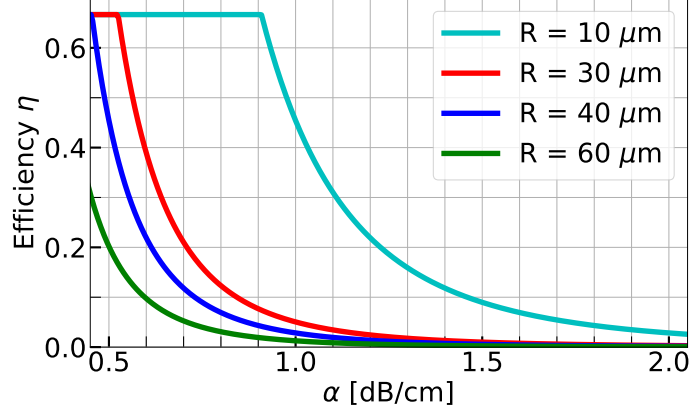


Figure 3.15: Plot of the conversion efficiency through BS-FWM in a critically-coupled ring resonator calculated from equation 3.23 as a function of the propagation losses, with $n_g = 4.05$, $\gamma = 112 \text{ m}^{-1}\text{W}^{-1}$, and $P_p = 0.1 \text{ mW}$

evaluate the efficiency [156]:

$$\eta = (2\gamma P_p L)^2 \text{IE}_P^2 \text{IE}_S \text{IE}_I \quad (3.23)$$

where the additional factor of 2 comes from the use of two non-degenerate pumps. It is important to underline that both equations (2.57) and (3.23) hold with the assumption that the intensity of the pumps does not decrease significantly (undepleted pump approximation), which implies $\eta \ll 1$ in (3.23). In addition, the upper bound limit for η is related to the ratio between the loaded and the intrinsic quality factor. In fact, not all the converted photons are coupled to the waveguide, and the maximum conversion efficiency is given by [156]:

$$\eta_{max} = \frac{1}{1 + Q_L/Q_i} \stackrel{\text{c.c.}}{=} \frac{2}{3} \quad (3.24)$$

In Figure 3.15 equation (3.23) is plotted for different resonators, assuming $n_g = 4.05$, $\gamma = 112 \text{ m}^{-1}\text{W}^{-1}$, and $P_p = 0.1 \text{ mW}$. The resonator is considered in critical coupling, with the intensity enhancement defined from the losses and the length of the ring. We can observe that accessing to low propagation losses leads to a higher efficiency region, where (3.23) is not accurate enough. However, it will be shown in Chapter 5 that reaching such high values for the intensity enhancement is not easy in silicon ring resonators, even with high quality waveguides. In addition, TPA limits the maximum power one can couple to the ring.

In this work, three subdies [(6,3), (6,4), and (7,4) as shown in Figure 3.16a] have been used to investigate the properties of the structure with three coupled rings. The device is presented in Figure 3.16b: on the right the structure with three coupled rings, while on the left two rings are placed to generate the input photons. The idea is to pump one of the two initial rings (radii R_a and R_b) with a third laser at ω_{P_3} and generating photons at ω_S and ω_H . Then, the photon at ω_I is converted and two single-photon detectors can be used to measure the coincidence rate of photons at ω_H and ω_I . Naturally, is crucial that the three-rings structure is resonant at ω_S and not at ω_H : this can be realized by choosing incommensurable values for R_a , R_b , and R_1 . In addition, the relative position of the resonances can be controlled through five thermal phase shifters.

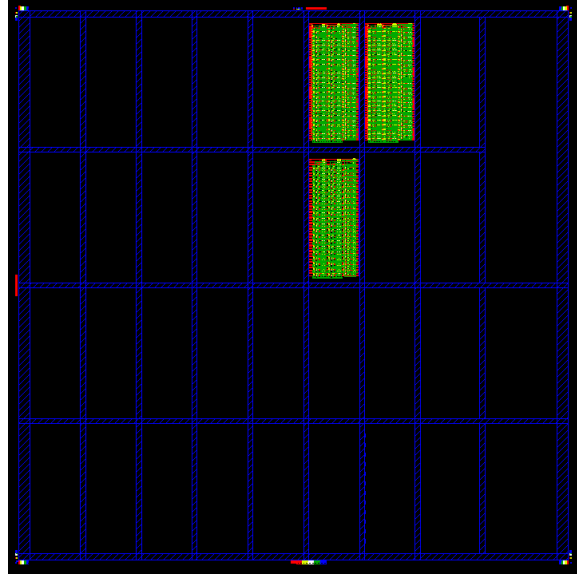
Different values of the radii and the gaps are used to explore different coupling conditions and to have a versatile mask that can be adapted to different values of the propagation losses. The subdie (6,4) has the three coupled rings with radii $R_1 = 30 \text{ }\mu\text{m}$, $R_2 = 10 \text{ }\mu\text{m}$, and $R_3 = 11.3 \text{ }\mu\text{m}$. The gap of the main resonator is spanned over a wide range: from 120 nm to 300 nm with 15-nm steps; the same thing holds for the gap between the three resonators, whose values are equal. R_a and R_b are chosen equal to 29.3 μm and 28 μm , respectively, with gaps equal to 120 nm, 150 nm, and 180 nm for the former resonator, while 210 nm, 240 nm, and 270 nm separate the latter from the waveguide. The other subdies have the same values, with the following exceptions: in (7,4) $R_2 = 20 \text{ }\mu\text{m}$ and $R_3 = 22.6 \text{ }\mu\text{m}$ while in (6,3) $R_1 = 39 \text{ }\mu\text{m}$, $R_2 = 13 \text{ }\mu\text{m}$, and $R_3 = 14.6 \text{ }\mu\text{m}$. Regarding the waveguide width, it is 600 nm for the subdies (6,4) and (7,4), while it is 500 nm for the subdie (6,3).

Finally, the waveguide layer is too dense to place electric pads for all the devices. Then, two different masks for the *vias* and for the *pads* level have been used, as detailed in Table 4.3: thus, not all the device are connected on all the subdies. A full list of the parameters of the devices can be found here [236].

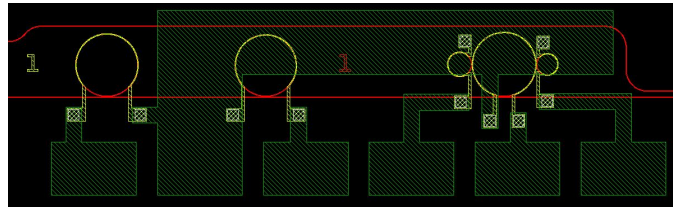
3.5 Linearly uncoupled resonators

In section 3.4 the optical behavior of linearly coupled resonators has been described. The linear coupling leads to the formation of a photonic molecule, with optical modes extended over the entire structure, and it has been shown [57, 246–248] this can lead to interesting advantages in the framework of nonlinear optics.

An alternative concept has been proposed by Menotti and colleagues [263] in which two resonators are coupled only through a nonlinear interaction, although their linear uncoupling. In other words, the system supports only optical modes confined in one resonator or the other, but it is possible to make them interact through the nonlinear interaction. Hence, two independent sets of modes can be obtained, and their relative position can be tuned independently by simple phase shifters.



(a) Location on the mask with the devices for the frequency conversion.



(b) Device for frequency conversion.

Figure 3.16: Images of the gds with the devices for the conversion in frequency through BS-FWM.

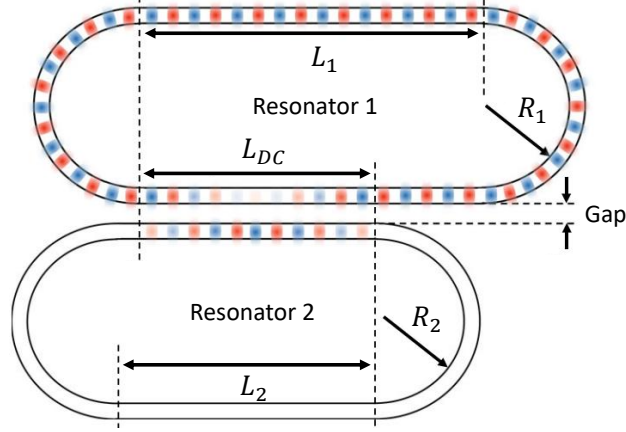


Figure 3.17: Schematic of the structure with the nonlinearly coupled resonators (adapted from FIG. 1 in [263]).

This structure exhibits several advantages with respect to simple resonators. First, it is possible to selectively enhance and suppress the nonlinear processes occurring in the device by changing the spectral alignment of the modes, and this can be exploited to reduce the noise of the generated signal. Furthermore, the dispersion engineering is not critical, since the sets of modes can be tuned independently to compensate fabrication errors as well as spectral shifts dependent on the circulating optical power. Finally, the pump beams can be tuned on resonance with one resonator and generate photons through the nonlinear interaction in the other: thus, an additional rejection of the pump takes place. However, the main drawback is the reduced interaction strength, since the nonlinear interaction takes place in a smaller portion of the resonators, and the overlap of the fields is not maximum.

In the next sections, the mechanism on which is based the device presented in [263] is discussed. Then, alternative structures based on the same concept are described, with the aim to enhance the efficiency of the nonlinear interaction. Some of these structures are tested experimentally: the results are shown in Chapter 6, where some key applications of the devices are detailed.

3.5.1 Directional coupler isolation

The device proposed in [263] (Figure 3.17) is based on two racetracks with different lengths which are located side-by-side forming a directional coupler of length L_{DC} . As it is displayed, the optical modes are confined in just one resonator: in fact, the directional coupler isolates the two racetracks. This is possible by choosing a proper length L_{DC} : if we suppose that the involved waveguides are identical, from

equation 2.31 we get:

$$L_{DC} = \frac{m\pi}{\kappa} - z_b, \quad (3.25)$$

which guarantees $K^2 = 0$ and, thus, the linear uncoupling. The directional coupler is also very important for the nonlinear coupling. In fact, it is the only region where the nonlinear interaction takes place: the modes of the two racetracks both propagate in the DC and their overlap integral is thus different than zero.

To calculate the generation efficiency of the nonlinear processes, we have to estimate the overlap integral $J(\omega_1, \omega_2, \omega_3, \omega_4)$ of the nonlinear interaction [149]. First, we focus on SFWM: we consider a pump laser at ω_P on resonance with one resonator of the structure (Resonator P), and two modes, idler and signal, of the other racetrack (Resonator S) having frequencies ω_S and ω_I such that conservation of energy and momentum are preserved (Figure 3.18). Thus, we can write [263]:

$$J(\omega_S, \omega_I, \omega_P, \omega_P) = \int d\mathbf{r} \Gamma_3^{ijkl}(\mathbf{r}) [D^{i,w_1}(\mathbf{r}, \omega_P) D^{j,w_1}(\mathbf{r}, \omega_P) D^{k,w_2}(\mathbf{r}, \omega_S) D^{l,w_2}(\mathbf{r}, \omega_I)], \quad (3.26)$$

where w_1 and w_2 indicate the waveguides that are coupled to, respectively, Resonator 1 and Resonator 2, while $\mathbf{D}^{w_i}(\mathbf{r}, \omega)$ is the properly normalized asymptotic field at ω entering in the structure from the waveguide w_i [264]. The generated power through SFWM in linearly uncoupled resonators, which is proportional to the second power of the overlap integral, is given by (the full calculations are detailed in [263]):

$$P_I = P_S = \left(\frac{\gamma}{4} L_{DC}\right)^2 (\text{IE}_P)^2 \sqrt{\text{IE}_S \cdot \text{IE}_I} \frac{\hbar\omega c}{2n_g L_S} P_P^2 \stackrel{\text{c.c.}}{\approx} \stackrel{\text{c.c.}}{\approx} \left(\frac{\gamma}{4} L_{DC}\right)^2 \left(\frac{\lambda}{\pi n_g}\right)^3 \frac{\hbar\omega c}{2n_g} \frac{Q_P^2 \sqrt{Q_S Q_I}}{L_P^2 L_S^2} P_P^2 \quad (3.27)$$

From equation (3.27) is clear that one has to find a trade-off between L_{DC} and the resonators' length. In fact, the longer is the directional coupler, the greater is the interaction length; however, this also increases L_S and L_P , with a reduction of the finesse and the intensity enhancement of the racetracks (2.51). Hence, the optimal values turn out to be $L_S \approx L_P = 2(L_{DC} + \pi R)$ and $L_{DC} = \pi R$, where R is the radius of curvature of the bent waveguides in the racetracks. Thus, assuming $Q_P \approx Q_S$, equation (3.27) becomes

$$P_I = P_S \stackrel{\text{c.c.}}{\approx} \frac{1}{256} (\gamma L)^2 \left(\frac{Q \cdot c}{\pi n_g L}\right)^3 \frac{\hbar\omega c}{2n_g L} P_P^2 \quad (3.28)$$

where $L \approx L_S \approx L_P$. One can observe, by comparing (3.28) and (2.63), that the process is less efficient with respect to what occurs in a conventional resonator with

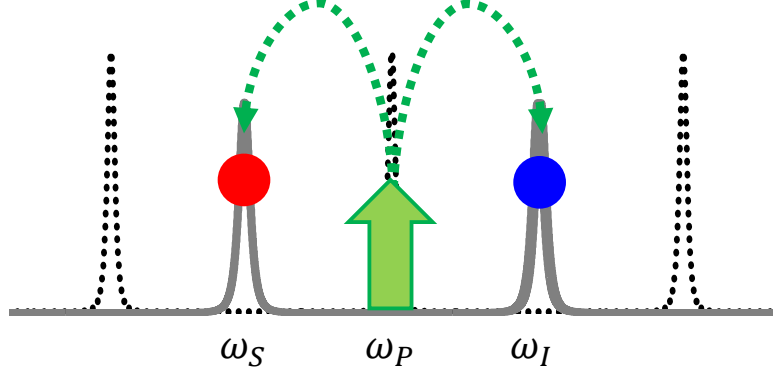


Figure 3.18: Scheme of SFWM with nonlinearly coupled resonators. The grey solid and the black dashed lines show the resonances of, respectively, Resonator S and Resonator P.

length L by a factor 256. From a physical point of view, this is due to the reduction of the interaction length ($L \rightarrow L/4$) and the decreased overlap between the fields in the directional coupler. In fact, as it is shown in Figures 2.11 and 3.17, the fields pass from a waveguide to the other in the DC. Thus, since at $z = 0$ the fields are located in different waveguides, when the pump field is maximum in one waveguide, idler and signal fields are minimum and vice-versa. Then, it is possible to find that the overlap integral of the fields is equal to 0.25 [263] (while it is 1 when the fields propagate in the same waveguide) and the strength of the interaction is reduced by a factor $(1/4)^2$.

Finally, it is clear that also the nonlinear coupled resonators allows one to generate pairs of identical photons at ω_T through d-SFMW. In this case, we can consider two lasers resonant with Resonator 1 at ω_{P_1} and ω_{P_2} generating photons within one resonance of Resonator 2 at $\omega_T = (\omega_{P_1} + \omega_{P_2})/2$, with the generation efficiency given by:

$$P_T = 4 \left(\frac{\gamma}{4} L_{DC} \right)^2 (\text{IE}_T)^2 \sqrt{\text{IE}_{P_1} \cdot \text{IE}_{P_2}} \frac{\hbar \omega c}{2 n_g L_T} P_{P_1} P_{P_2} \stackrel{\text{c.c.}}{\approx} \stackrel{\text{c.c.}}{\approx} 4 \left(\frac{\gamma}{4} L_{DC} \right)^2 \left(\frac{\lambda}{\pi n_g} \right)^3 \frac{\hbar \omega c}{2 n_g} \frac{Q_T^2 \sqrt{Q_{P_1} Q_{P_2}}}{L_P^2 L_T^2} P_{P_1} P_{P_2} \quad (3.29)$$

where L_P and L_T are, respectively, the length of Resonator 1 and Resonator 2.

In this work, linearly uncoupled resonators through a directional coupler have been investigated. The design started from the recognition of the bending radius of the racetrack: since the goal of the fabrication process is to minimize the losses and maximize the quality factor, a radius equal to 30 μm has been chosen. This allows one not to be affected by bending losses (which are negligible for radii greater

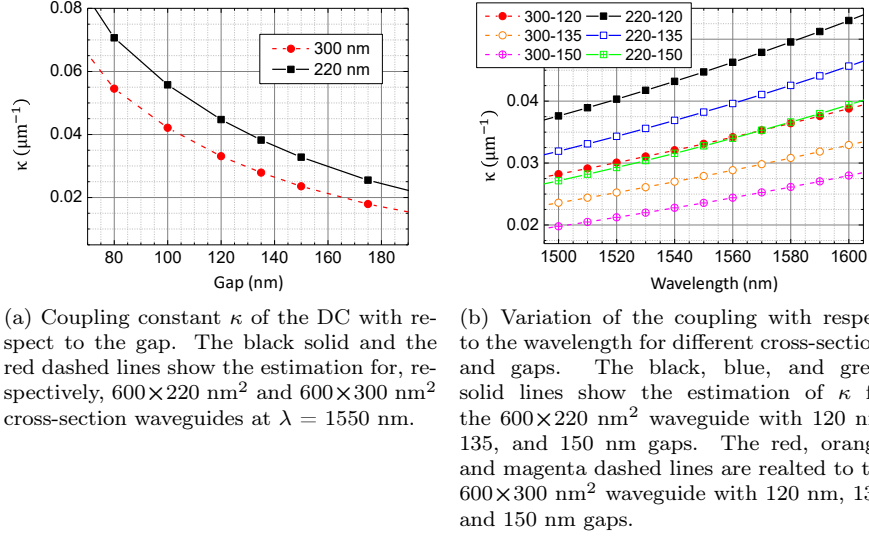


Figure 3.19: Estimation through the EME method of the coupling with different values of the cross-section, the gap, and the wavelength.

than 5-10 μm [265]), but also to fabricate more gentle curves, on which post-etching treatments should work more efficiently.

Then, the value of L_{DC} which maximize the generation efficiency is around 94 μm , and the value of κ that guarantees the linear uncoupling is around $0.033 \mu\text{m}^{-1}$. The coupling with different gaps and wavelengths has been evaluated through the EME method described in section 2.2.2, and the results are shown in Figure 3.19. At $\lambda = 1550 \text{ nm}$, the $600 \times 300 \text{ nm}^2$ waveguide needs a gap around 120 nm, while $600 \times 220 \text{ nm}^2$ has the right coupling with 150-nm gap. Therefore, three different gaps have been designed: 120 nm, 135 nm, and 150 nm. From Figure 3.19b it can be observed that κ is in the range $[0.029, 0.038] \mu\text{m}^{-1}$. Thus, considering z_b between 2 μm and 4 μm , three values of L_{DC} have been chosen: 82 μm , 92 μm , and 102 μm . It is important to take into account that the available experimental set-up and instruments, such as lasers, filters and detectors, allow to choose almost arbitrarily from 1500 nm to 1600 nm, and variation on the coupling can be compensated by slightly changing the portion of the spectral region.

The device is shown in Figure 3.20. The upper racetrack (Resonator 1) has the radius of curvature equal to 30 μm , while the lower (Resonator 2) has a smaller radius (29 μm) to guarantees different FSRs, which is crucial for the experiment described in detail in Chapter 6. One waveguide is coupled to Resonator 2, which can be considered as an all-pass ring with losses given by the coupling with Resonator

1 and the propagation losses. Hence, to guarantee the realization of the critical coupling condition, several values of the gap between the resonator and the coupled waveguide are used (120 nm, 150 nm, 180 nm, 210 nm, 240 nm, and 270 nm). On the other hand, Resonator 1 has two coupled waveguides, as in the add-drop filter configuration. Thus, critical coupling is obtained if the round-trip losses can be neglected with respect to the resonator-waveguides coupling, and two values of the gaps are chosen (120 nm and 160 nm). Finally, some TPSs are placed on the structure: two of them are used to change independently the effective index of the resonators, while two are placed asymmetrically with respect to the directional coupler, allowing a further solution to tune the structure and working with the maximum uncoupling (as explained in section 2.2.4 and shown in Figure 2.18). The distance between the centre of the waveguide in the directional coupler and the centre of the TPS is 0.8 μm , which correspond to $d_0 \approx 1.2 \mu\text{m}$ (following the results of the simulations shown in Figure 2.19). The full list of all the devices with the precise geometrical parameters can be found at [236].

3.5.2 Mach-Zehnder interferometer isolation

The use of the directional coupler is not the only solution to uncouple resonators while keeping the nonlinear coupling. An alternative approach consists in the adoption of a Mach-Zehnder interferometer (described in section 2.2.3). The device is shown in Figure 3.21: the resonators form a MZI which permits their linear uncoupling. Thus, two independent sets of modes can be found, and their spectral position can be controlled independently by some TPSs placed on them (TPS₁ and TPS₂ in Figure 3.21a). In addition, also the coupling between the resonators can be adjusted with an additional phase-shifter (TPS_{MZI}) on one arm of the MZI.

This structure has three advantages with respect to the device with the DC. First, the spectral band in which the resonator are uncoupled is larger. Then, the use of a simple phase shifter on one arm of the MZI allows to control the isolation and to compensate fabrication imperfection. Finally, the generation efficiency turns out to be 4 times bigger.

The optical isolation of the two resonators can be obtained if the cross-coupling power is equal to zero. The simplest way to do that is to use 50:50 beam splitters and to make the radiation entering in the upper input arm of the MZI to interfere destructively in the lower output arm. In this work two DCs are used as beam splitters, as shown in Figure 2.16. Thus, a π phase shift between the two arms of the MZI has to be set, and this can be done by designing the two arms having different lengths, or operating on the phase shifter. From Figure 3.22b is possible to see the different performance of the DC and the MZI: the optical response of the MZI is flatter, allowing the operations over a larger band. This can be easily explained from the power coupling ratios plot in Figure 2.2.2: if the length of the DC is such that the coupling is around 50% ($\kappa \cdot L_{DC} \approx \pi/4$), the optical response is almost flat. However, with larger values of L_{DC} , the frequency dependence of κ leads to

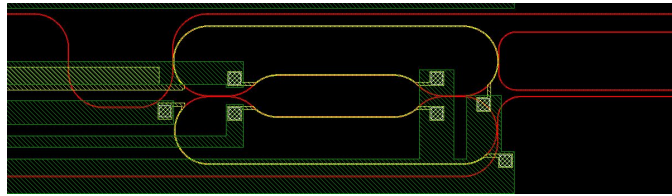
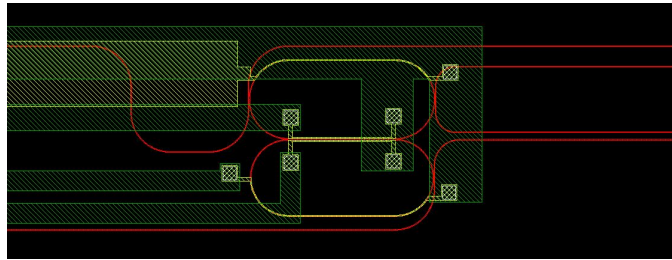
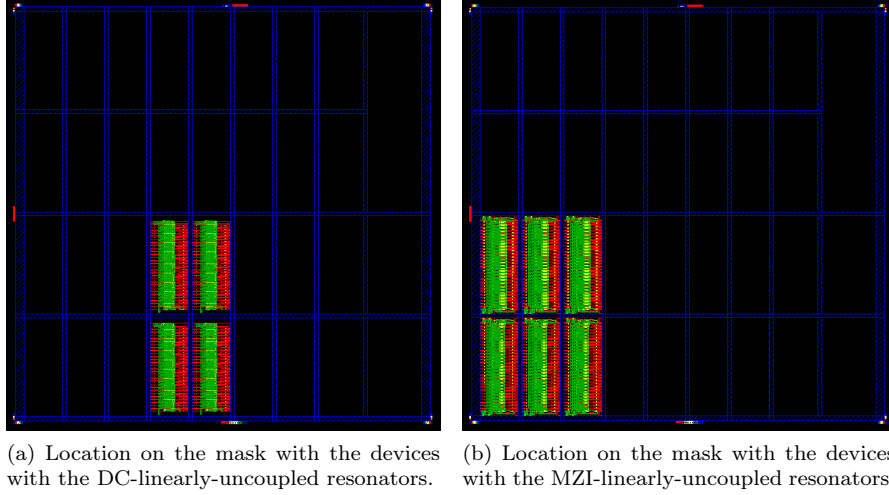


Figure 3.20: Images of the gds with the devices with the linearly uncoupled resonators.

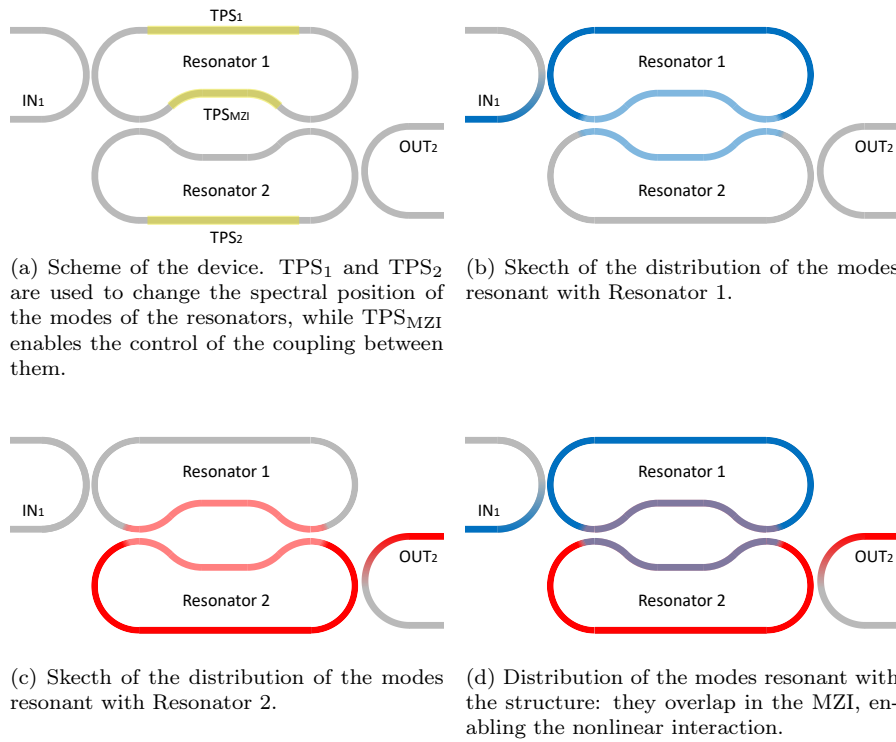


Figure 3.21: Sketches of linearly uncoupled resonators through a MZI.

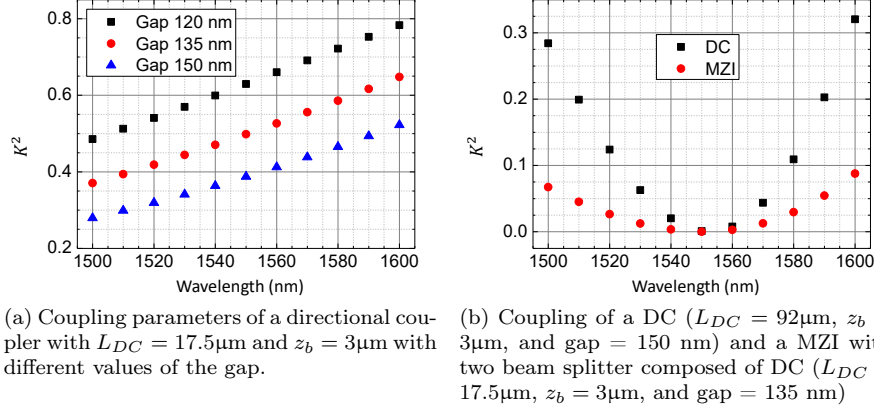


Figure 3.22: Dependence of the coupling of a directional coupler and a Mach-Zehnder interferometer as a function of the operating wavelength.

relevant variation of the coupling with respect to the frequency. Other strategies can be adopted to reduce the dependence on the optical frequency of the isolating device, such as directional coupler with asymmetric-waveguide based phase control sections [183], or curved waveguides [184]. However, the MZI is simpler to design, its optical response can be adjusted more easily in case of fabrication imperfections, and it allows an increase of the efficiency of the nonlinear interaction.

Finally, we can analyze the efficiency of the generation of photons through SFWM. In the previous section it is shown that SFWM can be realized in DC-isolated racetracks, but its efficiency is reduced by a factor 256 with respect to a conventional ring resonator having the same length. In fact, the nonlinear interaction occurs in a quarter of the length of the resonators ($L^2 \rightarrow L_{DC}^2 = (L/4)^2 = L^2/16$), and the interacting fields are not perfectly overlapped ($\gamma^2 \rightarrow (\gamma/4)^2 = \gamma/16$). In the device with the MZI, the fields overlap and the nonlinear interaction occurs in the arms of the interferometers, as shown in Figure 3.21d. The generation length which maximize the interaction is still a quarter of the total length of the resonators, but the overlap of the fields is maximum. However, there is still a penalty: in fact, the 50:50 beam splitters reduce the fields in each arm of the MZI by a factor $1/\sqrt{2}$.

Thus, the overlap integral in equation (3.5.1) becomes

$$\begin{aligned}
 J(\omega_S, \omega_I, \omega_P, \omega_P) &= 2 \int d\mathbf{r} \Gamma_3^{ijkl}(\mathbf{r}) \left[\frac{D^{i,w_1}(\mathbf{r}, \omega_P)}{\sqrt{(2)}} \frac{D^{j,w_1}(\mathbf{r}, \omega_P)}{\sqrt{(2)}} \right. \\
 &\quad \left. \frac{D^{k,w_2}(\mathbf{r}, \omega_S)}{\sqrt{(2)}} \frac{D^{l,w_2}(\mathbf{r}, \omega_I)}{\sqrt{(2)}} \right] = \\
 &= \frac{1}{2} \frac{L_{MZ}}{L} J_{\text{ring}}(\omega_S, \omega_I, \omega_P, \omega_P) \approx \\
 &\approx \frac{1}{8} J_{\text{ring}}(\omega_S, \omega_I, \omega_P, \omega_P)
 \end{aligned} \tag{3.30}$$

where the factor two before the first integral takes into account that the generation occurs on both the arms of the MZI. Since the strength of the interaction is proportional to the overlap integral to the second power, the process turns out to be 64 times less efficient with respect to conventional resonator, but 4 times more efficient with respect to DC-uncoupled resonators.

The designed devices are placed in six subdies, as shown in Figure 3.20b. The radii are chosen equal to 30 μm for Resonator 1 and 29 μm for Resonator 2. Resonator 1 has two coupled waveguides (as can be observed in Figure 3.20d) to guarantee the critical coupling condition. The length of the DCs acting as beam splitters is chosen equal to 17.5 μm , while the gap can be 120 nm, 135 nm, or 150 nm. The arms of the MZIs have a 100- μm (or 200- μm) long straight part, and their length is around 194 μm (or 294- μm); in addition, a small difference of length dl is added to guarantee the isolation even without acting on the phase shifter. Thus, the total length of the resonators is around 635 μm (or around 835 μm). Finally, the gaps between Resonator 1 and the coupled waveguides are 120 nm or 160 nm, while the waveguide coupled to Resonator 2 is placed at a distance equal to 120 nm, 140 nm, 160 nm, 180 nm, 200 nm, or 220 nm. A full list of the devices with their characteristics is available at [236].

3.5.3 Pump recycling

Another strategy can be embraced to realize a device based on the nonlinear coupling of linearly uncoupled modes which has a higher generation efficiency. In the previous sections, it is shown that both the DC and the MZI versions are affected by a reduction of the efficiency since the nonlinear interaction occurs in approximately a quarter of the length of the resonators. However, we could think about the addition of a third resonator placed on the other side of Resonator 2. The devices are shown in Figures 3.23c and 3.23d: one of the waveguides coupled to Resonator 1 is coupled to a third resonator (Resonator 3). Since Resonator 1 is in the Add-Drop configuration, the pump laser(s) resonant with it passes to the output waveguide and the light can be recycled and injected to another identical resonator. In this way, it is possible to exploit also the other side of the Resonator 2, and the generation efficiency is

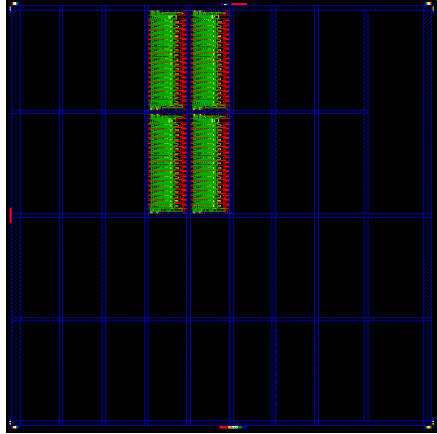
improved by a factor of 4, since we have two identical regions (the directional coupler and the Mach-Zehnder interferometer) in series that generate photon pairs through SFWM. In fact, it can be shown that if the coherence length of the laser is long enough, the power generated through SFWM by P_I sources in series is equal to $N^2 P_I$, where P_I is the power generated in the single element [238]. Naturally, the phase difference of the pump in the two regions where the nonlinear interaction takes place has to be carefully controlled: then, an additional phase shifter is placed on the waveguide connecting Resonators 1 and 3.

In Figure 3.23a the regions of the chip with the DC-linearly-uncoupled devices with pump recycling are highlighted. Naturally, Resonator 3 is identical to Resonator 1, since the aim is to replicate the same nonlinear interaction with Resonator 2. As for the simpler version, the radii are chosen equal to 30 μm for Resonator 1 (and 3) and 29.3 μm for Resonator 2. The gaps between Resonator 1 (and 3) and the coupled waveguides are chosen to find the critical coupling condition: 120 nm, 150 nm, and 180 nm. The gaps between Resonator 2 and the coupled waveguide are 120 nm, 140 nm, 160 nm, 180 nm, 200 nm, 220 nm, 240 nm, and 260 nm: in fact, different coupling conditions can be investigated and used depending on the applications. The gap of the directional coupler is equal to 120 nm or 150 nm, while its length can be 82 μm , 92 μm , or 102 μm .

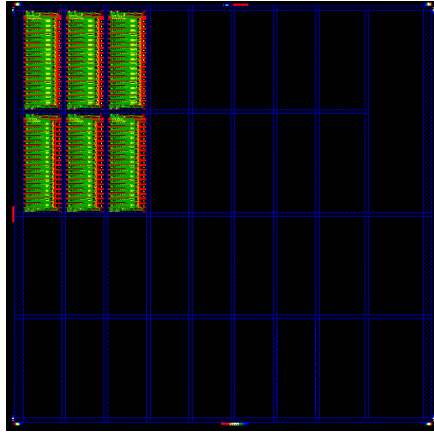
On the other hand, the MZI-based devices with pump-recycling are placed as shown in Figure 3.23b. The radii are 30 μm for Resonator 1 and 3, and 29 μm for Resonator 2. The gaps between Resonator 1 (and 3) and coupled waveguides are 120 nm, 140 nm, 160 nm, with the aim of reaching the critical coupling, while the waveguide coupled to Resonator 2 is spaced by 120 nm, 140 nm, 160 nm, 180 nm, 200 nm, or 220 nm. The length of the DCs acting as beam splitters is chosen equal to 17.5 μm , while the gap can be 120 nm, 135 nm, and 150 nm. The arms of the MZIs have a 100- μm (or 200- μm) long straight part, and their length is around 100 μm (or 200- μm); in addition, a small difference of length dl is added to guarantee the isolation even without acting on the phase shifter. Thus, the total length of the resonators is around 635 μm (or around 835 μm). A full list of the devices with their characteristics is available at [236].

3.6 Integrated bragg filters

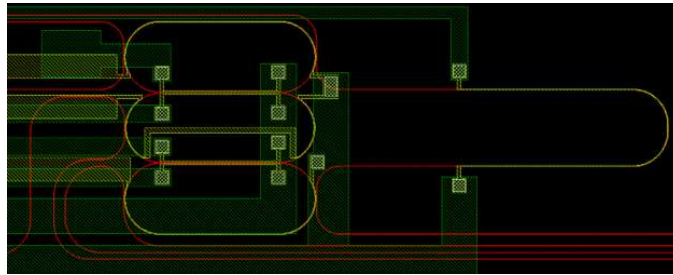
The final goal of the research conducted in academic and industrial institutions about integrated optical sources of nonclassical states of light is, as one can expect, the realization of a fully integrated device which allows to generate photon-states that can be processed on the chip or coupled to fiber networks. A clear advantage of working with silicon-based integrated quantum photonics is the possibility of exploit the results of more than twenty years of research on the fabrication process, and on the development of devices, initially developed for telecommunications systems [80], with which photons can be generated and manipulated, such as integrated



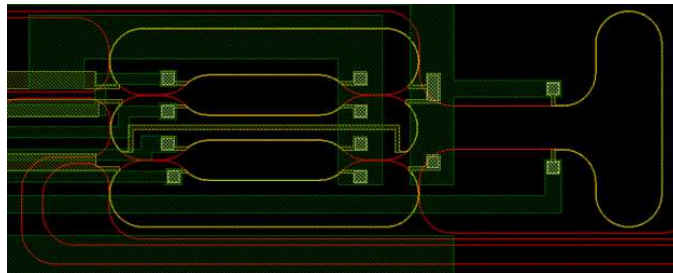
(a) Location on the mask with the devices with the DC-linearly-uncoupled resonators with pump recycling.



(b) Location on the mask with the devices with the MZI-linearly-uncoupled resonators with pump recycling.



(c) Device with the DC-linearly-uncoupled resonators with pump recycling.



(d) Device with the MZI-linearly-uncoupled resonators with pump recycling.

Figure 3.23: Images of the gds with the devices with the linearly uncoupled resonators.

lasers [59, 266], resonant structures [131, 243], optical filters [191, 267], multiplexers [268, 269], modulators [62, 190] and detectors [270, 271]. However, there are two key components that can't be found *on the shelf*, since are very specific of quantum photonics: integrated single-photon detectors [66–68] and high-extinction-ratio optical filters.

Since the generation of photons based on nonlinear optical process involves the presence of a (usually) intense pump lasers, it is crucial to suppress the input beam not to destroy the quality of the generated nonclassical states with spurious photons. Typically, lasers with power from 100 μW to 10 mW are used, which lead to the generation of photon fluxes with power from 1 pW to 1 nW , as one can observe from (2.16) and (2.63). Thus, filters with around 90-100 dB of extinction ratio (ER) are needed to effectively suppress the pump [50].

Among the investigated approaches, three of them allowed the reach of high level of extinction.

In 2013, Ong and colleagues proposed a device based on several coupled resonators [272] that allows one to increase the ER on resonance. The coupling of five devices allowed them to demonstrate 50 dB of attenuation, while 100 dB of filtering were obtained by connecting two devices in series. This approach has been recently used in [240], where the authors used two different chips with a reduced number of coupled rings (4+4), obtaining around 110 dB of ER. The proposed method, however, was demonstrated to work only with the use of two separate chips. In addition, it requires relevant efforts in the spectral tuning of the microring resonators: this can be realized and could be even managed by programmable circuits [81], but it adds some complexity to the circuit.

An alternative method was proposed later by Piekarek and colleagues [186], in which they used several Mach-Zehnder interferometers in series. In particular, they measured around 100 dB of ER by using two chips (with 6 and 4 cascaded Mach-Zehnder). This approach has the same problems that use of microrings: on-chip total suppression was not demonstrated and the phase on the MZIs' arms must be controlled very precisely.

A third solution is represented by Bragg gratings, in which the effective index of the waveguide is periodically changed leading to the formation of a photonic band-gap. Typically, the variation is induced by the modulation of the sidewalls of the waveguides: the idea is to induce a gentle perturbation not to increase the scattering losses. However, since the variation of the index is very weak, these structures must be very long (some millimetres), and their behavior is based on the regularity of the structure, which is hard to maintain for such long paths. With this approach, 65 dB of filtering on single chip and >100 dB with two chips have been demonstrated [63]. Recently, an innovative approach proved that short cascaded Bragg gratings can be designed: in fact, conventional gratings cannot be placed in series, since they would create Fabry-Perot cavities due to the back-reflection of the resonant radiation, and their phase control is essential. However, the device proposed in [273] leads to the

Device	Stages	ER	Chips	Cladding
CROW [272]	5+5	100	2	No
Bragg [63]	1+1	>100	2	No
MZI [186]	6+4	100	2	Yes
CROW [240]	4+4	110	2	Yes
Incoherent Bragg [225]	9	>80	1	No

Table 3.2: Comparison between the integrated high-ER filters presented in literature to realize the suppression of the pump used to generate photon-pairs through SFWM.

coupling of the resonant light to higher order modes, which are not supported by the waveguides before and after the filters. At least 80 dB of ER were proven, and this allowed them to detect photon-pairs generated through SFWM by adding two band-pass filter (20 dB of ER) tuned on the resonances within photons are generated [225]. This system is promising, since the external filters can be easily replaced by on-chip de-multiplexers. However, they proved a very high ER without the use of the cladding, which is very important for the realization of a reliable device.

In this work, some Bragg gratings are designed. They are based on the use of lateral pillars [274], as shown in Figure 3.24: the variation of the effective index is not due to a change of the width of the waveguide, but small structures are placed near the main waveguide, inducing a small variation of the effective index. This approach has been proposed in the framework of narrow-line integrated lasers [59], since it allows to fabricate integrated narrow mirrors (which require extinction ratios around 30 dB).

The advantage with respect to the sidewall modulation is that the perturbation is realized by bigger features, which are less sensitive to fabrication imperfections. This approach is also compatible with post-etching treatments, such as hydrogen annealing, which smoothen the sidewalls of the waveguides [116]; in addition, pillars should be more regular after the annealing [82].

The transmission, the bandwidth, and the resonant frequency of the device in Figure 3.24 can be roughly estimated through the multilayer model [91]. If we consider a variation Δn of the effective index of the waveguide n_0 , we can determine the length of the period by the $\lambda/4$ condition

$$\Lambda \approx \frac{\lambda}{4n_0} \quad (3.31)$$

where λ is the resonant frequency. Thus, the attenuation with N periods is given by

$$T = 4 \left(\frac{n_0}{n_0 + \Delta n} \right)^{2N} \approx 4 \left(1 - \frac{\Delta n}{n_0} \right)^{2N} \quad (3.32)$$

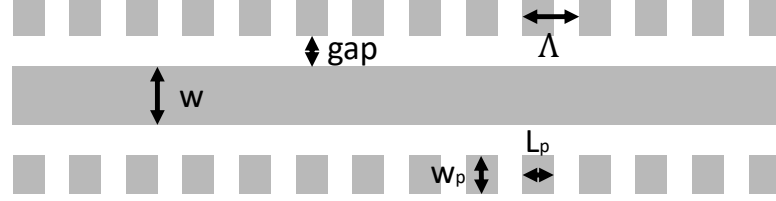
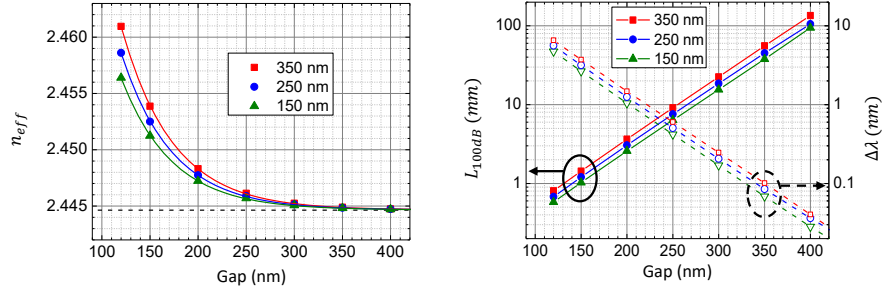


Figure 3.24: Scheme of the Bragg grating based on the presence of pillars near the waveguide.



(a) Effective index of the waveguide with the pillars. Three values of w_p are shown. The solid lines show the exponential fits, while the dashed black line shows the value of $n_0=2.44464$.

(b) Bandwidth and length of the bragg grating to obtain a suppression of around 100 dB.

Figure 3.25: FDE simulations of the waveguide with pillars.

and the bandwidth is given by

$$\frac{\Delta\lambda}{\lambda} \approx \frac{2}{\pi} \frac{\Delta n}{n_0} \quad (3.33)$$

where Δn is supposed much lower than n_0 .

To evaluate the variation of the index Δn , several FDE simulations have been performed with different values of the gap and of the width of the pillars, where a cross-section equal to $500 \times 220 \text{ nm}^2$ has been considered. The results are shown in Figure 3.25: as can be seen, the effective index depends on the gap g between the pillars and the waveguide with an exponential relation:

$$n_{eff} = Ae^{-g/\Gamma} + n_0 \quad (3.34)$$

In Figure 3.25b the bandwidth (3.33) and the needed length to reach around 100

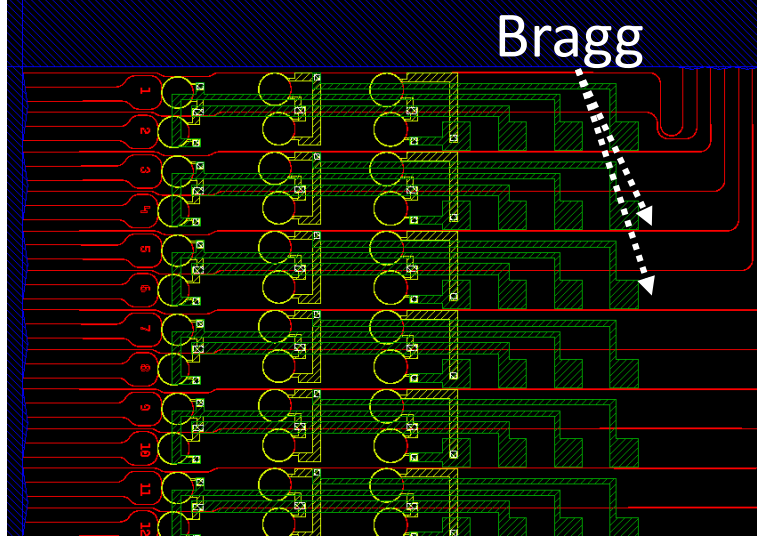


Figure 3.26: Area on the mask with bragg gratings and rings coupled to the same waveguide.

dB of attenuation are estimated. In fact, from (3.31) and (3.32) we get

$$T \approx 10^{-10} \Rightarrow L_{100} = N_{100} \cdot \Lambda \approx \frac{\log(4) + 10}{2\log(1 + \Delta n/n_0)} \frac{\lambda}{4n_0} \quad (3.35)$$

The Bragg gratings are designed in the subdies (9,1), (9,2), and (9,3). Different values of gratings' parameters have been used: in fact, the goal is to test the impact of the used fabrication technology on the filtering performance.

The subdie (9,1) includes structures with $N = 800$ ($L \approx 0.25mm$) and $N = 6400$ ($L \approx 2mm$). The period Λ is set equal to 153 nm, 158 nm, and 163 nm. The widths of the pillars are equal to 150 nm, 200 nm, 250 nm, 350 nm, 400 nm, and 450 nm, while the gaps are equal to 120 nm, 140 nm, 160 nm, 180 nm, 210 nm, 240 nm, and 270 nm.

The subdies (9,2) and (9,3) have Bragg gratings with the same values for gaps and widths of the (9,1): structures with $N = 1600$ ($L \approx 0.5mm$) and $N = 3200$ ($L \approx 1mm$) are placed on the (9,2), while the subdie (9,3) includes gratings with $N = 9600$ ($L \approx 3mm$), $N = 3200$ ($L \approx 4mm$), and $N \approx 30000$ ($L \approx 9mm$).

Before the filters, three rings are placed (one add-drop and two single-pass, as shown in Figure 3.26) to generate photons and test the performance of the gratings. Their radii are 28 μm , 29 μm , and 30 μm with gaps between 120 nm and 270 nm. A full list of the devices with their characteristics is available here [236].

3.7 Additional test structures

In this final section, I will briefly describe additional structures designed and realized on the chip that are meant to test the performances of the basic building blocks of the fabricated devices.

3.7.1 Microring resonators

As can be observed, microring resonators have a fundamental role in this work, since many devices are based on them. In addition, as discussed in section 2.3, their optical response allows one to estimate some parameters of the optical waveguide. Thus, several simple microring resonators are included in the chip in the subdie (6,2), and are divided into 8 groups. Each group includes rings with the same radius, and the gap is changed to investigate the different regimes of coupling, following the results on the simulations described in the Section 2.3.3.

The first group, starting from the top, is composed of rings having $117.2\text{ }\mu\text{m}$ of radius, which is chosen to obtain a FSR around 100 GHz, while the gaps are 120 nm, 150 nm, 180 nm, 210 nm, 240 nm.

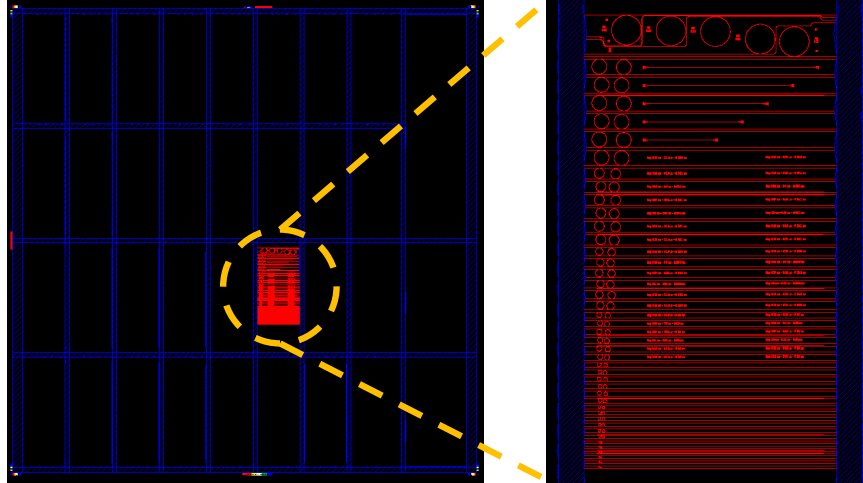
Then, the other three groups comprehend rings with radii equal to $58.6\text{ }\mu\text{m}$, $39.1\text{ }\mu\text{m}$, and $29.3\text{ }\mu\text{m}$ to get FSR around 200 GHz, 300 GHz, and 400 GHz. The number of device per group is higher, since for each value of the radius the gap spans from 120 nm to 300 nm, with 20-nm steps. On top of each group there are two additional rings with equal gap (180 nm) placed to test the capability of the fabrication process to realize identical resonators at short distance. Thus, there are twelve rings per radius.

Moreover, other 4 groups have been places, with radii equal to $20\text{ }\mu\text{m}$, $15\text{ }\mu\text{m}$, $10\text{ }\mu\text{m}$, and $5\text{ }\mu\text{m}$ to test the properties of smaller devices. The gaps span from 120 nm to 300 nm, with 20-nm steps.

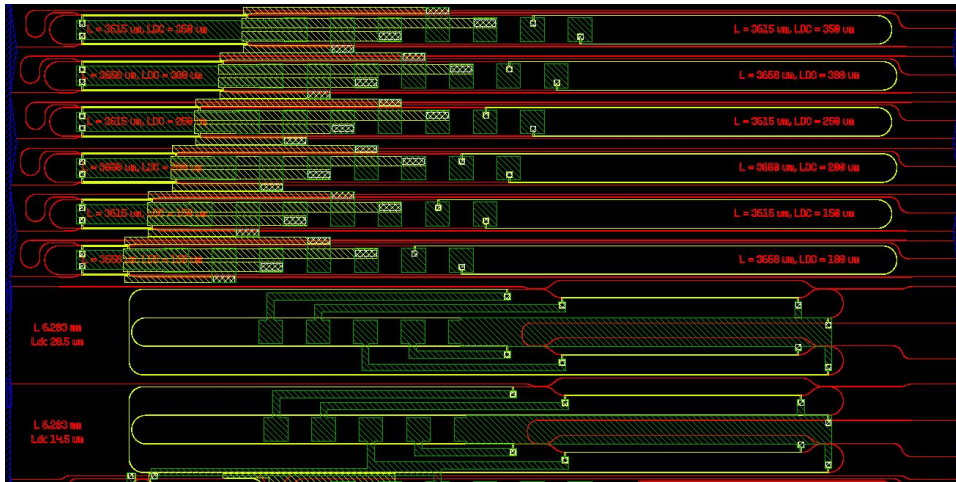
Finally, two other kinds of resonators (Figure 3.27b) are included in the subdie (7,2). They have a total length approximately equal to 3.66 mm and 6.28 mm (effective radii 0.58 mm and 1 mm). As can be seen, they are mainly composed of straight waveguides, while the bent parts have a radius of curvature equal to $30\text{ }\mu\text{m}$: the goal is to minimize the bends to see if the annealing is more effective on these devices with respect to conventional full-bent ring resonators. The device are coupled to two waveguides by using tunable DCs and MZs, which allows one to control the coupled power.

3.7.2 Edge Couplers

Some test structures have been placed on the mask (see Figure 3.28). The first test is focused on the distance between adjacent edge couplers, which is set to be equal to $20\text{ }\mu\text{m}$ in all the structures. Six pairs of straight waveguides are placed with different values of the distance ($5\text{ }\mu\text{m}$, $10\text{ }\mu\text{m}$, $15\text{ }\mu\text{m}$, $20\text{ }\mu\text{m}$, $25\text{ }\mu\text{m}$, and $30\text{ }\mu\text{m}$).



(a) Ring resonators on the mask.



(b) Longer resonators with tunable couplers.

Figure 3.27: Images of the gds with the devices with the microring resonators.

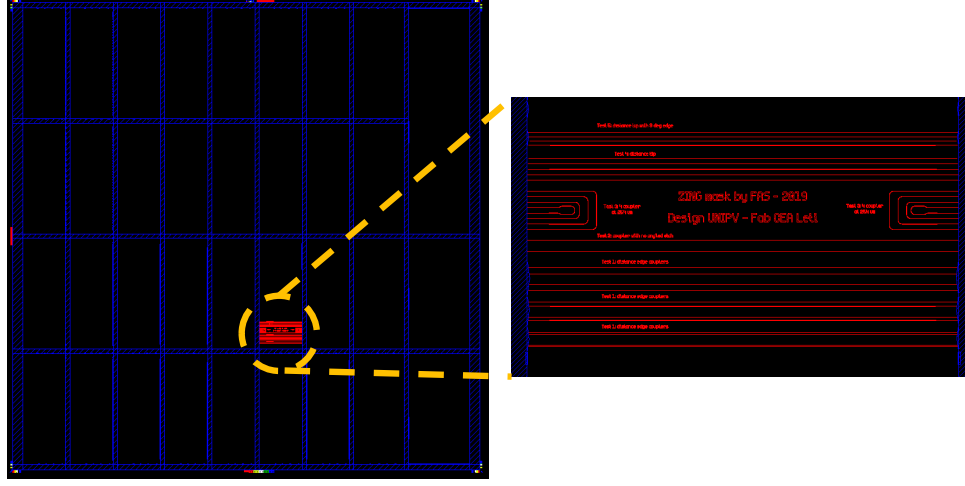


Figure 3.28: Structures on the mask to test different versions of edge couplers.

The second test is to evaluate the impact of the tilted faced: thus, two waveguides are placed in front of a perpendicular facet (with $1\text{ }\mu\text{m}$ of oxide gap). Finally, two other groups of waveguides are designed to test the impact of the oxide gap. One group is realized with the tilted facet (gaps $1\text{ }\mu\text{m}$, $3\text{ }\mu\text{m}$, $5\text{ }\mu\text{m}$, and $7\text{ }\mu\text{m}$) and another one with the perpendicular facet (gaps $0.5\text{ }\mu\text{m}$, $1\text{ }\mu\text{m}$, $3\text{ }\mu\text{m}$, $5\text{ }\mu\text{m}$

Chapter 4

Fabrication of Silicon Photonic Integrated Circuits

In this chapter, the fabrication process followed for the production of silicon integrated optical circuits is detailed. The fabrication was realized in the CEA-Leti's cleanroom at MINATEC Micro-nano technologies innovation center (Grenoble) during my visiting period there of six months there. I was in charge of the supervision of the fabrication run as process integration engineer, including the definition and the organization of the technological steps to be performed. I followed the realization of all the steps, and I performed morphological tests (e.g. inspections with optical and electronic microscopes), as well as characterization of devices, to test the functionality of the chips. 22 wafers have been used to try different conditions in the fabrication steps (resumed in Table 4.3 at the end of the chapter).

4.1 Silicon Optical Waveguides

The main part of the fabrication process is the patterning and encapsulation of silicon waveguides used to build the Photonic Integrated Circuits (PIC). In this section the main steps used to produce silicon waveguides with low edge roughness are described: in fact, the roughness of the lateral sidewalls of the waveguides is the main source of losses in integrated waveguides, as discussed in section 2.1.3. After the etching of the waveguides, an annealing treatment is realized to reduce the roughness and, therefore, the losses due to the scattering [116]. The main steps are represented in Figure 4.16.

The starting point is a 200-mm (8 inches) Silicon On Insulator (SOI) wafer. This kind of wafer is composed by a substrate of crystalline silicon, a layer of silica (Buried Oxide Layer BOX) and a second thin layer of crystalline silicon, which is patterned to obtain the optical circuits. There are several methods to fabricate SOI

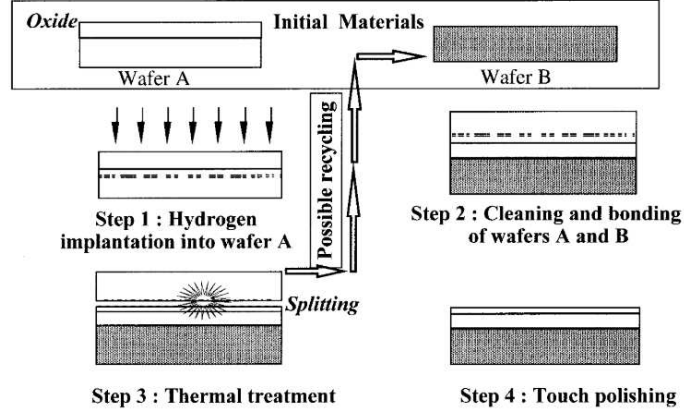


Figure 4.1: Principle of the Smart-Cut process. Image from [276].

wafers, which can be divided into three categories (more details can be found in the review [275]):

- ion implantation, which consists in the implantation of oxide and annealing to create the buried SiO_2 layer;
- wafer bonding, which implies the bondage of two externally-oxidized silicon wafers;
- seed methods, where silicon is grown on the surface.

One of the most used method is the SmartCutTM, a SOITEC bonding and cutting proprietary technology. A crystalline silicon wafer (produced with Czochralski crystal growth) is treated with a thermal oxidation process to create the BOX (wafer A in Figure 4.1), and it is bonded with another silicon wafer (wafer B). Then, H_2 implantation is performed to create a layer of defects in the wafer B, which allows one to cut it by applying thermal or mechanical stress. Then, a Chemical Mechanical Polishing (CMP) touch is performed to smoothen the surface. SOI wafers produced with this method have a high degree of thickness uniformity, a good crystal quality, and a precise control of the SiO_2 and upper Si layer [276].

Since the designed mask includes optical structures for both 220-nm and 300-nm thick Si waveguides, we used two different kinds of wafers. The former is a 200-mm SOI prime wafer with 220 nm of crystalline silicon (100) and 2000 nm, while the latter has a 340-nm silicon layer. To obtain 300-nm thick Si, we performed a thermal oxidation of 40 nm of Si with a mixture of O_2 and HCl at 1050°C (35 minutes). The use of HCl speeds up the process and guarantees a lower contamination of the wafers, since metal impurities form volatile compounds with chlorine [277]. The

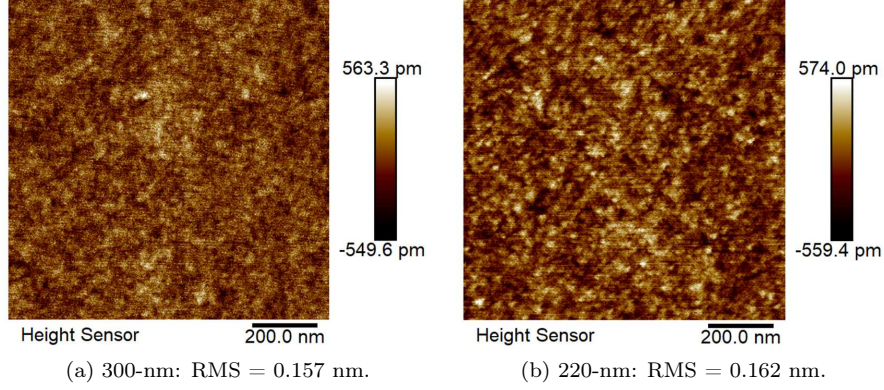


Figure 4.2: AFM scan of 300-nm and 220-nm silicon surface.

target thickness of the oxidized layer can be calculated from the ratio of the atomic and molecular density of Si and SiO_2 [278]:

$$T_{\text{SiO}_2} = \frac{\rho_{\text{Si}}}{\rho_{\text{SiO}_2}} T_{\text{Si}} = \frac{5.0 \cdot 10^{22} \text{ cm}^{-3}}{2.35 \cdot 10^{22} \text{ cm}^{-3}} \cdot 40 \text{ nm} \approx 2.12 \cdot 40 \text{ nm} \approx 85 \text{ nm} \quad (4.1)$$

Ellipsometric measures have been performed on the wafer to control the thickness of SiO_2 and they gave $85.0 \pm 0.2 \text{ nm}$. Then, a wet etching (HF solution) was performed to remove the oxide layer. Atomic Force Microscopy (AFM) measures have been performed on both 220-nm and 300-nm wafers to estimate the roughness of the surface: Root Mean Square (RMS) is equal to 0.157 nm for the latter, while for the former RMS is equal to 0.162 nm (Figure 4.2).

4.1.1 Optical Lithography

The lithographic patterning of the structures is probably the most important step in semiconductor technology, since it allows one to transfer the design of the PICs to the wafer. Basically, it consists in the impression of a resist layer deposited on the wafer to transfer the structures of the design. In fact, a successive etching process is performed on the wafer, and only those parts that are protected by the resist are not removed.

The patterning of the resist is performed by irradiating the wafer with a source of electromagnetic radiation (UV, extreme UV or X-ray) or a beam of electrons. If the resist is “positive”, only the portions to be removed are exposed, since the irradiation softens the resist and allows one to remove it with a solvent (called “developer”). On the other hand, a “negative” resist is hardened by the exposition. In our process, we used UV lithography with positive resist and quartz-chrome masks with the pattern

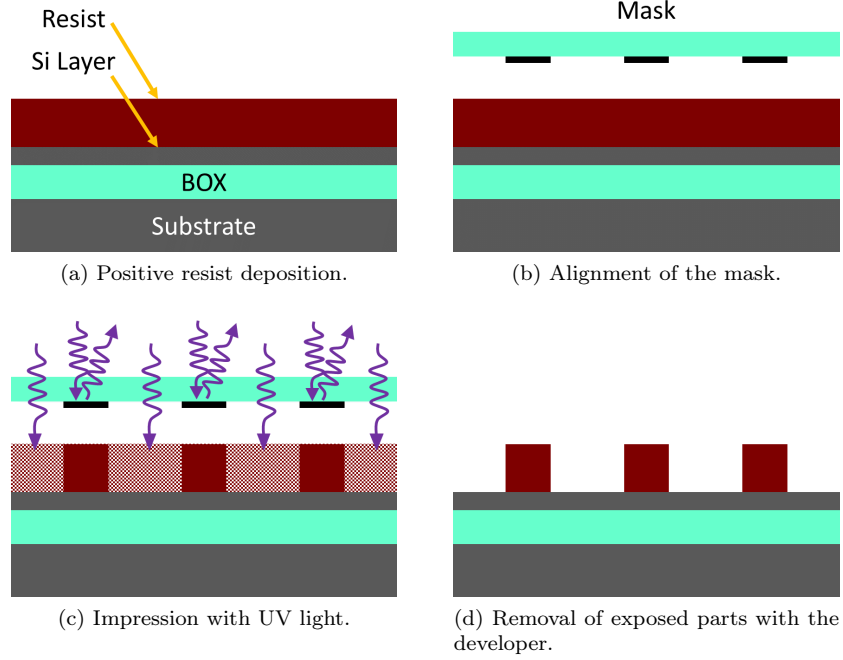


Figure 4.3: Representation of the lithographic process for the silicon layer.

on it (see figure 4.3). The masks have been realized starting from the designed gds (described in the previous chapter), whose layers have been treated: in fact, the structures must be fragmented to obtain simple shapes (squares and triangles) that can be exposed by the electron beam used to fabricate the lithographic masks [279, 280].

The choice of the lithographic process depends on the characteristics of the device and the final applications. They can be described through the following four parameters [277].

- Resolution, i.e. the minimum feature size that can be impressed on the resist. It depends on the wavelength of the source, on the exposition technique and on the resist. Rayleigh's criterion can be used to express the limit of the resolution:

$$W_{min} \approx k_1 \cdot \frac{\lambda}{NA} \quad (4.2)$$

where k_1 depends on the capability of the resist to distinguish between small changes in intensity, while λ and NA are the wavelength and the numerical

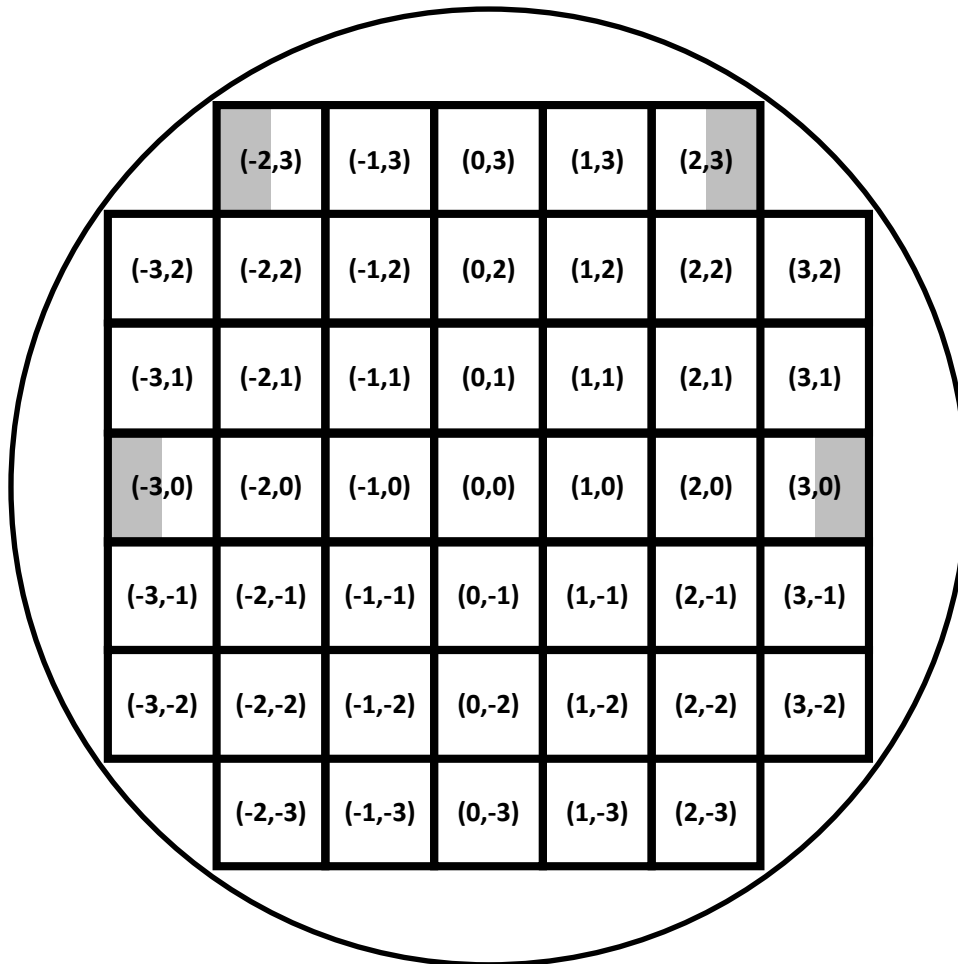


Figure 4.4: Wafer division into 45 dies, since we chose not to expose the borders of the wafer. In addition, the grey area are not expose, because of the presence of the PM markers (figure 4.5).

aperture of the projective system. It's worth to mention that the simplest lithographic methods involving a single chromium mask and a single layer of resist do not allow one to obtain a value of k_1 lower than 0.75. However, the use of resolution enhancement techniques lower k_1 , which is today close to the theoretical limit of 0.25 [281].

- Accuracy, i.e. the correspondence between designed and patterned features, which can be adjusted by varying lithographic parameters such as the focus of the beam and its optical intensity.
- Alignment between different layers of the fabrication process.
- Productivity, i.e. the number of wafers that can be realized in a fixed amount of time.

The lithographic process used to pattern the silicon layer is a 193-nm deep ultraviolet (DUV) lithography (ArF laser source). This system is one of the most used in semiconductor technology, since it allows to have a good resolution (up to 120 nm), and a reasonable productivity and cost. The resolution can be increased by using immersion lithography (which increases the NA), or Extreme UV (EUV) lithography (which reduces the wavelength); however, the equipment and the masks for these approaches are 10-100 times more expensive.

The lithographic process started with the deposition, on top of the thin silicon layer of the wafers, of a 82-nm thick bottom anti-reflective coating (BARC). The use of the BARC is important to reduce the formation of standing waves in the resist layer, which are detrimental for the definition of the pattern. Then we deposited 400 nm of a positive-tone resist for 193-nm lithography (JSR 1682), whose thickness is chosen by taking into account the selectivity of the etching with respect to the resist (i.e. the ratio between the etching rate of the material to be patterned and of the resist), which is typically between 1 and 2. Thus, we put a 100-nm thicker resist with respect to the thickest silicon layer in order to be sure we had enough resist budget. The exposure was realized with an ASM1100 stepper from ASML and using a quartz-chrome photomask produced by Toppan. The typical resolution with this kind of system is around 100 nm. In fact, the numerical aperture of the stepper is around 0.75, while k_1 in (4.2) is around 0.4. We set the process such that only complete dies ($22 \times 22 \text{ mm}^2$) were exposed (see the scheme in Figure 4.4). Then, 45 full dies were realized on the 200-mm wafer. However, some dies were truncated because of the positioning of the primary marks (PM, figure 4.5). These marks are patterned before all the other lithographic steps, since the stepper must use them to realize a general alignment [282], whose tolerance is $\pm 125 \text{ nm}$ (3σ) [283].

A very important part of the lithographic step is the definition of the optical parameters, such as the dose and the focus. We decided to fix the focus equal to zero and we tried a different dose on several wafers. Then, we analyzed the patterns

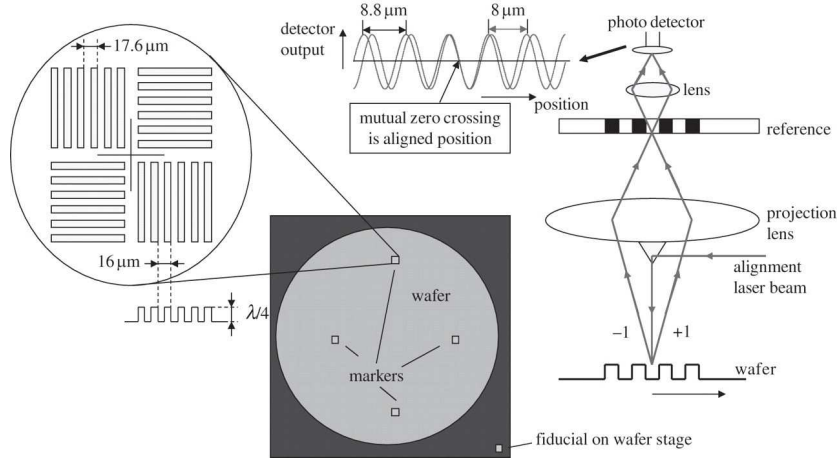


Figure 4.5: The alignment marks are diffraction gratings with a different periodicity to increase the capture range. One way to measure the markers is shown at the right, where both first orders are imaged on a reference grating and their interference is detected by a sensor. This configuration allows one to align the mask with an error lower than $\pm 125\ \text{nm}$ (3σ). (Image from [282])

and the critical dimensions through a scanning electron microscope (CD-SEM analysis) to establish which dose to use. In fact, the right value of the dose can change depending on the opening area of the mask (i.e. how much space is not protected by the mask) and the dimensions of the structures we want to fabricate. In our case, the most critical parameter is the gap of $120\ \text{nm}$ between waveguides in directional couplers and microring resonators coupled to waveguides. In the Table 4.1 there are the values we measured for different doses: there are several observations that can be done.

First of all, we were able to target the right dose. In fact, doses lower than $25\ \text{mJ}/\text{cm}^2$ are too weak to open the gaps of the directional couplers (DCs), and in particular $26.5\ \text{mJ}/\text{cm}^2$ allowed us to get closest values with respect to the design. In addition, it is clear that the design of the directional couplers should be corrected by a bias, in order to get the same width on DCs and on isolated waveguides. This is due to the fact that the two coupled waveguides protect themselves, and the effective dose that acts on them is lower than in the case of an isolated structure (and this effect is as stronger as smaller is the gap).

Regarding the different gaps, it seems clear that it is difficult to open properly gaps lower than $150\ \text{nm}$. In a new version of the mask, one should use only bigger gaps (for example $150\ \text{nm}$) and change the length of the coupling instead that the distance between coupled waveguides.

Dose mJ/cm ²	DC 120 nm		DC 135 nm		DC 150 nm		Isol. WG
	Width	Gap	Width	Gap	Width	Gap	Width
Nominal	600	120	600	135	600	150	600
22,5	closed		633	77	623	116	609
23,5	closed		631	75	632	114	608
24,5	closed		625	100	618	133	606
25,5	634	72	616	110	610	143	597
26,5	616	93	604	127	596	158	589
26,5	619	85	604	123	596	152	587
26,5	625	87	612	119	604	150	596

Table 4.1: Table with the measures of widths and gaps of directional couplers in the die (0,-1) for different doses (wafers). All the values are expressed in nm and the error on all the measures is ± 10 nm.

Dose mJ/cm ²	DC 120 nm		DC 135 nm		DC 150 nm		Isol. WG
	Width	Gap	Width	Gap	Width	Gap	Width
Nominal	600	120	600	135	600	150	600
22,5	closed		634	76	630	117	612
23,5	closed		628	94	625	125	607
24,5	632	66	621	107	614	137	602
25,5	630	73	617	110	608	142	594
26,5	620	85	604	123	598	154	589
26,5	622	80	608	120	597	156	589
26,5	620	87	607	124	600	153	588

Table 4.2: Table with the measures of widths and gaps of directional couplers in the die (-3,-2) for different doses (wafers). All the values are expressed in nm and the error on all the measures is ± 10 nm.

Finally, one can see how the measures on wafers with the same dose are similar, as well as the the uniformity within the wafer, as it is possible to see by comparing Table 4.1 and Table 4.2.

After the SEM analysis, we recycled the wafers with the wrong dose and we performed a second lithography varying the dose between 25.5 mJ/cm² and 27.5 mJ/cm² (as detailed in Table 4.3).

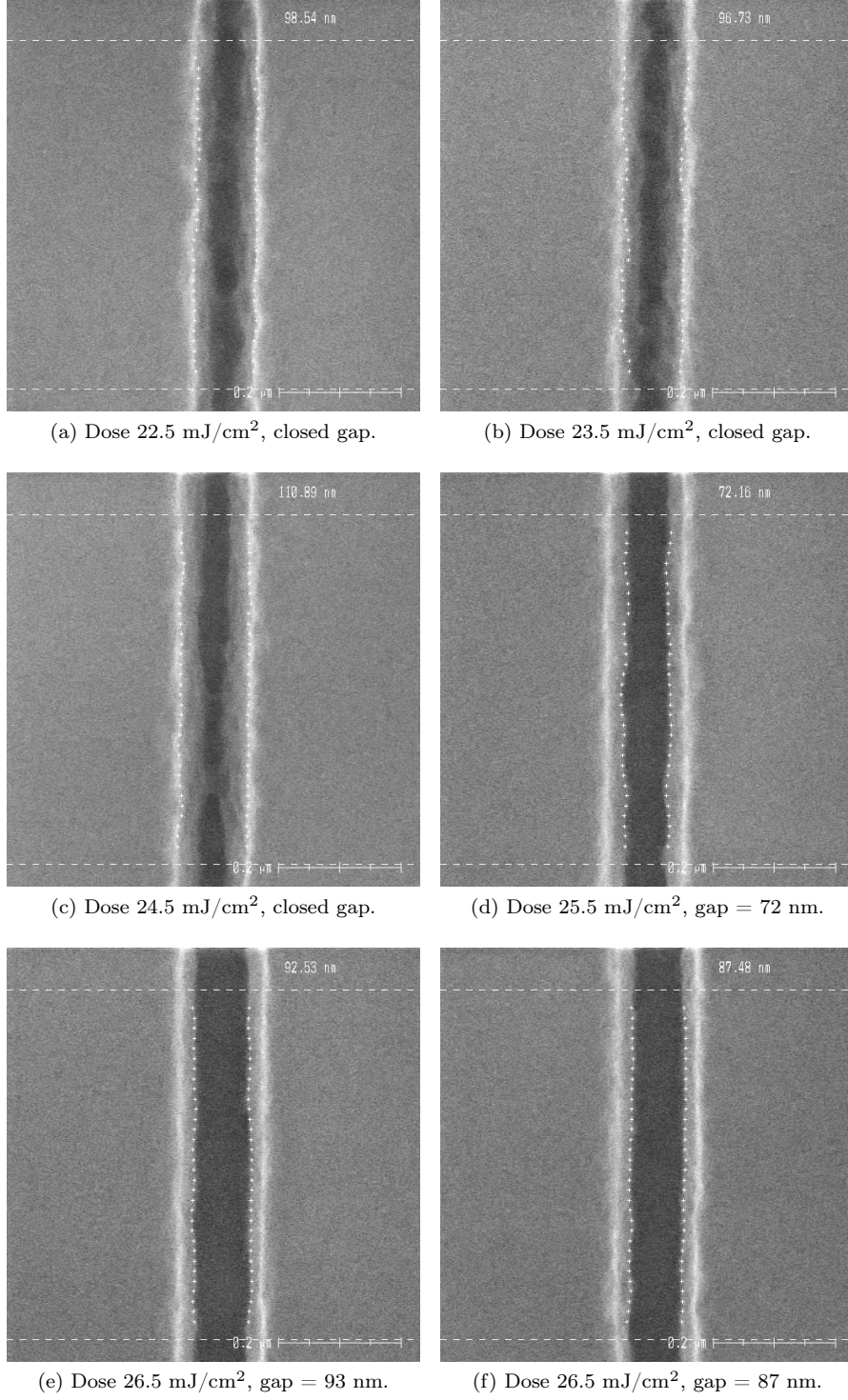
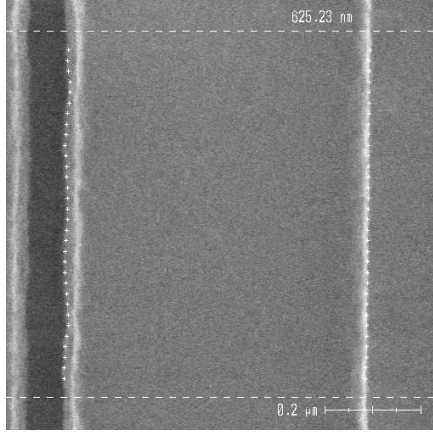
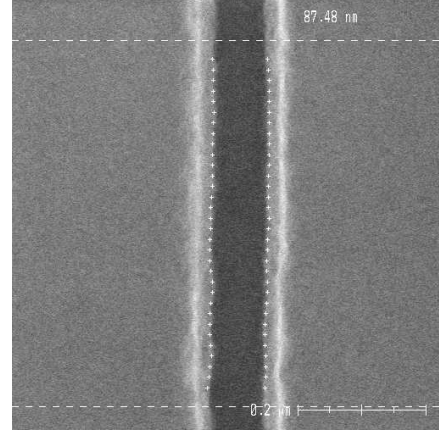


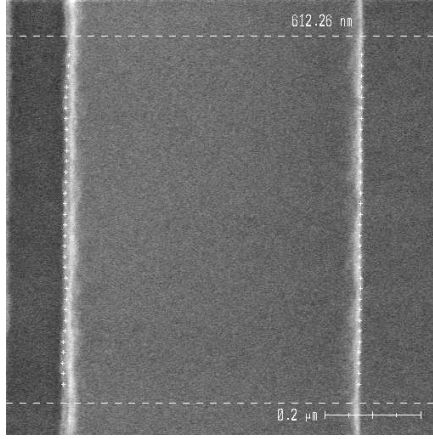
Figure 4.6: SEM images (300 V, 10 pA, field size 675×675 nm²) of the resist of the directional couplers' gaps for different doses. The nominal value is 120 nm.



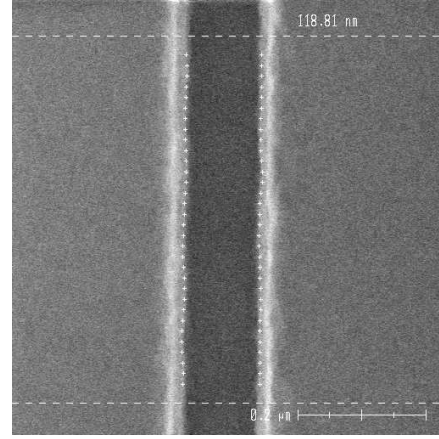
(a) Width = 625 nm (600 nm).



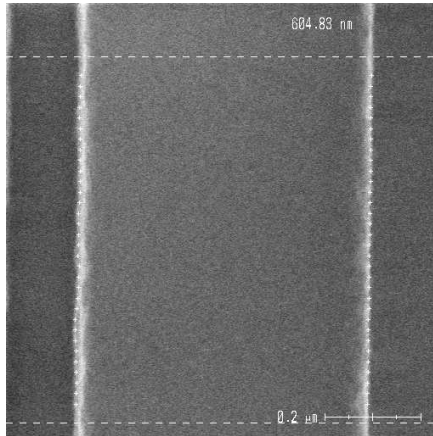
(b) Gap = 87 nm (120 nm).



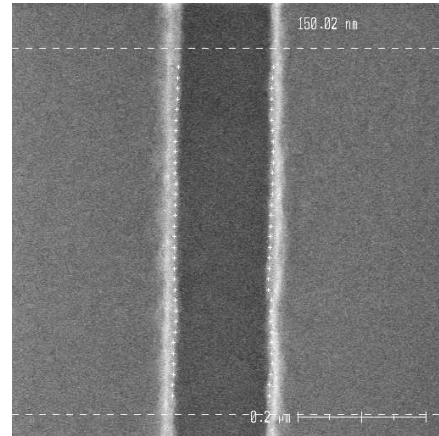
(c) Width = 612 nm (600 nm).



(d) Gap = 119 nm (135 nm).



(e) Width = 604 nm (600 nm).



(f) Gap = 150 nm (150 nm).

Figure 4.7: SEM images (300 V, 10 pA) of the resist of the directional couplers' widths (field size $900 \times 900 \text{ nm}^2$) and gaps ($675 \times 675 \text{ nm}^2$) with 26.5 mJ/cm^2 . Nominal values in brackets.

4.1.2 Etching

The following step is the etching of silicon to create the waveguides, which was realized in collaboration with LTM (Laboratoire des technologies de la microélectronique). As already anticipated, the etching consists in the use of chemical and/or physical removal of layers from the wafer, which attack only those portions that are not covered by the resist. Etching processes can be isotropic or anisotropic depending on the ratio of the etching rates in the different directions [277].

The etching of silicon waveguides has been realized with an inductively coupled plasma (ICP), which allows one to realize anisotropic etching. It was performed in a ICP source reactor (Centura 5200 by Applied Materials), which is equipped with 2 RF generators (working at 13.56 MHz). A simplified scheme can be seen in Figure 4.8.

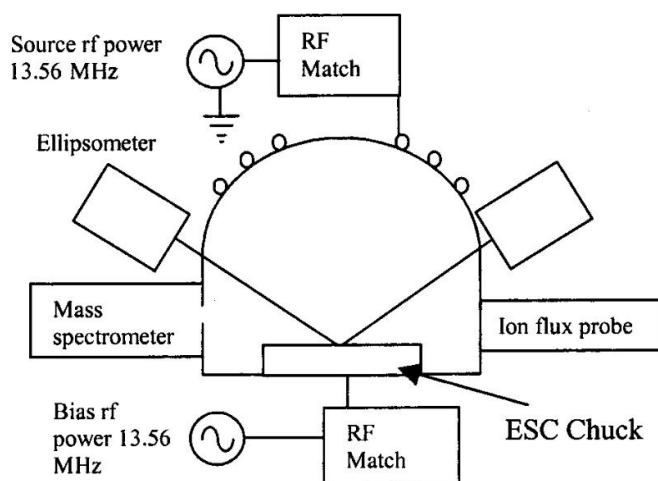


Figure 4.8: Scheme of the ICP reactor (Image [284]).

1. The “source” generator is coupled to an antenna located at the top of the chamber, which creates an electromagnetic field that accelerates the free electrons presents in the chamber. These currents of electrons interact with the gas molecules, leading to the formation of ions, radicals, UV radiation and all the species contained in a plasma. Therefore, the plasma is inductively coupled to the source generator, whose electrical power can drive ionization and dissociation processes.
2. The second generator (“bias”) is connected to a bottom electrode on which the substrate lies (“Electrostatic Chuck” (ESC) in figure 4.8). The plasma is

capacitively coupled to the bias, which drives the ions energy by accelerating them.

The specificity of a ICP reactor, compared to Capacitively Coupled Plasma (CCP) which has only one capacitative generator, is the possibility to control the ion energy thanks to the bias power independently from the ion flux (driven by the source power).

The etching procedure is composed by several passages. First, we cleaned the chamber: a SiO_2 wafer is etched with SF_6 and O_2 to create a covering layer on the walls of the reactor. This allows to protect the SOI wafers from impurities that could be present inside the chamber.

Then, we placed the SOI wafer and we etched the BARC with a plasma formed by a mixture of argon, chlorine and oxygen. In fact, the development of the resist does not remove the BARC from the areas that must be etched. Since the opening area is very high (98.7%), it is possible to monitor the process by using Optical Emission Spectroscopy (OES) or Interferometric Endpoint (IEP) detection systems [285] [286]. In fact, the composition of the plasma changes during the etching, and it is possible to detect the different compounds by analysing the emitted electromagnetic radiation through a spectrometer (OES) or by measuring the interferometric pattern made by a laser beam passing through the chamber (IEP).

The typical etching time of the BARC was 22 s (including the main etching and additional two or three seconds of overetch). At this point, however, the silicon layer is not exposed yet: in fact, it is very well known that silicon surfaces exposed to oxygen leads to the formation of a native oxide layer (around 2 nm). Then, it is important to remove this layer (*breakthrough* step), and this is done with a CF_4 plasma etching for 4 seconds.

Once the silicon is uncovered, the main etch can start. We used a plasma composed by HBr , Cl_2 (the reactive gases), He and O_2 . This kind of plasma is widely used in semiconductor technologies, and there are many physical phenomena involved during the etching of silicon [284] and the interaction between plasma and resist [287], which depend on gas fluxes, pressure of the chamber and voltages of source and bias generators.

The horizontal surfaces are bombarded by radicals and ions generated by Cl and Br , which are accelerated by the bias. Chlorine is very reactive with silicon, which leads to high etching rates and, consequently, a lower impact on the sidewalls and higher productivity. However, a too fast etching does not give very smooth sidewalls; in addition, chlorine's selectivity on SiO_2 is not very high, which can lead to a partial etching of the BOX. Hence, bromine is added, since it is less reactive with Si and more selective on SiO_2 , and the etching mechanisms depend on the synergy of the chemical species produced by both the gases.

When the plasma starts to etch the silicon layer, it is possible to observe the generation of a lot of volatile products [284], like SiCl_4 and SiBr_4 , and less volatile products, like SiCl_x and SiBr_x , which are ejected in the plasma gas phase and play

a important role in the etching of vertical surfaces. In fact, the sidewalls of resist and silicon waveguides can react with plasma due to the presence of isotropic radicals that can etch or deposit depending on their chemical reactivity; in particular, Cl and Br radicals are very reactive with these surfaces and they can lead to a lateral etching. SiCl_x and SiBr_x products redeposit on the surfaces and create a passivation layer, which is however not enough resistant to protect the sidewalls against Cl and Br radicals. Thus, O_2 is added to the gas to oxides the deposited products and form a passivation $\text{SiO}_x\text{Cl}_y\text{Br}_z$ layer on the sidewalls of silicon and resist. Nevertheless, if the thickness of this layer (strictly related on O_2 concentration) is too high, it can created big slopes in the Si patterned profiles. Thus, we used a mixture of He (3.4 sccm) and O_2 (1.7 sccm) in order to have a stable gas flow (possible with at least 5 sccm) and a low concentration of oxygen. More details can be found in [288], [289], and [290].

The etching time was around 102 ± 2 s for the 220-nm wafers, while it was 141 ± 1 s for the 300-nm wafers. These values are calculated from the etching times of the 22 wafers measured through the IEP method.

The stripping (i.e. the removal of the resist and etching residuals), was made with O_2 plasma, which removes the resist on top of the waveguides. This step is mainly isotropic, but the presence of oxygen leads to the formation of a nanometric layer of SiO_2 around the waveguides, and the selectivity of the etching of the resist with respect to silicon dioxide is very high. After the O_2 stripping, we performed a wet etching using HF (1% diluted for 10 s) to remove all the polymeric residuals that can be generated during the plasma etching (as shown in Figure 4.9).

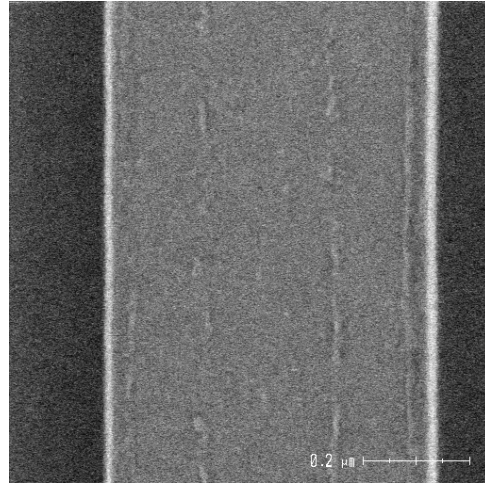


Figure 4.9: SEM image of the etched waveguide in which the traces after the etching and the O_2 stripping are visible.

4.1.3 H₂ Annealing

Once the waveguides are defined, we decided to apply an hydrogen annealing process, since it was recently showed it reduces the roughness of the waveguides and, thus, the scattering optical losses [116].

The annealing is preceded by a cleaning treatment (RCA clean) to remove the impurities that can be present on the wafer [291]. It starts with the immersion in a solution of water, ammonia (NH₃) and hydrogen peroxide (H₂O₂), which removes organic particles and creates a thin oxide layer. Then, oxide is removed by a wet etching in HF solution (1% for 15 s), and finally the wafer is immersed in an aqueous solution of hydrochloric acid (HCl) and H₂O₂ to remove metallic contaminants.

The annealing is realized in a high-density plasma reactor (Centura 5200 reactor by Applied Materials), and we performed two different treatments:

- 5 minutes at 40 Torr (0.053 atm) at 850°C;
- 1 minute at 20 Torr (0.026 atm) at 850°C.

These conditions were the most promising on the basis of morphological tests realized on previous fabrication runs. Without entering into the details of the process, the basic idea is to reach a crystalline re-organization of the atoms on the surface of the waveguides, and this is possible only if the plasma's conditions guarantees a significant mobility of the atoms. Regarding the temperature, it must be below the melting temperature of silicon (around 1200°C), but high enough to activate the process. The pressure must be calibrated with respect to the process time: in fact, higher pressure decreases the mobility of the atoms, and thus more time is needed to have a significant effect.

4.1.4 Line Edge Roughness analysis

After the annealing, we observed the waveguides using the SEM (Hitachi CG4000) and we were able to evaluate the Line Edge Roughness (LER) through the method described in [292]. 80 images per waveguide have been taken (see Figure 4.10), and performing the analysis in [292] allowed us to obtain the results shown in Figure 4.11. As can be seen, the annealing has a significant impact on the LER; in particular, LER is reduced by a factor of two by applying the 40 Torr plasma for 5 minutes.

Then, AFM is exploited to obtain the profile of the silicon waveguides, as shown in Figure 4.12a. As can be seen, the etched waveguides have a rectangular shape and the roughness is clearly visible. On the other hand, annealed ones have smoother sidewalls and rounded edges. The LER can be evaluated by these profiles, as discussed in [293], and the results are shown in Figure 4.12b: the etched waveguides have a higher value of the LER except than near the bottom (where is present the interface between silicon and the BOX). However, since the mode is less intense in

the four corners (as shown in Figure 2.2), it is likely that the defects at the bottom of the annealed waveguides are not significant for the scattering. Finally, we see that the data in Figure 4.11 and Figure 4.12b are in good agreement (it must be considered that only some waveguides on different wafers have been tested).

4.1.5 Encapsulation

Once the waveguides have been patterned and annealed, we were able to realize the SiO_2 encapsulation. First, we performed a thermal oxidation of around 2 nm of silicon to create a 5-nm layer of SiO_2 (4.1). This allows one to have a smoother contact surface between the waveguides and the cladding, in order to further reduce the scattering losses.

Finally, we deposited 1.1 μm of SiO_2 through High-Density Plasma (HDP) chemical-vapor deposition at 400°C, by using silane (SiH_4) as precursor. HDP deposition is excellent to create a very compact encapsulation layer on top of the waveguides. In addition, the surface is almost planar, even on top of the waveguides (see figure 4.14). However, the high density of the plasma used during the deposition can create some defects on the waveguides: to avoid this effect, 20 nm of SiO_2 were deposited through a Low Rate (LR) deposition by Plasma Enhanced Chemical Vapour Deposition (PECVD) at 400°C, by using Tetraethyl orthosilicate [TEOS , $\text{Si}(\text{OC}_2\text{H}_5)_4$] as precursor. In fact, this process is softer and it creates a protective layer which can be bombarded by HDP deposition without ruining the surface of the waveguides.

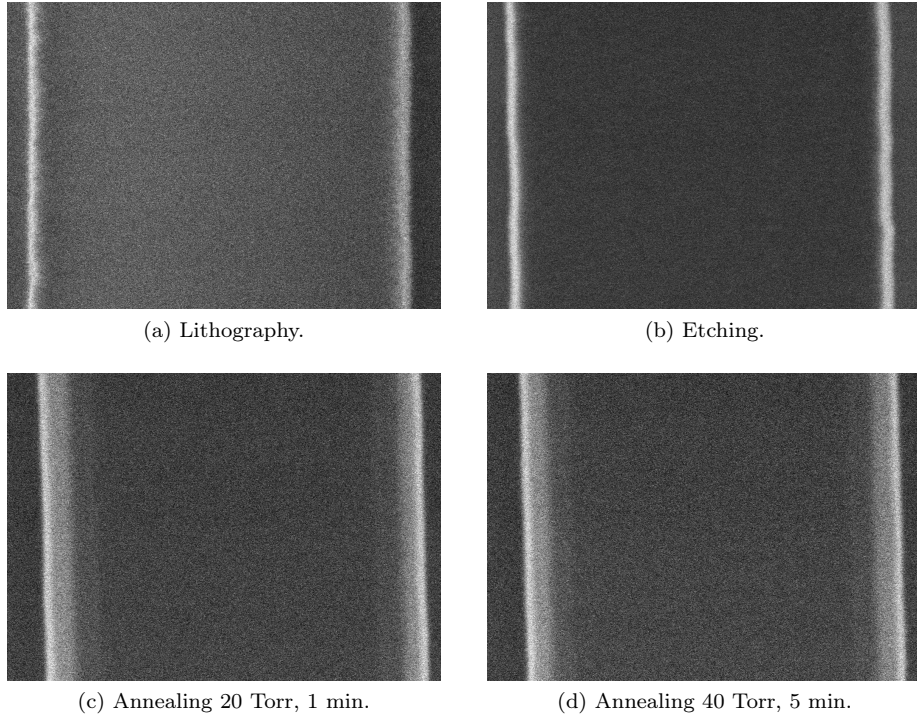


Figure 4.10: Images of the silicon waveguides taken by the Hitachi CG4000 CDSEM after different steps of the fabrication process. The field size is $0.68 \times 2.76 \mu\text{m}^2$ (1024×1024 pixels) with different condition of the electron beam for the images. With resist (4.10a), an accelerating voltage 300 V has been used and 8 frames have been taken not to ruin it, while with the harder silicon waveguides 16 frames with 800 V have been captured.

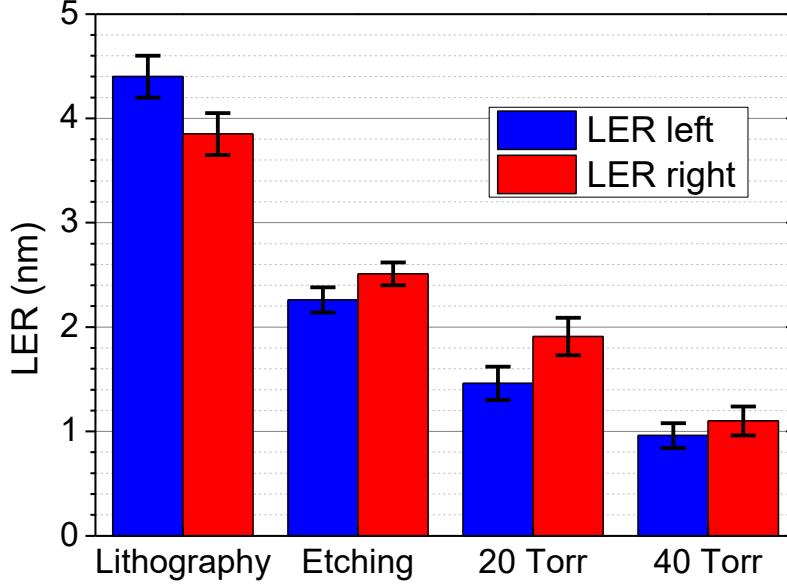
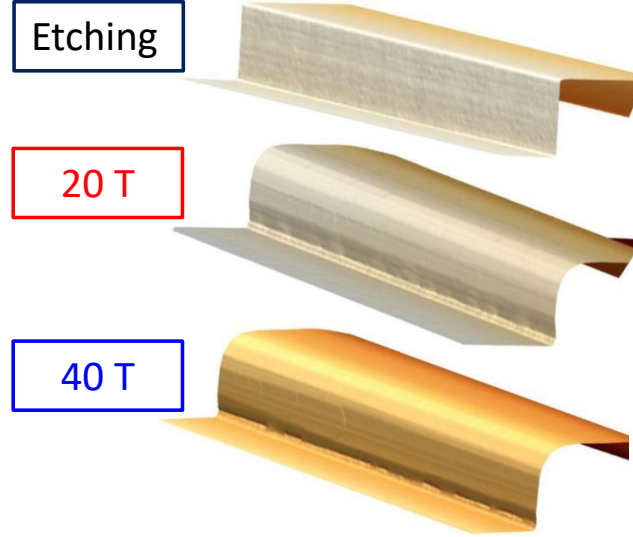


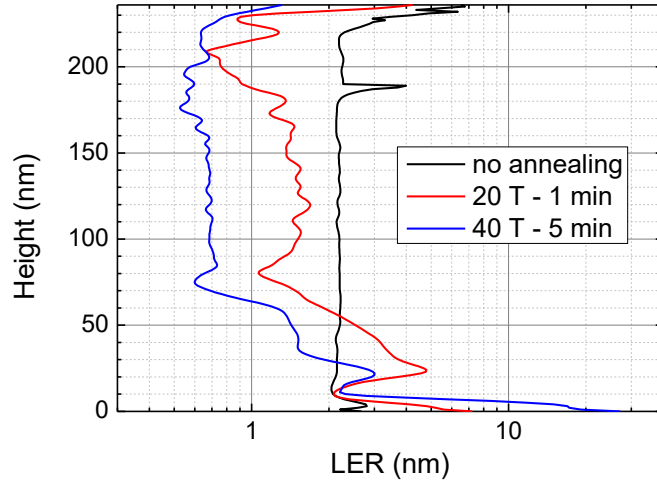
Figure 4.11: Results of the analysis of the LER by using CDSEM images (Figure 4.10 and by applying the method described in [292]). As can be observed, the best annealing condition is the 40 Torr for 5 minutes, which reduces by a factor of 2 the LER with respect to the etched waveguide.

4.2 Electrical circuits

After the fabrication of the PIC, we had to create the electrical circuits to tune the optical response of the structures. The first critical point is the definition of the thickness of the oxide layer between silicon waveguides and heaters. In fact, it is important that the distance between them is big enough to guarantee the absence of absorption due to the presence of the metal layer, but also close enough to obtain an efficient heating process. Thus, we performed some simulations to understand the SiO_2 thickness to target (as discussed in section 2.2.4), and we found out that the oxide layer deposited during the encapsulation (900 nm on top of 220-nm waveguides and 820 nm on top of 300-nm waveguides) is thick enough to prevent metal absorption and thin enough to heat up the waveguides and to change efficiently the effective index of the mode. Thus, we were able to go on with metal deposition without changing the oxide thickness (and, then, avoiding any removal of dioxide or further deposition).

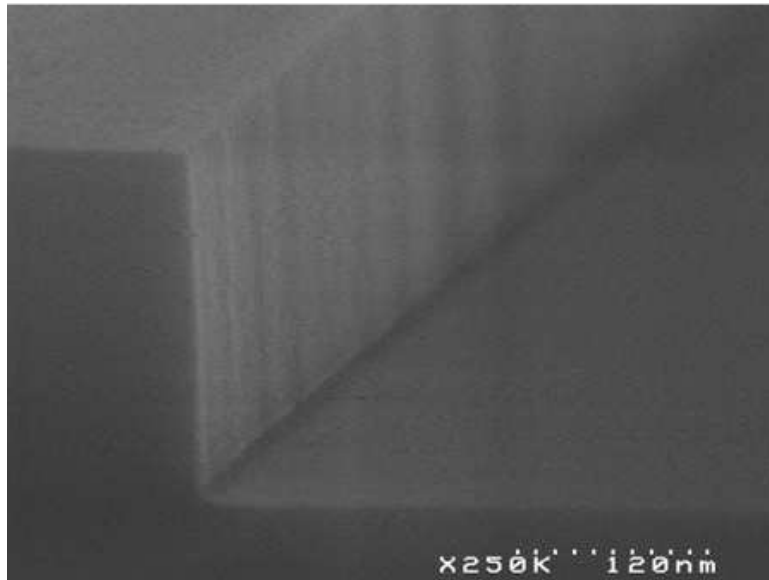


(a) 3D representation of the waveguides' profiles.

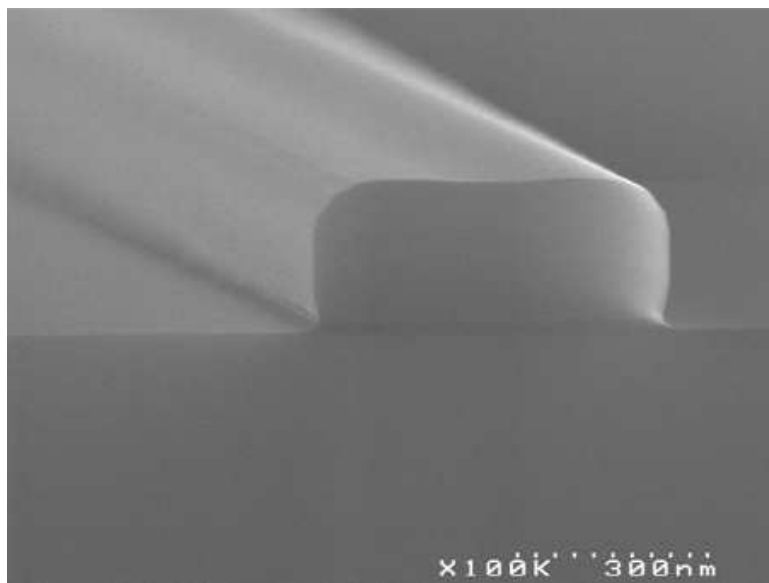


(b) Analysis of the waveguides profile to determine the LER, as detailed in [293]. The plot shows the average of the LER on six scans of the sidewall's profile. The annealed waveguides turn out to be more rough at the bottom, as can be seen also in Figure 4.12a, but they show a lower value of LER in the upper part of the waveguide. This results are in agreement with the CD-SEM estimation (see Figure 4.11)

Figure 4.12



(a) Straight waveguide with no annealing.



(b) Straight waveguide annealed at 850 °C, 40 Torr for 5 minutes.

Figure 4.13: SEM pictures of two waveguides from two different wafers. The sample in (b) has been annealed at 850 °C, 40 Torr for 5 minutes, while the one in (a) has not been treated.

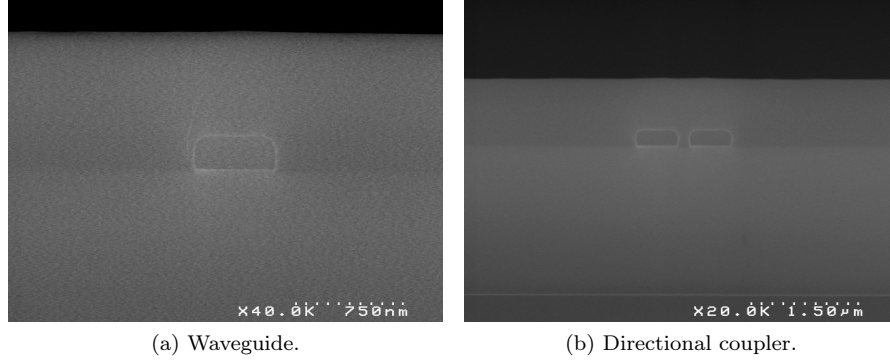


Figure 4.14: SEM cross section of a waveguide and a directional coupler after the HDP deposition.

4.2.1 Heaters

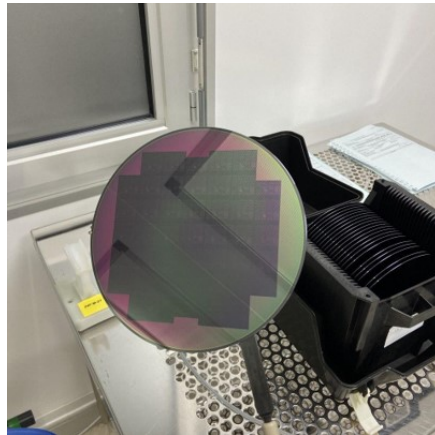
The heater structure is realized by using a $800 \times 110 \text{ nm}^2$ Titanium Nitride (TiN) wire. This material has been extensively used in CMOS fabrication, since it guarantees high resistivity, excellent reliability in the deposition and it is compatible with CMOS production [294]. TiN layer is deposited through a Physical Vapor Deposition (PVD) in a EnduraTM 5500 by Applied Materials. The deposition is realized at 350°C and it is preceded by a Titanium deposition (10 nm) to improve the adhesion with the oxide layer.

The expected resistivity of the TiN layer is around $5 \cdot 10^{-7} \Omega \text{ m}$. Usually, the designers deal with an alternative quantity: the resistivity per square (ρ_\square). In fact, they can control only the definition of the patterns, while the thickness and the material of the layer are fixed. Thus, if the target width of the electric wire is w and its length is L , its resistance turns out to be

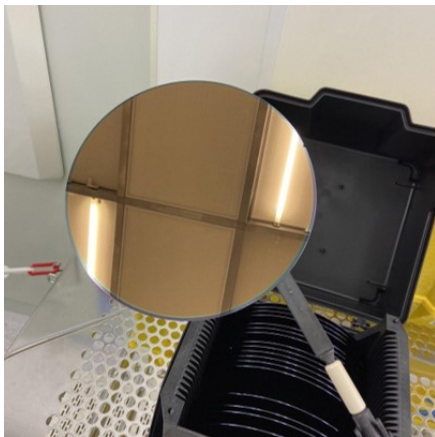
$$R = \rho \frac{L}{w \cdot \Delta z} = \frac{\rho}{\Delta z} \cdot \frac{L}{w} = \rho_\square \cdot N_\square \quad (4.3)$$

where N_\square is the number of squares with sides equal to w . In our case, the resistivity per square around $5 \Omega/\square$.

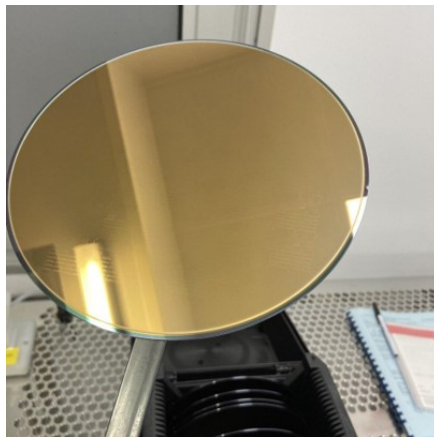
Then, we moved to the patterning of the heaters. This is realized with a second mask (ZING-B02-R), which must be aligned with the Silicon level by using the PM markers (see figure 4.5); thus, we had to remove the Ti/TiN layer on top of the PM. After that, we deposited 49 nm of BARC (DUV30) and 820 nm of a positive-tone resist (M78Y) for 248-nm lithography, which was realized on an ASM200 stepper by ASML. The error in the alignment was checked to be less than 100 nm in the X direction and less than 75 nm in the Y direction, which is good enough for our



(a) After the encapsulation.



(b) After Ti/TiN deposition.



(c) After Ti/TiN/AlCu/Ti/TiN deposition.

Figure 4.15: Pictures of the wafers at different fabrication steps.

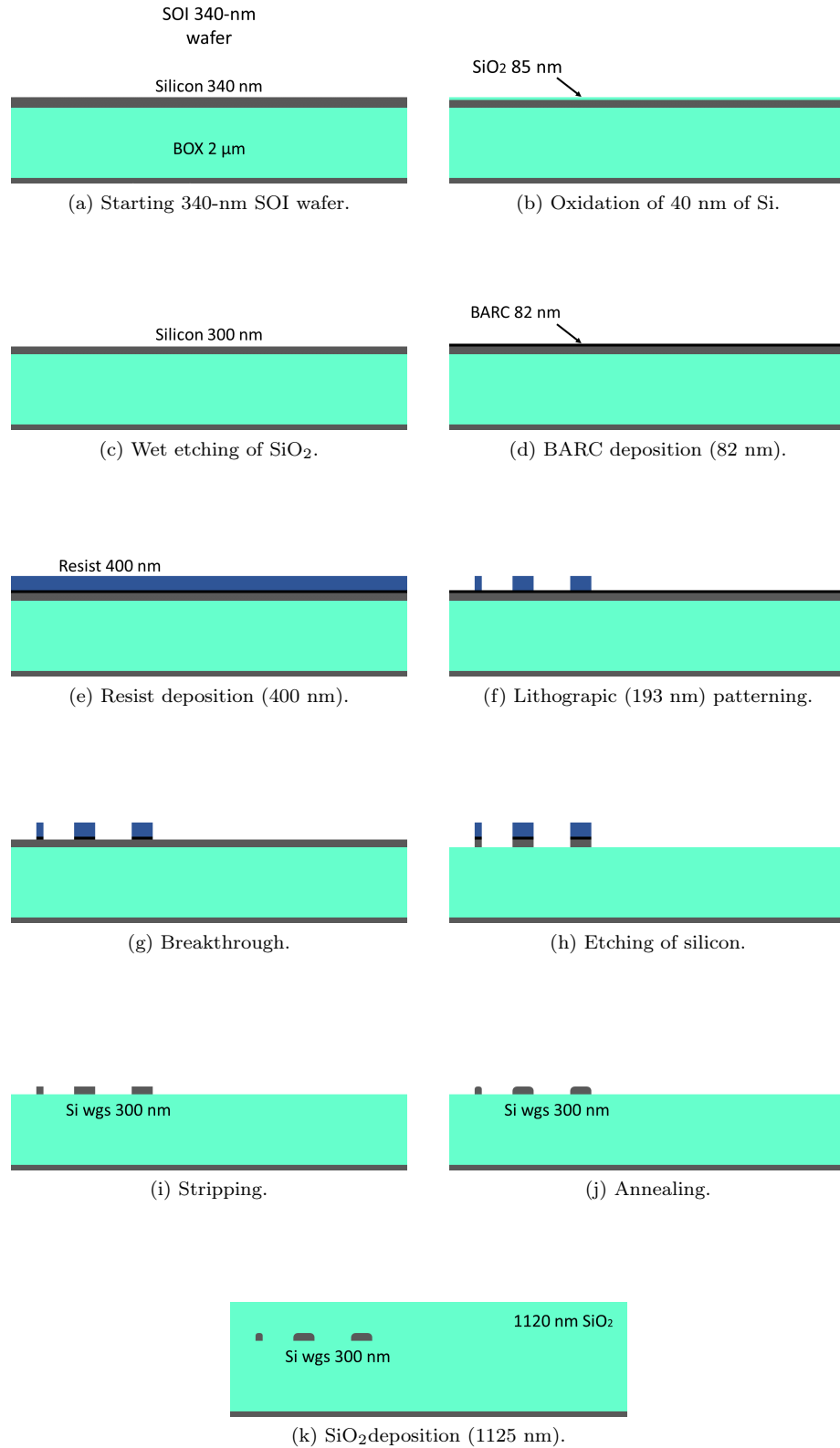


Figure 4.16: Fabrication steps to obtain encapsulated 300-nm thick silicon optical waveguides. In the process started from the 220-nm SOI wafers we skipped steps in figures 4.16b and 4.16c.

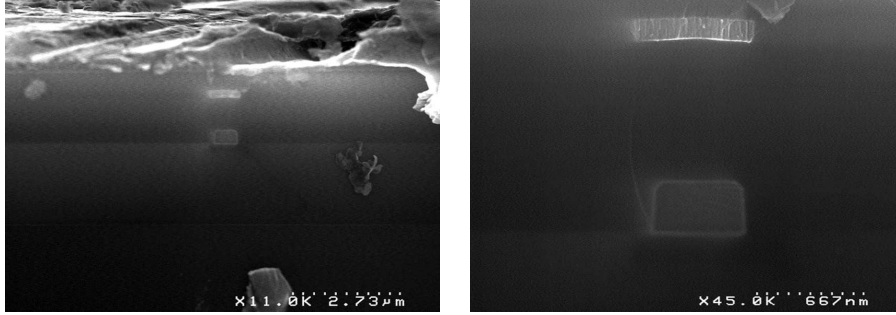


Figure 4.17: SEM images of a cross section of a 300-nm thick waveguide with a heater.

purposes. In addition, the width of the structure was checked, and the right value (800 nm) was found with a dose equal to 20 mJ/cm².

The etching was realized with a Cl₂/HBr plasma etching with the detection of the endpoint by using OES: in fact, the high opening rate of the mask (97%) guarantees a strong signal due to the high concentration of etching products in the chamber. The etching time was around 35 s for the BARC, 10 s for the breakthrough and 35 s for the Ti/TiN layer. Then, the resist was stripped by using a O₂N₂ plasma and a wet etching with DuPontTM PlasmaSolv[®] EKC265TM post-etch residue remover.

Then, we deposited another oxide layer by using the same method adopted for the encapsulation of silicon waveguides: 25 nm of SiO₂ deposited through TEOS PECVD, and 700 nm of SiO₂ HDP PECVD.

4.2.2 Pads

In order to have electrical contacts by using external metallic tips, we had to pattern a second metallic layer by which electrical pads can be created. Obviously, these circuits must be in contact with the Ti/TiN layer, and this is possible by opening some holes (called “vias”) through the oxide layer we deposited.

Since the layer with optical waveguides is very dense, we had to find a strategy to place all the pads on the die. In fact, the pads must be big enough to permit the alignment with electrical tips, and they shouldn't be placed on top of the optical waveguides, to avoid any damage during the alignment. Then, we had to order two different versions of the mask for the pads' level (ZING-B04-R and ZING-B04-S), and, consequently, also for the vias' level (ZING-B03-R and ZING-B03-S). We selected some wafers on which we patterned the R versions, and we used the S versions for the others.

The lithography of the vias was realized with a ASM200 stepper by ASML. We deposited 1500 nm of a 248-nm positive-tone resist (TDUR), and we checked the

alignment: we found an error less than 75 nm in the X direction and less than 50 nm in the Y direction, which is good enough for our purposes. It is possible to observe that these values are less than those found in the previous step. The reason is that this mask is aligned on a layer (heater) realized with the same stepper.

Since the minimum feature's size is 10 μm and the tolerance is around 1 μm , we didn't have to check for the right dose (variation is in the order of tens of nanometers). For the same reason, we did not deposit any BARC, since reflection effects are not relevant with this level of resolution.

Then, we realized the etching of the SiO_2 by using a $\text{C}_4\text{F}_8/\text{O}_2/\text{CO}/\text{Ar}$ plasma. Since the opening rate of the mask is very low (0.3 %), we were not able to use OES or IEP for the endpoint detection. Thus, we performed two tests by changing the etching time (150 s and 210 s), and we validated the process with an electrical test: we aligned two metallic tips on two big vias ($40 \times 40 \mu\text{m}^2$) and we measured the resistance of the heater. We found out that 150 s were not sufficient to open properly the areas (no electrical contact was reached). On the other wafer, we were able to measure the resistance of the heater in the center, but we had to apply some pressure to do the same on the border. Then, we decided to increase the etching time: we set different times (240 s, 260 s, 280 s, and 300 s) to be absolutely sure to open the vias. Since the selectivity of the etching of Ti/TiN with respect to SiO_2 is more than 13, we were able to make some calculation to check how much Ti/TiN we would have etched in the more unfavorable case. Let's suppose that the time needed to etch the 725 nm of SiO_2 is 150 s (even if the test was negative), and let's see how much Ti/TiN we would etch if we set a the total etching time equal to 300 s. The etching rates are 290 nm/min for SiO_2 and lower than 22 nm/min for Ti/TiN. In 150 s we would reach the Ti/TiN surface, and in the remaining 150 s we would etch less than 55 nm of Ti/TiN (out of the 110 nm deposited). Hence, we were sure that the planned overetching wouldn't have been detrimental for our structures. After the etching, we stripped the resist with O_2N_2 plasma and EKC265TM post-etch residue remover.

Finally, we went on with the deposition of the metal for the pads' level, and we chose to use aluminium copper (AlCu), which is characterized by a very low resistivity. We deposited a thick layer of AlCu (1.4 μm), which is embedded into two layers of Ti/TiN (30/60 nm) to improve the adhesion on the oxide and to protect the metal from oxidation and corrosion on top [295]. The deposition of Ti/TiN/AlCu/Ti/TiN (in the following parts of the text it will be indicated as "AlCu") was realized in the PVD EnduraTM 5500 (350° for Ti/TiN and 450° for AlCu). The advantage of using the EnduraTM 5500 is that we were able to realize the three deposition in the same machine without exposing the wafer to the external environment, since there are four chambers linked to the same transfer chamber.

Then, we repeated the same steps we performed with the heaters: we etched the area where PM markers are located and we used the masks for the pads' layer (ZING-B04) aligned on them. The lithography was realized with the ASM200 stepper.

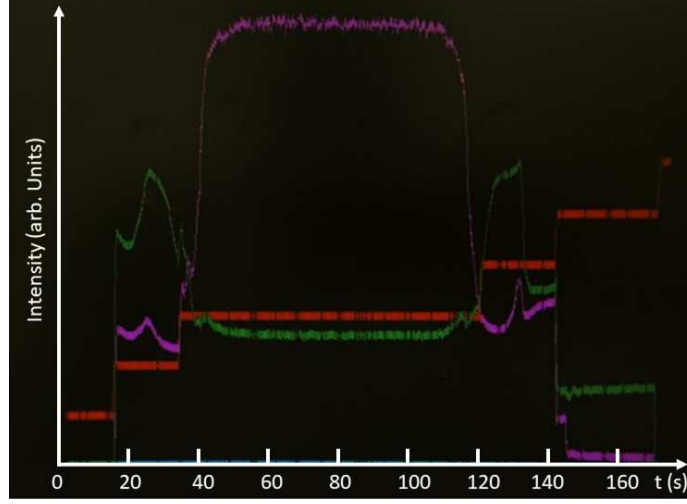


Figure 4.18: Optical signals dependent on the presence in the plasma reactor of etching products during the etching of AlCu. The red curve shows the different steps of the process. It starts with an initial step to stabilize the flows of gases followed by the etching of Ti/TiN (whose reactive products give the green signal) for 20 s. After the detection of the endpoint (drop of the green curve), plasma conditions are changed and the etching of AlCu starts (92 s); when the purple curve drops, the parameters are changed again to etch the bottom layer of Ti/TiN (22 s). Finally, after 30 s of overetch, the process is stopped.

Since we had to etch 1580 nm, we deposited 4000 nm of a 248-nm positive-tone resist (M78Y + M225G) with no BARC since the minimum feature's size is 10 μm . The etching is realized in a LAM 9600 reactor by using $\text{BCl}_3/\text{Cl}_2/\text{N}_2/\text{Ar}$. The mixture of gases was regulated automatically on the basis of OES signal, as it can be observed from Figure 4.18. After the etching, we stripped the resist with O_2/N_2 plasma and EKC265TM post-etch residue remover. Then, we performed again a plasma treatment with O_2/N_2 for 60 s to make the structures more stable.

Finally, a N_2/H_2 annealing (H_2 diluted in N_2) at 400°C at ambient pressure for 2 hours was realized in order to improve the electrical, chemical and mechanical stability of the AlCu electrical circuits. In fact, as it is possible to see in Figure 4.19, the AlCu alloy is characterized by the presence of grains, and the annealing procedure improves the cohesion of the material.

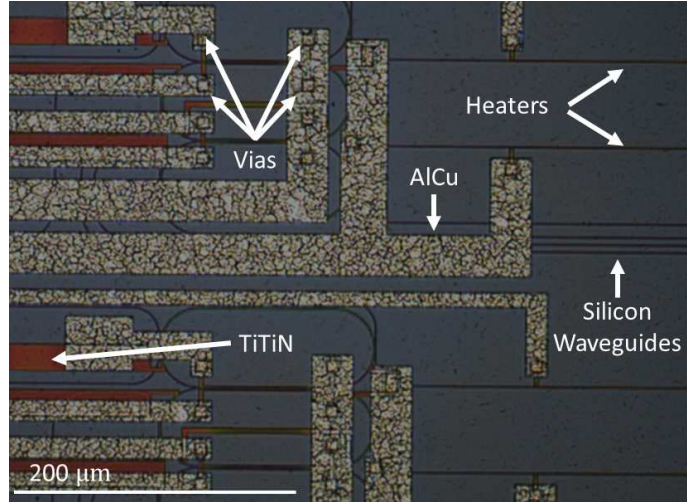


Figure 4.19: Optical image of part of the wafer. It is possible to see the presence of the silicon waveguides and the heaters. The vias ($10 \times 10 \mu\text{m}^2$) are within the AlCu circuits, which can be recognized from the grain pattern typical of alloys. On the other hand, TiN is more homogeneous, as it can be observed in some circuits (which appear red) on the left part of the image.

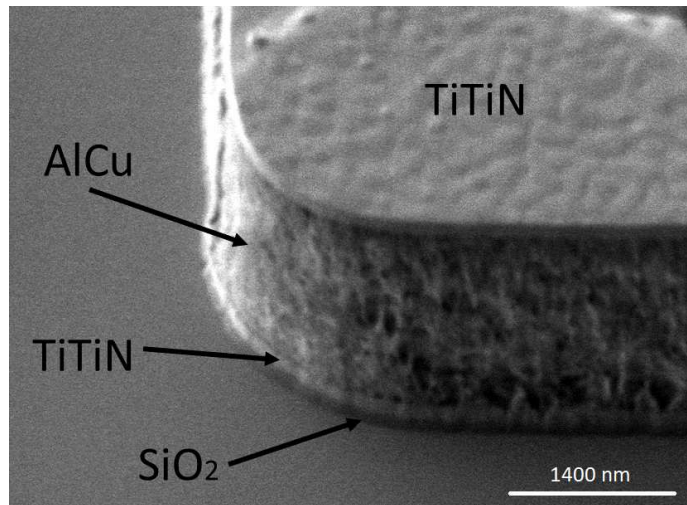
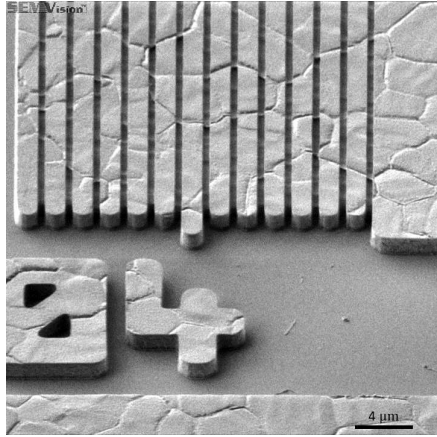
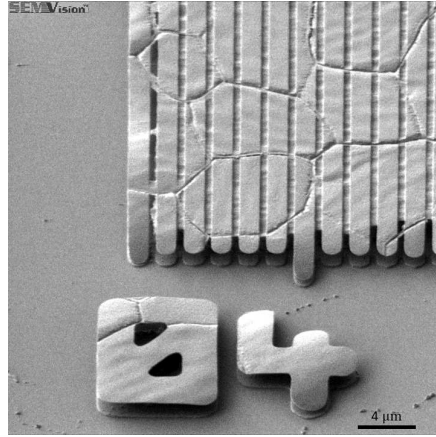


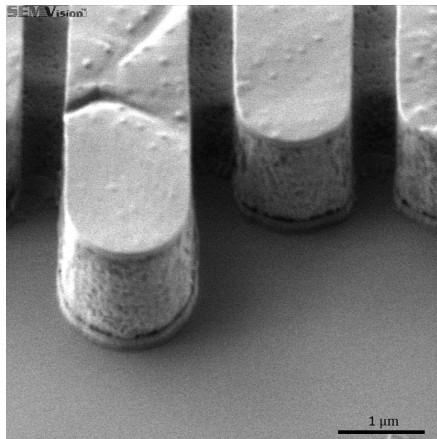
Figure 4.20: SEM image of the AlCu multistack layer. It is possible to recognize the light gray parts (Ti/TiN) which embeds the AlCu alloy. In addition, the thin dark gray layer it's SiO_2 , which is exposed due to some overetching.



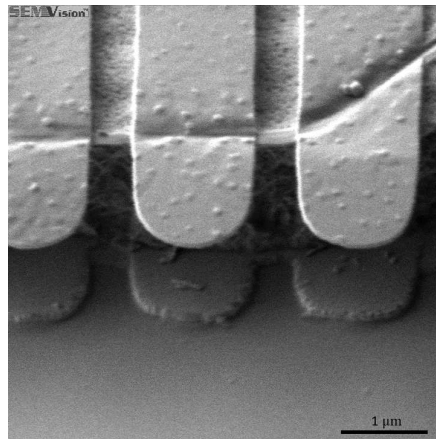
(a) P01 - control structures zoomed out.



(b) P02 - control structures zoomed out.



(c) P01 - control structures zoomed in.



(d) P02 - control structures zoomed in.

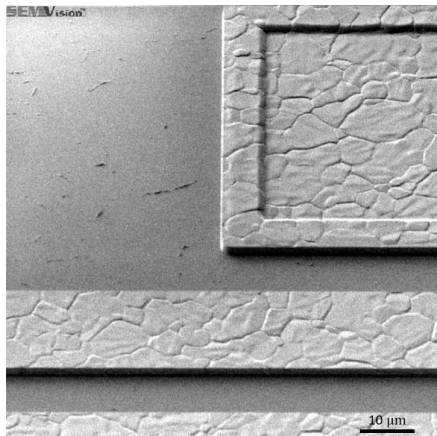
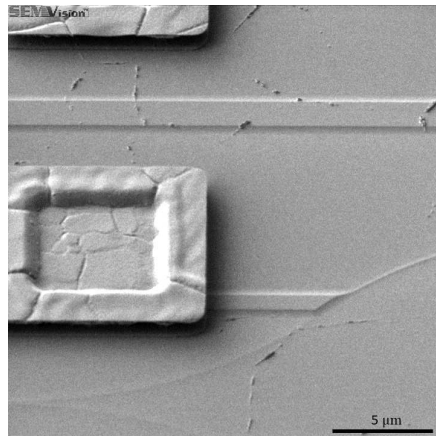
(e) Detail of the wafer P01 with an AlCu wire and a pad ($50 \times 50 \mu\text{m}^2$) on top of a big vias.(f) Detail of the wafer P02. It is possible to see the vias, the Ti/TiN links to the heater and the silicon waveguide covered by SiO_2 .

Figure 4.21: SEM images of some details of the AlCu layer. Right images show the wafer P02, in which an Cl_2 leakage at the end of the etching brought an isotropic etching of the metal.

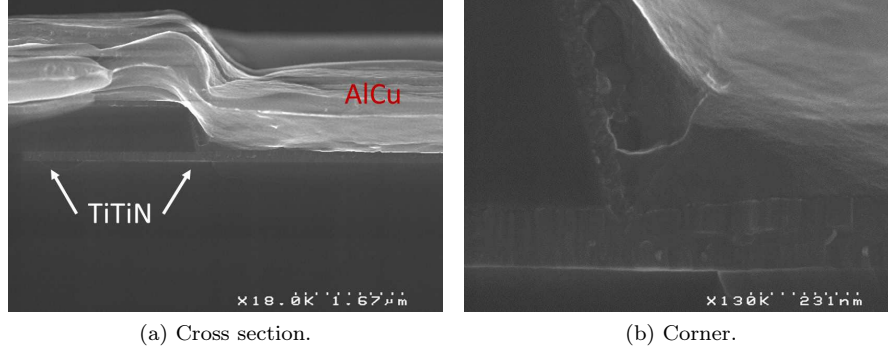


Figure 4.22: SEM images of a cross section of a vias with AlCu on top.

4.2.3 Electrical characterization

We tested a heater placed on a ring resonator with radius equal to $30\text{ }\mu\text{m}$ and we measured the I-V response as well as the electrical stability. To do that, we placed two metallic tips on the pads which guarantees the access to the heater (Figure 4.23a), and we changed the current by using a stabilized current source (Keithley SourceMeter[®] 2612A). The results are presented in figures 4.23 and 4.24. The I-V curve is linear with a voltage lower than 10 V , which corresponds to a power around 75 mW . Then, it is possible to use the device with electrical powers up to $250\text{--}300\text{ mW}$: at this level, the temperature in the structure is too high and the metal starts to melt. At 400 mW it is possible to see the melting area from the optical microscope (figure 4.23a), and the device breaks for a voltage equal to 30 V .

4.3 Deep Etch and Dicing

The final part of the fabrication process has the goal to isolate the subdies to realize the optical tests and experiments by using the edge coupling method described in section 2.2.1. To do this, we realized a final lithographic step to etch the silica around the subdies: in this way, the quality of the surface is defined by the plasma etching of silica, while the division can be realized by a saw which does not touch the facets.

The lithographic pattern is realized with another mask (ZING-B05) on the ASM200 stepper (alignment on PM). We deposited 6500 nm of 248-nm positive-tone resist (FUJI GKR4602) with no BARC since the minimum feature's size is larger than $100\text{ }\mu\text{m}$. The etching is realized in two steps, since we wanted to etch the SiO_2 (the deposited cladding and the BOX) and $150\text{ }\mu\text{m}$ out of $750\text{ }\mu\text{m}$ of the Si-substrate.

The etching of oxide (1850 nm deposited and 2000 nm of BOX) was performed on

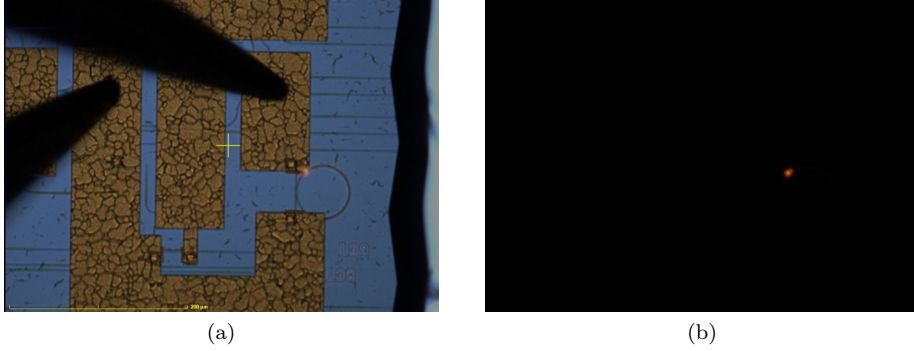


Figure 4.23: Optical images of the device on which we performed the electrical tests. The hot spot is due to the high electrical power (voltage equal to 28 V) in the device.

a Unity™ equipment by TEL (Tokyo Electron Limited), by using a $C_4F_8/O_2/CO/Ar$ plasma. The endpoint (non critical) was detected by using the OES signal after 8 minutes, and we continued for additional 30 seconds to guarantee a complete etching of oxide.

Then, we realized a deep etch of silicon by using the Bosch method [297] in the LAM 9600 reactor. It consists in alternated phases of etching by using SF_6 , which is highly isotropic, and deposition of a protective polymer by using a flow of C_4F_8 (Figure 4.26).

Note that the selectivity of the two etching procedures with respect to the resist are, respectively, around 4 and 40. Thus, the needed resist budget is

$$T_{resist} > \frac{3.85\mu m}{4} + \frac{150\mu m}{40} > 4.7\mu m \quad (4.4)$$

At the beginning, we overestimated the selectivity of the SF_6 etching and we put a 4- μm resist, leading to a slight etching of the AlCu layer on top (see Figure 4.27b). In addition, one has to take into account that the selectivity of SF_6 etching with respect to SiO_2 is 100: thus, it is clear why it was fundamental to etch all the oxide before starting the Bosch process.

Finally, we performed the stripping of the resist by using a O_2N_2 plasma, an EKC265™ post-etch residue remover wet etching and a final N_2H_2 plasma treatment to fix and stabilize the structures. The scheme of the final cross-section can be observed in figure 4.31.

After that, we were able to dice the wafer into the subdies. We put each wafer on a UV sticker, with a high adhesive power. We programmed an automatic dicing saw from DISCO to realize all the cuts. The procedure has been done using two blades cutting at the same moment into different parts of the wafer, in order to

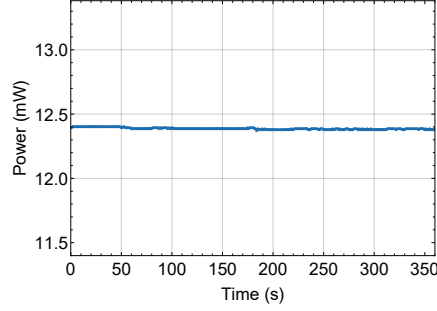
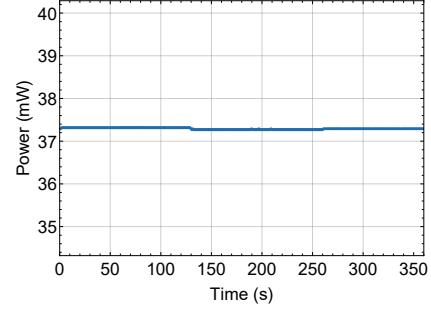
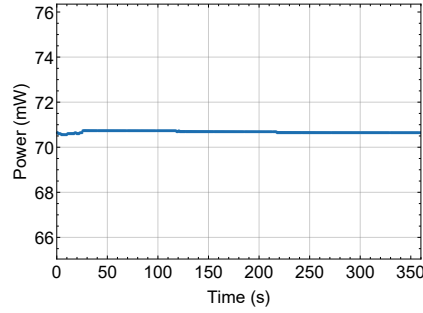
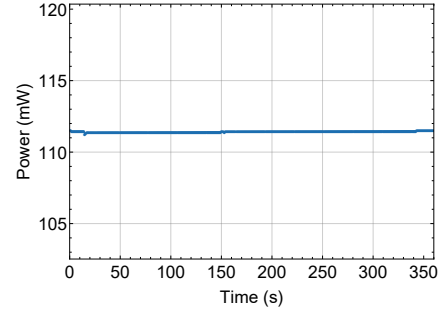
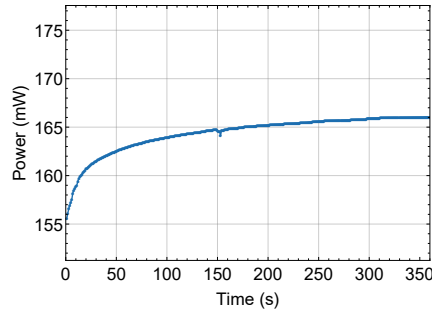
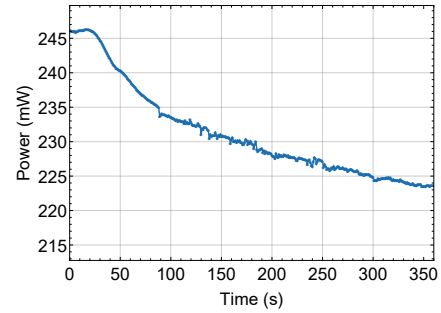
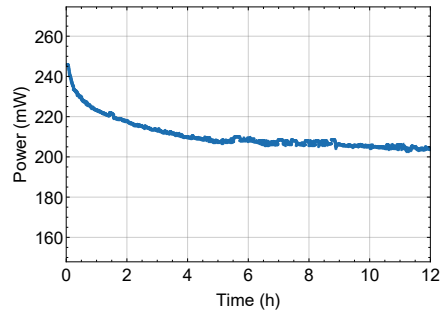
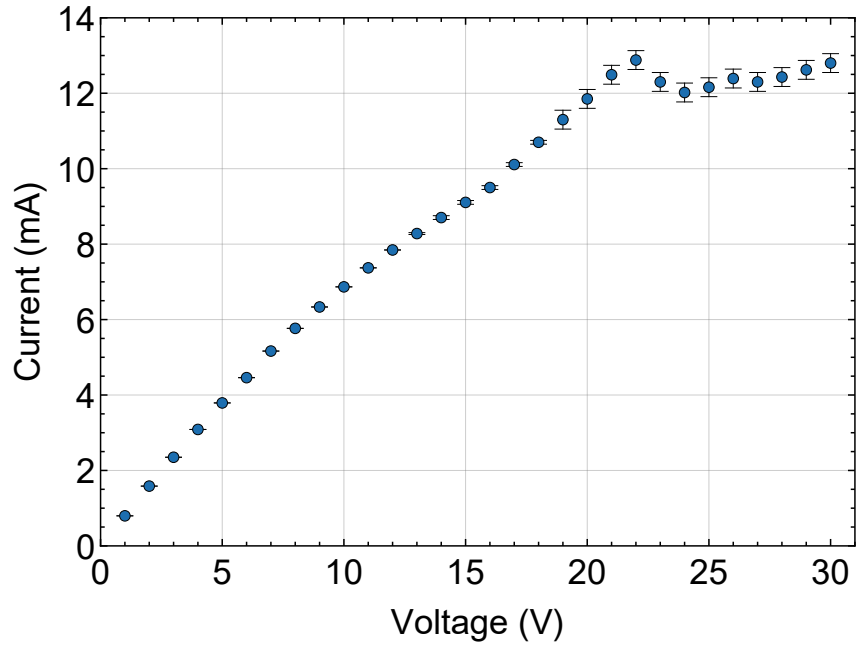
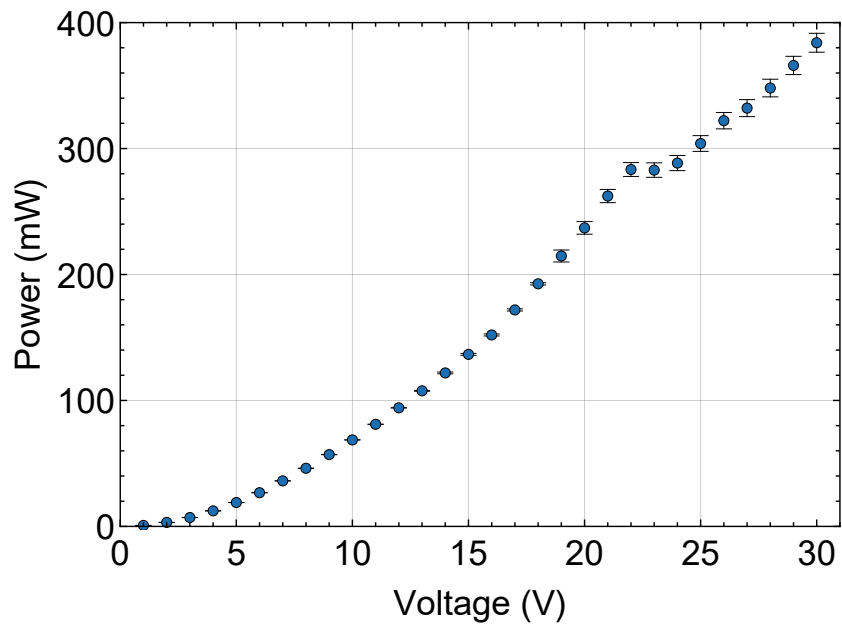
(a) $V = 4$ V, 1 hour.(b) $V = 7$ V, 1 hour.(c) $V = 10$ V, 1 hour.(d) $V = 13$ V, 1 hour.(e) $V = 16$ V, 1 hour.(f) $V = 20$ V, 1 hour.(g) $V = 20$ V, 12 hours.

Figure 4.24: Test of the stability of the heater for different values of the voltage.



(a) Current vs voltage plot.



(b) Power vs voltage plot.

Figure 4.25: Electrical characterization of the heater on top of the microring.

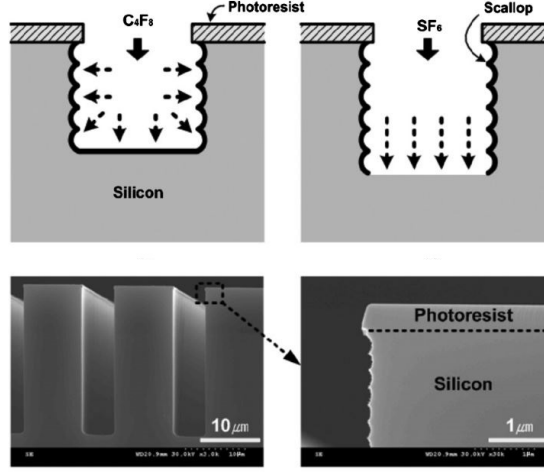
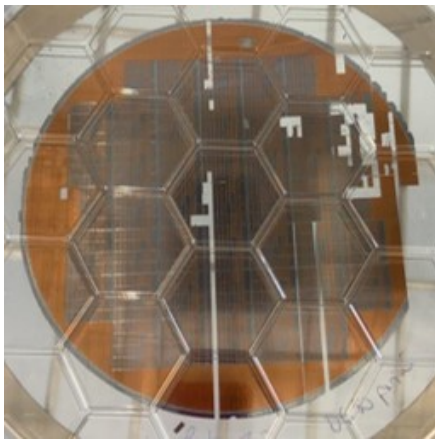
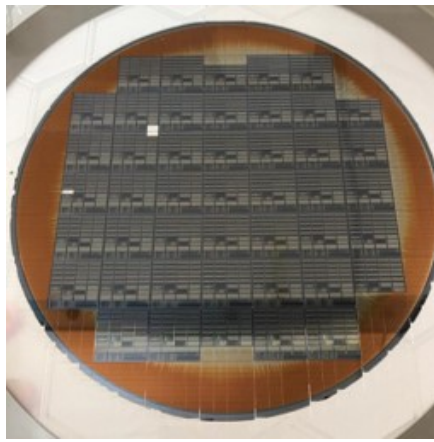


Figure 4.26: Schematic of Bosch method, showing the passivation using C_4F_8 , the silicon isotropic etching using SF_6 , and two SEM images of a treated sample (Image from [296]).

half the total cutting time (from two to one hour). Since the minimum trench is 200- μm wide, we decided to use a 50- μm blade for silicon aligned to the centre of the deep-etch areas. However, since we decided to pattern only the central part of the wafer (and not the borders, as shown in Figure 4.4), the blade had to cross an area with all the deposited materials on it (and not only 600 μm of silicon substrate). In particular, the passage through the areas with Ti/TiN and AlCu led to sudden misalignments of the blades during the procedure, which caused the detachment of some subdies from the sticker (Figure 4.27a), and eventually the break of the blade in some cases. Thus, we used thicker and more resistant blades (80 μm), which were able to cut the wafers with minimal detachments (Figure 4.27).



(a) Wafer P12 after the dicing. Several sub-dies detached from the sticky due to the problems with the $50\text{-}\mu\text{m}$ thick blade.



(b) Wafer P02 after the dicing. The use of the $80\text{-}\mu\text{m}$ thick blade solved the problem of detaching. The corona is due to a too thin resist ($4\text{ }\mu\text{m}$ instead of $6\text{ }\mu\text{m}$) used for the deep etch procedure: this led to a partial etching of the AlCu layer (which appears gray in the centre and red in the border).

Figure 4.27: Optical images of P12 (a) and P02 (b) after the dicing, showing the problems related to the wrong blade and the too thin resist.

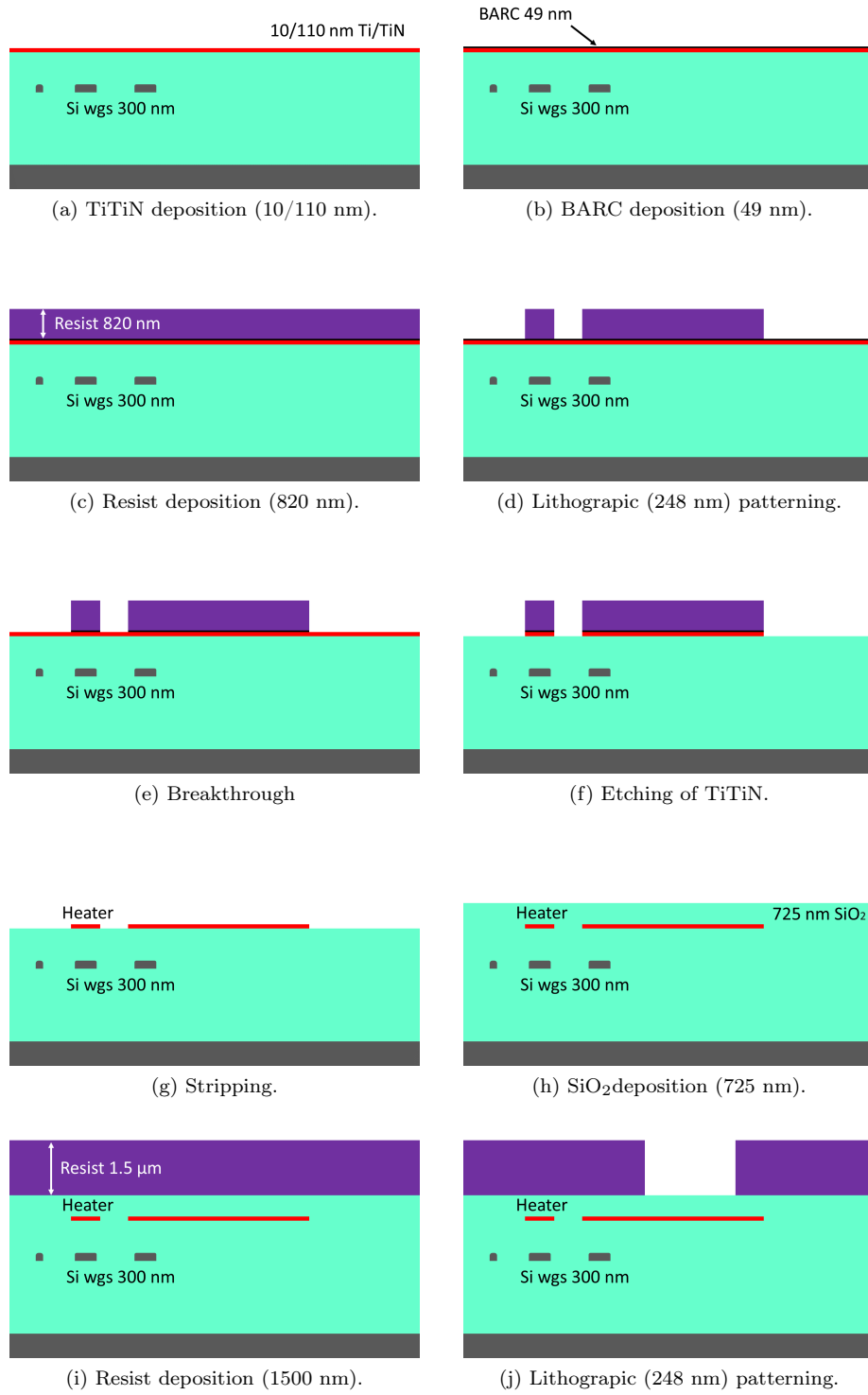


Figure 4.28: Fabrication steps to obtain the thermal phase-shifters (Part 1).

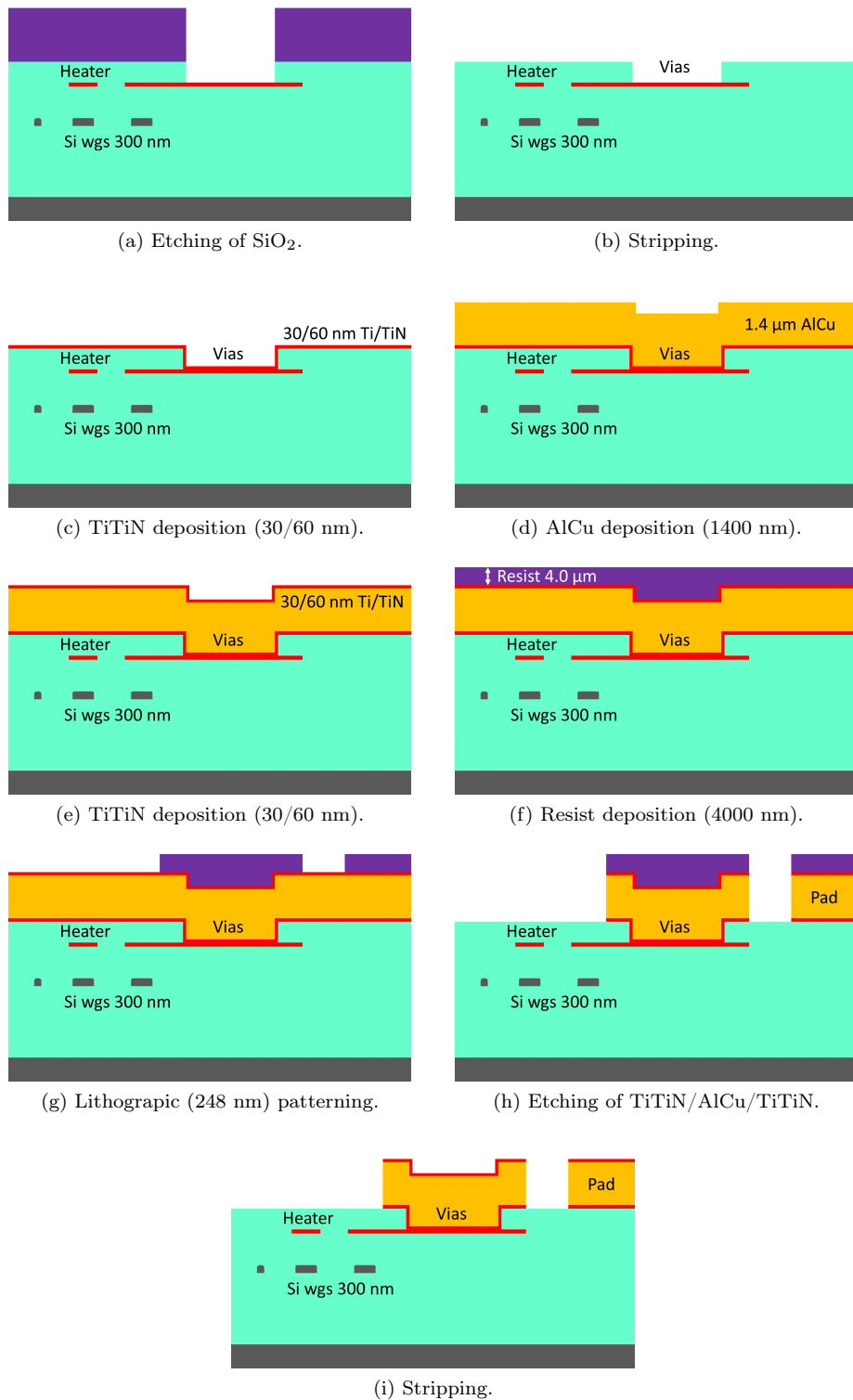


Figure 4.29: Fabrication steps to obtain the thermal phase-shifters (Part 2).

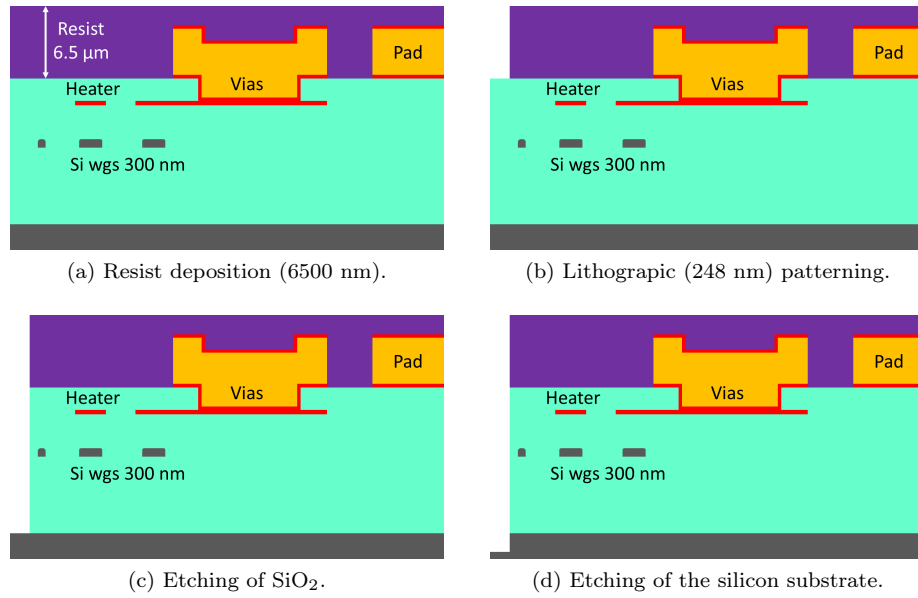


Figure 4.30: Fabrication steps to allow the edge coupling.

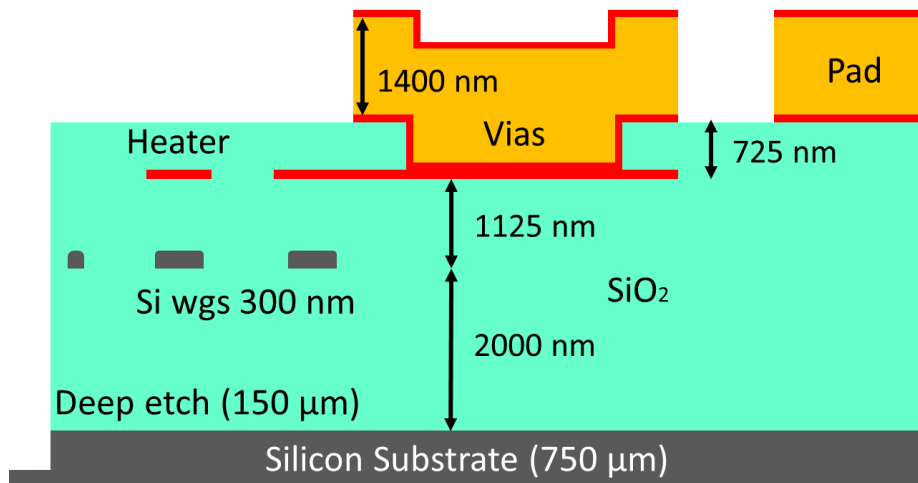


Figure 4.31: Schematic of the fabrication process.

Wafer	Thickness (nm)	Resistivity (Ω)	Dose (mJ/cm ²)	Annhealing (Torr - min)	Version Circuits	Etching time VIAS (s)	Thickness Resist Deep Etch (nm)
P01	300	8,5-22	25,5	40 - 5	S	260	6000
P02			25,5	40 - 5	S	150	4000
P03			26,5	40 - 5	R	240	6000
P04			27,5	40 - 5	S	300	6000
P05			26,5	40 - 5	-	-	4000
P06			25,5	20 - 1	S	300	6000
P07			26,5	20 - 1	S	260	6000
P08			26,5	20 - 1	R	210	6000
P09			27,5	20 - 1	-	-	4000
P10			27,5	20 - 1	R	280	6000
P11			25,5	-	R	240	4000
P12			27,5	-	S	300	6000
P13	220	14-18,9	25,5	40 - 5	R	240	6000
P14			26,5	20 - 1	S	260	6000
P15			27,5	40 - 5	S	300	6000
P16			26,5	40 - 5	-	-	4000
P17			26,5	-	-	-	-
P18			27,5	20 - 1	-	-	4000
P19		>750	27,5	-	R	240	6000
P20			26,5	20 - 1	S	260	6000
P21			26,5	40 - 5	-	-	-
P22			27,5	20 - 1	R	260	6000
P23			26,5	40 - 5	R	260	6000
P24			26,5	20 - 1	-	-	-
P25			30,5	40 - 5	S	250	6000

Table 4.3: Resume of the treatments performed on the wafers.

Chapter 5

High Quality Factor Ring Resonators

Ring resonators are very important devices for integrated photonics and for nonlinear quantum optics, as discussed in section 2.3. One of the goals of my work was to realize compact optical resonators in silicon taking advantage of the annealing process to reduce the round-trip losses and, thus, increasing the quality factor and the intensity enhancement in the resonators. In this chapter, the characterization of the fabricated ring resonators is described. In particular, it is shown the difference between the performance of the devices on annealed wafers with respect to not-treated ones. In addition, it is discussed the efficacy of the post-etching treatments on these structures depending on their round-trip length and their shape.

5.1 Characterization methods

The linear characterization of the devices is realized by coupling to the device the light from a tunable laser, and the variation on the transmission is detected by an optical power meter. In addition, a polarization controller is used to select the right polarization and to distinguish between TE and TM modes. The tunable laser, however, can be used in two different ways: the *step* mode and the *sweep* mode.

In the *step* mode, the frequency of the laser is set and, at each step, the value on the optical power is read. The procedure is handled with a LabVIEW program by which is possible to control the laser and to measure the transmission by the power meter. As one can imagine, the accuracy of this method is strictly related to the accuracy of the laser. For example, if we use a TSL-710 laser from Santec¹, the accuracy of the measurement of the spectral properties is lower than 1 pm, which is

¹<http://www.santec.com.cn/pdf/TSL-710-C-E-v1.216011.pdf>

good enough to realize the characterization of resonators with quality factors lower than 1 million. The problem is that this method is very slow. In fact, our program allows us to take from 2 to 4 values of the optical spectra per second, and this means that broad spectra (>10 nm) can be taken with the maximum resolution in more than 40 minutes.

Another possibility is to use the *sweep* mode, which consists in the continuous tuning of the frequency of the laser and the detection of the transmission by using a photodetector and an oscilloscope. This method is faster, since it allows to span even 100 nm in one second. However, the accuracy is now related to the measure of the tuning speed and the synchronization of the laser with the oscilloscope through the trigger detection. In this work, I used the *sweep* mode to characterize the samples. In fact, since many devices had to be studied, it was mandatory to have a fast method to analyze them. However, before starting the characterization, I analyzed the optical response of a C_2H_2 reference cell (50 Torr), whose absorption lines are at known frequencies [298] (see Table 5.1), to evaluate the performance of the method.

The transmission spectra of the cells are obtained by calculating the wavelength as

$$\lambda = v \cdot (t - t_0) \quad (5.1)$$

where v is the nominal tuning speed of the laser, t is the time on the oscilloscope and t_0 is the time of the trigger signal. Then, I fit the found resonances with a lorentzian function, and I compared the centers of the resonances to the nominal values. As can be seen from Figure 5.1a, this method is not very accurate: in fact, shifts much greater than the linewidth (around 5 pm) are measured. This error is composed of a constant term due to the synchronization of the laser and the oscilloscope (which is more critical with higher tuning speeds), and a varying term due to the error on the estimation of the tuning speed.

This result is not surprising: in fact, measuring the position of the resonances at around 1550 nm with an accuracy of 1 pm means that the relative error on the tuning speed should be around 10^{-6} , which is demanding for an external cavity tunable laser. It is possible to estimate the actual tuning speed by inverting equation (5.1) and, thus, the error with respect to the nominal value (Figure 5.1b). Hence, if one should use the *sweep* method to precisely determine the position of the resonances (to measure, for example, the dispersion of the waveguide), then it would be mandatory the use of reference cells [299], reference external cavities [300], or external comb sources [301] to calibrate the speed of the tuning.

Through the analysis of these data it is possible to estimate also the typical error of the *sweep* mode in the measure of another important optical quantity: the FSR. It is measured as the difference of the wavelength of two resonances: thus, the error given by the synchronization of the laser with the oscilloscope is not significant, since it results in a shift of both the values. To estimate the typical error of this method, I measured the spectral distance between the resonances of the reference

R Branch	Wavelength (nm)	P Branch	Wavelength (nm)
27	1512.45273	1	1525.7599
26	1512.8232	2	1526.3140
25	1513.2000	3	1526.87435
24	1513.5832	4	1527.44114
23	1513.9726	5	1528.01432
22	1514.3683	6	1528.59390
21	1514.7703	7	1529.1799
20	1515.1786	8	1529.7723
19	1515.5932	9	1530.3711
18	1516.0141	10	1530.97627
17	1516.44130	11	1531.5879
16	1516.8747	12	1532.2060
15	1517.3145	13	1532.83045
14	1517.7606	14	1533.46136
13	1518.2131	15	1534.0987
12	1518.6718	16	1534.7425
11	1519.13686	17	1535.3928
10	1519.6083	18	1536.0495
9	1520.0860	19	1536.7126
8	1520.5700	20	1537.3822
7	1521.06040	21	1538.0583
6	1521.5572	22	1538.7409
5	1522.0603	23	1539.42992
4	1522.5697	24	1540.12544
3	1523.0855	25	1540.82744
2	1523.6077	26	1541.5359
1	1524.13609	27	1542.2508

Table 5.1: Table with the nominal values of the absorption lines of the C₂H₂ reference cell at 50 Torr. The R-branch absorption lines are related to a transition of the molecular state in which the excited state has a higher (“R” stands for “rich”) rotational quantum number. On the other hand, P-branch absorption lines identify transitions to excited states with a lower rotational quantum number (“P” stands for “poor”).

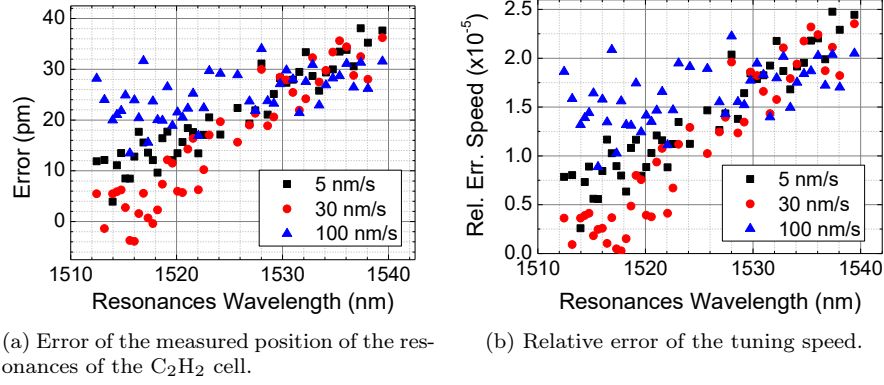


Figure 5.1

cell ($\Delta\lambda$), and I calculated the error by comparing to the nominal values. The results are shown in Figure 5.2: as can be seen the relative error is lower than 4%, which is good enough for our purposes.

Finally, some comments about the impact of the use of the *sweep* mode for the estimation of the quality factor and the visibility of the resonances, which allow to estimate the intrinsic quality factor and, thus, the power attenuation coefficient, as discussed in 2.3. Unfortunately, the reference cells do not have a precisely defined linewidth or depth, since they depend on temperature and pressure. Thus, I estimated the performance of the *sweep* mode by scanning a microring several times at different speeds and by comparing the results of the fits with respect to what is obtained by using the *step* mode.

In Figure 5.3 it is possible to observe the results of the analysis of three resonances of a ring resonator, which are fit by using a lorentzian function [191]

$$L(\lambda) = y_0 - A \frac{\Delta\lambda^2}{(\lambda - \lambda_0)^2 + \Delta\lambda^2} \quad (5.2)$$

where λ_0 is the center of the resonance and $\Delta\lambda$ is its FWHM. The black squared points are obtained with the *step* method, while the colored circles are got with the *sweep* mode; in particular, several consecutive scan are recorder for each value of the tuning speed (10 nm/s, 20 nm/s, 30 nm/s, 50 nm/s, 80 nm/s, and 100 nm/s). As can be seen, the evaluation of the quality factor with the *sweep* method is sometime quite different with respect to the *step* mode. In particular, it is possible to observe that higher tuning speeds gives more accurate results: in fact, slower sweeps seem to be affected by sudden (and repetitive) variation of the speed. On the other hand, the values of the visibility obtained with the two methods are in good agreement.

As we saw, the results obtained with the *sweep* mode are not completely reliable

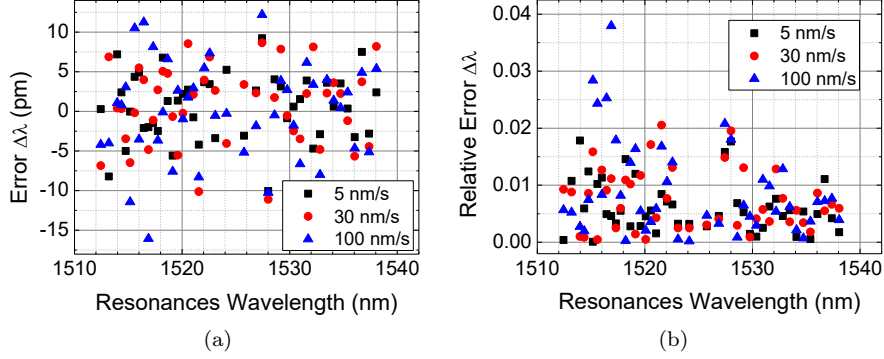


Figure 5.2: Error and relative error of the measure of the distance between adjacent resonances.

due to the uncertainty on the tuning speed and its instability. However, the derivation of the parameters of the waveguides (such as the group index n_g and the power attenuation coefficient α) is realized with the average of the FSR and the loaded quality factor obtained from several resonances, which allows to reduce the impact of the error of the tuning speed.

5.2 Characterization of ring resonators

In the subdie (6,2) many ring resonators are placed, as anticipated in section 3.7.1. Thus, I started the optical tests by characterizing these devices, since almost all the other structures are based on ring resonators, and their optical response can give important information about the optical parameters of the waveguides. To test many devices, it is fundamental the adoption of the *sweep* method described above to obtain the optical spectrum of the resonators in a quite large band in few seconds. The experimental setup is composed of a tunable laser (TSL-710 laser from Santec), two lensed fibers with nominal MDF equal to 3 μm , an InGaAs amplified detector (Thorlabs PDS10CS) and an oscilloscope. In addition, a polarization controller is used to select the polarization of the modes to test (TE or TM).

The main goal of the characterization of rings is to identify which process gives the best results in terms of quality factor and losses. First, I analyzed the spectra of nominal identical rings from three different wafers (P19, P20, and P23) which have been treated with a different post-etching process, as shown in Table 4.3: P20 has been processed with the annealing at 20 Torr for 1 minute, P23 at 40 Torr for 5 minutes, while P19 has not been annealed. I focused my attention on the rings having radius equal to 117.2 μm : on each die there are five of them with different

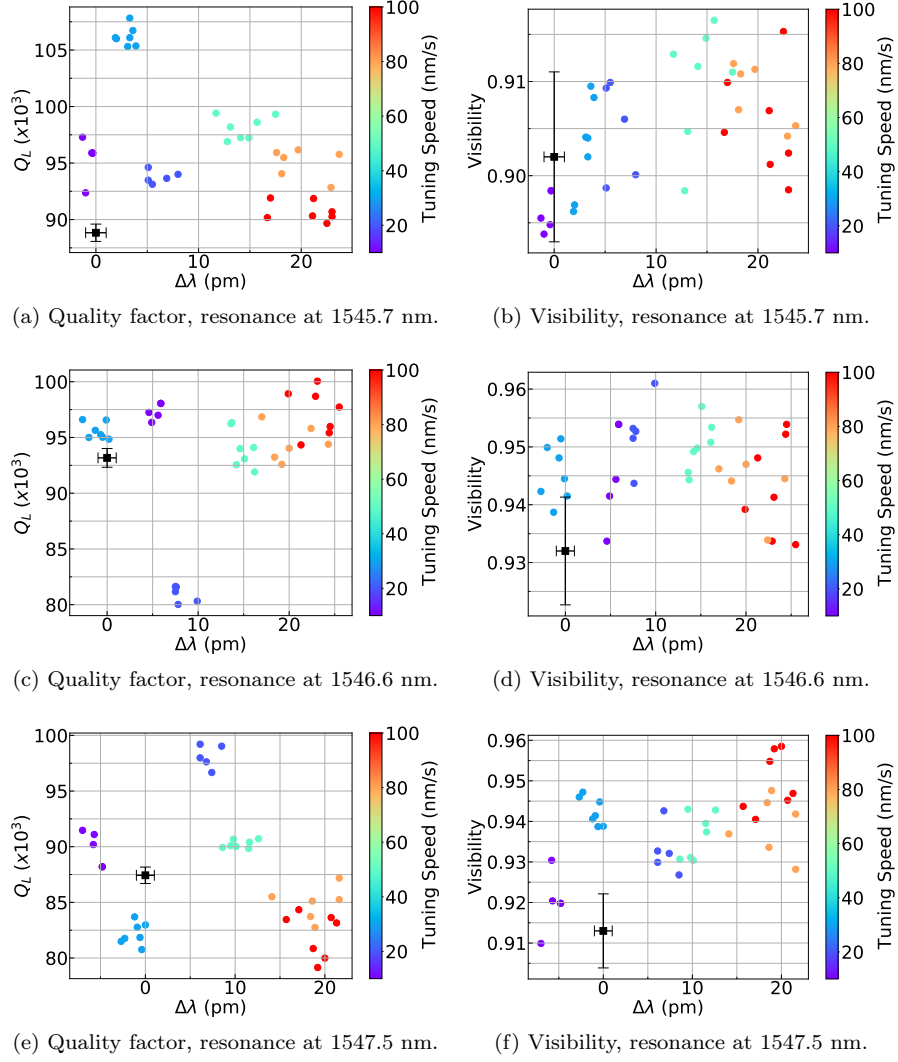


Figure 5.3: Comparison between the evaluation of the loaded quality factor and the visibility of three resonances by using the *sweep* mode (colored circles) and the *step* mode (black square) methods. The x axis represent the difference between wavelength of the resonance obtained with the *sweep* and the value obtained with the *step* mode.

gaps (120 nm, 150 nm, 180 nm, 210 nm, 240 nm), and this allows one to investigate the response of the resonator in different coupling regimes.

The optical response of each device is collected by tuning the laser from 1525 nm to 1575 nm at a *sweep* speed equal to 50 nm/s. The oscilloscope is set to register 10^5 samples per second, which means that the resolution of the spectra is equal to 0.5 pm. Then, the resonances are fitted by using a Lorentzian model (5.2) or with a more complex model that takes into account the splitting due to the coupling of the two counter-propagating modes[302]

$$D(\lambda) = A + \left| 1 - \frac{1}{2Q_c} [F_+(\lambda) + F_-(\lambda)] \right|^2 \quad (5.3)$$

$$F_{\pm}(\lambda) = \left(i \left(\frac{\lambda - \lambda_0}{\lambda_0} \pm \frac{1}{2Q_m} \right) + \frac{1}{2Q_i} + \frac{1}{2Q_c} \right)^{-1} \quad (5.4)$$

where Q_c and Q_i are, respectively, the coupled and the intrinsic quality factors, while Q_m is the quality factor related to the coupling of the modes. If the resonance is not split, we can easily determine its visibility ($V = A/y_0$), and we can plot it against the loaded quality factor to reconstruct Figure (2.22).

The results are displayed in Figure 5.4. As can be seen, the impact of the annealing is clear: while the rings on the reference wafer P19 show a critical coupling condition ($V \approx 1$) with a loaded quality factor lower than $150 \cdot 10^3$, the annealed wafers have rings in critical coupling with $Q_L \approx 200 \cdot 10^3$, which is due to the higher intrinsic quality factor and, thus, the lower losses. In all the plots, several points show a value higher than one for the visibility: this is due to the limited dynamic range and to the noise of the detector, which do not allow one to properly estimate the extinction on resonance.

As we discussed, the value that properly quantifies the optical losses is the intrinsic quality factor, which can be calculated from the visibility and Q_L obtained with the Lorentian fit (5.2) through the relations (2.56), or as a direct result of the doublet model (5.3). Thus, for each device we can calculate the average of the Q_i obtained from the fits of its resonances. In Figure 5.5a the estimated intrinsic quality factor of the rings with radii equal to 117.2 μm are displayed. As can be seen, Q_i is higher for the annealed samples ($Q_i \approx 450 \cdot 10^3$) than for the reference samples with no annealing ($Q_i \approx 350 \cdot 10^3$): this further proves that the post-etching treatments are effective. However, the value of the associated power attenuation coefficient α is approximately equal to 1.6 dB/cm, which is higher than what obtained in previous works with similar fabrication processes ([82, 116]).

To investigate more deeply this issue, I performed the characterization of other rings with different radii on the same subdie (-2,-2) of the wafer P23 (some spectra are displayed in Figure 5.7), and I evaluated the intrinsic quality factor for all these samples, as shown in Figure 5.5b. We can observe that all the devices provide similar values of Q_i , which are between $340 \cdot 10^3$ and $500 \cdot 10^3$ depending on the

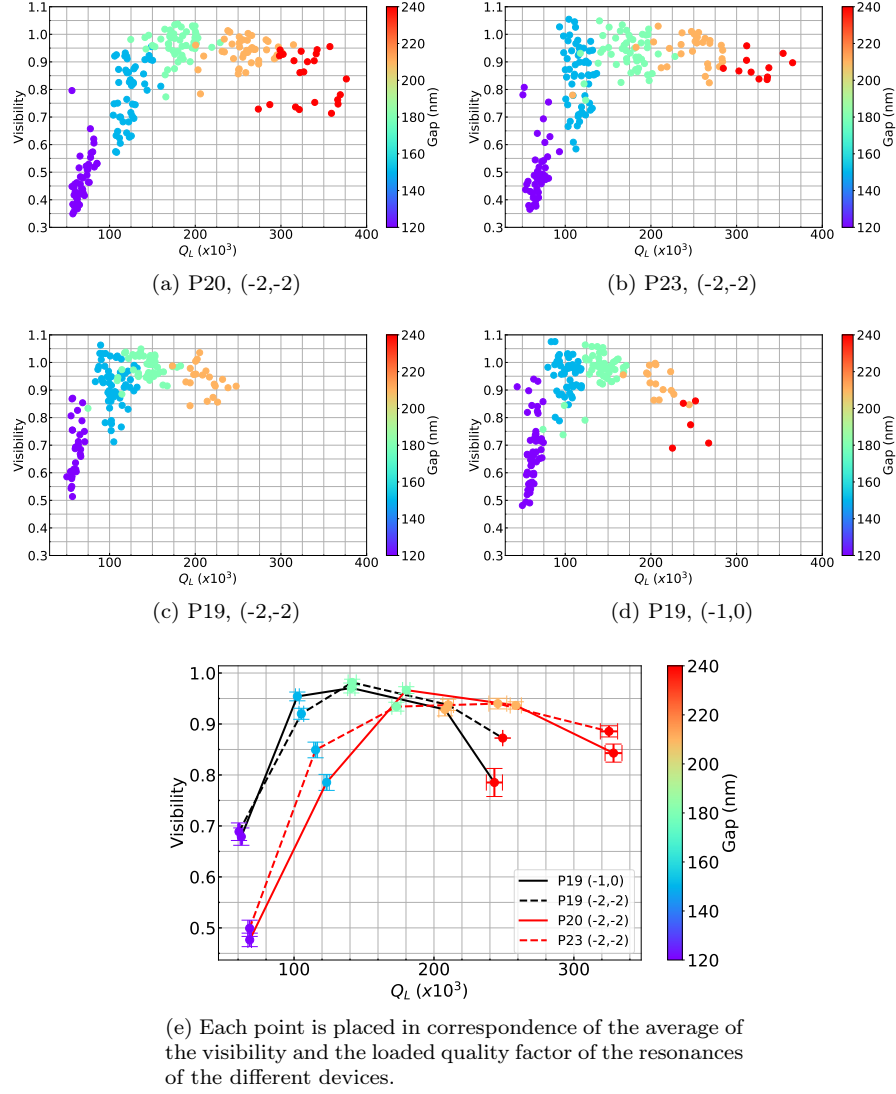
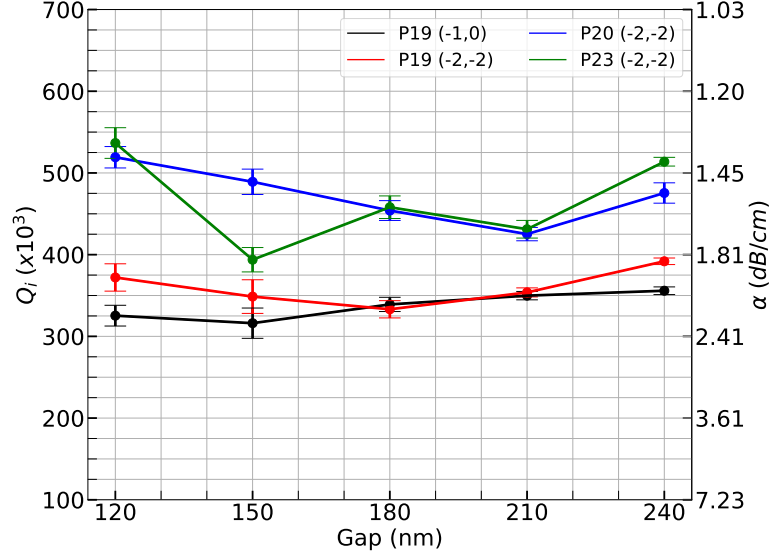
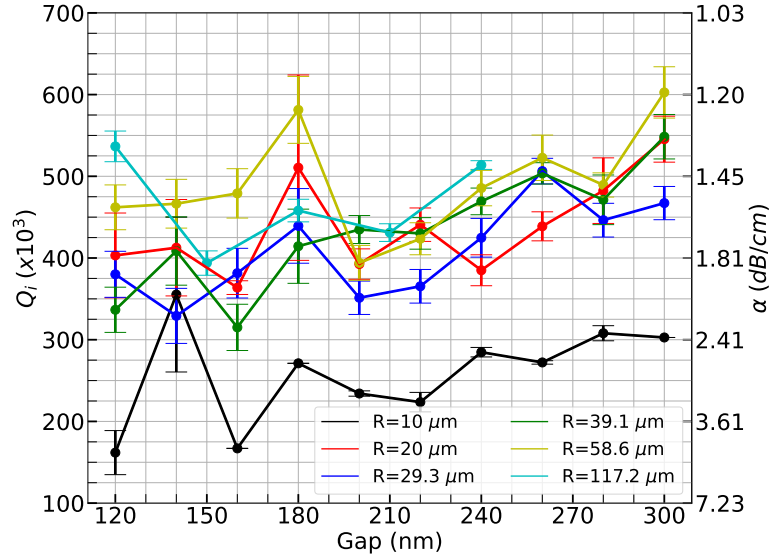


Figure 5.4: Plots showing the relation between the visibility and the loaded quality factor of rings having the radius equal to $117.2 \mu\text{m}$ on different wafers. Figures (a)-(d) shows the single resonances of the rings on P19, P20, and P23, and the impact of the annealing it is clear, since the critical coupling occurs at higher values of Q_L . Figure (e) is obtained from the average of the measures of all the resonances.

(a) Rings with $R = 117.2 \mu\text{m}$ on different wafers

(b) Ring on wafer P23.

Figure 5.5: Calculated values of the intrinsic quality factor for the devices characterized. Each point is given by the average over all the resonances of the spectrum, and the error is the standard deviation divided by the square root of the number of resonances.

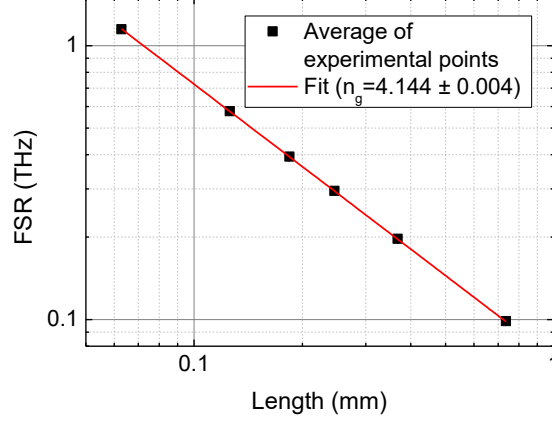


Figure 5.6: The points in the plot are obtained from the average of the FSR measured on the rings in the wafer P23, and the fit is done following equation (2.3.2). The value of the group index is assumed to be almost constant within the investigated spectral region (from 1525 nm to 1575 nm).

gap, except the ring with $R = 10 \mu\text{m}$, which probably takes less advantage from the annealing because of the smaller bending radius. In parallel, the comparison of the FSR of these devices allows the estimation of the group index, which turns out to be equal to 4.144 ± 0.004 (see Figure 5.6). This value is slightly higher than the results of the simulations: this can be due to the shrinking of the width of the waveguide and the modification of its cross-section because of the annealing, as shown in the previous chapter.

Finally, the characterization of the longer resonators (displayed in Figure Figure 3.27b) has been done. The laser is tuned between 1540 nm to 1560 nm in 1 second, with a resolution of 0.2 pm. As discussed in 3.7.1, these devices are coupled to two waveguides through tunable MZIs, which allow one to change the coupling ratio. One can imagine the device as a single-pass resonator where one coupler (MZI_1) changes the coupling of the ring, while the latter (MZI_2) changes the losses of the structure. The idea is, hence, to minimize the “losses” through MZI_2 and to investigate the different coupling regimes by tuning the optical response of MZI_1 . From an operative point of view, I made the laser to scan one single resonance while tuning the MZIs, and I minimized the losses: the working point can be detected when the linewidth is as narrow as possible, and a change in the MZI_2 response leads to a broadening of the resonance. Then, I changed the coupling with MZI_1 to explore the different coupling regimes. Two devices have been tested: one on P20 and one on P23. The best value of the electrical power P_2 applied to MZI_2 to

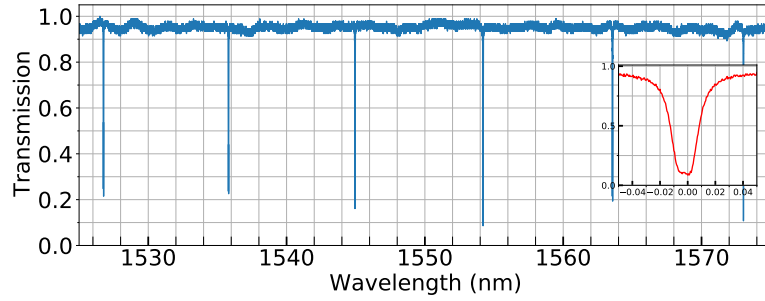
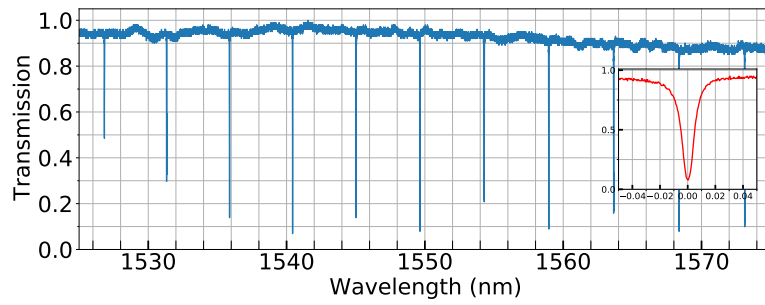
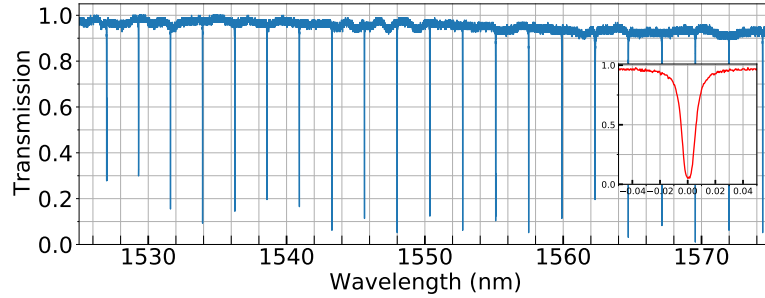
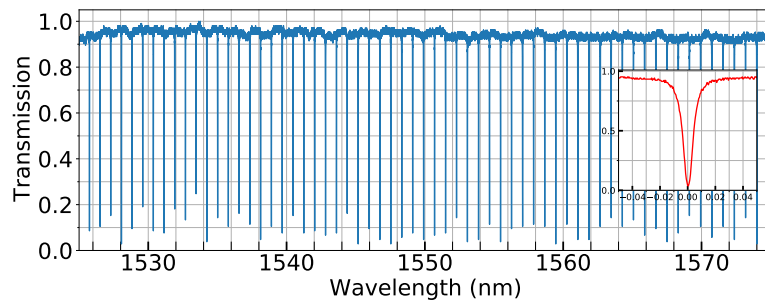
(a) $R = 10 \mu\text{m}$, gap = 200 nm(b) $R = 20 \mu\text{m}$, gap = 200 nm(c) $R = 39.1 \mu\text{m}$, gap = 200 nm(d) $R = 117.2 \mu\text{m}$, gap = 180 nm

Figure 5.7: Spectra of some ring resonators on P23. The insets show one resonance of the spectrum.

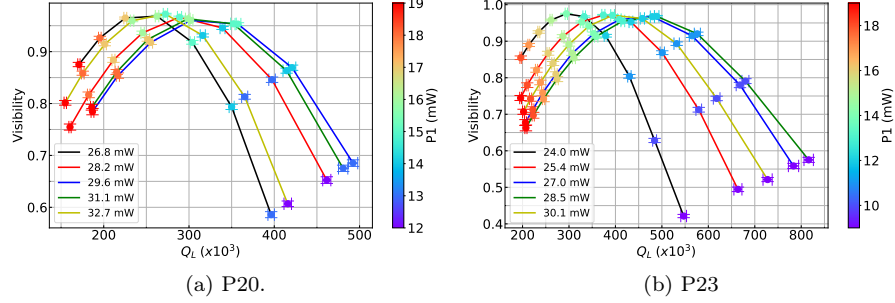


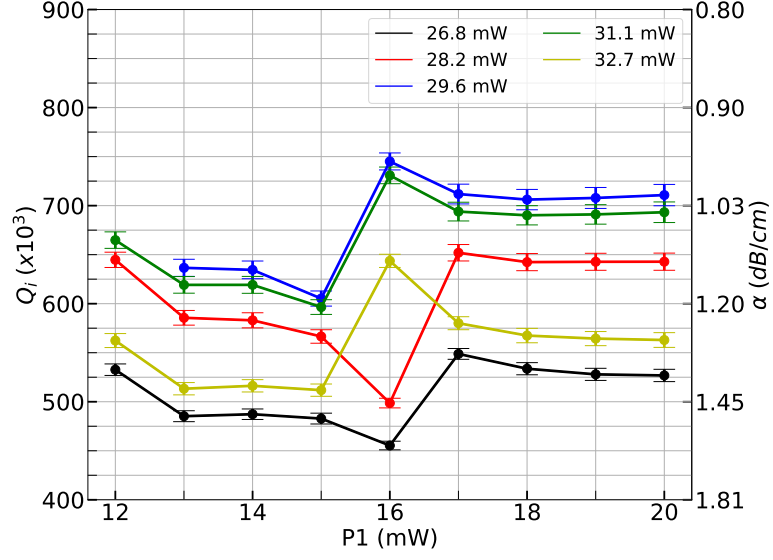
Figure 5.8: Plots showing the relation between the visibility and the loaded quality factor of the rings with the tunable couplers on P20 and P23.

minimize the losses was found to be 29.6 mW and 27.0 mW for, respectively, P20 and P23.

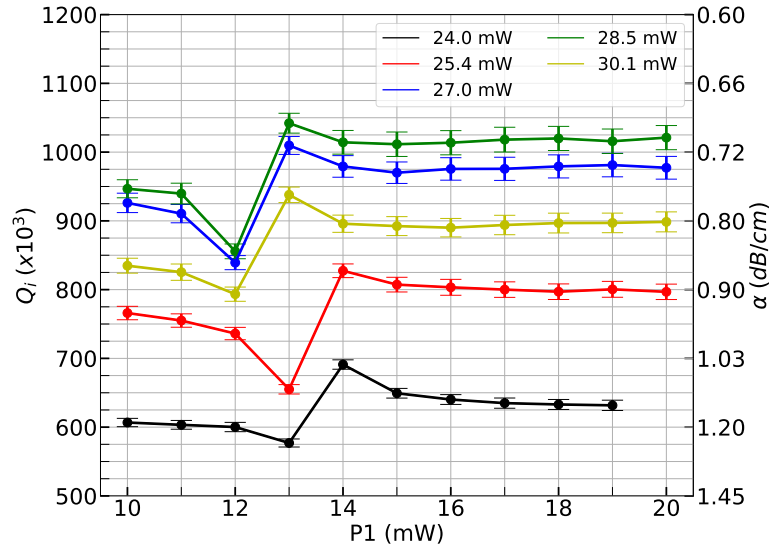
In Figure 5.8 the plots of the average visibility and loaded quality factors are displayed. Each curve represents the results of the characterization with P_2 fixed (as detailed in the legend), while the coupling of MZI₁ is changed through the tuning of the electrical power (P_1) applied to its phase shifter, as shown by the different colors of the points. The method described above worked well to find a rough estimation of the best value of P_2 for P20: in fact, the points on the blue line give the highest values of Q_L (given a certain value of the visibility) with respect to the results with higher or lower values of P_2 . On the other hand, the best value for P23 turned out to be 28.5 mW, as can be seen from Figure 5.8b. In Figure 5.9 are collected the estimation of the intrinsic quality factor of the devices, which turns out to be around $700 \cdot 10^3$ for the resonator on P20 and around 1 million on P23, with associated power attenuation coefficients around, respectively, 1.03 dB/cm and 0.72 dB/cm.

The estimation of the intrinsic quality factor and the associated power attenuation coefficient of the tested devices are collected in Table 5.2. Resuming, it has been proved that the annealing leads to a reduction the losses, as can be observed from the comparison of the results with identical resonators (with length 736 μm) on the wafers P19, P20, and P23. However, the devices on the annealed samples do not allow one to find any difference between the two treatments. On the other hand, longer resonators ($L \approx 6.28 \mu\text{m}$) show that the best performance can be found on P23, which is annealed for 5 minutes at 40 Torr, with an estimated value of the power attenuation coefficient around 0.7 dB/cm. It is important to underline that this estimation is, obviously, an upper bound, since it assumes that all the losses are related to the propagation in the waveguides and that the coupling of MZI₂ is negligible.

Now, some comments on the reason why the tested resonators on the same wafer give such different values of the intrinsic quality factor. It is possible to state that



(a) P20



(b) P23

Figure 5.9: Calculated values of the intrinsic quality factor of the rings with the tunable couplers on P20 and P23. Each point is given by the average over all the resonances of the spectrum, and the error is the standard deviation divided by the square root of the number of resonances.

it is not related to the curvature of the waveguide: in fact, as shown in Figure 5.5b, the device with a radius equal to 20 μm exhibits approximately the same behavior with respect to the device 6 times bigger.

However, the situation changes drastically with the very long resonator, and the key is likely to be its shape. In fact, it is not a circular structure, but it is mainly composed of straight waveguide, as shown in Figure 3.27b, and the coupler is realized with a MZI. One could think that the point coupler could introduce some punctual losses: however, if this would be the case, there might be a difference between the Q_i evaluated from rings with different radii on the same wafer. Thus, the most likely reason is that the annealing is most effective on the straight parts, which are around the 90% of the total length of the long resonator.

Wafer	Treatment	Length (mm)	Q_i $\times 10^6$	α (dB/cm)
P19	-	0.736	0.35	2.06
P20	20 T - 1 min	0.736	0.45	1.61
		6.28	0.70	1.03
P23	40 T - 5 min	$62.8 \cdot 10^{-3}$	0.28	2.58
		0.126, 0.246, 0.368, 0.736	0.45	1.61
		6.28	1.00	0.72

In Figure 5.10 some SEM pictures of the waveguides are displayed. We can recognize the effect of the annealing on the straight waveguide (left column), since the vertical stripes present in Figure 5.10a seem to be reduced in Figures 5.10c and 5.10e. However, the sidewalls of the annealed curved waveguides are still characterized by some roughness, which is likely to be the reason of the higher losses in the circular ring resonators.

To definitely state that, more tests should be performed. First, an AFM analysis of the roughness of the sidewalls can provide more information to quantitatively estimate the impact of the annealing on the bent waveguides. In addition, new devices can be designed. A racetrack configuration with variable curve parts (with radius R) and variable straight portions (L_S) would give an effective power attenuation coefficient equal to

$$\alpha_{eff} = \alpha_c \frac{2\pi R}{2\pi R + L_S} + \alpha_s \frac{L_S}{2\pi R + L_S} \quad (5.5)$$

where α_c and α_s are, respectively, the power attenuation coefficients of the straight and the curved waveguides. This kind of structure would allow one to fabricate compact resonators and to limit the losses due to the curved waveguides.

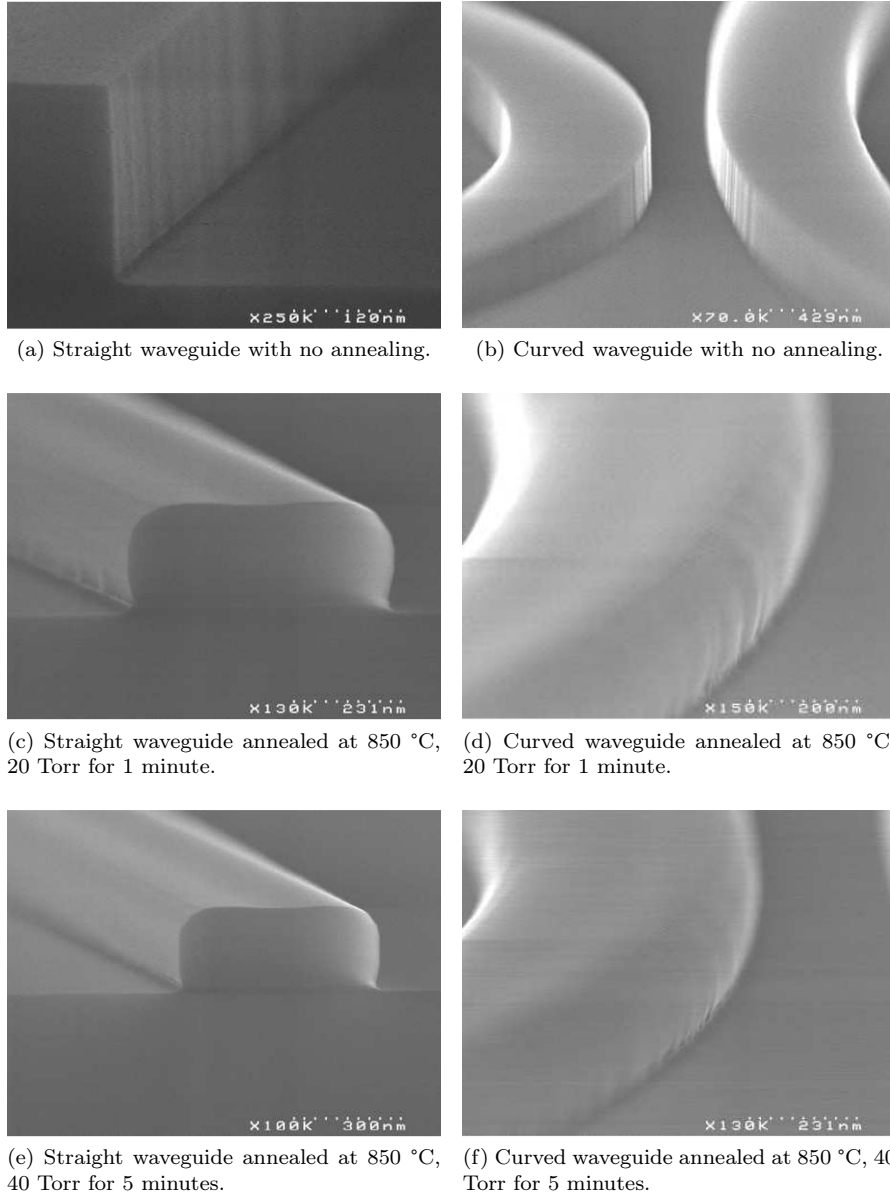


Figure 5.10: SEM pictures of the straight (left column) and the curved (right column) waveguides on three samples with no annealing and the two processes used. While the roughness on the sidewalls of straight waveguides is smoothened by the annealing, it seems to be still present on the curved waveguides.

Chapter 6

Nonlinear Coupling of Linearly Uncoupled Resonators

In this final chapter, the results about the nonlinear coupling of linearly uncoupled resonators (described in section 3.5) are detailed.

In the first section, the measures related to the device exploiting a directional coupler to isolate the modes (section 3.5.1) are presented. First, the linear characterization of different devices is shown, which allows to evaluate the impact on the optical behavior of the different geometrical parameters used. Then, the device is used to realize dual-pump SFWM with the suppression of the generation of unwanted parasitic photons due to single-pump SFWM: in fact, the capability of independently controlling the resonances of the two resonators allows one to selectively enhance and suppress specific nonlinear interaction between the modes.

Finally, in the second section the measure with resonators isolated through a Mach-Zehnder interferometer (section 3.5.2) are detailed. In particular, it is highlighted that the use of such a device has three advantages with respect to the DC-isolated counterparts: in fact, it allows to isolate the modes over a large bandwidth, it is easier to control through thermal phase shifter the coupling between the resonators and the strength of the nonlinear interaction is four times higher.

6.1 Directional coupler isolation

The first kind of devices investigated is the linearly uncoupled resonators through the directional coupler, which are described in section 3.5.1. Several versions are realized on the chip, which are placed on the subdies (4,1), (4,2), (5,1), and (5,2). In fact, the values of the gaps and the length of the directional couplers are changed to compensate eventual fabrication imperfections or errors in the estimation of the coupling and the losses.

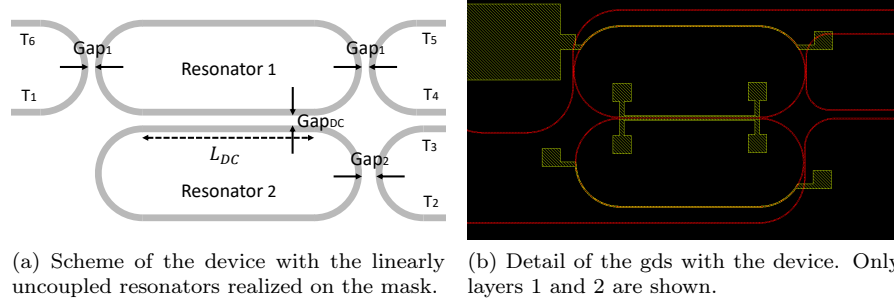


Figure 6.1

Device	L_{DC} μm	Gap_{DC} nm	Gap_1 nm	Gap_2 nm
24	92	150	120	180
63	92	120	160	150
72	92	135	160	150
78	82	150	160	150
81	92	150	160	150
84	102	150	160	150

Table 6.1: Parameters of the devices with the linearly uncoupled resonators tested in the characterization.

The device is sketched in Figure 6.1: the straight parts of the resonators have the same length ($L_{DC} = 82 \mu\text{m}$, $92 \mu\text{m}$, or $102 \mu\text{m}$), while the gaps between them are equal to 120 nm, 135 nm, and 150 nm. The gap between Resonator 1 and the two coupled waveguides are equal to 120 nm or 160 nm, while the gap between Resonator 2 and its coupled waveguide is equal to 120 nm, 150 nm, 180 nm, 210 nm, 240 nm, or 270 nm. Each device is associated to a different number, which is present on the chip and on the list of all the devices [236].

6.1.1 Linear characterization

First, I compared the optical spectra of three devices having the same gaps between the resonators and the coupled waveguides ($\text{gap}_1 = 160 \text{ nm}$ and $\text{gap}_2 = 150 \text{ nm}$) but different parameters of the directional coupler. Following the simulations presented in section 3.5.1, the device with $600 \times 220 \text{ nm}^2$ having the DC with $L_{DC} = 92 \mu\text{m}$ and a gap equal to 150 nm should provide the optical isolation between the two resonators. This is confirmed by looking at the spectra of the devices in Figure 6.2, which are obtained by injecting the light in the waveguide coupled to Resonator

2 through a lensed fiber aligned to the port T_2 and by collecting the optical response from the port T_3 (see Figure 6.1a). If the DC uncouples the racetracks, we should observe only one comb of resonances, except in the spectral region where the two resonators are resonant at approximately the same frequency. In fact, the isolation is guaranteed by two different mechanism: the low coupling of the directional coupler and the different spectral position of the resonances. This situation can be observed in the spectrum of the device 81 (Figure 6.2a), where the resonances of the second resonator are barely visible from 1510 nm to 1560 nm. On the other hand, the devices 84 and 78, whose spectra are displayed in Figures 6.2b and 6.2c, have the resonators uncoupled in a spectral region with, respectively, lower (<1530 nm) and higher (>1560 nm) wavelength. Finally, the devices with different gaps of the DC (72 and 63) show a significant coupling from 1500 nm to 1600 nm.

Then, I moved to the evaluation of the coupling between the resonators and the waveguides. Regarding the Resonator 1, I compared the devices 81 and 23, which have the same parameters of the DC and the same value of gap_2 (150 nm), but different values of gap_1 (160 nm and 120 nm, respectively). To do that, I aligned the external lensed fibers to the ports T_1 and T_6 in Figure 6.1a. Since Resonator 1 has two coupled waveguides, it should be in the critical coupling condition if the gaps are small enough to make the round trip losses negligible. Thus, I decided to work with devices having gap_1 equal to 120 nm: in fact, the quality factor should remain almost constant even at higher optical powers (which leads to nonlinear losses), and it would be easier the spectral alignment of the laser, since the resonance is broader.

In the end, I evaluated the coupling of the second resonator, whose resonances can be observed by aligning the lensed fiber to the ports T_2 and T_3 in Figure 6.1a. As can be seen from Figure 6.9b, the gap equal to 180 nm which separate Resonator 2 from the coupled waveguide allows the reaching of a visibility around 90 %, which suggests that the device is close to the critical coupling condition.

DC tuning Finally, I tested the behavior of the heaters placed asymmetrically on top of the directional coupler, as described in section 2.2.4. In Figure 6.3 the spectra of the device 78 with different values of the electrical power applied to the heater are shown. As can be seen, the cold device exhibits a recognizable coupling for lower values of the wavelength, since two sets of resonances can be seen, while the resonators are uncoupled around 1570 nm. The situation is the inverse with an electrical power around 150 mW. Thus, it is possible to note that the tuning of the coupling works, but quite high values of the electrical power are needed. This values can be reduced by thinning the silica layer on top of the waveguides, but this can lead to absorption losses as discussed in section 2.2.4.

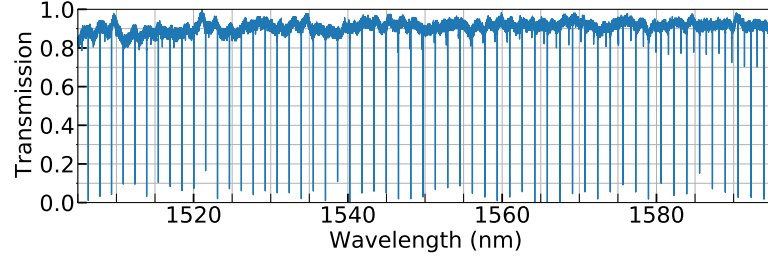
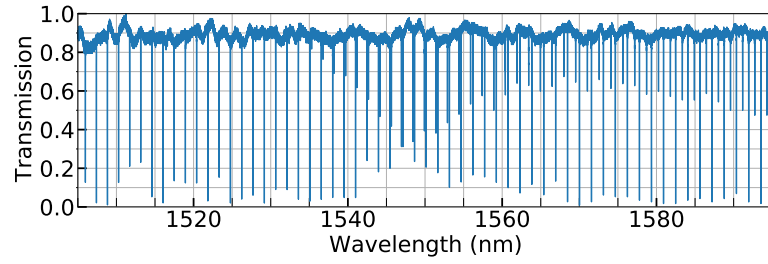
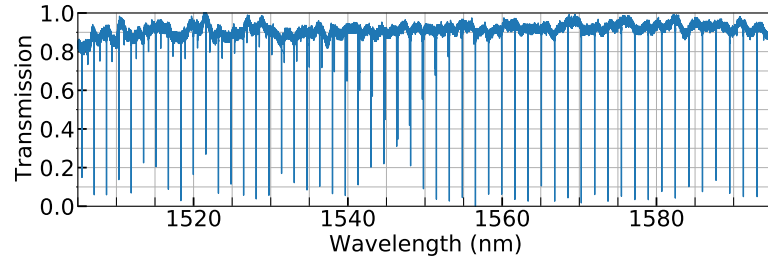
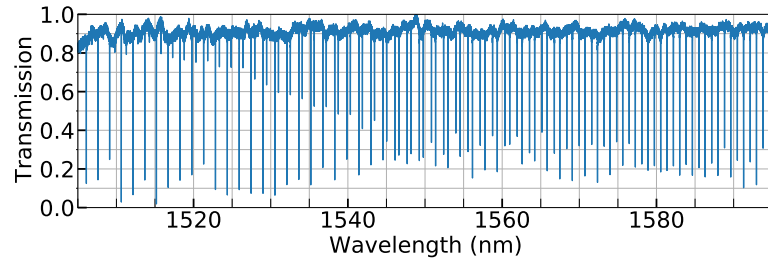
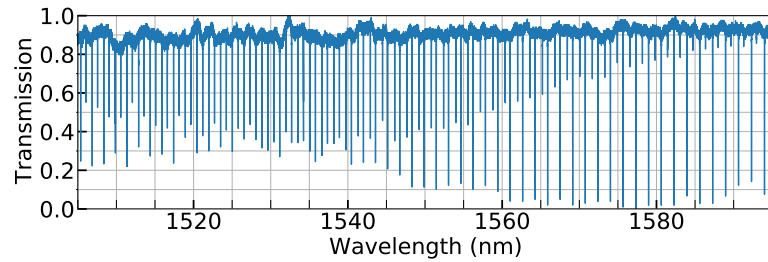
(a) Device 81: $L_{DC} = 92 \mu\text{m}$, $\text{Gap}_{DC} = 150 \text{ nm}$ (b) Device 84: $L_{DC} = 102 \mu\text{m}$, $\text{gap} = 150 \text{ nm}$ (c) Device 78: $L_{DC} = 82 \mu\text{m}$, $\text{gap} = 150 \text{ nm}$ (d) Device 72: $L_{DC} = 92 \mu\text{m}$, $\text{gap} = 135 \text{ nm}$ (e) Device 63: $L_{DC} = 92 \mu\text{m}$, $\text{gap} = 120 \text{ nm}$

Figure 6.2: Spectra of some devices with the linearly uncoupled resonators which differ only by the parameters of the directional coupler (length and gap).

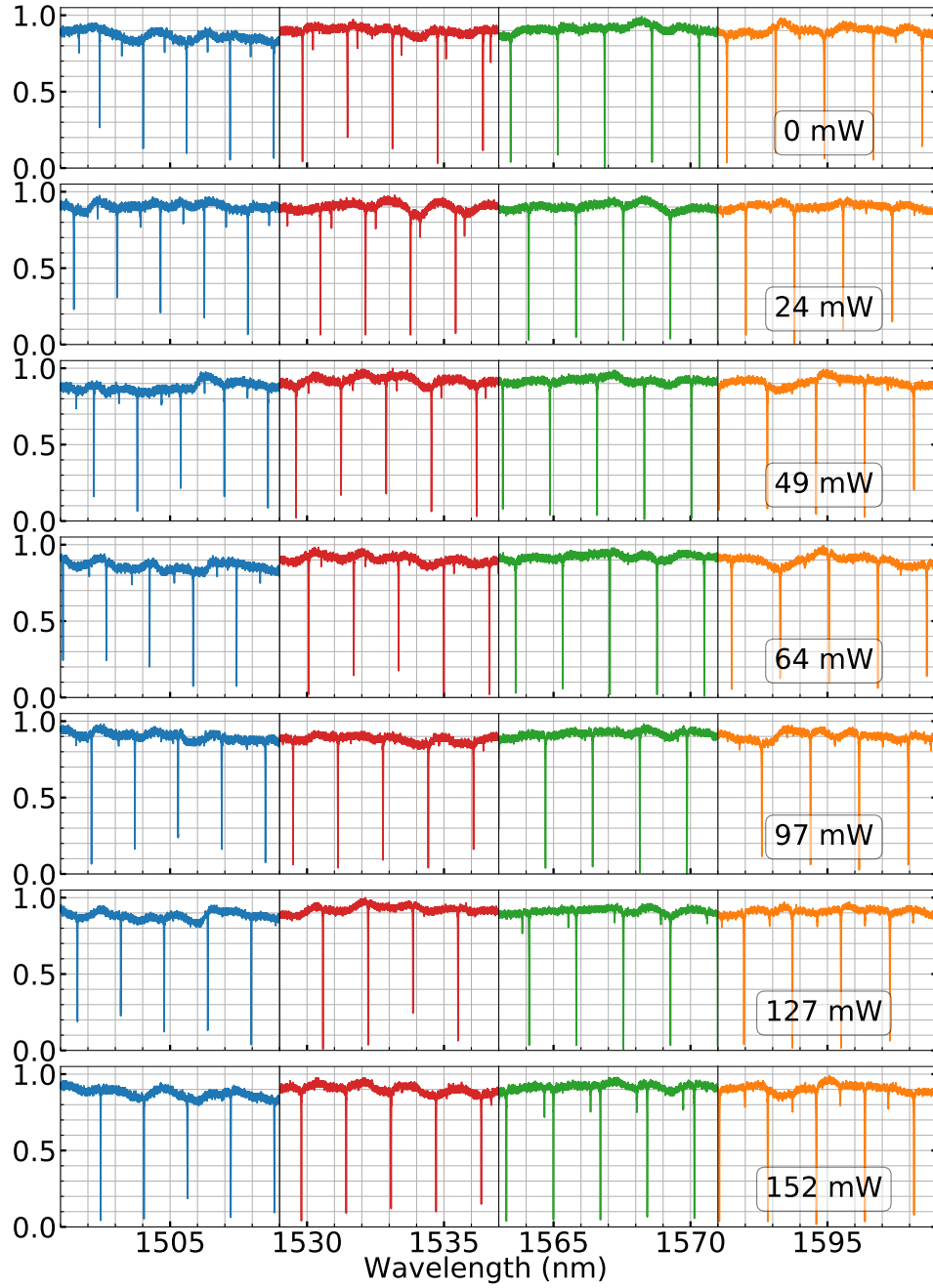
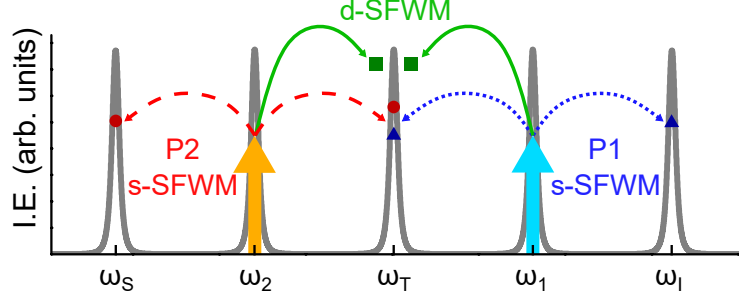
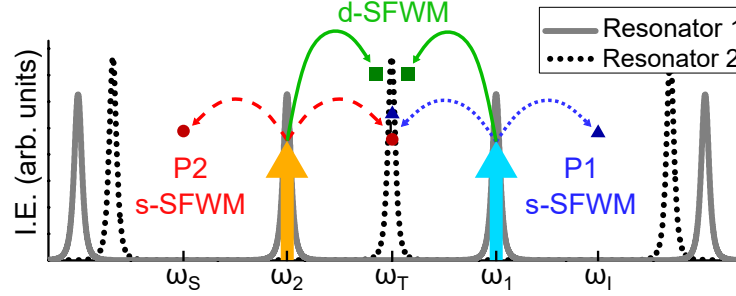


Figure 6.3: Spectrum of the device 78 by changing the electrical power applied to one of the heater placed asymmetrically with respect to the directional coupler. The electrical powers are displayed in the boxes.



(a) In a conventional ring resonator, photons at ω_T are generated by d-SFWM and by s-SFWM with pumps at ω_1 and ω_2



(b) In linearly uncoupled resonators, one can exploit the modes of the two racetracks and minimize the enhancement of the nonlinear parasitic processes.

Figure 6.4: Schemes of the d-SFWM process in a conventional ring resonators (a) and in a device with linearly uncoupled resonators.

6.1.2 Suppression of parasitic processes in d-SFWM

Dual-pump spontaneous four-wave mixing (d-SFWM) consists in the generation of photons at ω_T whose mode interacts nonlinearly with two pump lasers at ω_1 and ω_2 , such that $2\omega_T = \omega_1 + \omega_2$, as explained in section 2.1.2. This process can be used to generate single-mode squeezed light, a central resource in the development of continuous-variable quantum computing [303]. As described in section 2.3.4, d-SFWM can naturally exploit the enhancement of the nonlinear interaction of the optical modes that can be obtained in integrated microring resonators [304]. However, the multimode nature of the rings leads to the simultaneous amplification of other nonlinear phenomena. In Figure 6.4a is possible to observe that the presence of two resonant laser pumps (P_1 and P_2) having frequencies ω_1 and ω_2 leads to the generation of photon pairs at ω_T through d-SFWM. At the same time, additional photons at ω_T are generated through single-pump four-wave mixing (s-SFWM): P_1

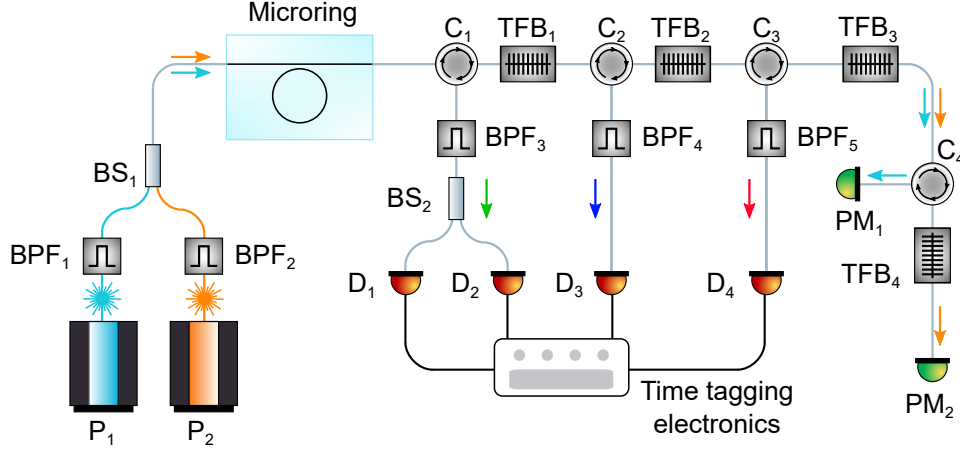


Figure 6.5: Experimental set-up used for the characterization of the d-SFWM and s-SFWM processes in a conventional resonator.

stimulates the creation of pairs with photons at ω_T and ω_I such that $2\omega_1 = \omega_I + \omega_T$, while P_2 creates photons at ω_T and ω_S such that $2\omega_2 = \omega_S + \omega_T$.

To quantitatively characterize these nonlinear parasitic processes, I used the experimental set-up shown in Figure 6.5, and I used the Resonator 1 of the device 24 as a conventional ring (i.e. I did not exploit the modes of Resonator 2). The light from two tunable lasers (Santec TSL710 and TSL510) is combined through a fiber beam splitter (BS_1) and coupled to the chip using a collimator and lens to match the mode field diameter of the edge coupling tip on the chip. Two band-pass filters BPF_1 and BPF_2 (FWHM around 8.8 nm) have been used to filter out the amplified spontaneous emission from the lasers. P_1 and P_2 are tuned on resonance with the resonator at ω_1 and ω_2 , and the set-up allows on eto detect photons generated within the resonances at ω_I , ω_S , and ω_T (displayed in Figure 6.6), which are collected through a lensed fiber coupled to the chip and connected to a circulator (C_1). The filtering of the generated photons is performed by fiber tunable Bragg filters¹ (TFB) and band-pass filters² (BPF): if the light is resonant with the TFB, it is back-reflected and routed to the BPF through a circulator. TFB used in reflection allows to obtain a narrow band (around 80 pm, as shown in Figure 6.7), while the broader BPFs effectively suppress the residual of the pumps. Four Superconductive Single-Photon Detectors (SSPD) supplied by Photon SpotTM are used to detect the incoming

¹OEDWDM-025 by O/E Land www.o-eland.com/FiberGratingProducts/FiberGrating_wdm.php

²composed of two single-band bandpass filter by Semrock www.semrock.com/filterdetails.aspx?id=nir01-1550/3-25

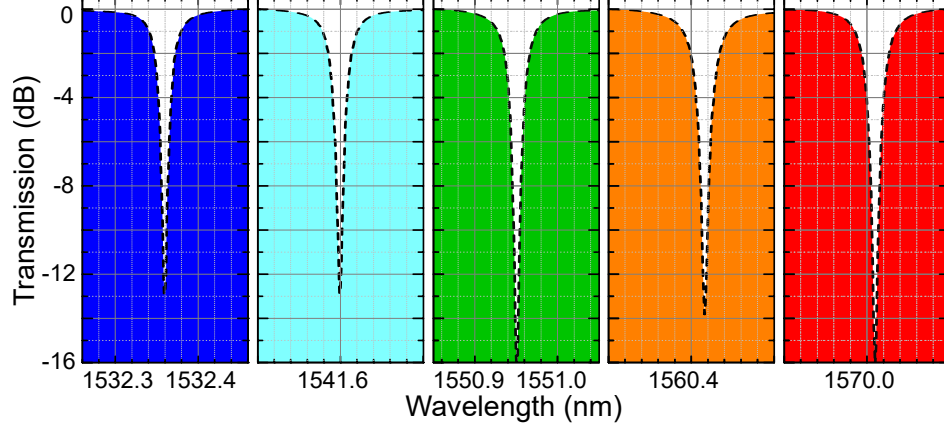


Figure 6.6: Resonance of the Resonator 1 of the device 24 used to characterize quantitatively the relation between d-SFWM and s-SFWM in a conventional resonator. Two lasers tuned at $\lambda_1 = 1541.599$ nm and $\lambda_2 = 1560.417$ nm generate photons at $\lambda_T = 1550.951$ nm through d-SFWM, but also pairs of photons at λ_T , $\lambda_I = 1532.360$ nm and $\lambda_S = 1570.010$ nm through s-SFWM.

photons: D_1 and D_2 reveal the ones selected by TFB_1 tuned at λ_T and split by the beam splitter BS_2 , while D_3 and D_4 detect photons at, respectively, λ_S and λ_I . Finally, the alignment of the two laser pumps is checked during the whole experiment using two power meters (PM_1 and PM_2), a circulator (C_4), and an additional band-pass filter (TFB_4).

In Figure 6.8 the results of the experiments are displayed. For all the values of the pump powers, I analyzed the histogram of the coincidences between the detectors. Since photons generated through FWM are generated simultaneously, the histograms show a peak, whose integral divided by the integration time gives the measured coincidence rate $R_{D_i D_j}$. Then, the generation rate of pairs in the coupled waveguide [R^{wg} in equation (2.65)] is obtained by dividing by the losses between the ring and the detectors:

$$R^{wg} = 2 \frac{R_{D_i D_j}}{\Gamma_{D_i} \Gamma_{D_j}} \quad (6.1)$$

where Γ_{D_i} are the losses between the waveguide coupled to the resonator and the detectors (including the efficiency of the detection), while the factor of two comes from equation (2.67). The losses associated to the detectors D_1 , D_2 , D_3 , and D_4 are, respectively, $\Gamma_1 \approx -9.1$ dB, $\Gamma_2 \approx -8.4$ dB, $\Gamma_3 \approx -10.3$ dB, and $\Gamma_4 \approx -6.5$ dB. Then, the errors on the measured coincidence rates are calculated by dividing the square root of the counts for the integration time.

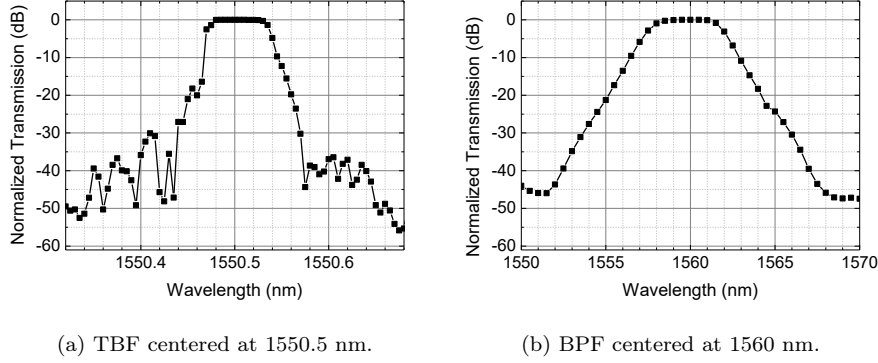


Figure 6.7: Relative transmission of a TBF and a BPF used.

The lines in Figure 6.8 are obtained from equations (2.63) and (2.68), where γ is assumed to be equal to $110 \text{ W}^{-1}\text{m}^{-1}$, $n_g = 4.144$, and the quality factors of the five resonances (displayed in Figure 6.6) are given by $Q_T = 63.8 \cdot 10^3$, $Q_S = 59.2 \cdot 10^3$, $Q_I = 75.5 \cdot 10^3$, $Q_1 = 67.99 \cdot 10^3$, $Q_2 = 55.1 \cdot 10^3$. Finally, the length of the resonator is equal to $372 \text{ }\mu\text{m}$.

As expected from the relations (2.63) and (2.68), the generation rate for the d-SFWM is unchanged as long as the product of the two pump powers is held fixed, while the generation rate of the s-SFWM processes scale quadratically with the appropriate pump powers. We can define the generation rates of the parasitic processes as the sum of the two s-SFWM rates (black solid line and black squares in Figure 6.8): as can be seen, it can even be one order of magnitude larger than the generation rate of the d-SFWM process, with a maximum signal-to-noise ratio (SNR) of only about 2 when the two pump powers are equal. This effect is a serious issue when dealing with the generation of squeezed light through d-SFWM, since the presence of parasitic photons at ω_T reduces the level of squeezing that can be generated³. In addition, it is worth to mention that parasitic nonlinear processes can lead to unwanted correlation between generated photons, as shown in [305].

Strategies have been proposed to overcome this intrinsic limit. In one approach, the two pump lasers are slightly detuned from resonance, such that the s-SFWM rates are suppressed [57] but with a trade-off between SNR and generation rate. Alternatively, one can use systems composed of two or more linearly coupled resonators, as discussed in section 3.4, to engineer the spectral position of the resonant modes, with nonlinear phenomena selectively enhanced or suppressed [56]. While this can be very effective, the suppression of the parasitic processes is limited by

³See the Supplemental Material of the work realized by Zhao and colleagues [57] for the theoretical analysis of the impact of the parasitic photons on the squeezing level.

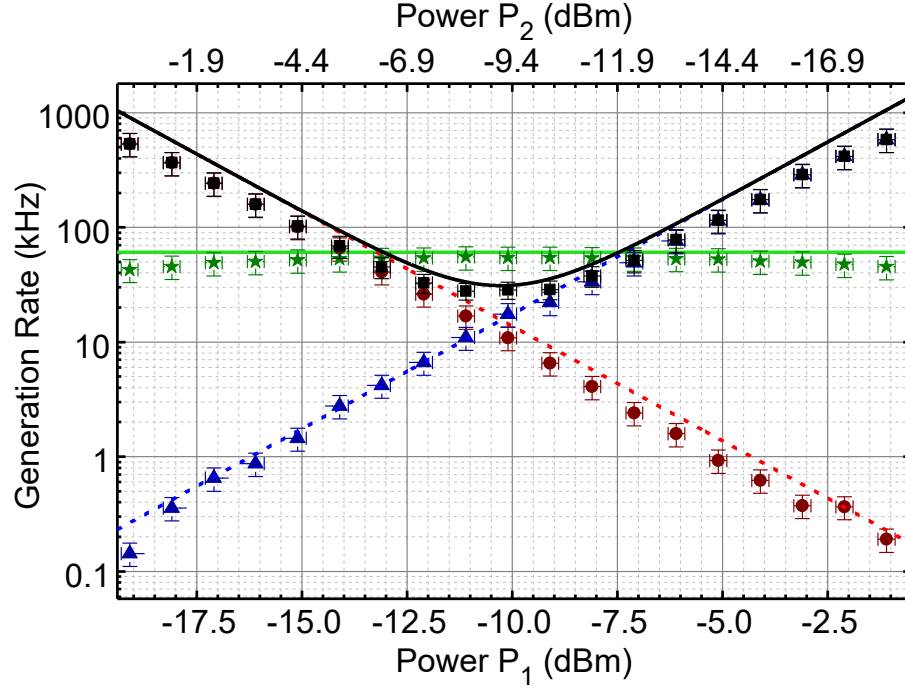


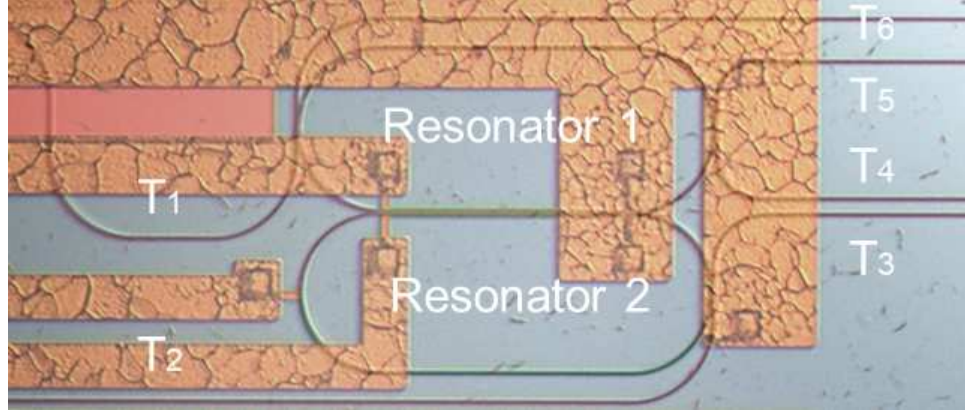
Figure 6.8: Measurement of the pair generation rate in a single silicon microring resonator when the product of the powers of the two pumps is fixed. The blue triangles and the red circles show the s-SFWM processes pumped by the lasers at ω_1 and ω_2 , respectively. The black squares show the sum of the parasitic process rates, and the green stars show the d-SFWM generation rate. The measures are compared with the theoretical calculation (shown with the dashed blue line for the P_1 -pumped s-SFWM, the dashed red line for the P_2 -pumped s-SFWM, and the green line for d-SFWM).

the achievable resonant splitting of the coupled modes.

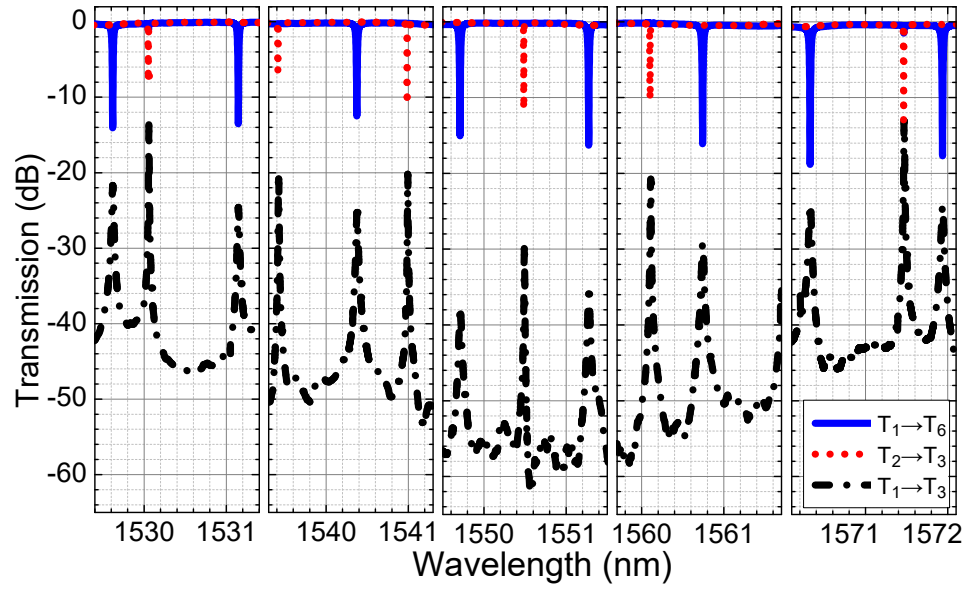
Another possible strategy consists in the use of linearly uncoupled resonators. In fact, the two sets of resonances associated to the two racetracks can be independently tuned to selectively enhance or suppress the nonlinear interaction of the modes. This permits, thus, to enhance d-SFWM and to reduce drastically the efficiency of the parasitic processes stimulated by the two pumps, as sketched in Figure 6.4b. In this work it is experimentally proved that the use of such a structure allows for the effective control of the nonlinear interaction between optical modes, leading to the ability to enhance or suppress the generation of photon pairs through spontaneous four wave mixing. In particular, an improvement of the signal-to-noise (SNR) ratio by over four orders of magnitude with respect to the conventional ring resonator is shown. In the following paragraphs it is detailed the procedure to measure the attenuation of the s-SFWM parasitic processes and the experiment of d-SFWM.

Suppression of s-SFWM First, I studied the dependence of s-SFWM with respect to the detuning of the modes of the resonators. The linear characterization of the device is shown in Figure 6.9b, in which it is possible to see the modes associated to Resonator 1, which are within the spectrum obtained by injecting the light in the port T_1 and collecting in from port T_6 (blue line), and the resonances of Resonator 2 (red dotted line, $T_2 \rightarrow T_3$). In addition, the spectrum obtained from the ports T_1 and T_3 (dashed black line) allows to estimate the isolation of the resonators, which is around 30 dB at 1550 nm and it decreases to around 13 dB at 1530 nm and 1570 nm.

The set-up used is shown in Figure 6.10: it is similar to the one used for the experiment with the conventional ring resonator (Figure 6.5). The main difference is the use of a voltage source (Keithley 2400 Source Meter) and a multi-contact edge to shift the spectral position of the resonances of Resonator 1 to selectively enhance or suppress the nonlinear interaction with the modes of Resonator 2. To measure s-SFWM, I switched of the laser P_1 and I aligned the laser P_2 to one resonance (Ω_2) of Resonator 1 at around 1560.7 nm (which is observable in the fourth panel of Figure 6.9b). Then, the filter TFB_1 is tuned on one resonance of Resonator 2 at around 1550.5 nm (Ω_T), while TFB_2 is tuned at frequency $2\omega_2 - \omega_T$, where ω_2 and ω_T are, respectively, the frequencies of the resonances Ω_2 and Ω_T . The starting point of the experiment consists in the measure of s-SFWM when Ω_2 is aligned with two resonances of Resonator 2 (Ω_T and Ω_U). This can be realized by tuning the Resonator 1 through the heater placed on top, and the resonances shift as shown in Figure 6.11a: at around 20.7 mW the resonances are equally spaced in frequency, and s-SFWM pumped by a laser tuned on Ω_2 is maximally enhanced. If the electrical power changes, the spectral alignment is lost, and the process reduces its efficiency since the involved fields experience a lower enhancement. The result is shown in Figure 6.12. As can be seen, the measured data are in quite good agreement with the theoretical model, which simulates the nonlinear interaction in the used



(a) Optical picture of the device 24 with the six access ports indicated.



(b) Linear characterization of the device 24. The blue solid and the dotted red lines display the resonances of, respectively, Resonator 1 and Resonator 2. The black dashed line is the cross-transmission, which highlights the uncoupling between the resonators.

Figure 6.9

structure. This result shows that by tuning the two sets of resonances one can manipulate the nonlinear coupling of the modes of the resonators, and, consequently, the generation of pairs due to the nonlinear processes occurring in the device. In particular, a detuning of around 65 pm (8.1 GHz, around 13 times the linewidth of the resonances of R_2) leads to a suppression of around three orders of magnitude with respect to perfect nonlinear coupling. The detuning of the resonances involved is estimated from the driving voltage and the characterization of the heater:

$$\delta_2 = (\bar{\omega}_2 - \omega_2) - \frac{(\bar{\omega}_T - \omega_T)}{2} - \frac{(\bar{\omega}_U - \omega_U)}{2} = \frac{\omega_U - \omega_S}{2} \quad (6.2)$$

where $\bar{\omega}_2$, $\bar{\omega}_T$, and $\bar{\omega}_U$ are the frequencies of Ω_2 , Ω_T , and Ω_U , respectively at 20.7 mW applied on the heater of R_1 (i.e. when the three resonances are equally spaced). During the experiment, the spectral position of the involved resonances are estimated from the characterization of the spectral response of the resonators with respect to the variation of the applied voltage, as shown in Figure 6.11c. In particular, from a linear fit of the resonance shifts, we estimate the tuning capability of our system. As can be seen, the main effect is the shift of the resonances of Resonator 1, but the thermal cross-talk leads also to a smaller shift of the resonances Ω_T and Ω_U .

It is worth to note that in the experiment is fundamental to align the Bragg filters at ω_T and at $2\omega_2 - \omega_T$. In fact, when the detuning is relevant, by two main mechanisms bring to the generation of pairs through s-SFWM:

- the emission of pairs with a photon within the resonance Ω_T (at ω_T) and another one at $2\omega_2 - \omega_T$, which exploits the enhancement of the field at ω_T
- the emission of pairs with a photon within the resonance Ω_U (at ω_U) and another one at $2\omega_2 - \omega_U$, which exploits the enhancement of the field at ω_U

Thus, if one keeps the filters TFB₁ and TFB₂ with, respectively, the resonances Ω_T and Ω_U , then the collected photons would belong to different pairs and no coincidences would be detected.

d-SFWM With the possibility of attenuating the parasitic processes demonstrated, I proceeded to the dual-pump SFWM experiment. I aligned the laser pumps to two resonances of Resonator 1 (Ω_1 and Ω_2 at vacuum wavelengths $\lambda_1 = 1540.374$ nm and $\lambda_2 = 1560.742$ nm), which are equally spaced in frequency about Ω_T (at $\lambda_T = 1550.491$ nm). This configuration is realized at around 12.5 mW, as shown in Figure 6.11b, and is associated with a detuning of the s-SFWM resonances of around -160 pm (-20 GHz), and the estimation of the resulting attenuation of the s-SFWM processes is around -37.3 dB. The quality factors of Ω_1 and Ω_2 are around, respectively, $Q_1 = 6.7 \cdot 10^4$ and $Q_2 = 5.7 \cdot 10^4$, while Ω_T has a much higher quality factor, $Q_T = 3.2 \cdot 10^5$. We align the tunable filter TFB₁ to λ_T , while TFB₂ and TFB₃ are tuned to route photons at $\lambda_I = 1530.388$ nm and $\lambda_S = 1571.129$

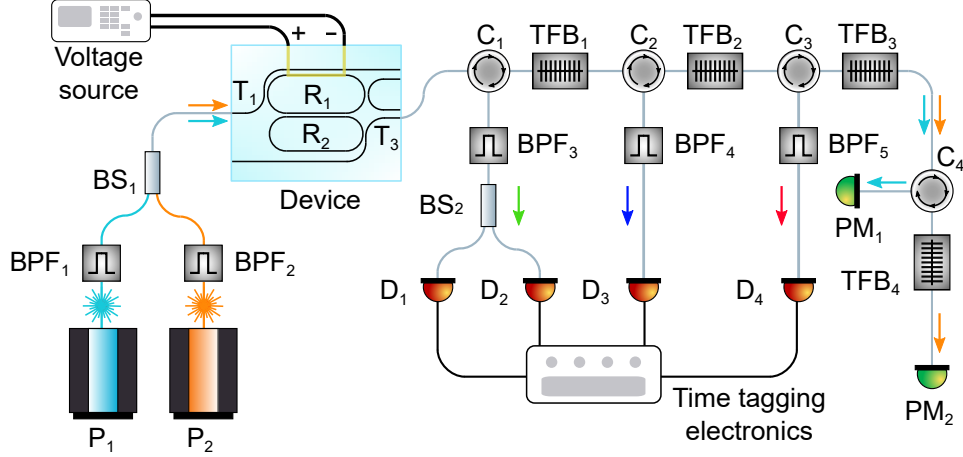
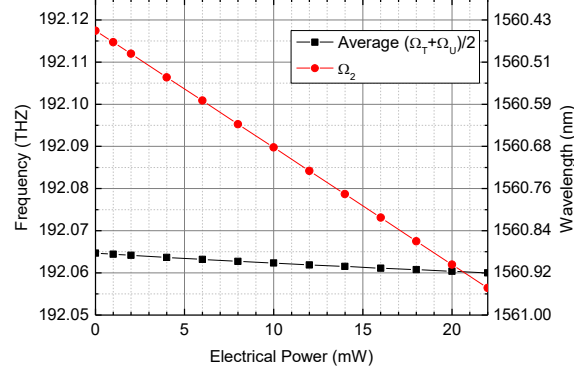


Figure 6.10: Experimental set-up used for the characterization of the d-SFWM and s-SFWM processes in a the device with linearly uncoupled resonators.

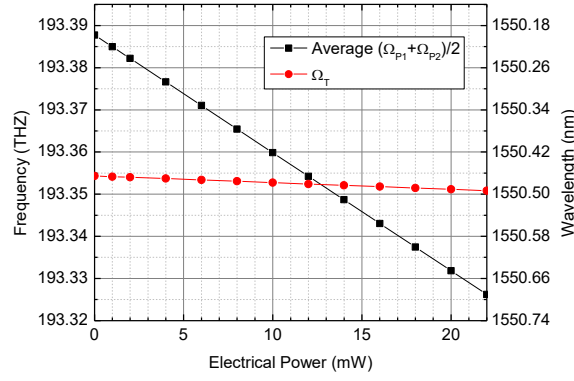
nm to D_3 and D_4 , respectively. The analysis of the coincidences on the detectors allows for the recognition of the pairs generated through the different processes. In particular, the d-SFMW should give coincidence between the detection events at D_1 and D_2 . Similarly, the single-pump processes should result in coincident detection: P_1 -SFWM between the events at D_3 and D_1 (or D_3 and D_2), and P_2 -SFWM between the events at D_4 and D_1 (or D_4 and D_2).

The total insertion losses from the lasers to the waveguide coupled with R_1 at the port T_1 are around -7.8 ± 0.1 dB for the light from both P_1 and P_2 . The losses from the waveguide coupled with R_1 at the port T_3 to D_1 and D_2 are around -10.7 ± 0.3 dB and -10.1 ± 0.3 dB, respectively, for the photons at ω_T ; the losses from T_3 to D_3 are -11.9 ± 0.3 dB for photons at ω_I , and -7.6 ± 0.3 dB from T_3 to D_4 for photons at ω_S . The efficiency of the detectors is -1.00 ± 0.05 dB.

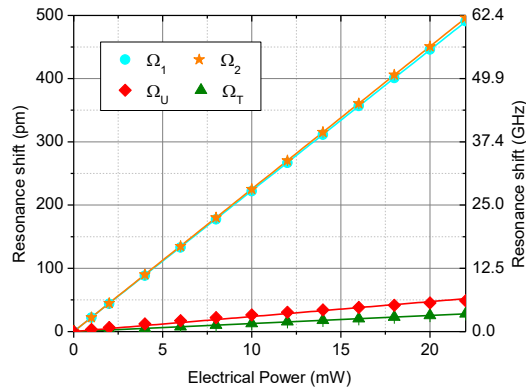
Figure 6.13 shows the result of a coincidence experiment with the current device, where 0.95 ± 0.05 mW of optical power is coupled into the waveguide from each pump laser. The data are acquired for 20 minutes, and the histograms have a bin-width equal to 35 ps, which is comparable with the time jitter of the detectors. The red peak shows that photons arriving on D_1 and D_2 are emitted at the same time, since their arrival time is correlated: this clearly demonstrates they are emitted through d-SFWM, since any other process that can generate photons at λ_T cannot be characterized by this temporal correlation. The measured coincidence rate is equal to 164.2 ± 0.4 Hz, which corresponds to an internal generation rate in the second resonator equal to 62 ± 6 kHz, and the CAR is 1190 ± 10 . The coincidence rate is estimated by integrating the peak within the whole window (and subtracting



(a) Alignment of the resonance Ω_2 of Resonator 1 between two resonances of Resonator 2 (Ω_T and Ω_U) to enhance s-SFMW.



(b) Alignment of the resonances Ω_1 and Ω_2 of Resonator 1 around one resonance of Resonator 2 (Ω_T) to enhance d-SFMW.



(c) Shifts of the resonances involved in s-SFMW and d-SFMW. From the fits, the tuning efficiencies of the resonances turn out to be $\alpha_1 = 22.3$ pm/mW, $\alpha_2 = 22.5$ pm/mW, $\alpha_T = 1.27$ pm/mW, and $\alpha_U = 2.36$ pm/mW.

Figure 6.11: Shift of the resonances with respect to the electrical power applied to the heater on top of Resonator 1.

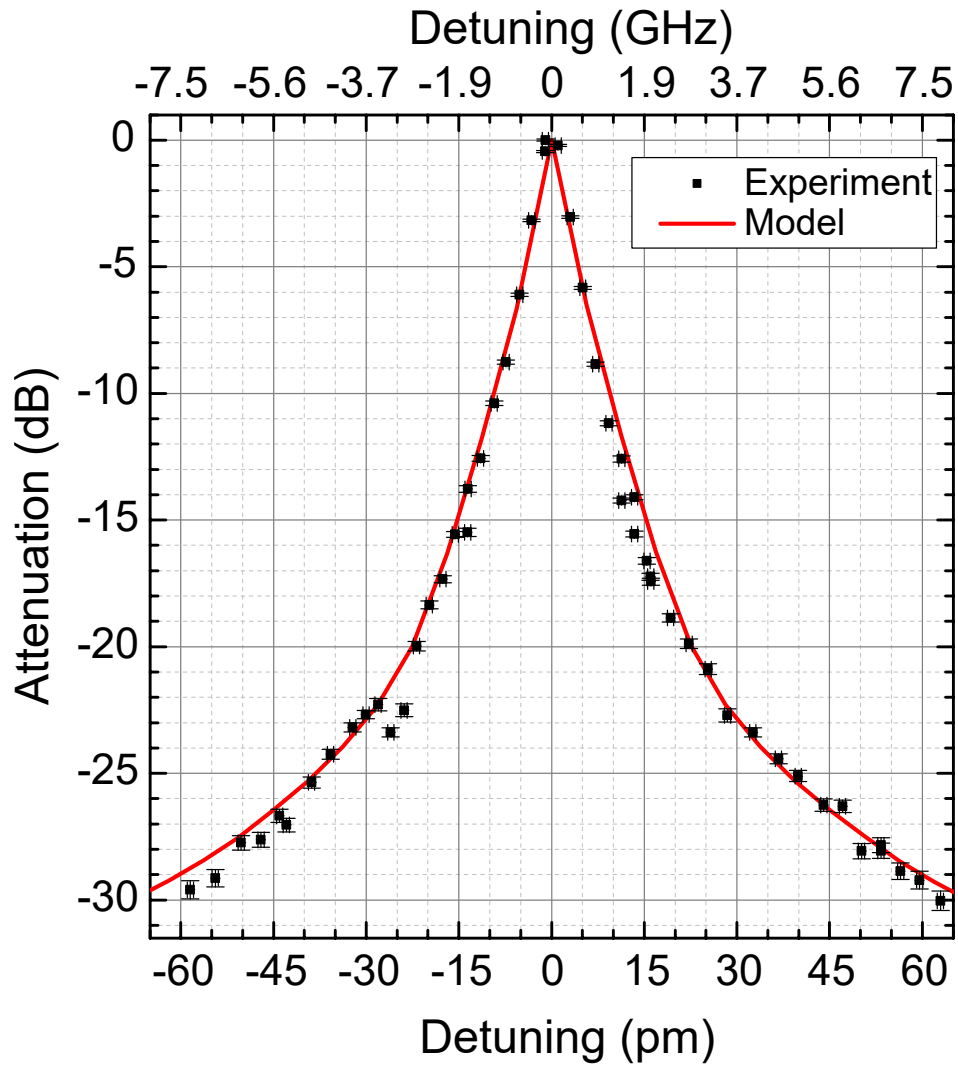


Figure 6.12: Plot showing the attenuation of s-SFWM as a function of the detuning of the resonances of the two resonators.

the noise), while the CAR is measured by taking into account the FWHM of the peak (16 bins of the histogram).

From the histograms in Figure 6.13 it is also possible to evaluate the photon pairs generated through s-SFWM, which lead to coincidence events between D_1 and D_2 with D_3 or D_4 . As can be seen, no peaks are clearly visible. In fact, the dark counts, the noise from the environment, and other parasitic processes occurring in the set-up (such as Raman emission from optical fibers) hide the signal given by time-correlated photons. This is due to the severe attenuation of the processes. Nevertheless, it is possible to estimate a lower bound for the SNR by analyzing the coincidences between D_1 and D_4 . The peak due to d-SFWM is integrated over its FWHM (16 bins), and divided by the noise, which is calculated as the average on the black histogram in Figure 6.13 multiplied by 16 bins. By taking into account the losses, one obtains a SNR equal to $(11.3 \pm 3.2) \cdot 10^3$. From the model, a SNR around $21 \cdot 10^3$ is expected, an improvement over that of a single ring system by over four orders of magnitude. The experimental estimation is lower, since the noise due to s-SFWM are overestimated.

Finally, I measured the variation of the generation efficiency with different values of the input powers. First, the product between the powers of P_1 and P_2 has been kept constant (around $0.324 \pm 0.032 \text{ mW}^2$), and the result is shown in Figure 6.14a. The black points represent the generation rate on the waveguide R^{wg} calculated from the measured coincidence rate between the detectors D_1 and D_2 and by considering the optical losses from the waveguide to the detectors ($-10.0 \pm 0.4 \text{ dB}$ and $-9.0 \pm 0.4 \text{ dB}$). As can be observed, the experimental data are in good agreement with the theoretical values calculated from (3.29) for P_2 power around -3 dBm , while the measured generation rate is reduced even by more than 20% at lower and higher values. This is related to the shift of the resonances of Resonator 1 with high optical power circulating in the device, which induces a shift of the spectral alignment of the two resonators and, then, a reduction of the generation rate, as it is shown more clearly in Figure 6.14b. In fact, I fixed the electrical power at the beginning of the experiment (with P_2 power equal to -2.84 dBm) and I changed the frequency of the laser at each step to tune them on resonance by checking the spectral alignment on the power meters.

In the end, I checked the linear dependence of the generation rate with respect to P_2 power when the intensity of P_1 is kept constant: the results displayed in Figure 6.14c show a good agreement between the experiment and the theory, confirming once again that the mechanism that gives rise to the coincidences on the detectors is dual-pump SFWM.

6.2 Mach-Zehnder interferometer isolation

In section 3.5.2 an alternative method to obtain linearly uncoupled resonators has been detailed. It is based on the use of a Mach-Zehnder interferometer, which allows

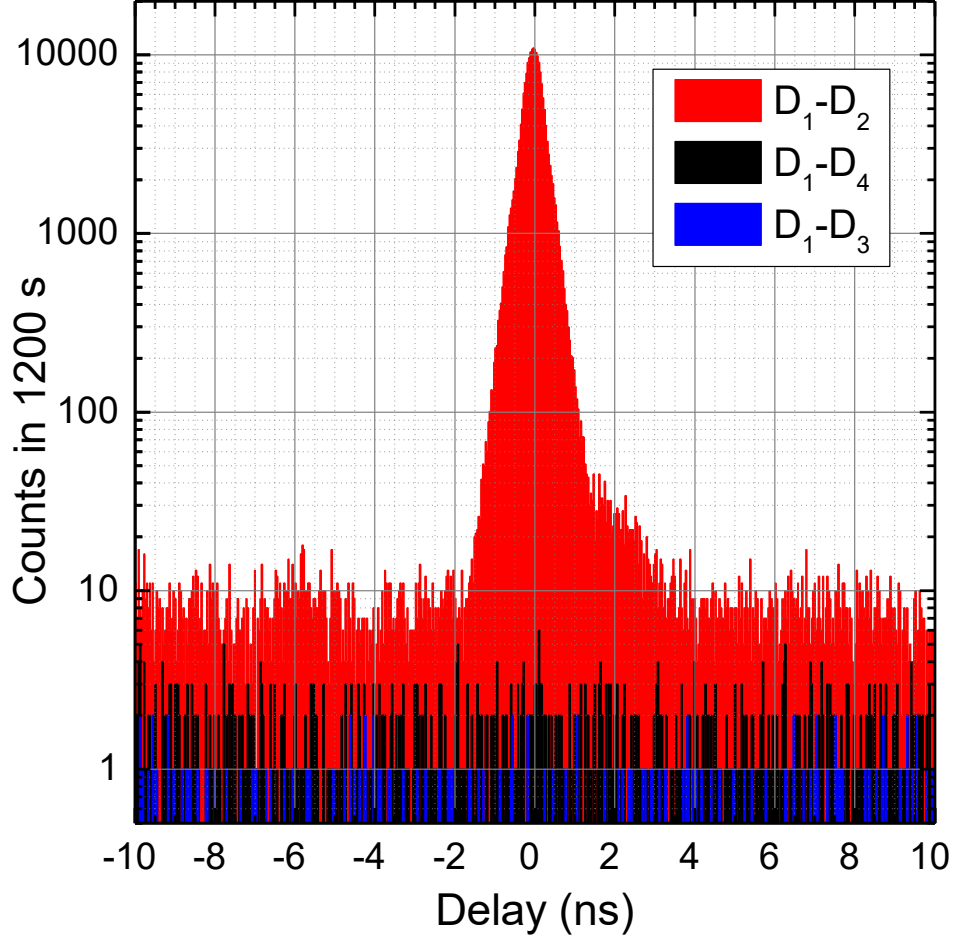
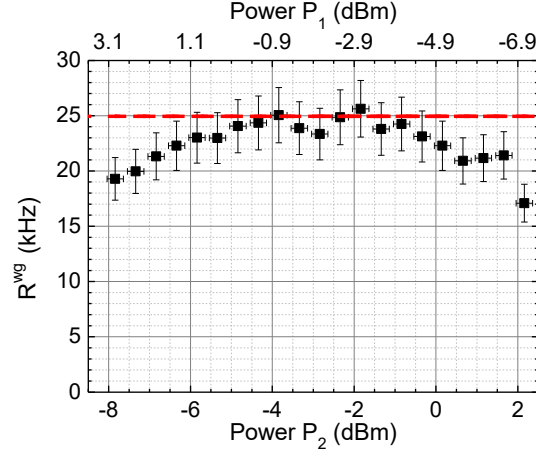
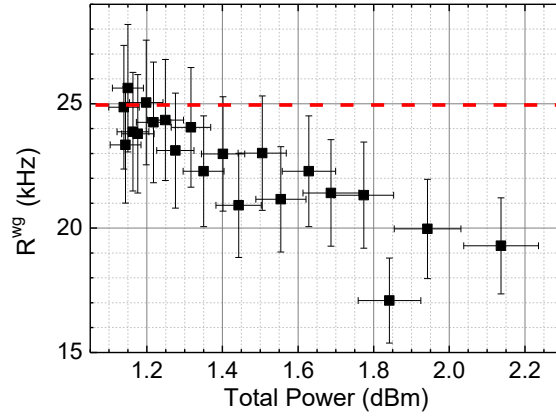


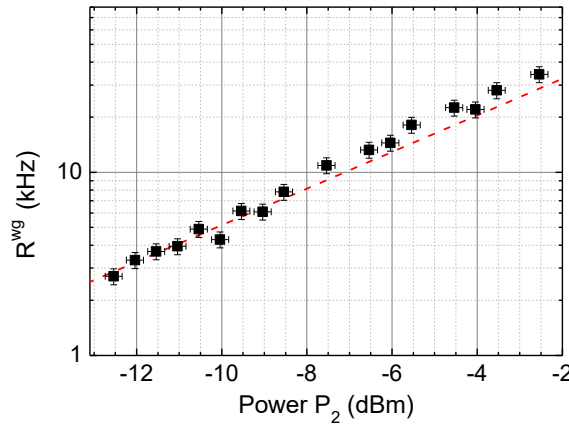
Figure 6.13: Histograms representing the coincidences events detected. The red, black, and blue histograms represent, respectively, the coincidences due to d-SFWM (events on D_1 and D_2), P_2 -SFWM (events on D_1 and D_4), and P_1 -SFWM (events on D_1 and D_3). The width of each bin is 35 ps. The delay is calculated by taking into account the different optical lengths of the fibers from the device to the detectors.



(a) Generation rate with the product between the powers of P_1 and P_2 fixed (around $0.324 \pm 0.032 \text{ mW}^2$) in the waveguide coupled to Resonator 1.



(b) Generation rate with the product between the powers of P_1 and P_2 fixed (around $0.324 \pm 0.032 \text{ mW}^2$) in the waveguide coupled to Resonator 1.



(c) Generation rate with P_1 power fixed ($-1.7 \pm 0.2 \text{ dBm}$) in the waveguide coupled to Resonator 1.

Figure 6.14: d-SFWM in linearly uncoupled resonators. The black squares represent the generation rate in the waveguide coupled to Resonator 2, which is calculated from the coincidence rate on the detectors D_1 and D_2 . The red lines are the theoretical values from (3.29).

the isolation of the modes of the resonators and, at the same time, their coupling through the nonlinear interaction. In this section the optical characterization of this kind of device is shown; in particular, the advantages with respect to the DC-isolation are highlighted, i.e. a larger spectral band in which the resonators are uncoupled, a simpler and more efficient way to tune the coupling and a higher efficiency of the nonlinear interaction.

6.2.1 Linear characterization

First, I performed the linear characterization of the device 68, which has the two waveguides coupled to Resonator 1 spaced by 120 nm with respect to the resonator, while the gap between Resonator 2 and its coupled waveguide is 140 nm. In Figure 6.15 the spectra of the device are shown: the characterization has been performed by coupling the light to the port T_1 and by collecting the variation on the transmission at the port T_6 : this allows, as in the case of the DC-isolated devices, the study of the resonances of Resonator 1 and the rough evaluation of the coupling between the resonators by the presence of smaller resonances related to the modes of Resonator 2.

From Figure 6.15 it is possible to observe immediately that the MZI allows one to tune efficiently the coupling between the resonators. In fact, the first plot from the top, which refers to the situation with no electrical power applied to the heater on top of the arm of the MZI, exhibits a imperfect isolation between the modes. By increasing the applied voltage, the coupling increases: at around 14.2 mW, in fact, the two resonators seem to be almost completely coupled, which leads to the formation of optical modes that are localized in the entire structure (i.e. they are not confined in one resonator). Then, with around 29.6 mW the uncoupling of the resonators is obtained and at 32.3 mW the initial coupling condition is regained. Thus, it is possible to observe that around 32 mW lead to a 2π phase shift on one arm, allowing the spanning of different coupling conditions between the modes. Finally, the comparison of Figures 6.15 and 6.3 show clearly that the tuning of the MZI is much more efficient.

To evaluate the spectral band in which the resonators are uncoupled and to compare the MZI-isolated device with respect to the DC-isolated one, I performed the scan of the resonances over a larger band (from 1480 nm to 1640) and I varied more finely the power applied to the MZI. As discussed in the previous section, the coupling can be evaluated by the presence of additional resonances in the spectrum. However, this depends also on the relative position between the sets of resonances associated to the two resonators. To evaluate the difference of the performance of the two kind of devices (DC and MZI based), it is fundamental to set the devices in similar conditions. In Figure 6.3 it is possible to observe that there is always a residual of the resonance of the second resonator in the 1500-1600 spectral region, and this characterization is obtained having the two resonators' resonances at approximately the same frequency around 1550 nm, as shown in Figure 6.2c. On the

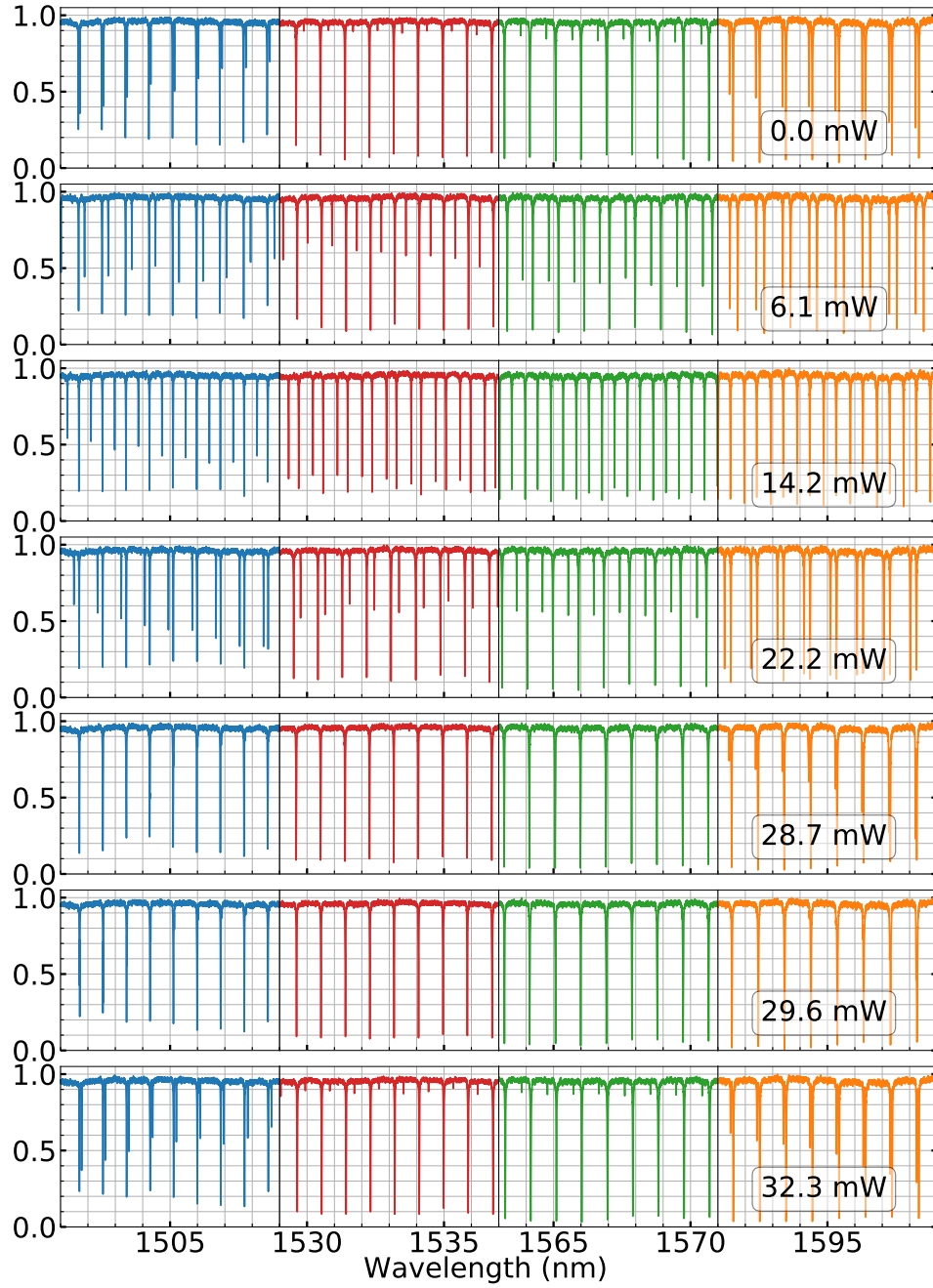


Figure 6.15: Spectra of the device 68 by changing the electrical power applied to one of the heater placed on the arms of the MZI. The electrical powers are displayed in the boxes. The tuning speed is set equal to 25 nm/s and the resolution of the spectra is 1 pm (10^5 points from 1500 to 1600 nm).

other hand, the MZI-isolated device exhibits the superposition of the resonances at around 1505 nm and 1595 nm, as can be observed in Figure 6.15. Thus, I applied some electrical power to the heater on top of Resonator 2 in the MZI-isolated device to align the resonances at around 1550 nm. The results of the fine tuning of the electrical power applied to the MZI are shown in Figure 6.16. As can be observed, with the electrical power equal to 30.1 mW, no additional resonances can be observed within the whole investigated spectral area, which confirms that the use of a MZI to isolate the resonators allows one to obtain a higher band in which they are uncoupled.

6.2.2 Nonlinear characterization

Finally, I measured the strength of the nonlinear interaction between the modes of the two resonators in the device 68. Once the voltage applied to the heater on one MZI's arm has been set to isolate the resonators, as discussed in the previous section, I checked the alignment of three resonances (one of Resonator 1 and two of Resonator 2), and it turned out that with 7.22 V (20.3 mW) applied on the heater on top of Resonator 2, two resonances of Resonator 2 (Ω_I at $\lambda_I = 1540.688$ nm and Ω_S at $\lambda_S = 1560.019$ nm) are equally spaced in frequency with respect to one resonance of Resonator 1 (Ω_P at $\lambda_P = 1550.293$ nm).

Thus, I placed the sample in the set-up shown in Figure 6.17 to measure the generation rate through sSFWM using such a structure. In the experiment, a tunable laser, whose spectrum is cleaned by the band-pass filter BPF₁ to suppress the ASE tails, is tuned on resonance at λ_P and coupled to Resonator 1 through the port T₁. Then, the photons generated at λ_S and λ_I are detected by, respectively, the superconductive single-photon detectors D₁ and D₂. Two tunable fiber Bragg filters (TBF₁ and TBF₂) and two band-pass filters (BPF₂ and BPF₃) are used to select the photons at λ_S and λ_I and to suppress the residual of the pump, whose spectral alignment with the device is checked through a power meter. Moreover, the power applied to the heaters is provided by two different voltage sources.

In Figure 6.18 the results of the experiments are shown. In Figure 6.18a is displayed the dependence of the coincidence rate measured on the detectors with respect to the detuning between the modes defined in (6.2): the data confirm that the maximum of the generation efficiency occurs at around 20.3 mW applied to the heater of Resonator 2. On the other hand, in Figure 6.18b is shown the variation of the generation rate R^{wg} of photons in the waveguide coupled to Resonator 2 with respect to the power of the laser tuned on resonance at λ_P . The values are obtained from the measured coincidence rates (20 s of integration time) through (6.1.2), where the losses associated to detectors D₁ and D₂ includes the efficiency of the detectors (-1 dB), the losses due to the fiber optical components (-4.5 dB and -3.1 dB respectively) and the coupling losses out of the chip (-3.5 dB). In addition, it is worth to mention that for each value of the input power, three acquisitions were performed by finely tuning the voltage applied to the heater on Resonator 2, and

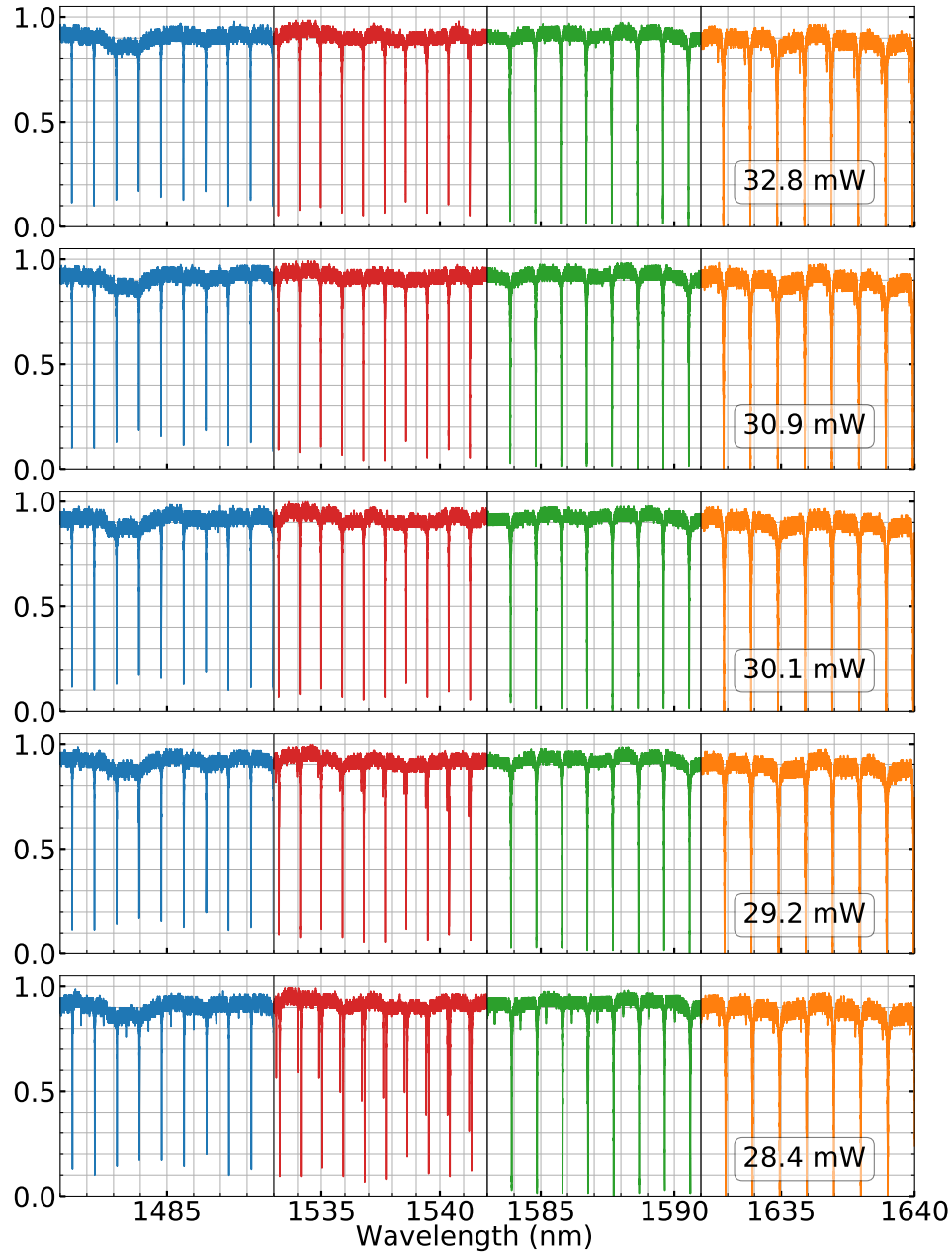


Figure 6.16: Spectra of the device 68 by changing the electrical power applied to one of the heater placed on the arms of the MZI. The electrical powers are displayed in the boxes. The tuning speed is set equal to 80 nm/s and the resolution of the spectra is 0.16 pm (10^6 points from 15480 to 1640 nm).

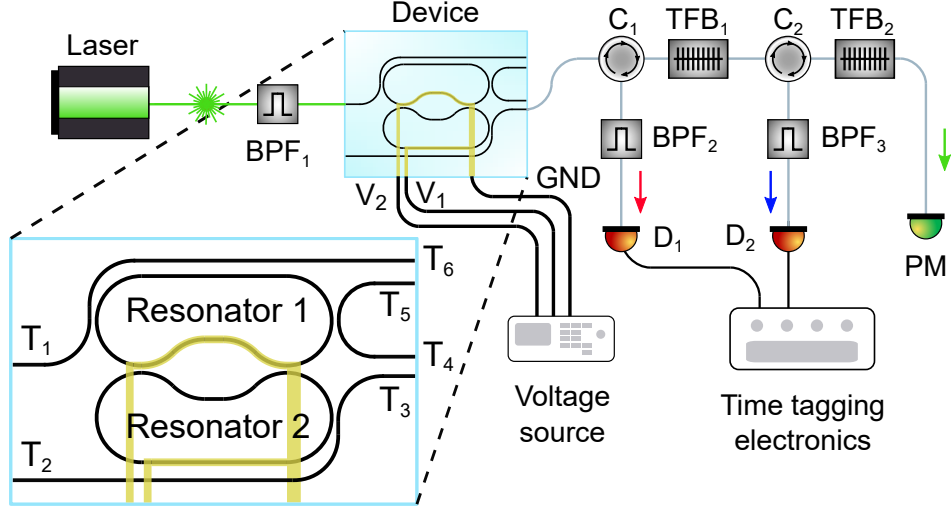
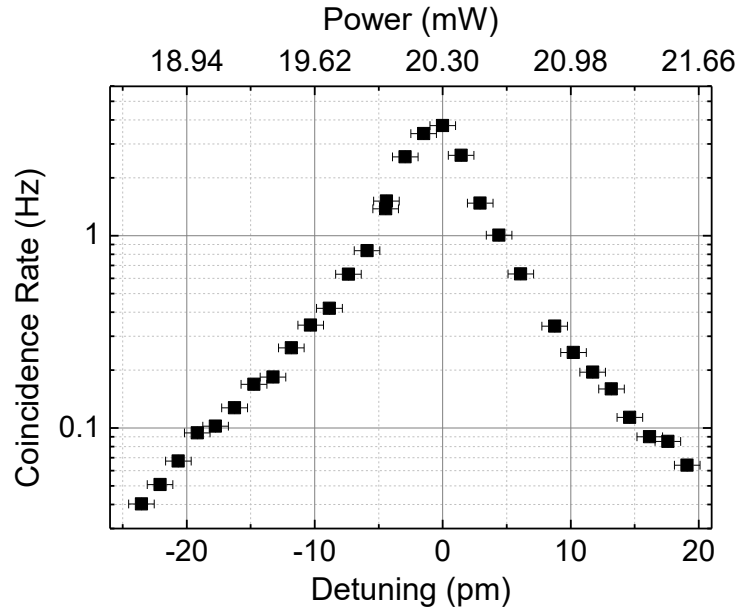


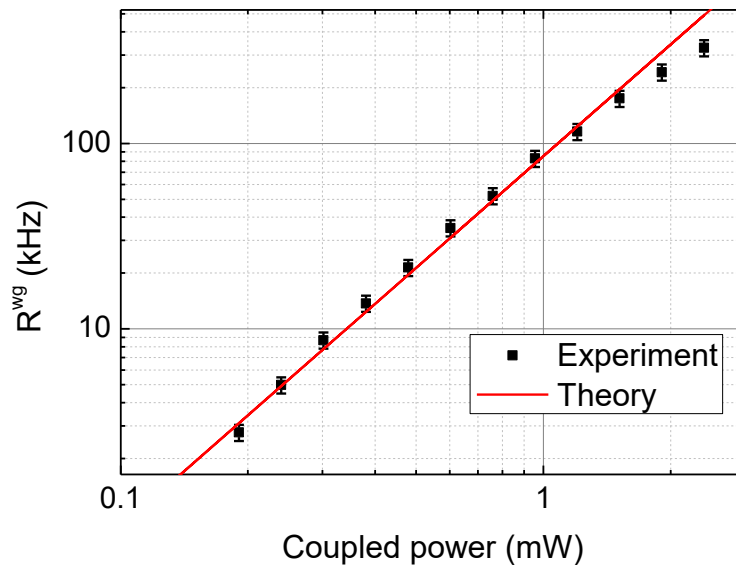
Figure 6.17: Set-up used to realize the nonlinear characterization of the device composed of two resonators linearly uncoupled through a MZI.

the maximum value has been taken. As can be seen, the data are in good agreement with the theoretical values calculated from 3.27 by considering $\gamma = 110 \text{ m}^{-1} \text{ W}^{-1}$, $n_g = 4.144$, the quality factors of the resonances Q_S , Q_P , and Q_I , equal to, respectively, $2.50 \cdot 10^5$, $8.9 \cdot 10^4$, and $2.56 \cdot 10^5$, the length of the resonators equal to $632 \text{ } \mu\text{m}$ and $639 \text{ } \mu\text{m}$ and the length of the MZI's arms equal to $194 \text{ } \mu\text{m}$. Finally, the coupled power is calculated by considering the losses from the laser to the waveguide coupled to Resonator 1 (-2.2 dB).

In conclusion, the results shown confirm the advantages of nonlinear coupled resonators which are linearly uncoupled through a MZI, since it has been proven the higher efficiency of the tuning of the coupling, as pointed out in Figure 6.15, the higher bandwidth of the isolation of the modes associated to the resonators, as shown in Figure 6.16, and the stronger nonlinear interaction, as anticipated in equation 3.27 and confirmed by the results displayed in Figure 6.18b.



(a) Voltage Shift.



(b) Power Scaling.

Figure 6.18: SFWM Zing MZI

Chapter 7

Conclusions and Perspectives

In this work I studied the development of integrated silicon photonic circuits (PICs) in the framework of quantum technologies. In particular, I realized several innovative PICs to efficiently generate nonclassical states of light, to manipulate them, and to solve important problems related to their generation on chip, such as the suppression of the pump and the increase of the signal to noise ratio when generating degenerate photons through dual-pump spontaneous four-wave mixing (d-SFWM). All these devices have been realized on a dedicated fabrication run exploiting an innovative post-etching treatment on silicon integrated optical waveguides with the aim of reducing the optical losses due to the roughness of the sidewalls, which has relevant implications on the efficiency of the sources of nonclassical states of light and on the manipulation of the generated photons.

In the first part of the work I focused on the design of the circuits and on their fabrication, as detailed in Chapters 2, 3, and 4. Then, I studied the impact of advanced post-etching treatments on silicon integrated optical waveguides. In particular, I tested the effect of thermal annealing on the optical propagation losses and on the quality factor of integrated ring resonators. One of the main sources of losses in integrated waveguides is related to the scattering due to the roughness on their sidewalls. However, the use of post-etching treatments can mitigate this effect. This has been demonstrated in previous works [82, 116] where losses lower than 0.5 dB/cm were reported for high confinement waveguides. Thus, we applied similar treatments in our fabrication run. After some morphological tests realized with the scanning electron microscope and the atomic force microscope, we found out that the line edge roughness of the waveguides was reduced from 2.2 nm to less than 0.8 nm. The impact of the annealing was clear also from the optical tests: I analyzed several ring resonators with different radii finding out that annealed samples showed higher quality factors with respect to the non-treated ones. However, the intrinsic quality factor of these devices tuned out to be around $4.5 \cdot 10^5$, which corresponds to propagation losses around 1.6 dB/cm. Thus, I tested some longer

resonators composed mainly by straight waveguides, which showed intrinsic quality factor around one million (0.7 dB/cm). These results suggested that the impact of the annealing is different on straight and curved waveguides, as confirmed by some observations performed with the scanning electron microscope which show that the reduction of the roughness on curved waveguide seems to be more mitigated. This effect is likely to be related to the fact that straight waveguides are always aligned with silicon crystalline axis, while curved ones are obviously misaligned.

In the future, some investigations will be done in order to further confirm this point. First, an estimation of the line edge roughness of the curved-waveguides's sidewalls will be performed with the atomic force microscope, to quantify the difference with respect to the values observed with the straight waveguides. In addition, different shapes of resonators will be investigated: in fact, racetracks should show a reduced impact of the rough curves.

In the final part of the thesis I investigated the use of linearly uncoupled resonators to selectively enhance specific nonlinear processes. As discussed, this can be extremely interesting when unwanted parasitic nonlinear processes can degrade the generated signal, as it occurs, for example, in dual-pump spontaneous four-wave mixing.

The possibility of use two pump lasers at ω_1 and ω_2 to generate photons at $\omega_T = (\omega_1 + \omega_2)/2$ through d-SFWM is very useful, since it allows to generate single-mode squeezed light, a central resource in the development of continuous-variable quantum computing. Conventional micrometric ring resonators have been used to enhance d-SFWM, but their multimode nature inevitably also leads to the amplification of unwanted nonlinear phenomena, such as single-pump spontaneous four-wave mixing (s-SFWM). In particular, I showed that the generation rates of the parasitic processes, given by the sum of the two s-SFWM rates, can even be one order of magnitude larger than the generation rate of d-SFWM, with a maximum signal-to-noise ratio (SNR) of only about 2 when the two pump powers are equal.

Linearly uncoupled resonators were proposed in 2019 [263]: the idea is to build two isolated optical resonators that can be coupled through their nonlinear interaction. This is possible, for example, by placing two racetrack resonators side-by-side forming a directional coupler, which allows the uncoupling of the modes. However, since the modes of the two resonators both propagate in the directional coupler, the nonlinear interaction between them can take place in this region if conservation of energy and momentum are satisfied. Thus, a proper spectral alignment of the modes, performed by activating some thermal phase shifters on the resonators, allows one to selectively enable or suppress the generation of photon pairs through the nonlinear interaction.

To prove this experimentally, I tuned one laser on resonance with one resonator and measured the generation rate of pairs resonant with the second racetrack: this allowed me to estimate the suppression of s-SFWM, which was found out to follow the theoretical predictions. Then, I realized a d-SFWM experiment by using two lasers

tuned on resonance with one resonator and detecting the generated pairs within one resonance of the other: the estimated SNR is equal to $(11.3 \pm 3.2) \cdot 10^3$. From the theoretical model, a SNR around $21 \cdot 10^3$ was expected, an improvement over that of a single ring system by over four orders of magnitude. Our experimental estimation is lower due to the presence of other sources of noise in the set-up (such as Raman noise from the fibers).

The main drawback of linearly uncoupled resonators is the reduced strength of the nonlinear interaction with respect to conventional resonators. In fact, the optical modes interact only in the directional coupler, which is around a quarter of the length of the resonators, and their overlap integral is equal to 0.25: this leads to a reduction of the interaction strength by a factor of $1/256$ with respect to conventional resonators having similar dimensions. However, some strategies can be adopted to reduce this penalty.

First, one can replace the directional coupler with a Mach-Zehnder interferometer. This approach does not modify the ratio between interaction and total length, but it increases the overlap of the modes, resulting in an enhancement of a factor 4 with respect to the device with the directional coupler, as confirmed by nonlinear experiments performed and shown in the manuscript. In addition, this strategy have other advantages: the isolation of the modes occurs in a larger spectral band (approximately twice the isolation bandwidth of the directional coupler's version), and the fabrication imperfections are easily compensated by applying a small voltage on some heaters placed on top of the Mach-Zehnder interferometers' arms.

Further improvements could be realized by adding an additional resonator which allows one to extend the nonlinear interaction and to enhance the process by a further factor of 4. These devices were designed and fabricated on the chip, and they will be characterized in future. The results will allow one to confirm this idea, which could be implemented on different platforms (for example silicon nitride) to test the generation of squeezed light exploiting this approach. In fact, it is difficult to realize a relevant level of squeezing with silicon waveguides where nonlinear losses limit the intensity of the coherent beams that can be used.

Finally, other structures were designed and fabricated on the wafers, targeting different goals such as the generation of entangled tripartite states (W states), the efficient generation of frequency-encoded entangled states, the improvement of the pair generation rates by exploiting series of ring resonators, and the on-chip suppression of the pump by using integrated Bragg filters. All these structures have relevant impact in the field of integrated quantum photonics, since they can prove the possibility to realize such systems on an integrated platforms, or improve the performance of the devices already described in literature.

List of Publications and Conferences

Peer review papers

- Federico Andrea Sabattoli, Houssein El Dirani, Laurene Youssef, Francesco Garrisi, Davide Grassani, Luca Zatti, Camille Petit-Etienne, Erwine Pargon, J.E.Sipe, Marco Liscidini, Corrado Sciancalepore, Daniele Bajoni, and Matteo Galli
Suppression of parasitic nonlinear processes in spontaneous four-wave mixing in linearly uncoupled resonators
Phys. Rev. Lett. (2021) - accepted, in press.
- Francesco Garrisi, Federico Andrea Sabattoli, Savda Sam, Andrea Barone,¹ Micol Previde Massara, Federico Pirzio, Francesco Morichetti, Andrea Melloni, Marco Liscidini, Matteo Galli, and Daniele Bajoni
Electrically driven source of time-energy entangled photons based on a self-pumped silicon microring resonator
Opt. Lett. 45 (10), 2768-2771 (2020).
- Micol Previde Massara, Federico Andrea Sabattoli, Federico Pirzio, Matteo Galli, and Daniele Bajoni
Four-wave mixing in a silicon microring resonator using a self-pumping geometry
Appl. Phys. Lett. 113 (12), 121111 (2018).

Conference proceedings

- Federico Andrea Sabattoli, Houssein El Dirani, Laurene Youssef, Francesco Garrisi, Davide Grassani, Luca Zatti, Linda Gianini, Camille Petit-Etienne, Erwine Pargon, Marco Liscidini, Corrado Sciancalepore, Daniele Bajoni, and Matteo Galli

Selective enhancement of nonlinear processes in linearly uncoupled silicon resonators

Smart Photonic and Optoelectronic Integrated Circuits XXIII (Vol. 11690, p. 116900U). International Society for Optics and Photonics.

- Federico Andrea Sabattoli, Houssein El Dirani, Laurene Youssef, Francesco Garrisi, Davide Grassani, Luca Zatti, Linda Gianini, Camille Petit-Etienne, Erwine Pargon, Marco Liscidini, Corrado Sciancalepore, Daniele Bajoni, and Matteo Galli
Selective enhancement of nonlinear processes in linearly uncoupled silicon resonators
 Smart Photonic and Optoelectronic Integrated Circuits XXIII (Vol. 11690, p. 116900U). International Society for Optics and Photonics.
- Federico Andrea Sabattoli, Houssein El Dirani, Laurene Youssef, Francesco Garrisi, Davide Grassani, Luca Zatti, Camille Petit-Etienne, Erwine Pargon, Marco Liscidini, Corrado Sciancalepore, Daniele Bajoni, and Matteo Galli
Dual Pump Photon Pair Generation with Suppression of Parasitic Processes in Linearly Uncoupled Silicon Resonators
 Frontiers in Optics. Optical Society of America, 2020. p. FM4A. 2.
- Francesco Garrisi, Federico Andrea Sabattoli, Savda Sam, Andrea Barone,¹ Micol Previde Massara, Federico Pirzio, Francesco Morichetti, Andrea Melloni, Marco Liscidini, Matteo Galli, and Daniele Bajoni
Emission of Time-Energy Entangled Photon Pairs by a Self-Pumped Silicon Microresonator
 CLEO: QELS Fundamental Science. Optical Society of America, 2020.
- Federico Andrea Sabattoli, Houssein El Dirani, Francesco Garrisi, Savda Sam, Camille Petit-Etienne, Jean-Michel Hartmann, Erwine Pargon, Cristhelle Monat, Marco Liscidini, Corrado Sciancalepore, Matteo Galli, and Daniele Bajoni
A Source of Heralded Single Photon Using High Quality Factor Silicon Ring Resonators
 21st International Conference on Transparent Optical Networks (ICTON). IEEE, 2019.
- Houssein El Dirani, Federico Andrea Sabattoli, Francesco Garrisi, Camille Petit-Etienne, Jean-Michel Hartmann, Erwine Pargon, Cristhelle Monat, Marco Liscidini, Daniele Bajoni, Matteo Galli, and Corrado Sciancalepore
Low-Loss Silicon Technology for High-Q Bright Quantum Sources
 IEEE 16th International Conference on Group IV Photonics (GFP). Vol. 1949. IEEE, 2019
- Micol Previde Massara, Federico Andrea Sabattoli, Federico Pirzio, Matteo Galli, and Daniele Bajoni

Four-Wave Mixing in a Silicon Self-Pumped Ring Resonator
CLEO: Applications and Technology. Optical Society of America, 2018.

Conference presentations

- Federico Andrea Sabattoli, Houssein El Dirani, Laurene Youssef, Francesco Garrisi, Davide Grassani, Luca Zatti, Camille Petit-Etienne, Erwine Pargon, Marco Liscidini, Corrado Sciancalepore, Daniele Bajoni, and Matteo Galli
Suppression of Nonlinear Parasitic Processes in Linearly Uncoupled Silicon Resonators
Conference on Laser and Electro Optics. Optical Society of America, 2021.
- Davide Grassani, Federico Andrea Sabattoli, Houssein El Dirani, Laurene Youssef, Davide Grassani, Linda Gianini, Camille Petit-Etienne, Sébastien Kerdiles, Erwine Pargon, Marco Liscidini, Corrado Sciancalepore, Daniele Bajoni, and Matteo Galli
A Method for Increasing Thermal Stability of Short-Living Solitons in Silicon Nitride Microresonators
Conference on Laser and Electro Optics. Optical Society of America, 2021.
- Federico Andrea Sabattoli, Houssein El Dirani, Laurene Youssef, Francesco Garrisi, Davide Grassani, Luca Zatti, Linda Gianini, Camille Petit-Etienne, Erwine Pargon, Marco Liscidini, Corrado Sciancalepore, Daniele Bajoni, and Matteo Galli
Selective enhancement of nonlinear processes in linearly uncoupled silicon resonators
SPIE Photonic West 2021 (invited).
- Federico Andrea Sabattoli, Houssein El Dirani, Laurene Youssef, Francesco Garrisi, Davide Grassani, Luca Zatti, Camille Petit-Etienne, Erwine Pargon, Marco Liscidini, Corrado Sciancalepore, Daniele Bajoni, and Matteo Galli
Dual Pump Photon Pair Generation with Suppression of Parasitic Processes in Linearly Uncoupled Silicon Resonators
Frontiers in Optics. Optical Society of America, 2020.

Acknowledgments

Il lavoro presentato in questo manoscritto è frutto di un duro lavoro durato tre anni, che non avrebbe mai potuto concretizzarsi senza la collaborazione, l'aiuto e il sostegno di tante persone che mi hanno accompagnato in questo percorso, con mio grande piacere e onore.

Per prima cosa, non posso che ringraziare le persone a cui questo scritto è dedicato: la mia famiglia. La mia compagna di vita, Greta, che come nessun altro ha condiviso con me le fatiche e le difficoltà del lavoro di questi anni, aspettandomi dopo lunghi pomeriggi e serate di laboratorio o per un weekend insieme dopo settimane a centinaia di chilometri di distanza. E che soprattutto mi ha regalato la mia gioia più grande, un piccolo angelo che ha donato tanta felicità e permesso di vivere un momento storico e di vita personale secondo la giusta prospettiva. Un segno della potenza costruttiva dell'amore!

E come per molte cose, non c'è cima senza una solida base su cui costruire. Ringrazio i miei genitori e mio fratello Marco per avermi accompagnato in questi anni di grandi cambiamenti e di avventure, sostenendomi sempre. Ringrazio inoltre Lella e Francesco, per il continuo supporto e aiuto, soprattutto nei periodi più impegnativi.

Ringrazio, naturalmente, Matteo Galli, che mi ha guidato e supportato nel lavoro svolto, sempre con grande partecipazione e pazienza, permettendomi di sperimentare e di imparare a gestire i problemi da risolvere. Ringrazio Daniele Bajoni, per le fruttuose discussioni, e per l'aiuto nello sviluppo delle idee e delle soluzioni sperimentali. E ringrazio, infine, Marco Liscidini, che è stato determinante per la mia formazione personale, ed è stato fondamentale nella progettazione e nella realizzazione degli esperimenti descritti, rendendosi sempre disponibile per aiutare, consigliare, guidare e incoraggiare.

Grazie ai colleghi di laboratorio, Andrea, Davide, Francesco, Linda, Marco, Sara e Savda e ai colleghi "teorici", Daniele, Luca, Nicola, Simone e Tommaso, per il proficuo lavoro realizzato insieme, per le interessanti discussioni e per i momenti di spensieratezza. Ringrazio inoltre il coordinatore del corso di Dottorato, prof. Lucio Andreani, per il notevole impegno profuso. Ringrazio i referee che hanno analizzato il mio manoscritto, prof. Antonio Badolato e dott.ssa Lucia Caspani, per il tempo

speso e per i preziosi suggerimenti forniti. Ringrazio infine tutto il personale del Dipartimento di Fisica per contribuire al funzionamento dell'infrastruttura che mi ha visto crescere dal punto di vista professionale.

My visiting period of six months in Grenoble has been fundamental for the results obtained in my PhD, and this was possible thanks to two extraordinary people: Corrado Sciancalepore and Houssein El Dirani. I found two exceptional people from a scientific and professional point of view, but I found also two dear friends. I feel very lucky to have meet them. Thanks also to Loraine, Erwine and Camille who helped me in the cleanroom and during the fabrication process, and thanks to all the people in the laboratory of integrated optics at the CEA-Leti Photonics Department for the warm welcome and the support during my visiting period.

Bibliography

- [1] Michael A. Nielsen and Isaac Chuang. *Quantum computation, and quantum information*. American Association of Physics Teachers, 2002.
- [2] Nicolas Gisin and Rob Thew. Quantum communication. *Nature Photonics*, 1(3):165–171, 2007.
- [3] Vittorio Giovannetti, Seth Lloyd, and Lorenzo Maccone. Quantum metrology. *Physical Review Letters*, 96(1):010401, 2006.
- [4] Stefano Pirandola, Roy Bardhan B., Tobias Gehring, Christian Weedbrook, and Seth Lloyd. Advances in photonic quantum sensing. *Nature Photonics*, 12(12):724–733, 2018.
- [5] Robert W. Boyd and Jonathan P. Dowling. Quantum lithography: status of the field. *Quantum Information Processing*, 11(4):891–901, 2012.
- [6] Antonio Acín, Immanuel Bloch, Harry Buhrman, Tommaso Calarco, Christopher Eichler, Jens Eisert, Daniel Esteve, Nicolas Gisin, Steffen J. Glaser, Fedor Jelezko, et al. The quantum technologies roadmap: a european community view. *New Journal of Physics*, 20(8):080201, 2018.
- [7] Max F. Riedel, Daniele Binosi, Rob Thew, and Tommaso Calarco. The european quantum technologies flagship programme. *Quantum Science, and Technology*, 2(3):030501, 2017.
- [8] Thaddeus D. Ladd, Fedor Jelezko, Raymond Laflamme, Yasunobu Nakamura, Christopher Monroe, and Jeremy Lloyd O’Brien. Quantum computers. *Nature*, 464(7285):45–53, 2010.
- [9] Richard P Feynman. Simulating physics with computers. *Int. J. Theor. Phys*, 21(6/7), 1982.
- [10] Jay M. Gambetta, Jerry M. Chow, and Matthias Steffen. Building logical qubits in a superconducting quantum computing system. *npj Quantum Information*, 3(1):1–7, 2017.

- [11] Michel H. Devoret and Robert J. Schoelkopf. Superconducting circuits for quantum information: an outlook. *Science*, 339(6124):1169–1174, 2013.
- [12] David P DiVincenzo. The physical implementation of quantum computation. *Fortschritte der Physik: Progress of Physics*, 48(9-11):771–783, 2000.
- [13] <https://research.google/teams/applied-science/quantum/>. Accessed: January 20, 2021.
- [14] <https://www.research.ibm.com/quantum-computing/>. Accessed: January 20, 2021.
- [15] <https://www.rigetti.com/>. Accessed: January 20, 2021.
- [16] <https://www.imec-int.com/en/articles/imec-enters-the-race-to-unleash-quantum-computing>. Accessed: January 20, 2021.
- [17] Frank Arute, Kunal Arya, Ryan Babbush, Dave Bacon, Joseph C. Bardin, Rami Barends, Rupak Biswas, Sergio Boixo, Fernando GSL. Brandao, David A. Buell, et al. Quantum supremacy using a programmable superconducting processor. *Nature*, 574(7779):505–510, 2019.
- [18] Roberto Stassi, Mauro Cirio, and Franco Nori. Scalable quantum computer with superconducting circuits in the ultrastrong coupling regime. *npj Quantum Information*, 6(1):1–6, 2020.
- [19] <https://www.theguardian.com/technology/2019/aug/02/quantum-supremacy-computers>. Accessed: January 20, 2021.
- [20] Hartmut Häffner, Christian F. Roos, and Rainer Blatt. Quantum computing with trapped ions. *Physics reports*, 469(4):155–203, 2008.
- [21] Colin D. Bruzewicz, John Chiaverini, Robert McConnell, and Jeremy M Sage. Trapped-ion quantum computing: Progress, and challenges. *Applied Physics Reviews*, 6(2):021314, 2019.
- [22] Neil A. Gershenfeld and Isaac L Chuang. Bulk spin-resonance quantum computation. *Science*, 275(5298):350–356, 1997.
- [23] David G. Cory, Amr F. Fahmy, and Timothy F Havel. Ensemble quantum computing by nmr spectroscopy. *Proceedings of the National Academy of Sciences*, 94(5):1634–1639, 1997.
- [24] Craig S. Lent and P Douglas Tougaw. A device architecture for computing with quantum dots. *Proceedings of the IEEE*, 85(4):541–557, 1997.
- [25] Christoph Kloeffel and Daniel Loss. Prospects for spin-based quantum computing in quantum dots. *Annu. Rev. Condens. Matter Phys.*, 4(1):51–81, 2013.

- [26] Jeremy L O’Brien. Optical quantum computing. *Science*, 318(5856):1567–1570, 2007.
- [27] Emanuel Knill, Raymond Laflamme, and Gerald J Milburn. A scheme for efficient quantum computation with linear optics. *Nature*, 409(6816):46–52, 2001.
- [28] Jeremy L. O’Brien, Geoffrey J. Pryde, Andrew G. White, Timothy C. Ralph, and David Branning. Demonstration of an all-optical quantum controlled-not gate. *Nature*, 426(6964):264–267, 2003.
- [29] Sara Gasparoni, Jian-Wei Pan, Philip Walther, Terry Rudolph, and Anton Zeilinger. Realization of a photonic controlled-not gate sufficient for quantum computation. *Physical Review Letters*, 93(2):020504, 2004.
- [30] Benjamin P. Lanyon, Marco Barbieri, Marcelo P. Almeida, Thomas Jennewein, Timothy C. Ralph, Kevin J. Resch, Geoff J. Pryde, Jeremy L. O’Brien, Alexei Gilchrist, and Andrew G White. Simplifying quantum logic using higher-dimensional hilbert spaces. *Nature Physics*, 5(2):134–140, 2009.
- [31] Chao-Yang Lu, Daniel E. Browne, Tao Yang, and Jian-Wei Pan. Demonstration of a compiled version of shor’s quantum factoring algorithm using photonic qubits. *Physical Review Letters*, 99(25):250504, 2007.
- [32] Ben P. Lanyon, Till J. Weinhold, Nathan K. Langford, Marco Barbieri, Daniel FV James, Alexei Gilchrist, and Andrew G White. Experimental demonstration of a compiled version of shor’s algorithm with quantum entanglement. *Physical Review Letters*, 99(25):250505, 2007.
- [33] Alberto Politi, Martin J. Cryan, John G. Rarity, Siyuan Yu, and Jeremy L O’Brien. Silica-on-silicon waveguide quantum circuits. *Science*, 320(5876):646–649, 2008.
- [34] Jeremy L. O’Brien, Akira Furusawa, and Jelena Vučković. Photonic quantum technologies. *Nature Photonics*, 3(12):687–695, 2009.
- [35] Seth Lloyd and Samuel L Braunstein. Quantum computation over continuous variables. In *Quantum information with continuous variables*, pages 9–17. Springer, 1999.
- [36] Samuel L. Braunstein and Peter Van Loock. Quantum information with continuous variables. *Reviews of Modern Physics*, 77(2):513, 2005.
- [37] S. Takeda and A Furusawa. Toward large-scale fault-tolerant universal photonic quantum computing. *APL Photonics*, 4(6):060902, 2019.

- [38] Austin P. Lund, Anthony Laing, Saleh Rahimi-Keshari, Terry Rudolph, Jeremy L. O'Brien, and Timothy C Ralph. Boson sampling from a gaussian state. *Physical Review Letters*, 113(10):100502, 2014.
- [39] Craig S. Hamilton, Regina Kruse, Linda Sansoni, Sonja Barkhofen, Christine Silberhorn, and Igor Jex. Gaussian boson sampling. *Physical Review Letters*, 119(17):170501, 2017.
- [40] Juan Miguel Arrazola and Thomas R Bromley. Using gaussian boson sampling to find dense subgraphs. *Physical Review Letters*, 121(3):030503, 2018.
- [41] Joonsuk Huh and Man-Hong Yung. Vibronic boson sampling: generalized gaussian boson sampling for molecular vibronic spectra at finite temperature. *Scientific reports*, 7(1):1–10, 2017.
- [42] Han-Sen Zhong, Hui Wang, Yu-Hao Deng, Ming-Cheng Chen, Li-Chao Peng, Yi-Han Luo, Jian Qin, Dian Wu, Xing Ding, Yi Hu, et al. Quantum computational advantage using photons. *Science*, 370(6523):1460–1463, 2020.
- [43] Nicolas Gisin, Grégoire Ribordy, Wolfgang Tittel, and Hugo Zbinden. Quantum cryptography. *Reviews of Modern Physics*, 74(1):145, 2002.
- [44] Jianwei Wang, Fabio Sciarrino, Anthony Laing, and Mark G Thompson. Integrated photonic quantum technologies. *Nature Photonics*, 14(5):273–284, 2020.
- [45] Charles H. Bennett and Gilles Brassard. Quantum cryptography: Public key distribution, and coin tossing. *arXiv preprint arXiv:2003.06557*, 2020.
- [46] Artur K Ekert. Quantum cryptography based on bell's theorem. *Physical Review Letters*, 67(6):661, 1991.
- [47] Fulvio Flamini, Nicolo Spagnolo, and Fabio Sciarrino. Photonic quantum information processing: a review. *Reports on Progress in Physics*, 82(1):016001, 2018.
- [48] Boris Korzh, Charles Ci Wen Lim, Raphael Houlmann, Nicolas Gisin, Ming Jun Li, Daniel Nolan, Bruno Sanguinetti, Rob Thew, and Hugo Zbinden. Provably secure, and practical quantum key distribution over 307 km of optical fibre. *Nature Photonics*, 9(3):163–168, 2015.
- [49] Sheng-Kai Liao, Wen-Qi Cai, Johannes Handsteiner, Bo Liu, Juan Yin, Liang Zhang, Dominik Rauch, Matthias Fink, Ji-Gang Ren, Wei-Yue Liu, et al. Satellite-relayed intercontinental quantum network. *Physical Review Letters*, 120(3):030501, 2018.

- [50] Lucia Caspani, Chunle Xiong, Benjamin J. Eggleton, Daniele Bajoni, Marco Liscidini, Matteo Galli, Roberto Morandotti, and David J Moss. Integrated sources of photon quantum states based on nonlinear optics. *Light: Science & Applications*, 6(11):e17100–e17100, 2017.
- [51] Davide Grassani, Stefano Azzini, Marco Liscidini, Matteo Galli, Michael J. Strain, Marc Sorel, J. E. Sipe, and Daniele Bajoni. A micrometer-scale integrated silicon source of time-energy entangled photons. *Optica*, 2(2):88–94, 2014.
- [52] Joshua W Silverstone, Raffaele Santagati, Damien Bonneau, Michael J. Strain, Marc Sorel, Jeremy L. O’Brien, and Mark G Thompson. Qubit entanglement between ring-resonator photon-pair sources on a silicon chip. *Nature Communications*, 6(1):1–7, 2015.
- [53] Poolad Imany, Jose A. Jaramillo-Villegas, Ogaga D. Odele, Kyunghun Han, Daniel E. Leaird, Joseph M. Lukens, Pavel Lougovski, Minghao Qi, and Andrew M Weiner. 50-ghz-spaced comb of high-dimensional frequency-bin entangled photons from an on-chip silicon nitride microresonator. *Optics Express*, 26(2):1825–1840, 2018.
- [54] Christian Reimer, Michael Kues, Piotr Roztock, Benjamin Wetzel, Fabio Grazioso, Brent E. Little, Sai T. Chu, Tudor Johnston, Yaron Bromberg, Lucia Caspani, et al. Generation of multiphoton entangled quantum states by means of integrated frequency combs. *Science*, 351(6278):1176–1180, 2016.
- [55] Xiyuan Lu, Qing Li, Daron A. Westly, Gregory Moille, Anshuman Singh, Vikas Anant, and Kartik Srinivasan. Chip-integrated visible–telecom entangled photon pair source for quantum communication. *Nature Physics*, 15(4):373–381, 2019.
- [56] Yong Zhang, M. Menotti, K. Tan, VD. Vaidya, DH. Mahler, L. Zatti, M. Liscidini, B. Morrison, and Z Vernon. Single-mode quadrature squeezing using dual-pump four-wave mixing in an integrated nanophotonic device. *arXiv preprint arXiv:2001.09474*, 2020.
- [57] Yun Zhao, Yoshitomo Okawachi, Jae K. Jang, Xingchen Ji, Michal Lipson, and Alexander L Gaeta. Near-degenerate quadrature-squeezed vacuum generation on a silicon-nitride chip. *Physical Review Letters*, 124(19):193601, 2020.
- [58] Di Liang and John E Bowers. Recent progress in lasers on silicon. *Nature Photonics*, 4(8):511–517, 2010.
- [59] Duanni Huang, Minh A. Tran, Joel Guo, Jonathan Peters, Tin Komljenovic, Aditya Malik, Paul A. Morton, and John E Bowers. High-power sub-khz linewidth lasers fully integrated on silicon. *Optica*, 6(6):745–752, 2019.

- [60] Qianfan Xu, Bradley Schmidt, Sameer Pradhan, and Michal Lipson. Micrometre-scale silicon electro-optic modulator. *Nature*, 435(7040):325–327, 2005.
- [61] Ling Liao, Dean Samara-Rubio, Michael Morse, Ansheng Liu, Dexter Hodge, Doron Rubin, Ulrich D. Keil, and Thorkild Franck. High speed silicon mach-zehnder modulator. *Optics Express*, 13(8):3129–3135, 2005.
- [62] Jeremy Witzens. High-speed silicon photonics modulators. *Proceedings of the IEEE*, 106(12):2158–2182, 2018.
- [63] Nicholas C. Harris, Davide Grassani, Angelica Simbula, Mihir Pant, Matteo Galli, Tom Baehr-Jones, Michael Hochberg, Dirk Englund, Daniele Bajoni, and Christophe Galland. Integrated source of spectrally filtered correlated photons for large-scale quantum photonic systems. *Physical Review X*, 4(4):041047, 2014.
- [64] Wim Bogaerts, Shankar Kumar Selvaraja, Pieter Dumon, Joost Brouckaert, Katrien De Vos, Dries Van Thourhout, and Roel Baets. Silicon-on-insulator spectral filters fabricated with cmos technology. *IEEE journal of selected topics in quantum electronics*, 16(1):33–44, 2010.
- [65] Seok-Hwan Jeong, Daisuke Shimura, Takasi Simoyama, Miyoshi Seki, Nobuyuki Yokoyama, Minoru Ohtsuka, Keiji Koshino, Tsuyoshi Horikawa, Yu Tanaka, and Ken Morito. Low-loss, flat-topped, and spectrally uniform silicon-nanowire-based 5th-order crow fabricated by arf-immersion lithography process on a 300-mm soi wafer. *Optics Express*, 21(25):30163–30174, 2013.
- [66] Simone Ferrari, Carsten Schuck, and Wolfram Pernice. Waveguide-integrated superconducting nanowire single-photon detectors. *Nanophotonics*, 7(11):1725–1758, 2018.
- [67] JP. Sprengers, A. Gaggero, D. Sahin, S. Jahanmirinejad, G. Frucci, F. Mattioli, R Leoni, Johannes Beetz, M. Lerner, M. Kamp, et al. Waveguide superconducting single-photon detectors for integrated quantum photonic circuits. *Applied Physics Letters*, 99(18):181110, 2011.
- [68] Wolfram HP. Pernice, C. Schuck, O. Minaeva, M. Li, GN. Goltsman, AV Sergienko, and HX Tang. High-speed, and high-efficiency travelling wave single-photon detectors embedded in nanophotonic circuits. *Nature Communications*, 3(1):1–10, 2012.
- [69] Hiroki Takesue, Yasuhiro Tokura, Hiroshi Fukuda, Tai Tsuchizawa, Toshifumi Watanabe, Koji Yamada, and Sei-ichi Itabashi. Entanglement generation using silicon wire waveguide. *Applied Physics Letters*, 91(20):201108, 2007.

- [70] Michael Kues, Christian Reimer, Piotr Roztock, Luis Romero Cortés, Stefania Sciara, Benjamin Wetzel, Yanbing Zhang, Alfonso Cino, Sai T. Chu, Brent E. Little, et al. On-chip generation of high-dimensional entangled quantum states, and their coherent control. *Nature*, 546(7660):622–626, 2017.
- [71] Christian Reimer, Lucia Caspani, Matteo Clerici, Marcello Ferrera, Michael Kues, Marco Peccianti, Alessia Pasquazi, Luca Razzari, Brent E. Little, Sai T. Chu, et al. Integrated frequency comb source of heralded single photons. *Optics Express*, 22(6):6535–6546, 2014.
- [72] H. Jin, F.M. Liu, P. Xu, J.L. Xia, M.L. Zhong, Y. Yuan, J.W. Zhou, Y.X. Gong, W. Wang, and S.N. Zhu. On-chip generation, and manipulation of entangled photons based on reconfigurable lithium-niobate waveguide circuits. *Physical Review Letters*, 113(10):103601, 2014.
- [73] Philip Sibson, Chris Erven, Mark Godfrey, Shigehito Miki, Taro Yamashita, Mikio Fujiwara, Masahide Sasaki, Hirotaka Terai, Michael G. Tanner, Chandra M. Natarajan, et al. Chip-based quantum key distribution. *Nature Communications*, 8(1):1–6, 2017.
- [74] Carlos Abellan, Waldimar Amaya, David Domenech, Pascual Muñoz, Jose Capmany, Stefano Longhi, Morgan W Mitchell, and Valerio Pruneri. Quantum entropy source on an inp photonic integrated circuit for random number generation. *Optica*, 3(9):989–994, 2016.
- [75] Jianwei Wang, Alberto Santamato, Pisu Jiang, Damien Bonneau, Erman Engin, Joshua W Silverstone, Matthias Lerner, Johannes Beetz, Martin Kamp, Sven Höfling, et al. Gallium arsenide (gaas) quantum photonic waveguide circuits. *Optics Communications*, 327:49–55, 2014.
- [76] Peter J. Shadbolt, Maria R Verde, Alberto Peruzzo, Alberto Politi, Anthony Laing, Mirko Lobino, Jonathan CF. Matthews, Mark G. Thompson, and Jeremy L O’Brien. Generating, manipulating, and measuring entanglement, and mixture with a reconfigurable photonic circuit. *Nature Photonics*, 6(1):45–49, 2012.
- [77] Andrea Crespi, Roberta Ramponi, Roberto Osellame, Linda Sansoni, Irene Bongioanni, Fabio Sciarrino, Giuseppe Vallone, and Paolo Mataloni. Integrated photonic quantum gates for polarization qubits. *Nature Communications*, 2(1):1–6, 2011.
- [78] Linda Sansoni, Fabio Sciarrino, Giuseppe Vallone, Paolo Mataloni, Andrea Crespi, Roberta Ramponi, and Roberto Osellame. Polarization entangled state measurement on a chip. *Physical Review Letters*, 105(20):200503, 2010.

- [79] <https://www.cisco.com/c/en/us/solutions/collateral/executive-perspectives/annual-internet-report/white-paper-c11-741490.html>. Accessed: January 21, 2021.
- [80] David Thomson, Aaron Zilkie, John E. Bowers, Tin Komljenovic, Graham T. Reed, Laurent Vivien, Delphine Marris-Morini, Eric Cassan, Léopold Virot, Jean-Marc Fédéli, et al. Roadmap on silicon photonics. *Journal of Optics*, 18(7):073003, 2016.
- [81] José Capmany and Daniel Pérez. *Programmable Integrated Photonics*. Oxford University Press, 2020.
- [82] Quentin Wilmart, Stephane Brision, Jean-Michel Hartmann, Andre Myko, Karen Ribaud, Camille Petit-Etienne, Laurene Youssef, Daivid Fowler, Benoit Charbonnier, Corrado Sciancalepore, et al. A complete si photonics platform embedding ultra-low loss waveguides for o-and c-band. *Journal of Lightwave Technology*, 2020.
- [83] Wesley D. Sacher, Ying Huang, Guo-Qiang Lo, and Joyce K.S. Poon. Multilayer silicon nitride-on-silicon integrated photonic platforms, and devices. *Journal of Lightwave Technology*, 33(4):901–910, 2015.
- [84] Günther Roelkens, Liu Liu, Di Liang, Richard Jones, Alexander Fang, Brian Koch, and John Bowers. Iii-v/silicon photonics for on-chip, and intra-chip optical interconnects. *Laser & Photonics Reviews*, 4(6):751–779, 2010.
- [85] Rowel Go, H. Krysiak, M. Fethers, Pedro Figueiredo, Matthew Suttinger, XM. Fang, A. Eisenbach, J.M. Fastenau, D. Lubyshev, A.W.K. Liu, et al. Inp-based quantum cascade lasers monolithically integrated onto silicon. *Optics Express*, 26(17):22389–22393, 2018.
- [86] Rodney Loudon. *The quantum theory of light*. OUP Oxford, 2000.
- [87] Damien Bonneau, Erman Engin, Kazuya Ohira, Nob Suzuki, Haruhiko Yoshida, Norio Iizuka, Mizunori Ezaki, Chandra M. Natarajan, Michael G. Tanner, Robert H. Hadfield, et al. Quantum interference, and manipulation of entanglement in silicon wire waveguide quantum circuits. *New Journal of Physics*, 14(4):045003, 2012.
- [88] Jianwei Wang, Stefano Paesani, Yunhong Ding, Raffaele Santagati, Paul Skrzypczyk, Alexia Salavrakos, Jordi Tura, Remigiusz Augusiak, Laura Mančinska, Davide Bacco, et al. Multidimensional quantum entanglement with large-scale integrated optics. *Science*, 360(6386):285–291, 2018.
- [89] David AB Miller. Perfect optics with imperfect components. *Optica*, 2(8):747–750, 2015.

- [90] Jacques Carolan, Uttara Chakraborty, Nicholas C Harris, Mihir Pant, Tom Baehr-Jones, Michael Hochberg, and Dirk Englund. Scalable feedback control of single photon sources for photonic quantum technologies. *Optica*, 6(3):335–340, 2019.
- [91] Amnon Yariv, Pochi Yeh, and Amnon Yariv. *Photonics: optical electronics in modern communications*, volume 6. Oxford University Press New York, 2007.
- [92] Kazuhiko Ogusu, Shojiro Kawakami, and Shigeo Nishida. Optical strip waveguide: an analysis. *Applied Optics*, 18(6):908–914, 1979.
- [93] Kazuhiko Ogusu. Optical strip waveguide: A detailed analysis including leaky modes. *JOSA*, 73(3):353–357, 1983.
- [94] JE Goell. Rib waveguide for integrated optical circuits. *Applied Optics*, 12(12):2797–2798, 1973.
- [95] Daoxin Dai and Sailing He. Analysis of characteristics of bent rib waveguides. *JOSA A*, 21(1):113–121, 2004.
- [96] P Andrew Anderson, Bradley S. Schmidt, and Michal Lipson. High confinement in silicon slot waveguides with sharp bends. *Optics Express*, 14(20):9197–9202, 2006.
- [97] Ran Ding, Tom Baehr-Jones, Woo-Joong Kim, Xugang Xiong, Richard Bojko, Jean-Marc Fedeli, Maryse Fournier, and Michael Hochberg. Low-loss strip-loaded slot waveguides in silicon-on-insulator. *Optics Express*, 18(24):25061–25067, 2010.
- [98] John D. Joannopoulos, Pierre R Villeneuve, and Shanhui Fan. Photonic crystals: putting a new twist on light. *Nature*, 386(6621):143–149, 1997.
- [99] Attila Mekis, JC. Chen, I. Kurland, Shanhui Fan, Pierre R Villeneuve, and JD Joannopoulos. High transmission through sharp bends in photonic crystal waveguides. *Physical Review Letters*, 77(18):3787, 1996.
- [100] Shankar Kumar Selvaraja and Purnima Sethi. Review on optical waveguides. *Emerging Waveguide Technol*, 95, 2018.
- [101] Graham T. Reed and Andrew P Knights. *Silicon photonics: an introduction*. John Wiley & Sons, 2004.
- [102] Richard Soref. The past, present, and future of silicon photonics. *IEEE Journal of selected topics in quantum electronics*, 12(6):1678–1687, 2006.
- [103] Lukas G. Helt, Zhenshan Yang, Marco Liscidini, and JE Sipe. Spontaneous four-wave mixing in microring resonators. *Optics Letters*, 35(18):3006–3008, 2010.

- [104] Toshiaki Suhara and Masatoshi Fujimura. *Waveguide nonlinear-optic devices*, volume 11. Springer Science & Business Media, 2003.
- [105] Marcello Ferrera, Luca Razzari, David Duchesne, Roberto Morandotti, Zhen-shan Yang, Marco Liscidini, JE. Sipe, S. Chu, BE. Little, and DJ Moss. Low-power continuous-wave nonlinear optics in doped silica glass integrated waveguide structures. *Nature Photonics*, 2(12):737–740, 2008.
- [106] Juerg Leuthold, Christian Koos, and Wolfgang Freude. Nonlinear silicon photonics. *Nature Photonics*, 4(8):535–544, 2010.
- [107] Michael Hochberg, Nicholas C. Harris, Ran Ding, Yi Zhang, Ari Novack, Zhe Xuan, and Tom Baehr-Jones. Silicon photonics: the next fabless semiconductor industry. *IEEE Solid-State Circuits Magazine*, 5(1):48–58, 2013.
- [108] Andrew Rickman. The commercialization of silicon photonics. *Nature Photonics*, 8(8):579–582, 2014.
- [109] Andy Eu-Jin Lim, Junfeng Song, Qing Fang, Chao Li, Xiaoguang Tu, Ning Duan, Kok Kiong Chen, Roger Poh-Cher Tern, and Tsung-Yang Liow. Review of silicon photonics foundry efforts. *IEEE Journal of Selected Topics in Quantum Electronics*, 20(4):405–416, 2013.
- [110] Pascal Del’Haye. *Optical frequency comb generation in monolithic microresonators*. PhD thesis, Ludwig Maximilian University of Munich, 2011.
- [111] Zhaoming Zhu and Thomas G Brown. Full-vectorial finite-difference analysis of microstructured optical fibers. *Optics Express*, 10(17):853–864, 2002.
- [112] HH Li. Refractive index of silicon, and germanium, and its wavelength, and temperature derivatives. *Journal of Physical, and Chemical Reference Data*, 9(3):561–658, 1980.
- [113] Edward D Palik. *Handbook of optical constants of solids*, volume 3. Academic press, 1998.
- [114] Ian H Malitson. Interspecimen comparison of the refractive index of fused silica. *Josa*, 55(10):1205–1209, 1965.
- [115] Daisuke Shimura, Tsuyoshi Horikawa, Hideaki Okayama, Seok-Hwan Jeong, Masatoshi Tokushima, Hironori Sasaki, and Tohru Mogami. High precision si waveguide devices designed for 1.31 μm , and 1.55 μm wavelengths on 300mm-soi. In *11th International Conference on Group IV Photonics (GFP)*, pages 31–32. IEEE, 2014.

- [116] Cyril Bellegarde, Erwine Pargon, Corrado Sciancalepore, Camille Petit-Etienne, Vincent Hugues, Daniel Robin-Brosse, Jean-Michel Hartmann, and Philippe Lyan. Improvement of sidewall roughness of submicron soi waveguides by hydrogen plasma, and annealing. *IEEE Photonics Technology Letters*, 30(7):591–594, 2018.
- [117] Lukas Chrostowski and Michael Hochberg. *Silicon photonics design: from devices to systems*. Cambridge University Press, 2015.
- [118] Amy C. Turner, Christina Manolatou, Bradley S. Schmidt, Michal Lipson, Mark A. Foster, Jay E. Sharping, and Alexander L Gaeta. Tailored anomalous group-velocity dispersion in silicon channel waveguides. *Optics Express*, 14(10):4357–4362, 2006.
- [119] HK. Tsang and Y Liu. Nonlinear optical properties of silicon waveguides. *Semiconductor Science, and Technology*, 23(6):064007, 2008.
- [120] M. Dinu, Francesco Quochi, and H Garcia. Third-order nonlinearities in silicon at telecom wavelengths. *Applied Physics Letters*, 82(18):2954–2956, 2003.
- [121] Q. Lin, Oskar J. Painter, and Govind P Agrawal. Nonlinear optical phenomena in silicon waveguides: modeling, and applications. *Optics Express*, 15(25):16604–16644, 2007.
- [122] Davide Grassani. *Generation of energy-time entangled photons on a silicon chip*. PhD thesis, University of Pavia, 2013.
- [123] I-Wei Hsieh, Xiaogang Chen, Jerry I. Dadap, Nicolae C. Panoiu, Richard M. Osgood, Sharee J. McNab, and Yurii A Vlasov. Cross-phase modulation-induced spectral, and temporal effects on co-propagating femtosecond pulses in silicon photonic wires. *Optics Express*, 15(3):1135–1146, 2007.
- [124] Alain Haché and Martin Bourgeois. Ultrafast all-optical switching in a silicon-based photonic crystal. *Applied Physics Letters*, 77(25):4089–4091, 2000.
- [125] Hon Ki Tsang, CS. Wong, TK. Liang, IE. Day, SW Roberts, A. Harpin, J. Drake, and M Asghari. Optical dispersion, two-photon absorption, and self-phase modulation in silicon waveguides at 1.5 μ m wavelength. *Applied Physics Letters*, 80(3):416–418, 2002.
- [126] Lianghong Yin and Govind P Agrawal. Impact of two-photon absorption on self-phase modulation in silicon waveguides. *Optics Letters*, 32(14):2031–2033, 2007.
- [127] Bill Corcoran, Christelle Monat, Christian Grillet, David J. Moss, Benjamin J. Eggleton, Thomas P. White, Liam O’Faolain, and Thomas F Krauss. Green

- light emission in silicon through slow-light enhanced third-harmonic generation in photonic-crystal waveguides. *Nature Photonics*, 3(4):206–210, 2009.
- [128] Matteo Galli, Dario Gerace, Karl Welna, Thomas F. Krauss, Liam O’Faolain, Giorgio Guizzetti, and Lucio Claudio Andreani. Low-power continuous-wave generation of visible harmonics in silicon photonic crystal nanocavities. *Optics Express*, 18(25):26613–26624, 2010.
 - [129] Amy C. Turner, Mark A. Foster, Alexander L. Gaeta, and Michal Lipson. Ultra-low power parametric frequency conversion in a silicon microring resonator. *Optics Express*, 16(7):4881–4887, 2008.
 - [130] Reza Salem, Mark A. Foster, Amy C. Turner, David F. Geraghty, Michal Lipson, and Alexander L. Gaeta. Signal regeneration using low-power four-wave mixing on silicon chip. *Nature Photonics*, 2(1):35–38, 2008.
 - [131] Stefano Azzini, Davide Grassani, Matteo Galli, Lucio Claudio Andreani, Marc Sorel, Michael J. Strain, LG. Helt, JE. Sipe, Marco Liscidini, and Daniele Bajoni. From classical four-wave mixing to parametric fluorescence in silicon microring resonators. *Optics Letters*, 37(18):3807–3809, 2012.
 - [132] Raul Del Coso and Javier Solis. Relation between nonlinear refractive index, and third-order susceptibility in absorbing media. *JOSA B*, 21(3):640–644, 2004.
 - [133] Mihaela Dinu. Dispersion of phonon-assisted nonresonant third-order nonlinearities. *IEEE journal of quantum electronics*, 39(11):1498–1503, 2003.
 - [134] Manuel Cardona and Y Yu Peter. *Fundamentals of semiconductors*. Springer, 2005.
 - [135] Hansuek Lee, Tong Chen, Jiang Li, Ki Youl Yang, Seokmin Jeon, Oskar Painter, and Kerry J Vahala. Chemically etched ultrahigh-q wedge-resonator on a silicon chip. *Nature Photonics*, 6(6):369–373, 2012.
 - [136] DK. Armani, TJ. Kippenberg, SM. Spillane, and KJ Vahala. Ultra-high-q toroid microcavity on a chip. *Nature*, 421(6926):925–928, 2003.
 - [137] Xingchen Ji, Felipe AS. Barbosa, Samantha P. Roberts, Avik Dutt, Jaime Cardenas, Yoshitomo Okawachi, Alex Bryant, Alexander L. Gaeta, and Michal Lipson. Ultra-low-loss on-chip resonators with sub-milliwatt parametric oscillation threshold. *Optica*, 4(6):619–624, 2017.
 - [138] Martin HP. Pfeiffer, Junqiu Liu, Arslan S. Raja, Tiago Morais, Bahareh Ghadiani, and Tobias J Kippenberg. Ultra-smooth silicon nitride waveguides based on the damascene reflow process: fabrication, and loss origins. *Optica*, 5(7):884–892, 2018.

- [139] Houssein El Dirani, Laurene Youssef, Camille Petit-Etienne, Sebastien Kerdiles, Philippe Grosse, Christelle Monat, Erwine Pargon, and Corrado Sciancalepore. Ultralow-loss tightly confining si 3 n 4 waveguides, and high-q microresonators. *Optics Express*, 27(21):30726–30740, 2019.
- [140] David J. Moss, Roberto Morandotti, Alexander L. Gaeta, and Michal Lipson. New cmos-compatible platforms based on silicon nitride, and hydex for nonlinear optics. *Nature Photonics*, 7(8):597–607, 2013.
- [141] Ivan S. Grudinin, Andrey B. Matsko, Anatoliy A. Savchenkov, Dmitry Strekalov, Vladimir S. Ilchenko, and Lute Maleki. Ultra high q crystalline microcavities. *Optics Communications*, 265(1):33–38, 2006.
- [142] Yoshitomo Okawachi, Kasturi Saha, Jacob S. Levy, Y Henry Wen, Michal Lipson, and Alexander L Gaeta. Octave-spanning frequency comb generation in a silicon nitride chip. *Optics Letters*, 36(17):3398–3400, 2011.
- [143] Tobias Herr, Victor Brasch, John D. Jost, Christine Y. Wang, Nikita M. Kondratiev, Michael L. Gorodetsky, and Tobias J Kippenberg. Temporal solitons in optical microresonators. *Nature Photonics*, 8(2):145–152, 2014.
- [144] Sylvain Boust, Houssein El Dirani, Laurène Youssef, Yannick Robert, Alexandre Larrue, Camille Petit-Etienne, Eric Vinet, Sébastien Kerdiles, Erwine Pargon, Mickaël Faugeron, et al. Microcomb source based on inp dfb/si 3 n 4 microring butt-coupling. *Journal of Lightwave Technology*, 38(19):5517–5525, 2020.
- [145] Lue Wu, Heming Wang, Qifan Yang, Qing-xin Ji, Boqiang Shen, Chengying Bao, Maodong Gao, and Kerry Vahala. Greater than one billion q factor for on-chip microresonators. *Optics Letters*, 45(18):5129–5131, 2020.
- [146] Xiyuan Lu, Steven Rogers, Thomas Gerrits, Wei C. Jiang, Sae Woo Nam, and Qiang Lin. Heralding single photons from a high-Q silicon microdisk. *Optica*, 3(12):1331, dec 2016.
- [147] Yingwen Liu, Chao Wu, Xiaowen Gu, Yuechan Kong, Xinxin Yu, Renyou Ge, Xinlun Cai, Xiaogang Qiang, Junjie Wu, Xuejun Yang, and Ping Xu. High-spectral-purity photon generation from a dual-interferometer-coupled silicon microring. *Optics Letters*, 45(1):73, jan 2020.
- [148] Govind P Agrawal. *Nonlinear fiber optics*. Springer, 2000.
- [149] Lukas G. Helt, Marco Liscidini, and John E Sipe. How does it scale? comparing quantum, and classical nonlinear optical processes in integrated devices. *JOSA B*, 29(8):2199–2212, 2012.

- [150] Zhenshan Yang, Marco Liscidini, and JE Sipe. Spontaneous parametric down-conversion in waveguides: A backward heisenberg picture approach. *Physical Review A*, 77(3):033808, 2008.
- [151] Bin Fang, Offir Cohen, Jamy B. Moreno, and Virginia O Lorenz. State engineering of photon pairs produced through dual-pump spontaneous four-wave mixing. *Optics Express*, 21(3):2707–2717, 2013.
- [152] Pierre Demongodin, Houssein El Dirani, Jérémy Lhuillier, Romain Crochemore, Malik Kemiche, Thomas Wood, Ségolène Callard, Pedro Rojo-Romeo, Corrado Sciancalepore, Christian Grillet, et al. Ultrafast saturable absorption dynamics in hybrid graphene/si3n4 waveguides. *Apl Photonics*, 4(7):076102, 2019.
- [153] Chaoxuan Ma and Shayan Mookherjee. Prospects for photon-pair generation using silicon microring resonators with two photon absorption, and free carrier absorption. *OSA Continuum*, 3(5):1138–1153, 2020.
- [154] Ivan D. Rukhlenko, Malin Premaratne, and Govind P Agrawal. Effective mode area, and its optimization in silicon-nanocrystal waveguides. *Optics Letters*, 37(12):2295–2297, 2012.
- [155] Angelica Simbula, GA. Rodriguez, M. Menotti, S. De Pace, SM. Weiss, M. Galli, M. Liscidini, and D Bajoni. Low-power four-wave mixing in porous silicon microring resonators. *Applied Physics Letters*, 109(2):021106, 2016.
- [156] Qing Li, Marcelo Davanço, and Kartik Srinivasan. Efficient, and low-noise single-photon-level frequency conversion interfaces using silicon nanophotonics. *Nature Photonics*, 10(6):406–414, 2016.
- [157] Paul E. Barclay, Kartik Srinivasan, and Oskar Painter. Nonlinear response of silicon photonic crystal microresonators excited via an integrated waveguide, and fiber taper. *Optics Express*, 13(3):801–820, 2005.
- [158] JDB. Bradley, PE. Jessop, and AP Knights. Silicon waveguide-integrated optical power monitor with enhanced sensitivity at 1550 nm. *Applied Physics Letters*, 86(24):241103, 2005.
- [159] M.W. Geis, S.J. Spector, M.E. Grein, R.T. Schulein, J.U. Yoon, D.M. Lennon, S. Deneault, F. Gan, F.X. Kaertner, and T.M Lyszczarz. Cmos-compatible all-si high-speed waveguide photodiodes with high responsivity in near-infrared communication band. *IEEE Photonics Technology Letters*, 19(3):152–154, 2007.

- [160] Francesco Morichetti, Stefano Grillanda, Marco Carminati, Giorgio Ferrari, Marco Sampietro, Michael J. Strain, Marc Sorel, and Andrea Melloni. Non-invasive on-chip light observation by contactless waveguide conductivity monitoring. *IEEE Journal of Selected Topics in Quantum Electronics*, 20(4):292–301, 2014.
- [161] Tom Baehr-Jones, Michael Hochberg, and Axel Scherer. Photodetection in silicon beyond the band edge with surface states. *Optics Express*, 16(3):1659–1668, 2008.
- [162] Hui Chen, Xianshu Luo, and Andrew W Poon. Cavity-enhanced photocurrent generation by 1.55 μ m wavelengths linear absorption in a pin diode embedded silicon microring resonator. *Applied Physics Letters*, 95(17):171111, 2009.
- [163] Andres Gil-Molina, Ivan Aldaya, Julián L. Pita, Lucas H. Gabrielli, Hugo L. Fragnito, and Paulo Dainese. Optical free-carrier generation in silicon nanowaveguides at 1550 nm. *Applied Physics Letters*, 112(25):251104, 2018.
- [164] Riccardo Marchetti, Cosimo Lacava, Lee Carroll, Kamil Gradkowski, and Paolo Minzioni. Coupling strategies for silicon photonics integrated chips. *Photonics Research*, 7(2):201–239, 2019.
- [165] Goran Z. Masanovic, Graham T. Reed, William Headley, Branislav Timotijevic, Vittorio MN. Passaro, Raghied Atta, Graham Ensell, and Alan GR Evans. A high efficiency input/output coupler for small silicon photonic devices. *Optics Express*, 13(19):7374–7379, 2005.
- [166] Laurent Vivien, Daniel Pascal, Sebastien Lardenois, Delphine Marris-Morini, Eric Cassan, Frédéric Grillot, Suzanne Laval, Jean-Marc Fédéli, and Loubna El Melhaoui. Light injection in soi microwaveguides using high-efficiency grating couplers. *Journal of Lightwave technology*, 24(10):3810–3815, 2006.
- [167] Christophe Kopp, Stephane Bernabe, Badhise Ben Bakir, Jean-Marc Fedeli, Regis Orobttchouk, Franz Schrank, Henri Porte, Lars Zimmermann, and Tolga Tekin. Silicon photonic circuits: on-cmos integration, fiber optical coupling, and packaging. *IEEE Journal of Selected Topics in Quantum Electronics*, 17(3):498–509, 2010.
- [168] Attila Mekis, Steffen Gloeckner, Gianlorenzo Masini, Adithyaram Narasimha, Thierry Pinguet, Subal Sahni, and Peter De Dobbelaere. A grating-coupler-enabled cmos photonics platform. *IEEE Journal of Selected Topics in Quantum Electronics*, 17(3):597–608, 2010.
- [169] Wissem Sfar Zaoui, Andreas Kunze, Wolfgang Vogel, Manfred Berroth, Jörg Butschke, Florian Letzkus, and Joachim Burghartz. Bridging the gap between optical fibers, and silicon photonic integrated circuits. *Optics Express*, 22(2):1277–1286, 2014.

- [170] Lee Carroll, Dario Gerace, Ilaria Cristiani, Sylvie Menezes, and Lucio C Andreani. Broad parameter optimization of polarization-diversity 2d grating couplers for silicon photonics. *Optics Express*, 21(18):21556–21568, 2013.
- [171] Pavel Cheben, Przemek J. Bock, Jens H. Schmid, Jean Lapointe, Siegfried Janz, Dan-Xia Xu, Adam Densmore, André Delâge, Boris Lamontagne, and Trevor J Hall. Refractive index engineering with subwavelength gratings for efficient microphotonic couplers, and planar waveguide multiplexers. *Optics Letters*, 35(15):2526–2528, 2010.
- [172] C. Alonso-Ramos, P. Cheben, A. Ortega-Moñux, JH. Schmid, D-X. Xu, and I Molina-Fernández. Fiber-chip grating coupler based on interleaved trenches with directionality exceeding 95%. *Optics Letters*, 39(18):5351–5354, 2014.
- [173] Vilson R. Almeida, Roberto R. Panepucci, and Michal Lipson. Nanotaper for compact mode conversion. *Optics Letters*, 28(15):1302–1304, 2003.
- [174] Jaime Cardenas, Carl B. Poitras, Kevin Luke, Lian-Wee Luo, Paul Adrian Morton, and Michal Lipson. High coupling efficiency etched facet tapers in silicon waveguides. *IEEE Photonics Technology Letters*, 26(23):2380–2382, 2014.
- [175] Long Chen, Christopher R. Doerr, Young-Kai Chen, and Tsung-Yang Liow. Low-loss, and broadband cantilever couplers between standard cleaved fibers, and high-index-contrast Si_3N_4 or Si waveguides. *IEEE Photonics Technology Letters*, 22(23):1744–1746, 2010.
- [176] Martin Papes, Pavel Cheben, Daniel Benedikovic, Jens H. Schmid, James Pond, Robert Halir, Alejandro Ortega-Moñux, Gonzalo Wangüemert-Pérez, N Ye Winnie, Dan-Xia Xu, et al. Fiber-chip edge coupler with large mode size for silicon photonic wire waveguides. *Optics Express*, 24(5):5026–5038, 2016.
- [177] Siddharth Nambiar, Purnima Sethi, and Shankar Kumar Selvaraja. Grating-assisted fiber to chip coupling for soi photonic circuits. *Applied Sciences*, 8(7):1142, 2018.
- [178] Rongqing Hui. *Introduction to fiber-optic communications*. Academic Press, 2019.
- [179] Amnon Yariv. Coupled-mode theory for guided-wave optics. *IEEE Journal of Quantum Electronics*, 9(9):919–933, 1973.
- [180] Piero Orlandi, Francesco Morichetti, Michael John Strain, Marc Sorel, Andrea Melloni, and Paolo Bassi. Tunable silicon photonics directional coupler driven by a transverse temperature gradient. *Optics Letters*, 38(6):863–865, 2013.

- [181] K. Jinguji, N. Takato, A. Sugita, and M Kawachi. Mach-zehnder interferometer type optical waveguide coupler with wavelength-flattened coupling ratio. *Electronics Letters*, 26(17):1326–1327, 1990.
- [182] MZ. Alam, J Niklas Caspers, J Stewart Aitchison, and Mo Mojahedi. Compact low loss, and broadband hybrid plasmonic directional coupler. *Optics Express*, 21(13):16029–16034, 2013.
- [183] Zeqin Lu, Han Yun, Yun Wang, Zhitian Chen, Fan Zhang, Nicolas AF. Jaeger, and Lukas Chrostowski. Broadband silicon photonic directional coupler using asymmetric-waveguide based phase control. *Optics Express*, 23(3):3795–3808, 2015.
- [184] Hisayasu Morino, Takeo Maruyama, and Koichi Iiyama. Reduction of wavelength dependence of coupling characteristics using si optical waveguide curved directional coupler. *Journal of lightwave technology*, 32(12):2188–2192, 2014.
- [185] A P. Ovvyvan, N. Gruhler, S. Ferrari, and W.H.P. Pernice. Cascaded mach-zehnder interferometer tunable filters. *Journal of Optics*, 18(6):064011, 2016.
- [186] Mateusz Piekarek, Damien Bonneau, Shigehito Miki, Taro Yamashita, Mikio Fujiwara, Masahide Sasaki, Hirotaka Terai, Michael G. Tanner, Chandra M. Natarajan, Robert H. Hadfield, et al. High-extinction ratio integrated photonic filters for silicon quantum photonics. *Optics Letters*, 42(4):815–818, 2017.
- [187] Folkert Horst, William MJ. Green, Solomon Assefa, Steven M. Shank, Yurii A. Vlasov, and Bert Jan Offrein. Cascaded mach-zehnder wavelength filters in silicon photonics for low loss, and flat pass-band wdm (de-) multiplexing. *Optics Express*, 21(10):11652–11658, 2013.
- [188] Tzu-Hsiang Yen and Yung Hung. Fabrication-tolerant cwdm (de) multiplexer based on cascaded mach-zehnder interferometers on silicon-on-insulator. *Journal of Lightwave Technology*, 2020.
- [189] Seok-Hwan Jeong and Yu Tanaka. Silicon-wire optical demultiplexers based on multistage delayed mach-zehnder interferometers for higher production yield. *Applied Optics*, 57(22):6474–6480, 2018.
- [190] Graham T. Reed, G. Mashanovich, F Yand Gardes, and DJ Thomson. Silicon optical modulators. *Nature Photonics*, 4(8):518–526, 2010.
- [191] Wim Bogaerts, Peter De Heyn, Thomas Van Vaerenbergh, Katrien De Vos, Shankar Kumar Selvaraja, Tom Claes, Pieter Dumon, Peter Bienstman, Dries Van Thourhout, and Roel Baets. Silicon microring resonators. *Laser & Photonics Reviews*, 6(1):47–73, 2012.

- [192] Andrea Melloni, Raffaella Costa, Paolo Monguzzi, and Mario Martinelli. Ring-resonator filters in silicon oxynitride technology for dense wavelength-division multiplexing systems. *Optics Letters*, 28(17):1567–1569, 2003.
- [193] Andreas Vorckel, Mathias Monster, Wolfgang Henschel, P Haring Bolivar, and Heinrich Kurz. Asymmetrically coupled silicon-on-insulator microring resonators for compact add-drop multiplexers. *IEEE Photonics Technology Letters*, 15(7):921–923, 2003.
- [194] Lu Yangyang, Tian Yonghui, and Yang Lin. Integrated reconfigurable optical add-drop multiplexers based on cascaded microring resonators. *Journal of Semiconductors*, 34(9):094012, 2013.
- [195] Qianfan Xu, Sasikanth Manipatruni, Brad Schmidt, Jagat Shakya, and Michal Lipson. 12.5 gbit/s carrier-injection-based silicon micro-ring silicon modulators. *Optics Express*, 15(2):430–436, 2007.
- [196] Joyce K.S. Poon, Jacob Scheuer, Yong Xu, and Amnon Yariv. Designing coupled-resonator optical waveguide delay lines. *JOSA B*, 21(9):1665–1673, 2004.
- [197] Andrea Melloni, Antonio Canciamilla, Carlo Ferrari, Francesco Morichetti, L. O’Faolain, T.F. Krauss, Re De La Rue, A. Samarelli, and M Sorel. Tunable delay lines in silicon photonics: coupled resonators, and photonic crystals, a comparison. *IEEE Photonics Journal*, 2(2):181–194, 2010.
- [198] Hongying Zhu, Paul S. Dale, Charles W Caldwell, and Xudong Fan. Rapid, and label-free detection of breast cancer biomarker ca15-3 in clinical human serum samples with optofluidic ring resonator sensors. *Analytical Chemistry*, 81(24):9858–9865, 2009.
- [199] Katrien De Vos, Irene Bartolozzi, Etienne Schacht, Peter Bienstman, and Roel Baets. Silicon-on-insulator microring resonator for sensitive, and label-free biosensing. *Optics Express*, 15(12):7610–7615, 2007.
- [200] Gilberto A. Rodriguez, Shuren Hu, and Sharon M Weiss. Porous silicon ring resonator for compact, high sensitivity biosensing applications. *Optics Express*, 23(6):7111–7119, 2015.
- [201] M. Ferrera, D. Duchesne, L. Razzari, M. Peccianti, R Morandotti, P. Cheben, S. Janz, D-X. Xu, BE. Little, S. Chu, et al. Low power four wave mixing in an integrated, micro-ring resonator with $Q=1.2$ million. *Optics Express*, 17(16):14098–14103, 2009.
- [202] P.P. Absil, J.V. Hryniewicz, B.E. Little, P.S. Cho, R.A. Wilson, L.G. Joneckis, and P-T Ho. Wavelength conversion in gaas micro-ring resonators. *Optics Letters*, 25(8):554–556, 2000.

- [203] Andrea Melloni, Francesco Morichetti, and Mario Martinelli. Four-wave mixing, and wavelength conversion in coupled-resonator optical waveguides. *JOSA B*, 25(12):C87–C97, 2008.
- [204] Alessia Pasquazi, Raja Ahmad, Martin Rochette, Michael Lamont, Brent E. Little, Sai T. Chu, Roberto Morandotti, and David J Moss. All-optical wavelength conversion in an integrated ring resonator. *Optics Express*, 18(4):3858–3863, 2010.
- [205] Marcelo Davanco, Jun Rong Ong, Andrea Bahgat Shehata, Alberto Tosi, Imad Agha, Solomon Assefa, Fengnian Xia, William MJ. Green, Shayan Mookherjee, and Kartik Srinivasan. Telecommunications-band heralded single photons from a silicon nanophotonic chip. *Applied Physics Letters*, 100(26):261104, 2012.
- [206] FA. Sabattoli, H. El Dirani, F. Garrisi, S. Sam, C. Petit-Etienne, JM. Hartmann, E. Pargon, C. Monat, M. Liscidini, C. Sciancalepore, et al. A source of heralded single photon using high quality factor silicon ring resonators. In *2019 21st International Conference on Transparent Optical Networks (ICTON)*, pages 1–4. IEEE, 2019.
- [207] Yingwen Liu, Chao Wu, Xiaowen Gu, Yuechan Kong, Xinxin Yu, Renyou Ge, Xinlun Cai, Xiaogang Qiang, Junjie Wu, Xuejun Yang, et al. High-spectral-purity photon generation from a dual-interferometer-coupled silicon microring. *Optics Letters*, 45(1):73–76, 2020.
- [208] Chaoxuan Ma, Xiaoxi Wang, Vikas Anant, Andrew D. Beyer, Matthew D. Shaw, and Shayan Mookherjee. Silicon photonic entangled photon-pair, and heralded single photon generation with $\text{car} > 12,000$, and $g^{(2)}(0) < 0.006$. *Optics Express*, 25(26):32995–33006, 2017.
- [209] Francesco Garrisi, Federico Andrea Sabattoli, Savda Sam, Andrea Barone, Nicol Previde Massara, Federico Pirzio, Francesco Morichetti, Andrea Melloni, Marco Liscidini, Matteo Galli, et al. Electrically driven source of time-energy entangled photons based on a self-pumped silicon microring resonator. *Optics Letters*, 45(10):2768–2771, 2020.
- [210] Lin Chang, Weiqiang Xie, Haowen Shu, Qi-Fan Yang, Boqiang Shen, Andreas Boes, Jon D. Peters, Warren Jin, Chao Xiang, Songtao Liu, et al. Ultra-efficient frequency comb generation in algaas-on-insulator microresonators. *Nature Communications*, 11(1):1–8, 2020.
- [211] Avik Dutt, Chaitanya Joshi, Xingchen Ji, Jaime Cardenas, Yoshitomo Okawachi, Kevin Luke, Alexander L. Gaeta, and Michal Lipson. On-chip dual-comb source for spectroscopy. *Science advances*, 4(3):e1701858, 2018.

- [212] Alessia Pasquazi, Lucia Caspani, Marco Peccianti, Matteo Clerici, Marcello Ferrera, Luca Razzari, David Duchesne, Brent E. Little, Sai T. Chu, David J. Moss, et al. Self-locked optical parametric oscillation in a cmos compatible microring resonator: a route to robust optical frequency comb generation on a chip. *Optics Express*, 21(11):13333–13341, 2013.
- [213] Sven Ramelow, Alessandro Farsi, Zachary Vernon, Stephane Clemmen, Xingchen Ji, JE. Sipe, Marco Liscidini, Michal Lipson, and Alexander L. Gaeta. Strong nonlinear coupling in a si₃n₄ ring resonator. *Physical Review Letters*, 122(15):153906, 2019.
- [214] Francesco Garrisi. *Nonclassical states of light : fundamental physics, and CMOS devices Nonclassical states of light : fundamental physics, and CMOS devices*. PhD thesis, University of Pavia, 2019.
- [215] Martin HP. Pfeiffer, Junqiu Liu, Michael Geiselmann, and Tobias J Kippenberg. Coupling ideality of integrated planar high-q microresonators. *Physical Review Applied*, 7(2):024026, 2017.
- [216] Kane Yee. Numerical solution of initial boundary value problems involving maxwell’s equations in isotropic media. *IEEE Transactions on antennas, and propagation*, 14(3):302–307, 1966.
- [217] Matthew NO Sadiku. *Numerical techniques in electromagnetics with MATLAB*. CRC press, 2018.
- [218] Remco Stoffer, Kirankumar R Hiremath, and Manfred Hammer. Comparison of coupled mode theory, and fdtd simulations of coupling between bent, and straight optical waveguides. In *AIP Conference Proceedings*, volume 709, pages 366–377. American Institute of Physics, 2004.
- [219] Benedetto Troia, Francesco De Leonardis, and Vittorio MN Passaro. Generalized modelling for the design of guided-wave optical directional couplers. *Optics Letters*, 39(5):1161–1164, 2014.
- [220] Yoshitomo Okawachi, Mengjie Yu, Kevin Luke, Daniel O. Carvalho, Sven Ramelow, Alessandro Farsi, Michal Lipson, and Alexander L Gaeta. Dual-pumped degenerate kerr oscillator in a silicon nitride microresonator. *Optics Letters*, 40(22):5267–5270, 2015.
- [221] Angelica Simbula. *Microring Resonators as Integrated Sources of Nonclassical States of Light*. PhD thesis, University of Pavia, 2017.
- [222] James D Franson. Bell inequality for position, and time. *Physical Review Letters*, 62(19):2205, 1989.

- [223] JD Franson. Two-photon interferometry over large distances. *Physical Review A*, 44(7):4552, 1991.
- [224] Jose A. Jaramillo-Villegas, Poolad Imany, Ogaga D. Odele, Daniel E. Leaird, Zhe-Yu Ou, Minghao Qi, and Andrew M Weiner. Persistent energy-time entanglement covering multiple resonances of an on-chip biphoton frequency comb. *Optica*, 4(6):655–658, 2017.
- [225] Dorian Oser, Sébastien Tanzilli, Florent Mazeas, Carlos Alonso-Ramos, Xavier Le Roux, Grégory Sauder, Xin Hua, Oliver Alibart, Laurent Vivien, Éric Cassan, et al. High-quality photonic entanglement out of a stand-alone silicon chip. *npj Quantum Information*, 6(1):1–6, 2020.
- [226] Davide Grassani, Angelica Simbula, Stefano Pirotta, Matteo Galli, Matteo Menotti, Nicholas C. Harris, Tom Baehr-Jones, Michael Hochberg, Christophe Galland, Marco Liscidini, et al. Energy correlations of photon pairs generated by a silicon microring resonator probed by stimulated four wave mixing. *Scientific reports*, 6:23564, 2016.
- [227] Asher Peres. *Quantum theory: concepts, and methods*, volume 57. Springer Science & Business Media, 2006.
- [228] Z. Vernon, M. Menotti, CC. Tison, JA. Steidle, ML. Fanto, PM. Thomas, SF. Preble, AM. Smith, PM. Alsing, M. Liscidini, et al. Truly unentangled photon pairs without spectral filtering. *Optics Letters*, 42(18):3638–3641, 2017.
- [229] Jeremy L. O’Brien, Geoffrey J. Pryde, Andrew G. White, Timothy C. Ralph, and David Branning. Demonstration of an all-optical quantum controlled-not gate. *Nature*, 426(6964):264–267, 2003.
- [230] Amin Babazadeh, Manuel Erhard, Feiran Wang, Mehul Malik, Rahman Nouroozi, Mario Krenn, and Anton Zeilinger. High-dimensional single-photon quantum gates: concepts, and experiments. *Physical Review Letters*, 119(18):180510, 2017.
- [231] Lana Sheridan and Valerio Scarani. Security proof for quantum key distribution using qudit systems. *Physical Review A*, 82(3):030301, 2010.
- [232] YJ. Lu, RL. Campbell, and ZY Ou. Mode-locked two-photon states. *Physical Review Letters*, 91(16):163602, 2003.
- [233] Laurent Olislager, Johann Cussey, Anh Tuan Nguyen, Philippe Emplit, Serge Massar, J-M. Merolla, and K Phan Huy. Frequency-bin entangled photons. *Physical Review A*, 82(1):013804, 2010.
- [234] José Capmany and Carlos R Fernández-Pousa. Quantum model for electro-optical phase modulation. *JOSA B*, 27(6):A119–A129, 2010.

- [235] Marco Liscidini and JE Sipe. Scalable, and efficient source of entangled frequency bins. *Optics Letters*, 44(11):2625–2628, 2019.
- [236] Folder with additional information about the design of the mask. https://drive.google.com/drive/u/1/folders/1jbvM2saKgA9KtgmJzsb0deo8aMTUz_Gj. Last modification: June 5, 2021.
- [237] Robert H Dicke. Coherence in spontaneous radiation processes. *Physical review*, 93(1):99, 1954.
- [238] T. Onodera, Marco Liscidini, JE. Sipe, and LG Helt. Parametric fluorescence in a sequence of resonators: An analogy with dicke superradiance. *Physical Review A*, 93(4):043837, 2016.
- [239] Amnon Yariv, Yong Xu, Reginald K. Lee, and Axel Scherer. Coupled-resonator optical waveguide: a proposal, and analysis. *Optics Letters*, 24(11):711–713, 1999.
- [240] Rakesh Ranjan Kumar, Xinru Wu, and Hon Ki Tsang. Compact high-extinction tunable crow filters for integrated quantum photonic circuits. *Optics Letters*, 45(6):1289–1292, 2020.
- [241] Francesco Morichetti, Andrea Melloni, Carlo Ferrari, and Mario Martinelli. Error-free continuously-tunable delay at 10 gbit/s in a reconfigurable on-chip delay-line. *Optics Express*, 16(12):8395–8405, 2008.
- [242] Jacob B. Khurgin and Rodney S Tucker. *Slow light: Science, and applications*. CRC press, 2018.
- [243] Francesco Morichetti, Carlo Ferrari, Antonio Canciamilla, and Andrea Melloni. The first decade of coupled resonator optical waveguides: bringing slow light to applications. *Laser & Photonics Reviews*, 6(1):74–96, 2012.
- [244] Shayan Mookherjea and Amnon Yariv. Coupled resonator optical waveguides. *IEEE Journal of selected topics in quantum electronics*, 8(3):448–456, 2002.
- [245] Youg Xu, Reginald K. Lee, and Amnon Yariv. Propagation, and second-harmonic generation of electromagnetic waves in a coupled-resonator optical waveguide. *JOSA B*, 17(3):387–400, 2000.
- [246] Cale M. Gentry, Xiaoge Zeng, and Miloš A Popović. Tunable coupled-mode dispersion compensation, and its application to on-chip resonant four-wave mixing. *Optics Letters*, 39(19):5689–5692, 2014.

- [247] Mikkel Heuck, Jacob Gade Koefoed, Jesper Bjerger Christensen, Yunhong Ding, Lars Hagedorn Frandsen, Karsten Rottwitt, and Leif Katsuo Oxenløwe. Unidirectional frequency conversion in microring resonators for on-chip frequency-multiplexed single-photon sources. *New Journal of Physics*, 21(3):033037, 2019.
- [248] Xiaoge Zeng, Cale M. Gentry, and Miloš A Popović. Four-wave mixing in silicon coupled-cavity resonators with port-selective, orthogonal supermode excitation. *Optics Letters*, 40(9):2120–2123, 2015.
- [249] Ryszard Horodecki, Paweł Horodecki, Michał Horodecki, and Karol Horodecki. Quantum entanglement. *Reviews of Modern Physics*, 81(2):865, 2009.
- [250] Jian-Wei Pan, Matthew Daniell, Sara Gasparoni, Gregor Weihs, and Anton Zeilinger. Experimental demonstration of four-photon entanglement, and high-fidelity teleportation. *Physical Review Letters*, 86(20):4435, 2001.
- [251] Yu Guo, Bi-Heng Liu, Chuan-Feng Li, and Guang-Can Guo. Advances in quantum dense coding. *Advanced Quantum Technologies*, 2(5-6):1900011, 2019.
- [252] Jiu-Cang Hao, Chuan-Feng Li, and Guang-Can Guo. Controlled dense coding using the greenberger-horne-zeilinger state. *Physical Review A*, 63(5):054301, 2001.
- [253] Manfred Eibl, Nikolai Kiesel, Mohamed Bourennane, Christian Kurtsiefer, and Harald Weinfurter. Experimental realization of a three-qubit entangled w state. *Physical Review Letters*, 92(7):077901, 2004.
- [254] Bao-Sen Shi and Akihisa Tomita. Teleportation of an unknown state by w state. *Physics Letters A*, 296(4-5):161–164, 2002.
- [255] Nikolai Kiesel, Mohamed Bourennane, Christian Kurtsiefer, Harald Weinfurter, D. Kaszlikowski, W Laskowski, and Marek Zukowski. Three-photon w-state. *Journal of Modern Optics*, 50(6-7):1131–1138, 2003.
- [256] M. Menotti, L. Maccone, JE. Sipe, and M Liscidini. Generation of energy-entangled w states via parametric fluorescence in integrated devices. *Physical Review A*, 94(1):013845, 2016.
- [257] Yu-Yang Ding, Hua Chen, Shuang Wang, De-Yong He, Zhen-Qiang Yin, Wei Chen, Zheng Zhou, Guang-Can Guo, and Zheng-Fu Han. Polarization variations in installed fibers, and their influence on quantum key distribution systems. *Optics Express*, 25(22):27923–27936, 2017.

- [258] Jürgen Brendel, Nicolas Gisin, Wolfgang Tittel, and Hugo Zbinden. Pulsed energy-time entangled twin-photon source for quantum communication. *Physical Review Letters*, 82(12):2594, 1999.
- [259] Todd Pittman. It’s a good time for time-bin qubits. *Physics*, 6:110, 2013.
- [260] Antonio Acin, Dagmar Bruß, Maciej Lewenstein, and Anna Sanpera. Classification of mixed three-qubit states. *Physical Review Letters*, 87(4):040401, 2001.
- [261] C.J. McKinstrie, J.D. Harvey, S. Radic, and M.G. Raymer. Translation of quantum states by four-wave mixing in fibers. *Optics Express*, 13(22):9131–9142, 2005.
- [262] M.E. Marhic, Y. Park, F.S. Yang, and L.G. Kazovsky. Widely tunable spectrum translation, and wavelength exchange by four-wave mixing in optical fibers. *Optics Letters*, 21(23):1906–1908, 1996.
- [263] M. Menotti, B. Morrison, K. Tan, Z. Vernon, J.E. Sipe, and M. Liscidini. Nonlinear coupling of linearly uncoupled resonators. *Physical Review Letters*, 122(1):013904, 2019.
- [264] M. Liscidini, L.G. Helt, and J.E. Sipe. Asymptotic fields for a hamiltonian treatment of nonlinear electromagnetic phenomena. *Physical Review A*, 85(1):013833, 2012.
- [265] Yurii A. Vlasov and Sharee J. McNab. Losses in single-mode silicon-on-insulator strip waveguides, and bends. *Optics Express*, 12(8):1622–1631, 2004.
- [266] Zhiping Zhou, Bing Yin, and Jürgen Michel. On-chip light sources for silicon photonics. *Light: Science & Applications*, 4(11):e358, 2015.
- [267] Fengnian Xia, Mike Rooks, Lidija Sekaric, and Yurii Vlasov. Ultra-compact high order ring resonator filters using submicron silicon photonic wires for on-chip optical interconnects. *Optics Express*, 15(19):11934–11941, 2007.
- [268] Daoxin Dai. Silicon nanophotonic integrated devices for on-chip multiplexing, and switching. *Journal of Lightwave Technology*, 35(4):572–587, 2016.
- [269] Daoxin Dai and John E. Bowers. Silicon-based on-chip multiplexing technologies, and devices for peta-bit optical interconnects. *Nanophotonics*, 3(4-5):283–311, 2014.
- [270] Laurent Vivien, Andreas Polzer, Delphine Marris-Morini, Johann Osmond, Jean Michel Hartmann, Paul Crozat, Eric Cassan, Christophe Kopp, Horst Zimmermann, and Jean Marc Fédéli. Zero-bias 40gbit/s germanium waveguide photodetector on silicon. *Optics Express*, 20(2):1096–1101, 2012.

- [271] Tao Yin, Rami Cohen, Mike M. Morse, Gadi Sarid, Yoel Chetrit, Doron Rubin, and Mario J Paniccia. 31ghz ge nip waveguide photodetectors on silicon-on-insulator substrate. *Optics Express*, 15(21):13965–13971, 2007.
- [272] Jun Rong Ong, Ranjeet Kumar, and Shayan Mookherjea. Ultra-high-contrast, and tunable-bandwidth filter using cascaded high-order silicon microring filters. *IEEE Photonics Technology Letters*, 25(16):1543–1546, 2013.
- [273] Dorian Oser, Florent Mazeas, Xavier Le Roux, Diego Pérez-Galacho, Olivier Alibart, Sébastien Tanzilli, Laurent Labonté, Delphine Marris-Morini, Laurent Vivien, Éric Cassan, et al. Coherency-broken bragg filters: Overcoming on-chip rejection limitations. *Laser & Photonics Reviews*, 13(8):1800226, 2019.
- [274] Daryl T. Spencer, Mike Davenport, Sudharsanan Srinivasan, Jacob Khurgin, Paul A. Morton, and John E Bowers. Low kappa, narrow bandwidth si 3 n 4 bragg gratings. *Optics Express*, 23(23):30329–30336, 2015.
- [275] GK. Celler and Sorin Cristoloveanu. Frontiers of silicon-on-insulator. *Journal of Applied Physics*, 93(9):4955–4978, 2003.
- [276] Michel Bruel. Separation of silicon wafers by the smart-cut method. *Materials Research Innovations*, 3(1):9–13, 1999.
- [277] Stephen A Campbell. *The science, and engineering of microelectronic fabrication*. Oxford university press, 2001.
- [278] Badih El-Kareh and Lou N Hutter. *Fundamentals of semiconductor processing technology*. Springer Science & Business Media, 2012.
- [279] Frank E. Abboud, Michael Asturias, Maesh Chandramouli, and Yoshihiro Tezuka. Mask data processing in the era of multibeam writers. In *Photomask Technology 2014*, volume 9235, page 92350W. International Society for Optics, and Photonics, 2014.
- [280] Syed Rizvi. *Handbook of photomask manufacturing technology*. CRC Press, 2018.
- [281] Alfred Kwok-Kit Wong. *Resolution enhancement techniques in optical lithography*, volume 47. SPIE press, 2001.
- [282] Robert-H Munnig Schmidt. Ultra-precision engineering in lithographic exposure equipment for the semiconductor industry. *Philosophical Transactions of the Royal Society A: Mathematical, Physical, and Engineering Sciences*, 370(1973):3950–3972, 2012.

- [283] Keith Best, Pankaj Raval, Norbert Kappel, Nazneen Jeewakhan, Milan Prejda, Kevin Kassekert, Michael Moore, Charles Yang, May Wang, and Ye Wang. Novel lithography technique using an asml stepper/scanner for the manufacture of display devices in mems world. In *Proc. NSTI Nanotechnol. Conf. Trade Show*, volume 1, page 726, 2007.
- [284] G. Cunge, RL. Inglebert, O. Joubert, L. Vallier, and N Sadeghi. Ion flux composition in hbr/cl 2/o 2, and hbr/cl 2/o 2/cf 4 chemistries during silicon etching in industrial high-density plasmas. *Journal of Vacuum Science & Technology B: Microelectronics, and Nanometer Structures Processing, Measurement, and Phenomena*, 20(5):2137–2148, 2002.
- [285] James P. Roland, Paul J. Marcoux, Gary W Ray, and Glenn H Rankin. End-point detection in plasma etching. *Journal of Vacuum Science & Technology A: Vacuum, Surfaces, and Films*, 3(3):631–636, 1985.
- [286] N. Layadi, SJ. Molloy, TC. Esry, T. Lill, J. Trevor, MN. Grimbergen, and J Chinn. Interferometry for end point prediction during plasma etching of various structures in complementary metal–oxide–semiconductor device fabrication. *Journal of Vacuum Science & Technology B: Microelectronics, and Nanometer Structures Processing, Measurement, and Phenomena*, 17(6):2630–2637, 1999.
- [287] E. Pargon, O. Joubert, T. Chevolleau, G. Cunge, Songlin Xu, and Thorsten Lill. Mass spectrometry studies of resist trimming processes in h br/ o 2, and cl 2/ o 2 chemistries. *Journal of Vacuum Science & Technology B: Microelectronics, and Nanometer Structures Processing, Measurement, and Phenomena*, 23(1):103–112, 2005.
- [288] L. Vallier, J. Foucher, X. Detter, E. Pargon, O. Joubert, G. Cunge, and T Lill. Chemical topography analyses of silicon gates etched in hbr/cl 2/o 2, and hbr/cl 2/o 2/cf 4 high density plasmas. *Journal of Vacuum Science & Technology B: Microelectronics, and Nanometer Structures Processing, Measurement, and Phenomena*, 21(2):904–911, 2003.
- [289] X. Detter, R. Palla, I. Thomas-Bouterin, E. Pargon, G. Cunge, O. Joubert, and L Vallier. Impact of chemistry on profile control of resist masked silicon gates etched in high density halogen-based plasmas. *Journal of Vacuum Science & Technology B: Microelectronics, and Nanometer Structures Processing, Measurement, and Phenomena*, 21(5):2174–2183, 2003.
- [290] E. Pargon, Maxime Darnon, O. Joubert, T. Chevolleau, L. Vallier, L. Molard, and T Lill. Towards a controlled patterning of 10 nm silicon gates in high density plasmas. *Journal of Vacuum Science & Technology B: Microelectronics, and Nanometer Structures Processing, Measurement, and Phenomena*, 23(5):1913–1923, 2005.

- [291] Werner Kern. The evolution of silicon wafer cleaning technology. *Journal of the Electrochemical Society*, 137(6):1887, 1990.
- [292] L. Azarnouche, E. Pargon, K. Mengueli, M. Fouchier, D. Fuard, P. Gouraud, C. Verove, and O. Joubert. Unbiased line width roughness measurements with critical dimension scanning electron microscopy, and critical dimension atomic force microscopy. *Journal of Applied Physics*, 111(8):084318, 2012.
- [293] M. Fouchier, E. Pargon, and Benjamin Bardet. An atomic force microscopy-based method for line edge roughness measurement. *Journal of applied physics*, 113(10):104903, 2013.
- [294] Piet De Moor, Ann Witvrouw, Veerle Simons, and Ingrid De Wolf. Fabrication, and reliability testing of ti/tin heaters. In *Micromachining, and Micro-fabrication Process Technology V*, volume 3874, pages 284–293. International Society for Optics, and Photonics, 1999.
- [295] Joseph Fauty, Steve Strouse, Jay Yoder, Carlos Acuna, and Phil Evard. Al-cu metal bond pad corrosion during wafer saw. *The International journal of microcircuits, and electronic packaging*, 24(1):19–29, 2001.
- [296] Banqiu Wu, Ajay Kumar, and Sharma Pamarthy. High aspect ratio silicon etch: A review. *Journal of applied physics*, 108(5):9, 2010.
- [297] Franz Laermer and Andrea Schilp. Method of anisotropically etching silicon, March 26 1996. US Patent 5,501,893.
- [298] Sarah L. Gilbert and William C Swann. ‘acetylene 12c2h2 absorption reference for 1510 nm to 1540 nm wavelength calibration—srm 2517a. *NIST special publication*, 260(133), 2001.
- [299] Marco Clementi, Andrea Barone, Thomas Fromherz, Dario Gerace, and Matteo Galli. Selective tuning of optical modes in a silicon comb-like photonic crystal cavity. *Nanophotonics*, 9(1):205–210, 2019.
- [300] Houssein El Dirani, Ayman Kamel, Marco Casale, Sébastien Kerdiles, Christelle Monat, Xavier Letartre, Minhao Pu, Leif Katsuo Oxenløwe, Kresten Yvind, and Corrado Sciancalepore. Annealing-free si3n4 frequency combs for monolithic integration with si photonics. *Applied Physics Letters*, 113(8):081102, 2018.
- [301] Pascal Del’Haye, Olivier Arcizet, Michael L. Gorodetsky, Ronald Holzwarth, and Tobias J Kippenberg. Frequency comb assisted diode laser spectroscopy for measurement of microcavity dispersion. *Nature Photonics*, 3(9):529, 2009.

- [302] Qiang Li, Ziyang Zhang, Jing Wang, Min Qiu, and Yikai Su. Fast light in silicon ring resonator with resonance-splitting. *Optics Express*, 17(2):933–940, 2009.
- [303] Z. Vernon, N. Quesada, M. Liscidini, B. Morrison, M. Menotti, K. Tan, and JE Sipe. Scalable squeezed-light source for continuous-variable quantum sampling. *Physical Review Applied*, 12(6):064024, 2019.
- [304] Yuan Guo, Wei Zhang, Shuai Dong, Yidong Huang, and Jiangde Peng. Telecom-band degenerate-frequency photon pair generation in silicon microring cavities. *Optics Letters*, 39(8):2526–2529, 2014.
- [305] Yanbing Zhang, Michael Kues, Piotr Roztock, Christian Reimer, Bennet Fischer, Benjamin MacLellan, Arstan Bisianov, Ulf Peschel, Brent E Little, Sai T Chu, et al. Induced photon correlations through the overlap of two four-wave mixing processes in integrated cavities. *Laser & Photonics Reviews*, 14(9):2000128, 2020.